PhD-FSTC-2016-40
The Faculty of Sciences, Technology and Communication

DISSERTATION

Defence held on 27/09/2016 in Belval

to obtain the degree of

DOCTEUR DE L'UNIVERSITÉ DU LUXEMBOURG

EN PHYSIQUE

by

Jonathan CREPELLIERE
Born on 08th December 1985 in Clamart (France)

METALORGANIC CHEMICAL VAPOUR DEPOSITION OF P-TYPE DELAFOSSITE $CuCrO_2$ SEMICONDUCTOR THIN FILMS: CHARACTERIZATION AND APPLICATION TO TRANSPARENT P-N JUNCTION

Dissertation defense committee

Dr Damien Lenoble, dissertation supervisor
Luxembourg Institute of Science and Technology, Belvaux

Dr Susanne Siebentritt, dissertation supervisor
Professor, Université du Luxembourg

Dr Ludger Wirtz, Chairman
Professor, Université du Luxembourg

Dr Jean-Pierre Raskin,
Professor, Université de Louvain-la-Neuve

Dr Negar Naghavi,
Professor, Ecole Nationale Supérieure de Chimie de Paris

REMERCIEMENTS

Je tiens à remercier en premier lieu Damien Lenoble. D'abord pour m'avoir accepté dans son unité de recherche, anciennement « UGN » et la confiance qu'il m'a donné en faisant ce choix (j'espère qu'il ne le regrette pas maintenant ☺). Je le remercie aussi pour l'encadrement de la thèse qu'il a géré jusqu'aux dernières lignes de ce manuscrit ou plutôt jusqu'aux derniers cheveux qu'il a tiré de sa tête, lui provoquant une calvitie prématurée. Ses conseils et remarques ont été déterminants afin de mener à bien cette thèse. Je n'oublierai jamais ses qualités humaines que peu de personnes ont.

Mes profondes reconnaissances vont aussi à Susanne Siebentritt. Je lui exprime ma gratitude pour la patience qu'elle a eu avec moi et mon anglais pourri, et mes présentation orales pourri et… je crois que c'est tout. Ses connaissances scientifiques ont été indispensables dans la compréhension et l'interprétation de résultats de cette thèse. Son bagage scientifique est impressionnant. Je remercie également Ludger Wirtz pour avoir accepté de faire partie du comité d'encadrement de cette thèse malgré que le sujet ne soit pas de son domaine. Je le remercie aussi pour son rôle de président du jury qu'il a accepté.

Je remercie les membres du jury: madame Negar Naghavi et monsieur Jean-Pierre Raskin, pour avoir accepté d'évaluer mes travaux et m'avoir fait l'honneur de leur présence lors de ma soutenance.

Ensuite, je tiens à remercier profondément Naoufal Bahlawane qui a contribué au succès de cette thèse (et oui il y a eu quand même des succès…), par ses connaissances très solide en matière de CVD et d'en d'autre domaines. J'ai beaucoup apprécié les discussions scientifiques qu'on a eu ensemble et son regard critique sur les résultats. Il fut plus qu'un collègue pour moi, mais un ami proche de par notre religion qu'on a en commun.

Je remercie Renaud Leturcq pour m'avoir aidé et encadré dans mes travaux sur une grosse partie de cette thèse que sont les mesures électriques. Son expérience dans le domaine ont été, I mean, indispensable ☺. Merci encore Renaud. Je veux aussi remercier mon très cher collègue et ami Petru. Men, on a partagé de nombreuses discussions scientifiques sur notre matériaux en commun, mais aussi les belles rigolades qu'on a eu sur la machine et en général…

Je suis reconnaissant envers Noureddine pour m'avoir aidé à certains moments sur la machine de la mort et ses caprices incessants, mais aussi pour son style de travail inimitable qui m'a tant fait rire. Envers Didier, pour son travail de qualité sur le FIB, pour ses grandes qualités humaines et aussi parce qu'il aime les Vosges ☺. Je remercie Jérôme Guillot pour les analyses XPS et d'avoir pris de son temps pour discuter et interpréter les résultats ensemble. Son effort a été indéniable. Par contre, il n'a plus de cheveux sur la tête mais ce n'est pas de ma faute…. De même, je remercie Germain Rey pour ses explications sur les modèles optiques de couches minces et sa disponibilité pour discuter. Ainsi que Florian Werner pour les mesures d'effet Hall sur des échantillons si peu standard et si peu évidant à mesurer.

Je remercie plus généralement les gens de l'ancienne « UGN », Bianca Ritta, Kévin, Jean-Sébastien, Guillaume et Manuel, qui m'ont un jour ou l'autre aidé, mais aussi pour les bons moments qu'on a partagé ensemble. Ce fut un plaisir d'avoir fait leurs connaissances.

Un grand merci aux anciens doctorants de mon bureau, la F 1.14, avec lesquels on a passé tellement de moments inoubliables : Vincent, Moustapha, Rodolphe, Florian, Cédric et Sébastien. Tellement inoubliables que je ne me souviens plus si un jour on a vraiment parlé de science dans ce bureau… Sans oublié ceux qui galère encore pour leur thèse : Olga, Sunil, David, Alex, Divia… En revanche je ne remercie pas Nohora, mais elle sait pourquoi ☺.

Mes derniers remerciements envers les gens du CRP, et non des moindres, reviennent à mes amis Samir, Brahime, Rachid et Asmaa. Ça fait beaucoup d'arabes je sais…. Mais un grand un merci à chacun d'eux, pour leur aide qu'ils m'ont apporté durant toutes ces années et pour leur gentillesse. Ils vont beaucoup me manquer….

Je tiens à remercier mon père pour m'avoir permis de faire toutes ces années d'études. Que le chemin a été long et dur pour en arriver là. J'espère qu'il sera fier de moi. Je remercie enfin ma chère épouse pour le soutient qu'elle m'apporte depuis sept ans déjà dans mes études, sans oublier bien sur mes deux filles.

CONTENTS

TABLE OF FIGURES

TABLES

ACRONYMS

ALD: Atomic Layer Deposition
AZO: Aluminium doped Zinc Oxide
CBM: Conduction Band Minimum
CVD: Chemical Vapour Deposition
DEZ: Diethylzinc
DOS: Density of States
DFT: Density Functional Theory
EDOS: Electronic Density of States
EDX: Energy Dispersive X-ray spectroscopy
FIB: Focused Ion Beam
FTO: Florine doped Tin Oxide
GGA: Generalized Gradient Approach
GIXRD: Grazing Incidence X-Ray Diffraction
HAAF: High Angle Annular Dark Field
HRTEM: High Resolution Transmission Electron Microscopy
ICDD: International Center for Diffraction Data
ITO: Indium doped Tin Oxide
LDA: Local Density Approximation
Mg_{Cr}: Chromium substituted by magnesium
MOCVD: Metal Organic Chemical Vapour Deposition
MS: Magnetron Sputtering
O_i: Oxygen interstitial
OMCVD: Organometallic Chemical Vapour Deposition
PLD: Pulsed Laser Deposition
PVD: Physical Vapour Deposition
RT: Room Temperature
SAED: Selected Area Electron Diffraction
SCLC: Space Charge Limited Current
SEM: Scanning Electron Microscopy
SG: Sol-gel
SIMS: Secondary Ion Mass Spectroscopy
SS: Solid State
sX-LDA: Screened exchange Local Density Approximation
TCM: Transparent Conducting Materials
TCO: Transparent Conducting Oxides
TEM: Transmission Electron Microscopy
TGA: Thermogravimetric Analysis
TOS: Transparent Oxide Semiconductors
VBM: Valence Band Maximum
V_{Cu}: Copper vacancy
XPS: X-Ray photoemission Spectroscopy
XRD: X-Ray Diffraction

INTRODUCTION

Nowadays, electronic is everywhere in our societies like computer, mobile phone, household appliance, means of transport and more recently in renewable energy. In the second half of the 20th century, transparent conducting materials (TCM) were discovered, opening new horizons of electronic applications, called "transparent electronic"[1], like transparent modern circuitry, transparent solar cells, UV detector, etc…

TCM mixed both electrical conductivity and optical transparency which are antagonistic properties as the band structure requirements contrast significantly. While for a good transparency, a wide band gap (>3 eV) is necessary in order to avoid the light absorption, conducting semiconductor materials are usually characterized by a narrow band gap (<2 eV) and low activation energy of charge carriers to tune their electrical conductivity at room temperature. The very first reported TCM was cadmium oxide CdO back in 1952[2]. It belongs to the transparent oxides semiconductor (TOS) class, an important sub-category of TCMs. TOS have initially wide band gaps and are subsequently extrinsically doped in order to modify the charge carrier concentration without altering the optical properties[3], [4].

Nowadays TOS are widely used in different technology fields as transparent electrodes in flat panel displays, light-emitting diodes, solar cells and touch panels[5]–[9]. The most used TOS are ITO[10], FTO[11] or AZO[12] which are known as "transparent conducting oxides" (TCO) for their high n-type conductivity (>1000 S.cm^{-1}). However, the development of modern electronic circuitry or optoelectronic devices is based on p–n junctions, and therefore needs also the use of p-type materials[13]. Although n-type materials with high conductivity and transparency were demonstrated[3], p-type TOS still need an archetypal material. The poor properties of current p-type TOS is a barrier of transparent electronic development and TOS are actually only used as transparent electrode as passive applications.

The development of active transparent electronic devices appeared to be stalled until the end of the 20th century when a new design of p-type TOS emerged with works of Kawazoe et al.[14]. The authors proposed a model for the chemical modulation of the valence band in order to explain the high mobility measured for $CuAlO_2$, a delafossite compound[14], [15]. For twenty years, delafossite compounds AMO_2 (with A = Cu or Ag and M = Al, Sc, Cr, Fe, Ga, or Y)[16] demonstrated a promising but still insufficient trade-off between electrical conductivity and visible transparency compared to n-type TCO materials. Therefore, delafossite compounds could be the most promising materials to further studied and optimized for the fabrication of transparent p-n junction. To date, the highest reported conductivity of delafossite was 220 S cm^{-1} for Mg doped $CuCrO_2$[17]. Copper chromium oxides contrast with other delafossites, in terms of: (i) high density of state of 3d M cations (Cr^{3+}) near the valence band maximum, (ii)

covalent mixing between chromium and oxygen ions and (iii) good dopability, making $CuCrO_2$ a good p-type candidate for transparent electronic devices[18]–[23].

Delafossite $CuCrO_2$ was synthesized with various method like solid-state reaction[18], [21], [24]–[31], sol-gel[32]–[38], pulsed laser deposition[39]–[43] or magnetron sputtering[17], [44]–[47]. However, all of these methods are either too complex or need high growth temperature ($\geq 600°C$) and/or too long processing for an up scaling to the industry for an application on glass. Moreover, in almost all cases, the trade-off between electrical conductivity and visible transparency have to be improved for an archetypal transparent p-n junction.

MOCVD synthesis has demonstrated very good performance of semiconductors synthesis in term of low growth temperature and fast synthesis, mainly due to the physico-chemical properties of metal-organic precursors[48]. Electrical properties of semiconductors were also compatible with the manufacturing requirement of the industry. However, delafossite $CuCrO_2$ synthesized with MOCVD method was still poorly investigated compared to others methods[49].

Therefore, the objectives of this thesis are: (i) synthesize delafossite $CuCrO_2$ thin films with pulsed injection MOCVD method, (ii) obtain good trade-off electrical conductivity-visible transparency for a possible up scaling to the industry and (iii) synthesize a transparent p-n junction $CuCrO_2$/ZnO on glass with CVD based method.

In the first chapter of this manuscript, we will present the state of the art of delafossite $CuCrO_2$ and ZnO, the second chapter will relate the used experimental methods while in the third chapter we will present an optical model that we developed during this thesis to characterize our thin films. The fourth chapter will be dedicated to the CVD synthesis of delafossite $CuCrO_2$ and the fifth chapter will deal with electrical and optical characterizations of the films. The last chapter will present the application of our $CuCrO_2$ thin films to the p-n junction. We will finish by providing conclusions and perspectives of this works.

I. STATE OF THE ART OF TRANSPARENT OXIDES SEMICONDUCTORS: $CuCrO_2$ AND ZnO

In this chapter, based on works described in literature, we introduce the benefits of delafossite $CuCrO_2$ and ZnO as p-type and n-type materials respectively, for the synthesis of transparent p-n junctions. Firstly, we describe existing p-type TCM and their respective limitations in the framework of our thesis goal. Then, we thoroughly describe p-type delafossite $CuCrO_2$ and highlight its advantages when the integration of p-type materials into electronic devices is considered together with its manufacturability. We finish with a short resume of n-type ZnO, which will be used as n-type material for our elaborated transparent p-n junctions.

I.1 P-type TCM

In this section we briefly talk about p-type TCMs which were investigated for their electrical conductivity and optical transparency and we highlight their limitations as potentials p-type TCM for technologies integration.

I.1.1 P-type non-TOS

TCMs can be divided in two categories: TOS and non-TOS (Figure 1). In both categories, there are p-type or n-type materials. In this paragraph we discuss only p-type non-TOS.

The reported p-type non-TOS materials belong to chalcogenides family which contains at least one chalcogen anion (Ch=S, Se, Te, Po) and at least one more electropositive element. Binary compounds, ZnSe and ZnTe, exhibit good mobility, between 50-340 $cm^2/V.s$, but they have too low band gap, 2.4-2.7 eV, that impairs their visible transparency[50]–[52]. It was demonstrated with calculations that compounds like $CsZn_3Se_4$ and $CsZn_3Te_4$ have higher band gap than ZnCh and have a low effective mass at the valence band maximum (VBM)[53]. However, experimentally it was shown that ZnCh impurities colour the material in yellow or black for $Cs_2Zn_3Se_4$ and $Cs_2Zn_3Te_4$ respectively[53].Moreover, the cesium is highly reactive with carbon coating used in some reactor[53]. Two other chalcogenides were also investigated: $CuAlS_2$ and $CuAlSe_2$. Chalcogenide $CuAlS_2$[54]–[58] have demonstrated high conductivity up to 40 $S.cm^{-1}$ when it is doped with zinc [56]–[58] and a transmittance of 80% [57], [58] in the visible range for a 100 nm thickness. However, the synthesis method is either inadequate for an up-scaling to the industry (pulsed laser deposition (PLD) and channel spark ablation)[57], [58]

or produces $Cu_{2-x}S$ phase (atomic layer deposition (ALD))[54]. Chalcogenide $CuAlSe_2$ has a too low band gap (2.3-2.5 eV) for transparent electronic applications[59], [60].

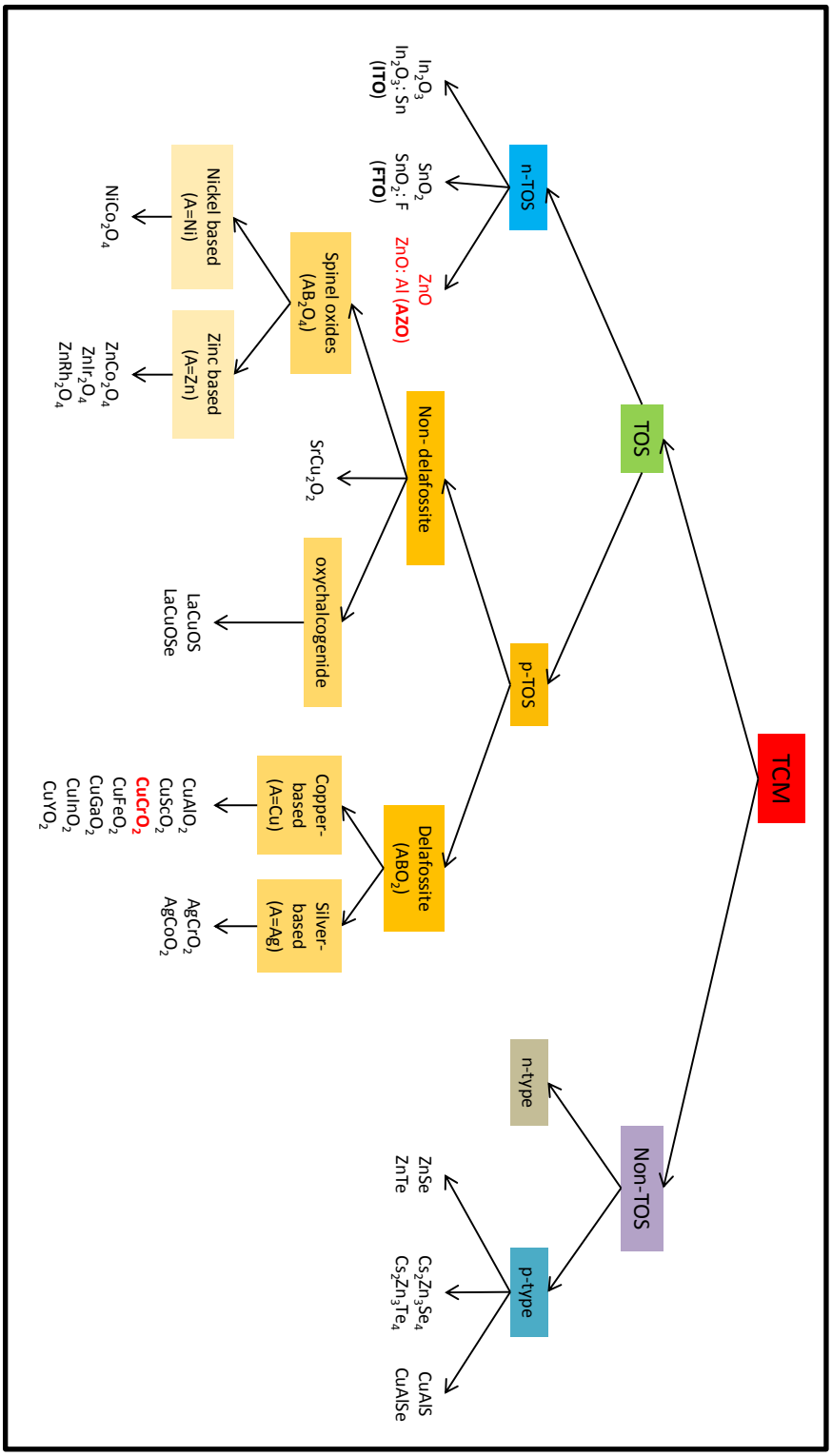

Figure 1 TCM categories and their materials

I.1.2 P-type TOS

TCM's oxides (TOS) are of particular interest due to their chemical stability, high negative formation enthalpy and wide band gap [3]. We first describe in this section the conditions required for selecting the most promising p-type TOS, then, we introduce some non-delafossite p-type TOS.

I.1.2.1 Kawazoe valence band modulation

The main impediment in finding a p-type TOS (Figure 1) matching physical properties of actual n-type TOS, is the strong localization of oxygen 2p states at the valence band edge, resulting in flat energy bands and therefore a high hole effective mass[61]. This is due to the O 2p levels lying far lower than the valence orbital of metallic atoms[62], resulting in a non-dispersive VBM (Figure 2 (a)) and a high negative partial charge on the oxygen atoms that is a deep trap for positive charge carriers (holes). In order to avoid this phenomenon without compromising the optical transparency, Kawazoe and al.[14], [15] proposed a new design of p-type TOS based on the valence band modulation. The energy levels of the shell of metallic cations must be close to those of the 2p levels of oxide ions. By enhancing the bonds covalency, a more dispersive band is pushed up above the non-bonding O 2p or metallic cations 3d states (Figure 2 (b)).

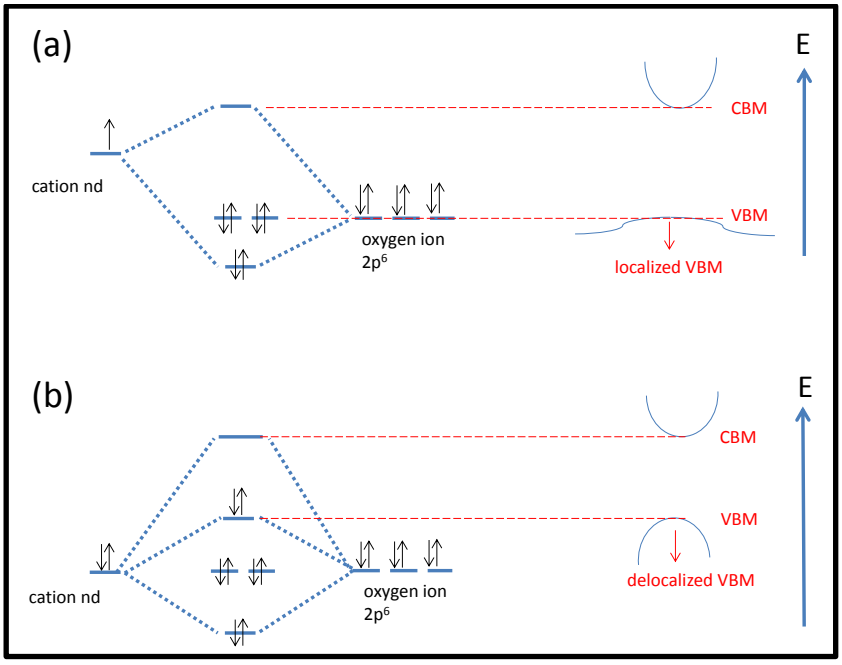

Figure 2 (a) Non-dispersive and (b) dispersive valence band due to covalence bond between metallic cation and O

Moreover, the metallic cations must have closed electronic shells to avoid any coloration, due to d-d transitions (Figure 3).

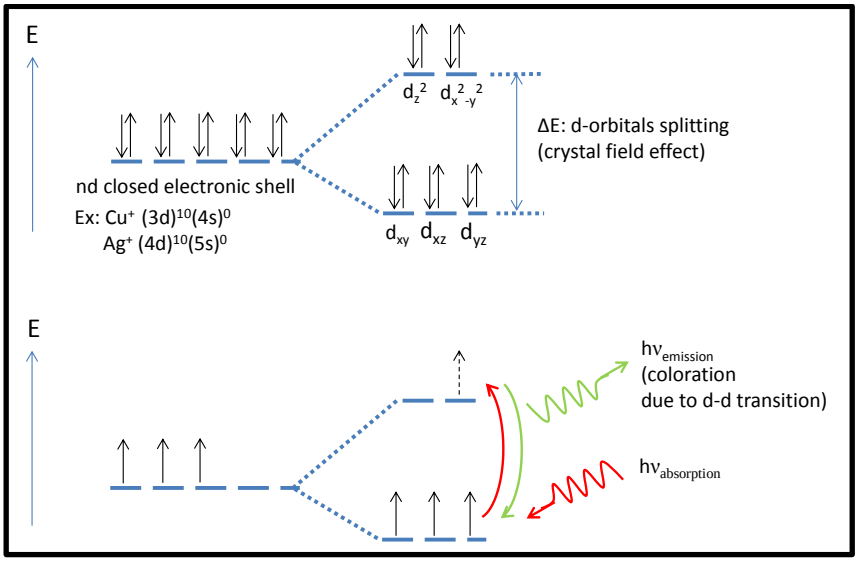

Figure 3 Absorption and emission of light by d-d transitions for atoms without closed shell electronic

The third aspect is related to the tetrahedral coordination of oxide ions. This configuration allows pair electrons (in 2s and 2p orbitals of oxygen) to bond with two other atoms. Therefore, the non-bonding nature of oxide ions in Figure 2 disappear and the strong localization of carriers at the valence band edge is diminished.

I.1.2.2 Non delafossite compounds

The first p-type TOS reported was NiO[63] in 1993. Nickel oxides thin films[63]–[69], with lithium, potassium or copper doping[65], [67]–[69], have conductivity between 4-21 $S.cm^{-1}$ with an optical gap between 3.3-3.7 eV. However, with doping, transparency is only 40-50% for 70-200 nm thin films due to the visible light absorption by the hole polarons localized on oxygen ions[70], [71]. Even if NiO was used as p-type material for transparent diode[72]–[74], transistors[75] and solar cells[68], [76]–[78], the trade-off electrical conductivity-visible transparency is still not acceptable.

Another p-type TOS is $SrCu_2O_2$. Despite its optical band gap at 3.3 eV and its relative good transmittance (60-70%) for 100-220nm thicknesses [79]–[83], the highest electrical conductivity reported, when the e-beam deposition technic is used, is only 0.05 $S.cm^{-1}$[79],

which is insufficient for device applications. The low conductivity in $SrCu_2O_2$ is due to the high effective mass at VBM, according to different band structure calculations[84].

Spinel compounds can be also p-type TOS[85]. Spinel $NiCo_2O_4$[85]–[92], have electrical conductivity, with cations off-stoichiometry, reported between 200-300 $S.cm^{-1}$ at room temperature[86], [91]. However, the transparency in the visible range is much less interesting and is limited to 10-15% for a 100 nm thick film [86], [91]. This is due to the direct band gap value of $NiCo_2O_4$ being less than 2.0 eV. Zn-based spinel can also exhibit p-type TOS properties as $ZnCo_2O_4$[86], [93]–[96], $ZnRh_2O_4$[95]–[97] and $ZnIr_2O_4$[93], [95], [96]. The reported electrical conductivity is between 0.4-3.4 $S.cm^{-1}$ [86], [94], [96], [97] and optical transparency between 15-60%[94], [96] with optical gaps of 2.3-3.0 eV[96]. However, these high optical gap values were called into question since any calculation [95] did not match the experimental values and no more deep studies confirmed these results.

The last reported non-delafossite p-type TOS are oxychalcogenides LaCuOS[98] and LaCuOSe [98], [99]. While an exceptional conductivity up to 900 $S.cm^{-1}$ and an optical gap at 2.8 eV can be obtained, the transmittance values were not published and no research group did confirm these results. Moreover, the experimental synthesis, reactive solid state epitaxy, is not compatible for an up-scaling of the process to the industry. We summarize structural, electrical and optical properties of p-type non-delafossite TOS in Table 16 (in Annexes).

Although materials presented in this section (non-delafossite) have p-type TOS properties, the trade-off electrical conductivity-visible transparency is still poor to consider their integration in transparent electronics. Actually, the most promising p-type TOS are still delafossite compounds because they demonstrate, during this last twenty years, good electrical conductivity, high optical transparency and very good stability in air.

I.1.2.3 Delafossite compounds

Delafossite compounds AMO_2 are a ternary oxides family[16], with a coordination (II) on A, (VI) on M, and (IV) on O[a]. Compounds with a large atomic radius for M cation, such as Al, Ga, Cr, Fe, Sc, In, Y or La and small for A cation radius are feasible, such as Ag, Cu or Pd. Indeed, coordination (II) is favoured when A cation has relatively small atomic radius in ternary oxides [100]. Paladium based delafossite are not considered, because they are metallic material,

[a] Coordination is the number of atom bonds. It is not the oxidation state number.

in the opposite of copper based or silver based delafossite which are semiconductors materials[16].

According to the Kawazoe valence band modulation approach, delafossite compounds match all the required conditions for getting promising p-type TOS: (i) the A cation has a closed electronic shell nd^{10} (Cu^{+} and Ag^{+}), (ii) it has also a shell energy level closed to those of O 2p[62] giving more dispersive a valence band, and (iii) oxygen ions are in a tetrahedral configuration.

Delafossite compounds with p-type TOS properties can be sub-divided into two categories, Cu-based and Ag-based. Only two p-type materials were reported for Ag-based, $AgCrO_2$ [101] and $AgCoO_2$ [7] [102]. Ag-based thin films syntheses were very difficult to achieve[103] and low electrical conductivity were measured (10^{-4}-10^{-6} $S.cm^{-1}$ for a transparency of 40-60 % with a thickness of 150-200nm)[101] [7] [102]. Cu-based delafossites are much more interesting in terms of materials diversity and synthesis: seven p-type materials $CuMO_2$ (M=Al, Ga, Fe, In, Sc, Y and Cr) were reported up to date (Figure 1). Electrical conductivities (see Table 15 in Annexe) are also higher than Ag-based due to better alignment of energy levels of Cu 3d (when compared with Ag 4d) with O 2p. VBM is more dispersive (Figure 2 (b)) and effective mass shall decrease. Delafossite $CuAlO_2$ exhibit an interesting trade-off electrical conductivity-visible transparency (0.01-0.5 $S.cm^{-1}$ for 55-75% transparency with thickness of 100-250 nm), better than any other delafossite $CuMO_2$ except one: delafossite $CuCrO_2$. Therefore, we present in the next section, an overview of delafossite $CuCrO_2$ properties which led us to use $CuCrO_2$ as p-type material for the synthesis of transparent p-n junction.

I.2 Delafossite p-type $CuCrO_2$

Delafossite $CuCrO_2$ has attracted much attention since Nagarajan et al., has reported the highest conductivity of delafossite compounds for Mg doped $CuCrO_2$[17] at 220 $S.cm^{-1}$. While they obtained optical transparency of only 30% for 270nm thin film thickness, other works demonstrated one of the highest trade-off electrical conductivity-visible transparency for p-type TOS. In this section, we provide a detailed review of the state of the art of $CuCrO_2$ in which, through physical and chemical arguments, we expose the reasons why this high trade-off and we highlight its potential technology applications.

I.2.1 Structural properties of delafossite $CuCrO_2$

I.2.1.1 Delafossite crystal structure

I.2.1.1.1 Spatial representation

Delafossite $CuCrO_2$ structure (A=Cu and M=Cr), has Cu cations linearly coordinated to two oxygen and is expected in +I oxidation state (see Figure 4). The Cr cation is located in a distorted edge shared CrO_6 octahedra with Cr as central position with a nominally +III oxidation state. The oxygen ion is in pseudo-tetrahedral coordination with one Cu and three Cr cations. The delafossite $CuCrO_2$ structure can be visualized as consisting of two alterning layers: a planar layer of Cu cations in a triangular pattern and a layer of edge-sharing CrO_6 octahedra flattened with respect to the c-axis. Depending on the orientation of each layer in the stacking, $CuCrO_2$ has two polytypes. By stacking the double layers with alterning Cu layers being oriented 180° relative by to each other, the hexagonal 2H is formed (Figure 4 (a) and (b)). This structure has $P6_3/mmc$ space group symmetry. If the double layers are stacked with the Cu layers oriented in the same direction but offset from each other in a three layer sequence, the rhombohedral 3R type is formed (Figure 4 (c)-(d)). This structure has space group symmetry of $R\bar{3}m$. Hexagonal structure is more stable with M=Sc, Y, La [104]–[106] (unoccupied 3d levels), while rhombohedral structure is more stable with the others M cations [16], [104], especially with $CuCrO_2$.

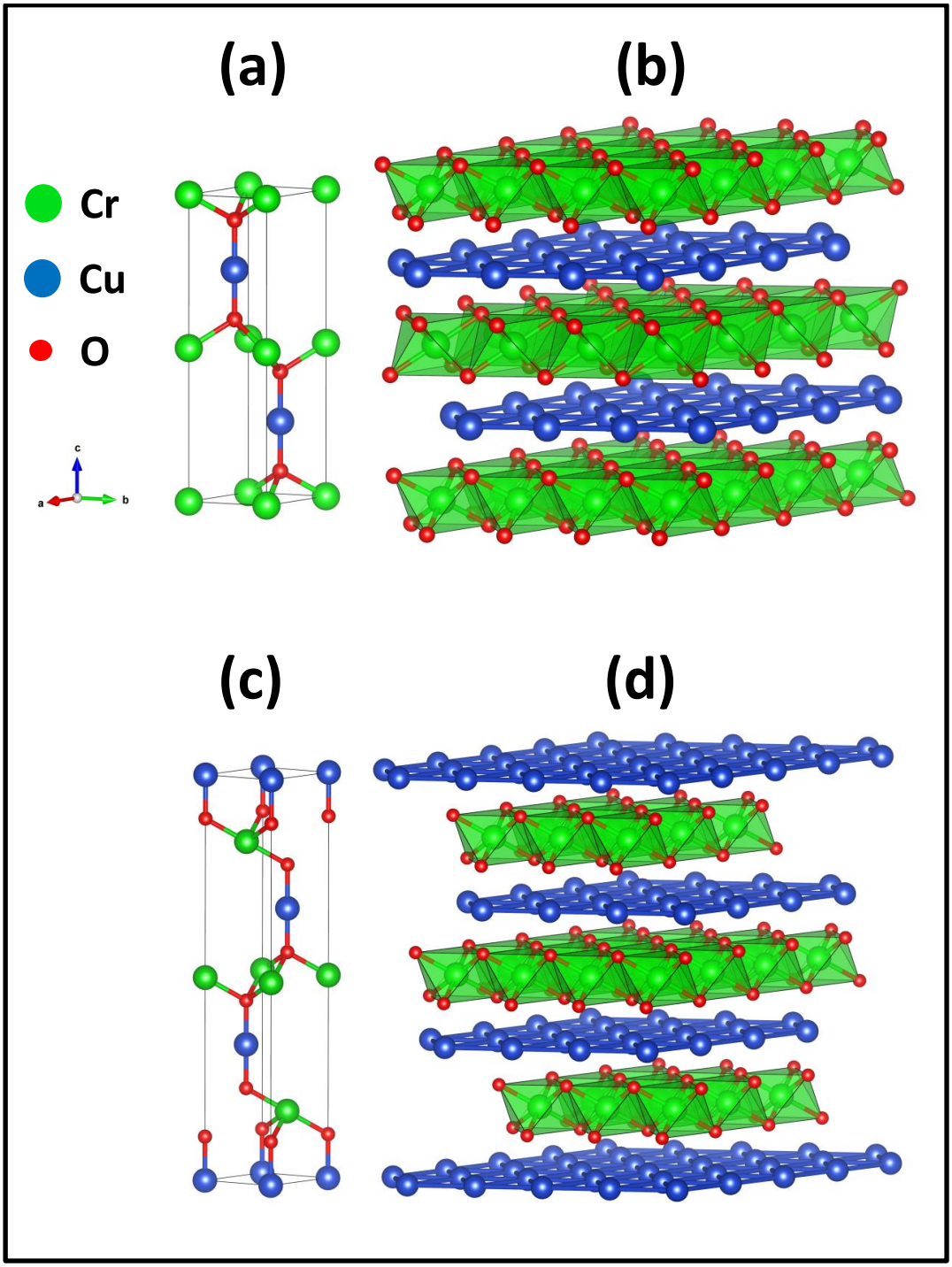

Figure 4 Crystal structures of delafossite $CuCrO_2$: (a) Unit cell and (b) several cells of hexagonal structure, (c) unit cell and (d) several cells of rhombohedral structure (done with VESTA software).

I.2.1.1.2 Lattice parameters

Lattice parameters in delafossite, can be correlated with the sizes of A and M cations, who influence the O-A-O, M-O, A-A or M-M distances[107]. In delafossite, all the O-A-O

linkages are strictly parallel to the c-axis, it is expected that the lattice value of the a-axis will scale according to the A-A or M-M interaction. Experimentally, it appears that lattice parameters along the a-axis depends preferably on M cations (Figure 5). This is mainly attributed to the larger size of M cations as compared to A cations, leading to a higher M-M repulsion and thus an increasing of the a-axis lattice parameters. Moroever, the charge +III on M compared to +I on A, influenced also the higher M-M repulsion [107]. Delafossite $CuCrO_2$ has relatively small a-axis and c-axis (a=2.97-3.05 Å and c=17.09-17.10 Å for rhombohedral crystal structure), compared to other delafossite compounds; a summary of $CuCrO_2$ data is given in Table 1.

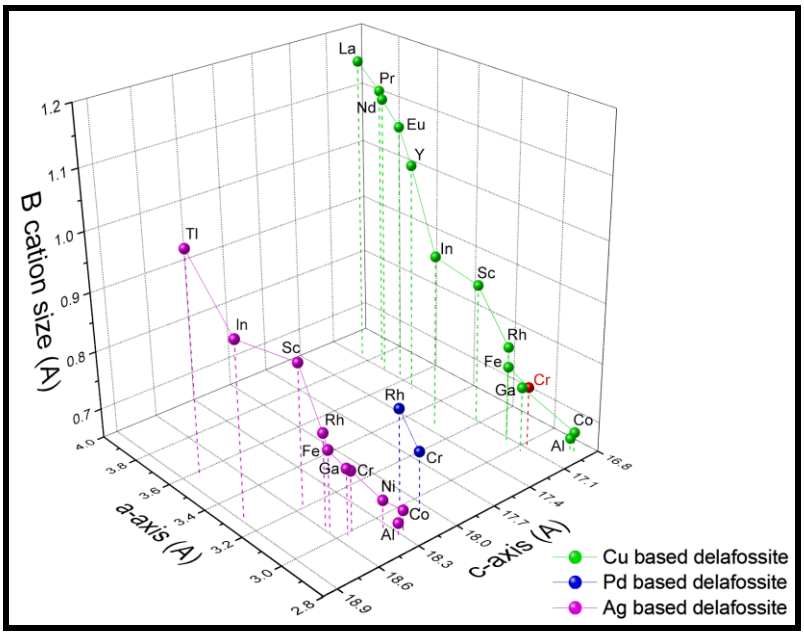

Figure 5 Influence of M cations on a-axis and c-axis of delafossite. Lattice parameters datas are from [1] and M cation size datas from [2]

Table 1 Reported lattice parameters of $CuCrO_2$ by theorical and experimental approach

a (Å)	c (Å)	V (Å^3)	System	Method	Reference
2.9748(1)	17.1016(5)	131.06	Rhombohedral	Exp. *	[24]
2.9734(3)	17.100(4)	130.93	Rhombohedral	Exp. *	[108]
2.974514	17.058992	130.71	Rhombohedral	Exp. *	[109]
2.962	17.01	129.24	Rhombohedral	Exp. *	[110]
3.050	17.09		Rhombohedral	Th.	[31]
2.9740(3)	11.400(1)	87.32	Hexagonal	Exp. *	[111]
2.97	11.40	87.09	Hexagonal	Exp. *	[112]
3.01-3.05	11.40-10.47	89.73-92.25	Hexagonal	Th.	[22]

I.2.1.1.3 Air stability

It is essential to consider, for the integration of the grown thin-films into a device fabrication process-flow, the stability of $CuCrO_2$ phase when heating exposed to humidity, oxygen-rich atmosphere etc... Thermogravimetric analysis (TGA) of $CuCrO_2$ and several delafossites under heating up to 1000°C are presented Figure 6 [31]. In nitrogen atmosphere (at amospheric pressure), no significant weight variation was observed for all delafossite (Figure 6 (a)) showing their very high stability. However, under air atmosphere (Figure 6 (b)) the increasing weight for $CuGaO_2$, $CuFeO_2$ and $CuMnO_2$ is due to the thermal decomposition of delafossite, according to the following chemical reaction:

$$CuMO_2 + O_2 \rightarrow CuM_2O_4 + CuO$$

The typical decomposition temperature of usual delafossite compounds is reported in Table 2. Delafossite $CuAlO_2$ has no significant weight variation even at 1000°C but XRD analysis feature a structural change at 900°C (Figure 6 (c)). These contradictory results are explained by the slow thermal decomposition of $CuAlO_2$, not detected by usual TGA measurements. Regarding $CuCrO_2$, its stability was demonstrated above 1000 °C with TGA and XRD [27], [31], [113], therefore $CuCrO_2$ is the most stable delafossite under air heating (Table 2). This feature is particularly attractive when considering the integration of transparent semiconductors into devices and the long-term stability of the materials when aged.

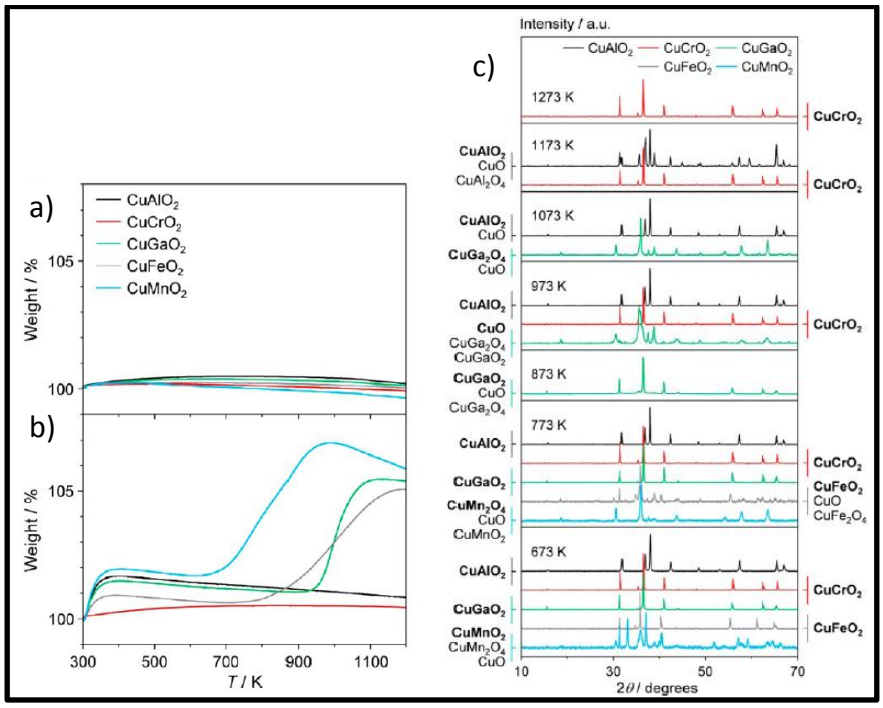

Figure 6 TGA profiles of copper based delafossite in a) N_2 and b) air. XRD patterns of copper based delafossite treated at different temperatures for 5h in air c) [31]

Table 2 Temperature decomposition of delafossite compounds $CuMO_2$ (with M=Cr, Al, Ga, Fe, Y and La)

Compounds	$T_{decomposition}$ (°C)	Analysis	Ref
$CuCrO_2$	> 1000 > 1000	TGA XRD	[31]
$CuCrO_2$	> 1000	TGA	[27]
$CuCrO_2$	> 1000 > 1000	TGA XRD	[113]
$CuAlO_2$	> 1000 800-900	TGA XRD	[31]
$CuAlO_2$	> 1000	TGA	[114]
$CuGaO_2$	700	TGA	[114]
$CuGaO_2$	600	TGA	[27]
$CuGaO_2$	700 600	TGA XRD	[31]
$CuFeO_2$	500 650	TGA XRD	[113]
$CuFeO_2$	500	TGA	[27]
$CuFeO_2$	600 500	TGA XRD	[27]
$CuYO_2$	400	TGA	[106]
$CuLaO_2$	600	TGA and XRD	[115]

Lalanne et al. [113] compared the mechanism underlying the thermal decomposition under air atmosphere of $CuFeO_2$ and $CuCrO_2$. They propose that the interstitial site in $CuFeO_2$ (site between copper atoms in the same plane) is large enough to enable the intercalation of oxygen while the lower size of interstitial site in $CuCrO_2$ impairs the oxygen intercalation mechanism. Therefore, $CuFeO_2$ tend to oxidize into CuO and $CuFe_2O_4$ compounds, while $CuCrO_2$ is still stable under air atmosphere. However, it is worth stating that this interpretation does not fit the accommodation of oxygen in $CuGaO_2$ interstices and its oxidation near 600°C [27], [31], [114]. Indeed, the size of interstitial site of $CuGaO_2$ is very similar to the one in $CuCrO_2$, and $CuGaO_2$ decomposed under air heating, while $CuCrO_2$ is very stable.

Amrute et al. preferably considered that the thermal stability of delafosite compounds are triggered by the surface rather than the bulk one [31]. They showed by calculations, that the formation of oxygen interstitial is endothermic in the bulk for $CuAlO_2$ and $CuCrO_2$, which is in line with previous statements highlighting that the interstitial size in $CuAlO_2$ and $CuCrO_2$ is insufficient to accommodate interstitial oxygen. On surface terminated by an oxygen layer, the formation of oxygen interstitial is exothermic in $CuAlO_2$ but is still endothermic for $CuCrO_2$. This is attributed to the structural relaxation and the charge transfer (between oxygen and metal cations) at the surface, which are different for $CuAlO_2$ and $CuCrO_2$ [31]. The exothermic energy of oxygen interstitial can explain the oxidation of $CuAlO_2$.

I.2.2 Band structure

I.2.2.1 Energy gap

Band structure calculation of $CuCrO_2$ is presented in Figure 7 (a), when a density functional theory (DFT) calculation with a hybrid functional approach (screened-exchange local density approximation (sX-LDA)) is used [116]. The energy band gap is well estimated with this method (E_g^{direct}=3.1 eV and $E_g^{indirect}$=2.9eV) when compared to experimental data (E_g^{direct}=3.05-3.2 eV[17], [33], [34], [37], [39], [41], [44], [47], [49] and $E_g^{indirect}$=2.7-3.0 eV[33], [34], [37], [117]) (Figure 7 (c)). It is noteworthy that $CuCrO_2$ gap is different from Cu_2O.

I.2.2.2 Effective mass

The $CuCrO_2$ hole effective mass at the VBM is lower than typical p-type TOS. The example is given Figure 7 (b) with $CuCrO_2$ and $SrCu_2O_2$ band structure with sX-LDA approach. A flat band was observed at the VBM for $SrCu_2O_2$ due to localization of O 2p states which do not favour p-type TOS (Figure 2 (a)) and thus give a large effective mass, which does not favour conduction by holes. Delafossite $CuCrO_2$ exhibit less localized states at the VBM which favour more dispersive VBM (Figure 2 (b)) and more mobile hole.

I.2.2.3 Density of states (DOS)

Delafossite $CuCrO_2$ has four distinctive parts in the total electronic density of states, (total EDOS), as illustrated in Figure 8 (a). The parts I and II are mainly O 2p states, while the parts III is dominated by Cu 3d states as the part IV is also a major contribution of Cu 3d (Figure 8 (a) and (b)). Experimentally, the four parts were confirmed by X-Ray resonant photoemission and X-Ray absorption spectroscopies, especially for the part IV where Cu^{+I} and Cu^{+II} oxidation states for Mg-doped $CuCrO_2$ were observed [21], [118].

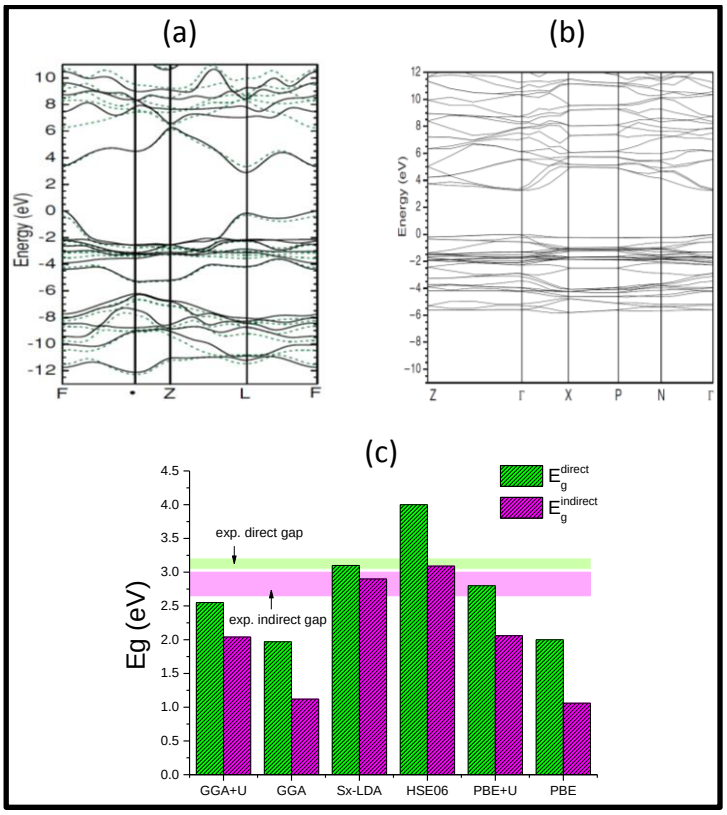

Figure 7 Band structure calculations with sX-LDA of (a) $CuCrO_2$ [116] and (b) $SrCu_2O_2$[3].(c) Comparison of direct and indirect bandgaps from calculations and experimental results[b]

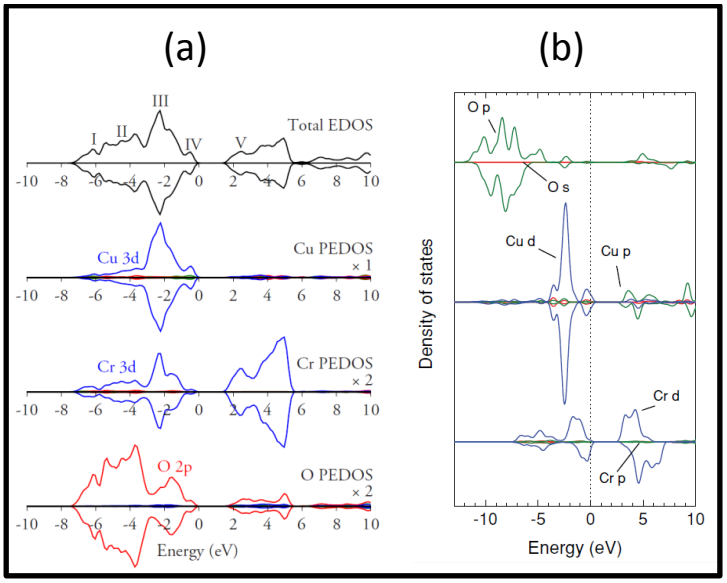

Figure 8 Total EDOS and partial DOS with (a) PBE+U [19] and (b) sX-LDA [116] calculations. The up and down parts correspond to calculations with spin "up" and spin "down" (of chromium atoms) respectively

[b] PBE is a generalized gradient approximation (GGA) calculation, which have the acronyms of the authors (Perdew, Burke, and Ernzerhof [[334]]). HSE is a screened hybrid functional calculation (Heyd, Scuseria, and Ernzerhof [[335]])

More precisely, the deep levels (between -10 and -4 eV) are mainly O 2p states which are broad and intense, following by narrow but also intense Cu 3d nonbonding states (at -2eV). The Cu 3d nonbonding states are energetically degenerate with the weakly dispersive states from nonbonding O 2p orbitals (at -2eV). The bonding Cu 3d states and O 2p states interact together and push up a mixed Cu-O state above the undispersed background at the VBM. This phenomenon is well aligned with the Kawazoe valence band modulation (Figure 2 (b)).

The Cr 3d states mainly contribute to the conduction band minimum (CBM), whatever the used calculation models used (Figure 8 (a) and 8b)). It appears that O 2p levels contributed to the CBM (less pronounced with sX-LDA), extending up to 5 eV like Cr 3d states, due to the Cr 3d and O 2p interactions. The Cr 3d sates have also minor contribution at VBM [20]. This contribution at VBM is a consequence of the valence bound between three Cr ions and one O ion (Figure 4) which produce hybridized Cr-O bonds.

Valence band of $CuCrO_2$ obtained by XPS with Al Kα beam (hν=1486.6 eV) is presented Figure 9 (a) [118]. With Al Kα excitation, the electron cross section for ionization of Cu 3d states is 20x higher than for the one O 2p states and 10x higher than Cr 3d states [119]. As a consequence, Cu 3d states of valence band $CuCrO_2$ are preferably detected by Al Kα beam. Experimental works feature broad Cu 3d states at 3 eV for both delafossites $CuCrO_2$ (Figure 9 (a)) and $CuAlO_2$ (Figure 9 (b))[118]. An additional Cu 3d peak near the VBM (1 eV) is also observed for both materials, but is more intense for $CuCrO_2$ than $CuAlO_2$ (as observed by calculation [19]). Even if Cr 3d states exhibit a minor contribution to the valence band DOS, they interact indirectly with Cu 3d states. The interaction between Cr 3d and Cu 3d states is mediated by O 2p states which are directly hybridized with Cr 3d states. As a consequence of Cu 3d states and Cr-O bond states, Cu 3d states are pushed up near the VBM. In $CuAlO_2$, Al 2p states do not interact with O 2p like Cr 3d in $CuCrO_2$, since Al has only 2p valence states impairing O 2p - Al 3d hybridization.

In $CuCrO_2$, the covalent nature between O and Cr is evidenced when the partial charge calculation is considered (Figure 10) [20]. Delafossite $CuCrO_2$ has the highest covalent interaction M-O (with M=Al, Cr, Sc and Y) decreasing the partial charge of oxygen, then dispersive VBM would be optimal for the hole mobility.

Among other parameters which determine the electrical conductivity in a semiconductor, is the intrinsic or extrinsic dopability of material which is particularly important.

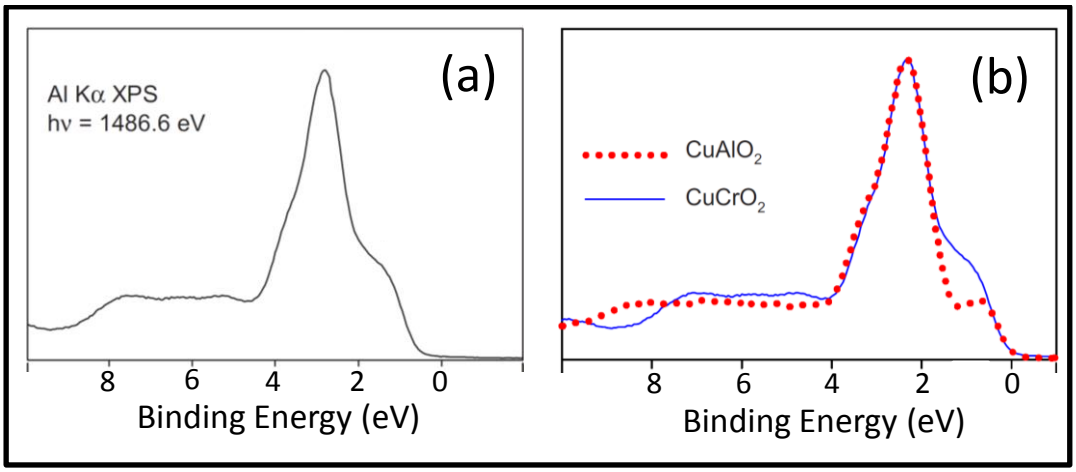

Figure 9 Valence band by XPS Al Kα excitation of (a) $CuCrO_2$ and (b) comparison of valence bands between $CuCrO_2$ and $CuAlO_2$[118]

	$CuAlO_2$	$CuCrO_2$	$CuScO_2$	$CuYO_2$
Cu	+0.52	+0.52	+0.52	+0.51
M^{III}	+2.48	+1.68	+2.03	+2.18
O	−1.50	−1.10	−1.27	−1.34

Figure 10 Partial charge calculations on Cu, M (M=Al, Cr, Sc, Y) and O in delafossite compounds [20]

I.2.2.4 Defects and doping

In this part, we discuss the impact of intrinsic or extrinsic doping on the electronic properties of delafossite $CuCrO_2$. We first resume doping rules of n-type/p-type TOS and then summarize some key results regarding dopability of $CuCrO_2$.

a) Rules of p-type/ n-type doping in TOS

The conditions needed for a TOS to be an electron-hole conductor are: dopants (intrinsic or extrinsic) must be readily ionized, i.e have energetically electrical levels near the CBM (n-type doping) or VBM (p-type doping) and the second condition is electron (hole) producing dopant should be abundant in n-type (p-type system), i.e defects have low formation enthalpy[120], [121]. The formation enthalpy of dopant defines if the dopant will be integrated in the host crystal (low formation enthalpy) or will be hard to create (high formation enthalpy). Formation enthalpy of dopant D of charge q in host crystal is defined as[122]:

$$\Delta H^{(D,q)}(\mu, E_F) = qE_F + n_D(\mu_D - \mu_H) + \Delta E_b \quad (1)$$

where μ_D and μ_H are the chemical potentials of the dopants and host, E_F is the Fermi energy, n_D is the number of dopants, $\Delta E_b = E(host+defect) - E(host)$ is the excess energy of the local chemical bonds around the dopant. Each term in equation 1 is assign to a doping rule.

(i) Compensating defects should not develop

When a material is n-type doped, E_F moves towards the conduction band, and inversely, when a material is p-type doping, E_F moves towards the valence band. The first term in Equation (1) , qE_F, shows that the donor (acceptor) formation enthalpy increase (decrease) linearly with E_F. Therefore, it becomes favorable to create acceptor (donor) for high n-type (high p-type) doping (Figure 11)[121]. These acceptor (donor) defects are called "compensation defects" because they "kill" the n-type (p-type) doping. The Fermi energy limit, when doping will be spontaneously compensated, is call "Fermi energy pinning" ($\varepsilon_F^{(n)}$ for n-type doping limit and $\varepsilon_F^{(p)}$ for p-type doping limit). The Fermi pinning energy define the n-type, p-type or ambivalent doping of the considered materials[121][122]. The levels of Fermi pinning energy are aligned (or universal) in materials (Figure 12) due to the compensation of the energy required to form defect level and the energy needed to fully occupy them[123].

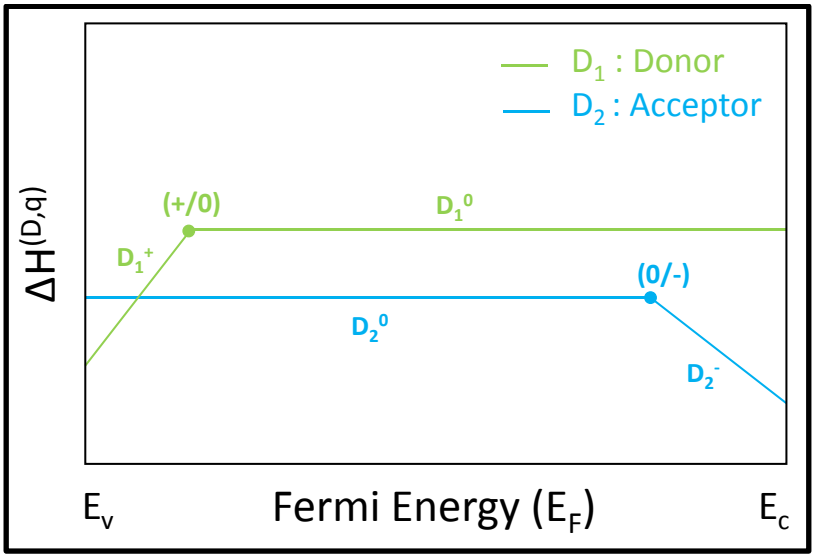

Figure 11 Dependence of the formation enthalpy of defects D_1 (donor) and D_2 (acceptor) in charge states q_1=+ and 0 and q_2=0 and – respectively, on the Fermy energy. The dots are the donor (+/0) and acceptor (0/-) transitions energies

One way to avoid compensating defects is to consider material with CBM far from the vacuum level (for n-type doping) i.e large electron affinities χ_A. Then Fermi energy pinning is

far in the conduction band and allows high n-type doping (Figure 12). In_2O_3, SnO_2 , ZnO or CdS are very relevant examples (Figure 12).For p-type doping, materials with VBM close to the vacuum level, i.e small ionization potential Φ are considered. Then Fermi energy pinning is far in the valence band and allows high p-type doping. One way to shift the VBM upwards is to use a 3d element with active d states, so that the coupling with the p band of anions move up the latter to higher energies, i.e Kawazoe condition in Figure 2 (b). Cu_2O, $CuAlO_2$, $SrCu_2O_2$ and also $CuCrO_2$ (Figure 12) are very relevant examples of p-type doping.

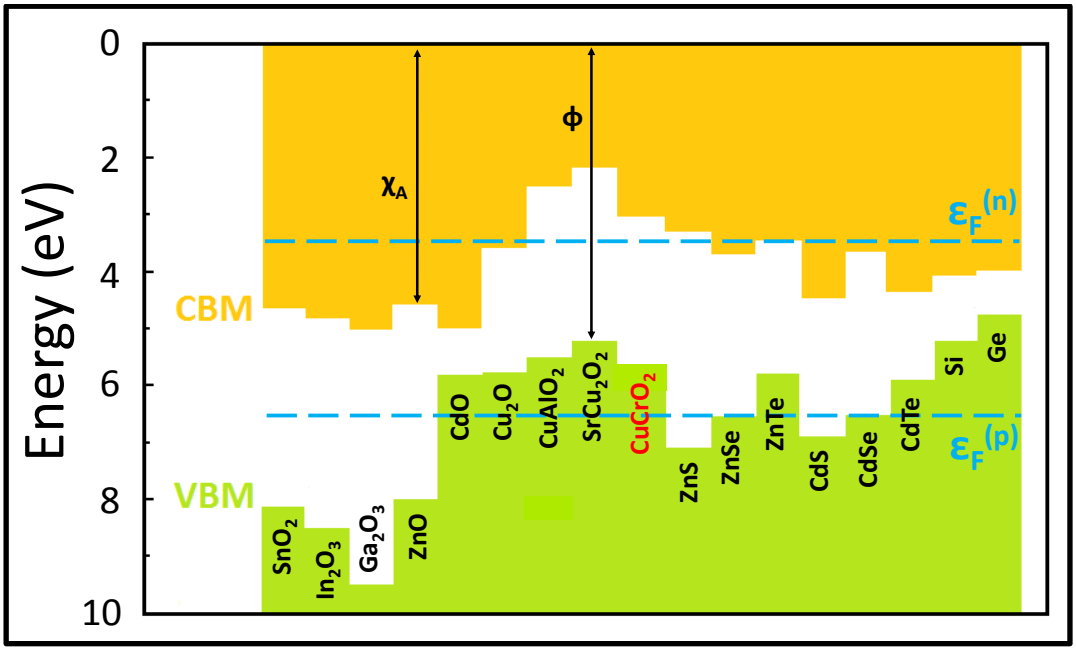

Figure 12 Fermi energy pinning of n-type ($\varepsilon_F^{(n)}$) and p-type ($\varepsilon_F^{(p)}$) for TOS and semiconductors. Electron affinities and potential ionization are extracted from [3]

(ii) Adjusting the chemical potentials of the different elements

The second term in Equation (1) shows how ΔH for the formation of anionic or cationic dopants can be regulated via the control of the chemical potentials during the growth of the materials. Anion substituting dopants will be more soluble under host cation-rich[c] growth conditions ($\mu_H=\mu_H^{\text{cation rich}}$) and cation substituting dopants will be more soluble under host anion-rich growth conditions ($\mu_H=\mu_H^{\text{anion rich}}$). It was demonstrated that n-type doping is easier via anion substitution using cation-rich conditions and p-type doping is easier via cation substitution using anion-rich conditions[121].

[c] Cation-rich conditions is equivalent to anion-poor conditions

(iii) Local bonding effects of the dopant should be minimized

The last term of Equation (1), the energy ΔE_b, is minimized by the dopant bonding which disrupt as low as possible the host bonds [124]. For example, acceptor A^{2+} dopant in $CuCrO_2$ (substitution of chromium cations) should have similar Cr^{3+} size and adequate electron shell in order to disrupt as low as possible oxygen bonds.

b) Defects in $CuCrO_2$

Defects calculations in $CuCrO_2$ were investigated with LDA, PBE, PBE+U and HSE06 approach [22], [125]. In all cases, it was found that chromium substitution by magnesium (Mg_{Cr}) has the lowest formation enthalpy, following by copper vacancies (V_{Cu}) and oxygen interstitial (O_i) (Table 3). We give an example of defects calculations Figure 13. It appears that (0/-1) transition level energy for V_{Cu} with HSE06 is 0.37 eV (ΔH=1.45 eV), which is considerably shallower than the HSE06 calculated transition levels for $CuAlO_2$ at 0.68 eV (ΔH=1.33 eV) in the same growth conditions [23].

Table 3 Compilation of theorical results on V_{Cu}, O_i defects and Mg_{Cr} doping

Defect	Calculation method	Transition level	Transition level energy (eV)	ΔH	Ref.
V_{Cu}	PBE	(0/-1)	0.25	0.16	[22]
V_{Cu}	PBE+U	(0/-1)	0.30	0.95	[22]
V_{Cu}	HSE06	(0/-1)	0.37	1.45	[22]
V_{Cu}	LDA	(0/-1)	0.9	-2.5	[125]
O_i	PBE	(0/-1)	0.63	1.27	[22]
O_i	PBE+U	(0/-1)	1.6	1.38	[22]
O_i	HSE06	(0/-1)	2.38	1.63	[22]
O_i	LDA	(0/-1)	1.25	-2.1	[125]
Mg_{Cr}	PBE	(0/-1)	0.25	-0.54	[22]
Mg_{Cr}	PBE+U	(0/-1)	0.3	0.46	[22]
Mg_{Cr}	HSE06	(0/-1)	0.5	0.62	[22]
Mg_{Cr}	LDA	(0/-1)	0.25	-2.13	[125]

In order to validate these theorical investigations of the electronic properties of delafossite $CuCrO_2$, we propose to consider experimental results dealing with the transport properties of $CuCrO_2$, and to compare them with other delafossite p-TOS when relevant. In first we review the reported methods that have been used to grow $CuCrO_2$ and then we summarize the typical performances that have been obtained so far.

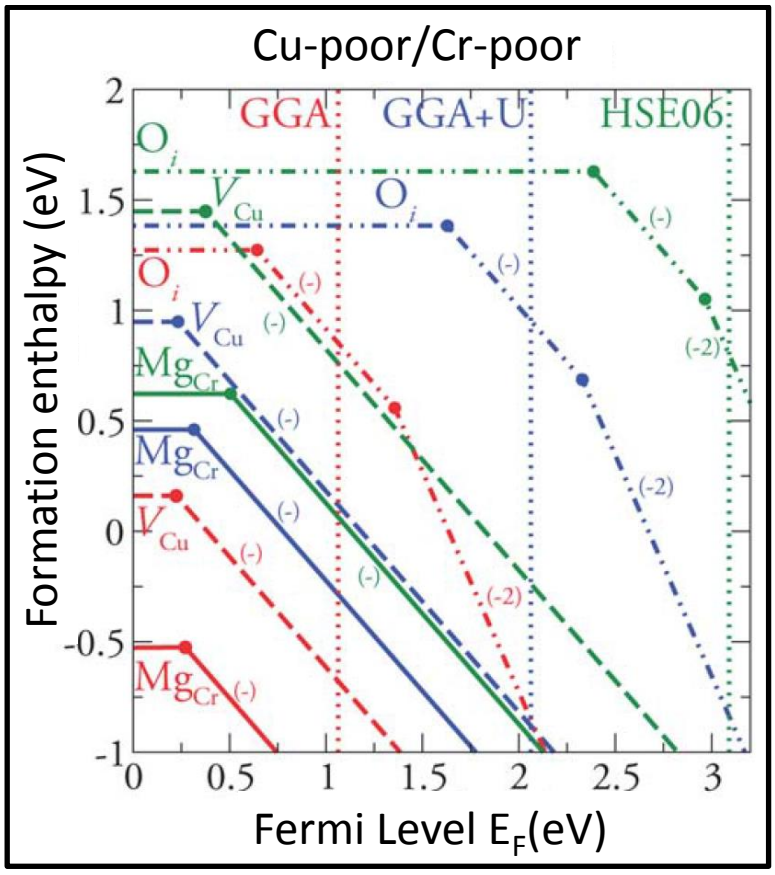

Figure 13 : Calculated formation energies for p-type defects in $CuCrO_2$ as a function of Fermi energy under Cu-poor/Cr-poor growth conditions using PBE, PBE + U and HSE06 calculations approach. Solid dots denote the transition levels. The intersection between vertical dash lines and the Fermi level axis, give the calculated band gap with the respective calculation approach[22]

I.2.3 Synthesis methods

Several methods were reported to synthesized delafossite $CuCrO_2$ thin films. Each method leads to different stoichiometry, morphology, electrical and optical properties of thin-films. In this section, we provide the specific features of the discussed synthesis methods.

I.2.3.1 Solid state reaction

The most intensively reported $CuCrO_2$ synthesis is the solid-state (SS) method. The $CuCrO_2$ SS synthesis consists in mixing and grinding Cu_2O and Cr_2O_3 powders before sintering at 800-1200°C in air or nitrogen atmosphere during 12-48 hours. Additional steps of regrinding and calcination of the mixture can be necessary, at 900-1200 °C during 10-100h to achieve good crystalline quality [21], [24]–[31], [118].

The mechanism of delafossite formation by SS synthesis, was studied in more details by Amrute *et al.*[31]. The temperature of formation of $CuCrO_2$ was found at 800°C under air and nitrogen atmosphere. However the mechanism of formation is dependent on the used atmosphere (Figure 14). Considering the Cu_2O + Cr_2O_3 mixture in air, Cu_2O underwent oxidation to CuO up to 400°C. Formation of the $CuCr_2O_4$ spinel phase by reaction of CuO and Cr_2O_3 occurred at 500−700°C. Copper oxide CuO and spinel $CuCr_2O_4$ react to form $CuCrO_2$ at 800°C. In N_2, $CuCrO_2$ originates by the direct reaction of Cu_2O with Cr_2O_3 from 700°C.

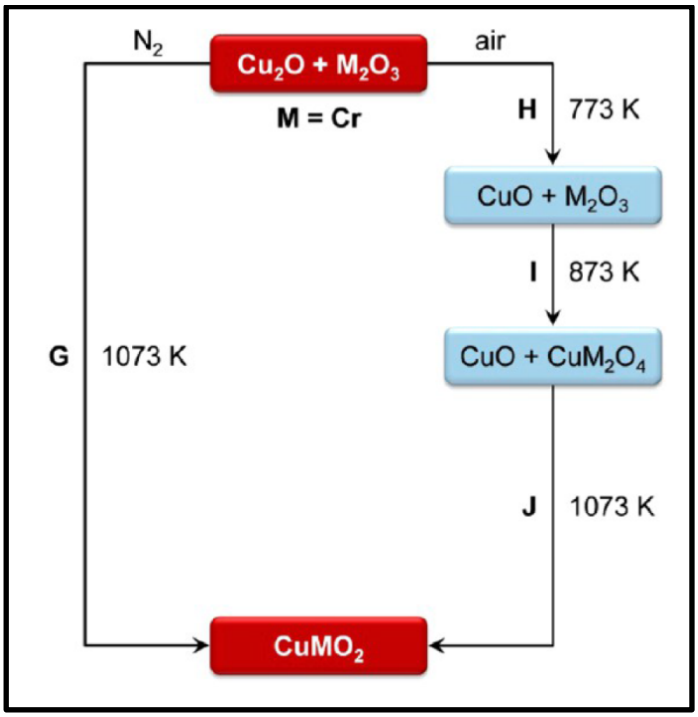

Figure 14 Steps involved in the formation of $CuCrO_2$ by the solid-state reaction of Cu_2O+M_2O_3 oxides (M being Cr in our case)[31]

Delafossite $CuCrO_2$ synthesized by SS, have a typical morphology of large plate grain [30], [126] with a 1-10 µm length, and 0.3-1 µm thick. An example of morphology is illustrated by the Figure 15.

The SS synthesis method is still essentially used to provide model materials for fundamental studies related to electronic structure [118], carrier transport mechanisms [21], magnetic [28]–[30], thermoelectric [24], [25] and photocatalytic[26] investigations.

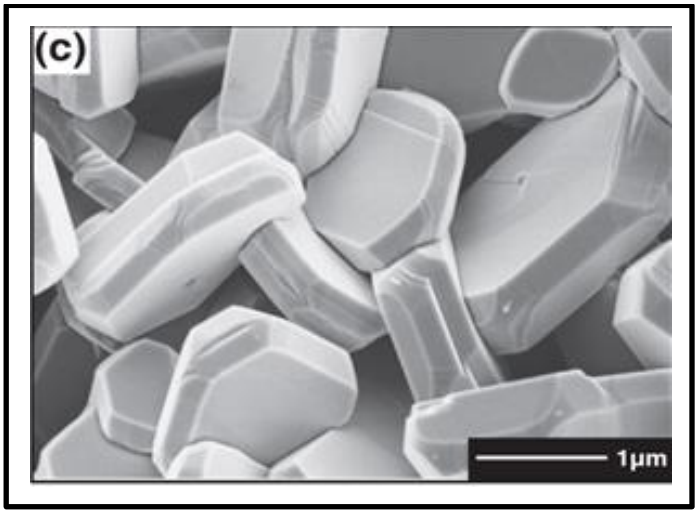

Figure 15 SEM image of $CuCr_{0.99}Mg_{0.01}O_2$ synthesized by solid state reaction [30]

I.2.3.2 Sol-gel

Sol-gel is an other well reported synthesis method of $CuCrO_2$. Copper and chromium hydrate precursors are dissolved in alcoholic solution and then deposited by spin coating on quartz or sapphire substrates. After a drying between 300-500 °C during 5-60 min, the deposition and drying are repeated until the desired thickness is reached. Annealing at 700-800 °C under pure nitrogen atmosphere is necessary to obtain films with a pure delafossite structure [32]–[38]. Thin films have a granular morphology with a grain size (≈50 nm) (Figure 16 (a) and (b)). Cross section feature polycrystalline, porous and rough films (Figure 16 (c) and (d)). Appropriate transparency (between 60-70% for 100-200nm thickness) but relative low conductivity (10^{-4}-10^{-2} $S.cm^{-1}$) are obtained with the films grown by sol-gel.

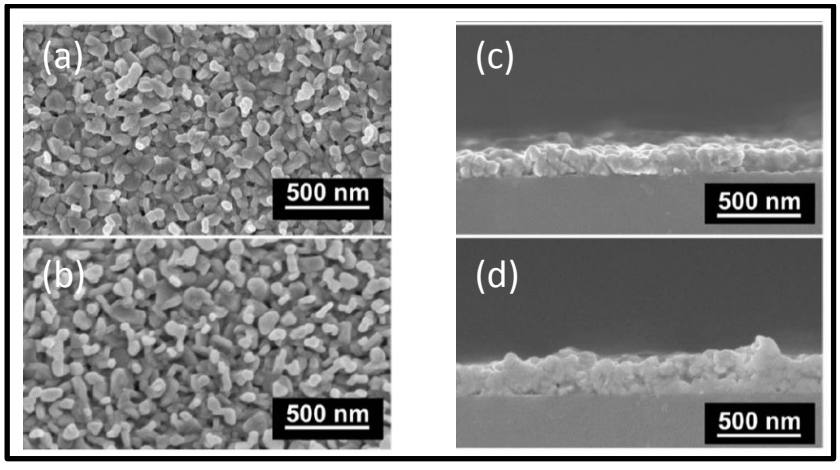

Figure 16 : Top view SEM images of $CuCrO_2$ thin films annealed at (a) air and (b) nitrogen. Cross section of these films annealed at (c) air and (d) nitrogen [127]

The required high temperatures exclude the direct use of solid state and sol-gel techniques for the fabrication of transparent electronic devices. However, solid state and sol-gel are typically used for the synthesis of targets for the physical deposition processes, i.e. pulsed laser deposition and magnetron sputtering methods.

I.2.3.3 Pulsed Laser Deposition (PLD)

PLD synthesis consists of evaporating solid targets by using a high power pulsed laser under vacuum. The substrate is also heated during the deposition. For delafossite $CuCrO_2$, the reported temperature is between 450-750 °C. Crystalline delafossite $CuCrO_2$ is only observed for temperature higher than 550 °C [39]–[43]. In terms of morphology, thin films are smoother and grains are more compact than sol-gel synthesis (Figure 17 (a) and (b)).

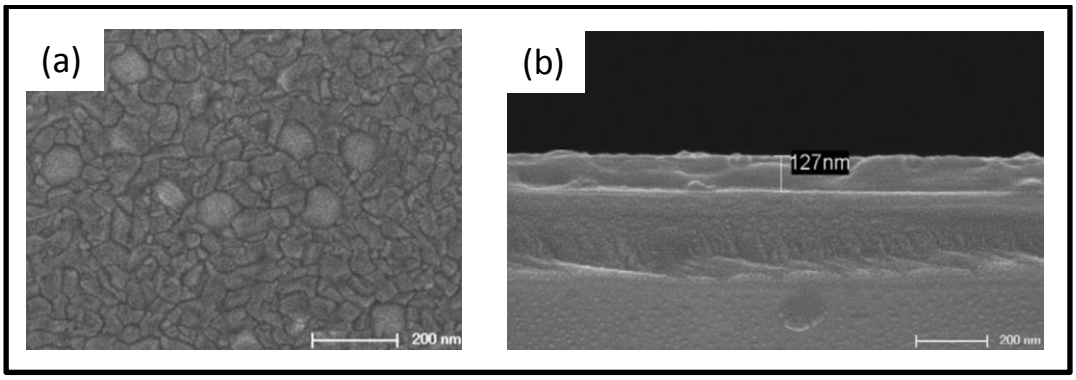

Figure 17 SEM top view (a) and cross-section (b) on $CuCrO_2$ thin films synthesized by pulsed laser deposition [128]

Thin films synthesized by PLD exhibit high electrical conductivity (> 1 $S.cm^{-1}$) (see Table 14 in Annexes). Transparent p-n junction $CuCrO_2$/ZnO was also synthesized by PLD with a good transmittance (80%) in the visible wavelength range [42]

I.2.3.4 Magnetron Sputtering (MS)

Two approaches were reported using MS for the synthesis of delafossite $CuCrO_2$. In a first approach, the deposition is performed at room temperature followed by annealing at high temperature, 600-900°C [17], [44]–[46], [129] or the deposition is performed directly at high temperature, 750 C [47]. The optical transparency of films obtained with these processes is comparable to the films obtained by sol-gel (40% for thicknesses near 300nm), but electrical conductivity is enhanced by a factor of 10 to reach typically 0.1-1 S/cm

I.2.3.5 CVD

Two papers address the growth of $CuCrO_2$ by chemical vapour deposition (CVD) [49], [130]. In these latter cases, contaminated delafossite $CuCrO_2$ films with the spinel $CuCr_2O_4$ phase were reported at processing temperatures between 450 and 550 °C. Annealing under argon atmosphere at 800°C, was used to convert the spinel phase into a delafossite one.

Very recently, it was reported the growth of Cu_xCrO_y at low temperature (≈ 345°C) by spray pyrolysis[131], [132]. However, the reported XRD diffraction peaks can also be attributed to copper or chromium oxides phases and the 1:2:4 ratio of Cu:Cr:O in films raises doubts about the exclusive presence of the $CuCrO_2$ phase in films. Good conductivity (12 $S.cm^{-1}$) and transparency (40%) were disclosed for such thin films grown with $Cu(acac)_2$ **(**bis[2,4-pentanedionato]copper(II)) and $Cr(acac)_3$ (tris[2,4-pentanedionato]chromium(III)) precursors precursors.

At that point, as-deposited polycrystalline pure phase of $CuCrO_2$ thin films were obtained only above 550°C otherwise annealing were needed. Therefore, quartz or sapphire as substrates was chosen because of their high thermal stability. Glass substrates used in industrial applications soften at temperatures above 600-650°C. Any device fabrication in industrial glass requires synthesis methods below 600°C. Metal-organic CVD (MOCVD) synthesis is compatible with low temperature synthesis because of the low temperature decomposition of metal-organic precursors. Moreover, a large choice of chemical precursors is available to tune the range of the temperature synthesis and the chemical composition of the grown thin films. Thus, we decide in this work, to focus on the MOCVD to grow polycrystalline delafossite $CuCrO_2$ thin films.

I.2.4 Transport properties

I.2.4.1 Electrical conductivity

I.2.4.1.1 Room temperature

Many papers report the conductivity of undoped and doped $CuCrO_2$, at room temperature. Table 14 in Annexes provides a summary of these values. The conductivity depends strongly on the synthesis method as shown Figure 18. The highest conductivity

reported of undoped $CuCrO_2$ was 12 $S.cm^{-1}$ for the CVD synthesis[131], and 220 $S.cm^{-1}$ for Mg doped thin-films[17]. However these best values were never confirmed by other works. In Figure 18, we plot the conductivity of undoped Cu-based delafossite depending on the synthesis method. It appears that undoped delafossite $CuCrO_2$ is the most conductive whatever the used synthesis method.

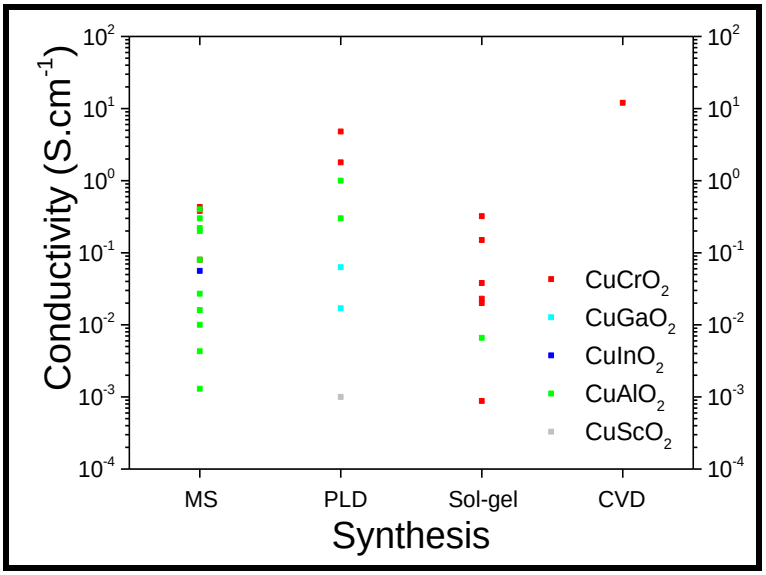

Figure 18 Electrical conductivity of $CuMO_2$ delafossite (M=Cr, Ga, In, Al, Sc) depending on synthesis method

I.2.4.2 Temperature dependence

Electrical conductivity measurements were done depending on the temperature. Two carrier transport mechanisms were reported in $CuCrO_2$:

(i) band conduction mechanism (above 150-200 K) [17], [25], [30], [33], [38], [41], [47], [49], [129], [133], [134] where the conductivity is expressed as:

$$\boldsymbol{\sigma = \sigma_0 e^{\frac{-E_a}{k_B T}}} \quad (2)$$

where σ_0 is a pre-exponential factor, E_a is the activation energy, k_B is Boltzmann constant and T is the temperature. Activation energies for undoped $CuCrO_2$ are reported between 100-300 meV.

(ii) variable range hopping mechanism (below 150 K) [25], [33], [47] where the conductivity is expressed as:

$$\boldsymbol{\sigma = \sigma_0 e^{-\left(\frac{T_0}{T}\right)^{1/(n+1)}}} \quad (3)$$

where σ_0 is a pre-exponential factor, T_0 is Mott temperature and n is the dimension of the system (n=3 for transport in three-dimensional space).

I.2.4.3 Carrier concentration and mobility

We plot mobility versus carrier concentrations of undoped and doped $CuCrO_2$ thin films reported in the literature (Figure 19), data are in Table 14 in Annexes. We considered

(i) only samples with pure $CuCrO_2$ phase

(ii) only carrier concentrations and mobility measured by Hall effect (carrier concentration deducted by thermoelectric measurements or any measurements were not ploted)

Delafossite $CuCrO_2$ reaches high carrier concentration (10^{19}-10^{20} cm^{-3}) due to shallow acceptor defects and low formation energy of copper vacancies[22]. Only two experimental results disclose holes concentration around 10^{21} and 10^{22} cm^{-3} when SS[25] and PLD[135] synthesis methods are used respectively. In these two cases, thin films were doped with magnesium with concentrations of 4 and 10% respectively. SS resulted in polycrystalline bulk of Mg-doped $CuCrO_2$ with averaged crystallite sizes near 1µm, and PLD led to single crystal thin films (135 nm).

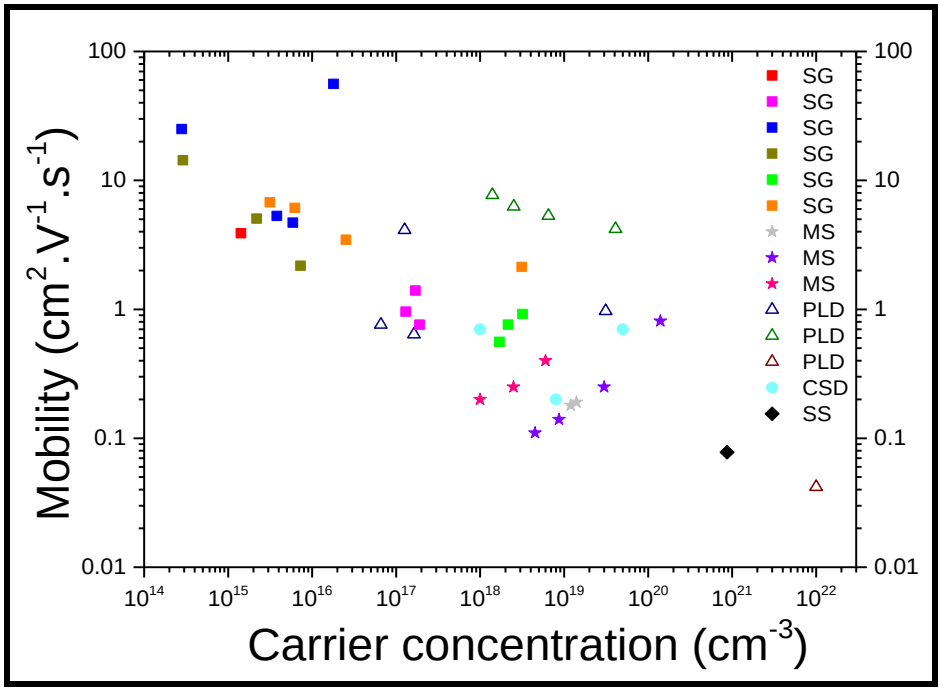

Figure 19 Mobility versus carrier concentrations of reported datas for undoped and doped $CuCrO_2$ in literature (Table 14 in Annexes). CSD abbreviation is for Chemical Solid Deposition

We compared also data of delafossite undoped and doped $CuCrO_2$ and $CuAlO_2$ (Figure 20). Delafossite $CuAlO_2$ reach carrier concentration up to 2.10^{19} cm^{-3}, the maximum carrier concentration is one decade lower than $CuCrO_2$ thin films. However, when taking into account the same synthesis method and the same range of carrier concentrations, the experimental mobility of $CuAlO_2$ seems to be 2-3x higher than the one measured for $CuCrO_2$. These experimental results seem contradictory to the theorical calculation regarding the mobility in $CuAlO_2$ vs $CuCrO_2$ (Figure 10)[20]. However, the experimental mobility can depend on impurities scattering, lattice scattering and grain boundaries (for polycrystalline films)[3]. Therefore, it is difficult to compared experimental and theorical mobility if the effective mass of materials is in the same range[20]. The highest conductivity in $CuCrO_2$ is more associated to its shallow energy level of defects close to the VBM and its capability to accommodate high defect and dopant concentrations in its crystalline structure (Figure 13) [22][23].

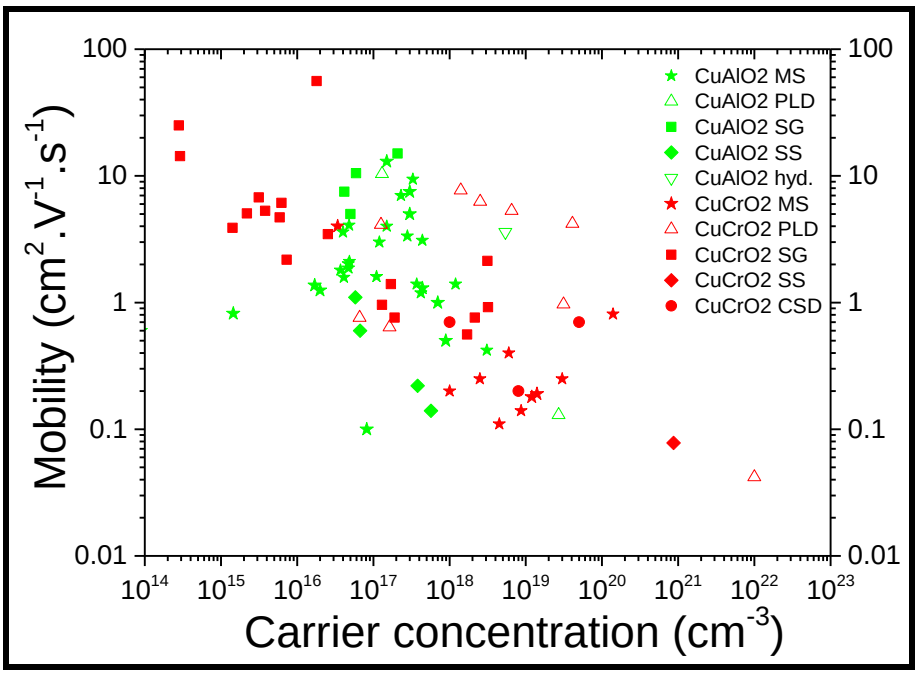

Figure 20 Comparison of carrier concentration versus mobility for undoped and doped $CuCrO_2$ and $CuAlO_2$ (see Table 14 and Table 15 in Annexes)

I.2.4.4 Thermoelectric properties

(i) Room temperature

Thermoelectric properties provide also information on carrier transport through the material, like the type of carrier majority or dominant scattering mechanisms. In our case, thermoelectric properties are evaluated with the Seebeck coefficient defined as:

$$S = \frac{\Delta V}{\Delta T} \quad (4)$$

where ΔV is the variation of the electrical potential and ΔT is the variation of temperature through the material. Seebeck coefficient of $CuCrO_2$ is reported, at room temperature to range between: +50 to +1100 $\mu V.K^{-1}$ (Table 14 in Annexe). The positive sign confirms a p-type semiconductor. As shown in Figure 21, Seebeck coefficient depends strongly on the electrical conductivity. Any increase of the conductivity leads to decrease the Seebeck coefficient.

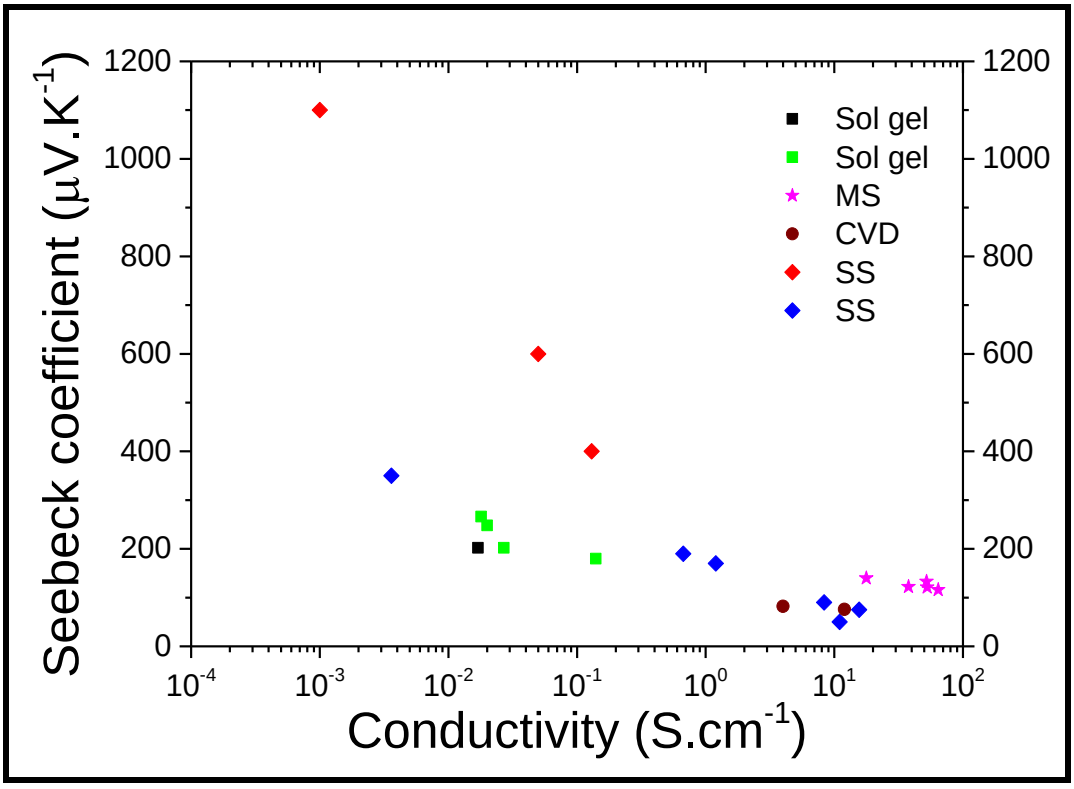

Figure 21 Seebeck coefficients at room temperature of undoped and doped $CuCrO_2$ reported in literature (Table 14 in Annexes)

Seebeck coefficient, for a non-degenerate p-type semi-conductor, is expressed as[136]:

$$S = +\frac{k_B}{e}\left[ln\left(\frac{N_v}{p}\right) + A\right] \quad (5)$$

where k_B is Boltzmann constant, N_v is the effective density of state, p the carrier concentration and A is a constant depending on dominant scattering in the material. Because carrier concentration is correlated with electrical conductivity, σ, and mobility, μ, by following equation[d][137]:

[d] This relation assume free electrons model in the material

$$\mathbf{p} = \frac{\boldsymbol{\sigma}}{\mathbf{e}\boldsymbol{\mu}} \qquad (6)$$

By substituting Equation (6) in Equation (5), S becomes:

$$\mathbf{S} = +\frac{\mathbf{k_B}}{\mathbf{e}}\left[\frac{\mathbf{ln}(\mathbf{N_v}\mathbf{e}\boldsymbol{\mu})}{\mathbf{ln}\boldsymbol{\sigma}} + \mathbf{A}\right] \qquad (7)$$

Seebeck coefficient is linearly dependent with lnσ assuming that μ and A are constant.

(ii) Temperature dependence :

Seebeck coefficient depends also on the temperature range. We show in Figure 22 (a) the temperature dependence below room temperature [25], and in Figure 22 (b) the dependence above room temperature [24] for undoped and Mg-doped $CuCrO_2$. While undoped $CuCrO_2$ show that the Seebeck coefficient decreases with the temperature between 250-800 K, the opposite trend is observed when $CuCrO_2$ is doped with Mg.

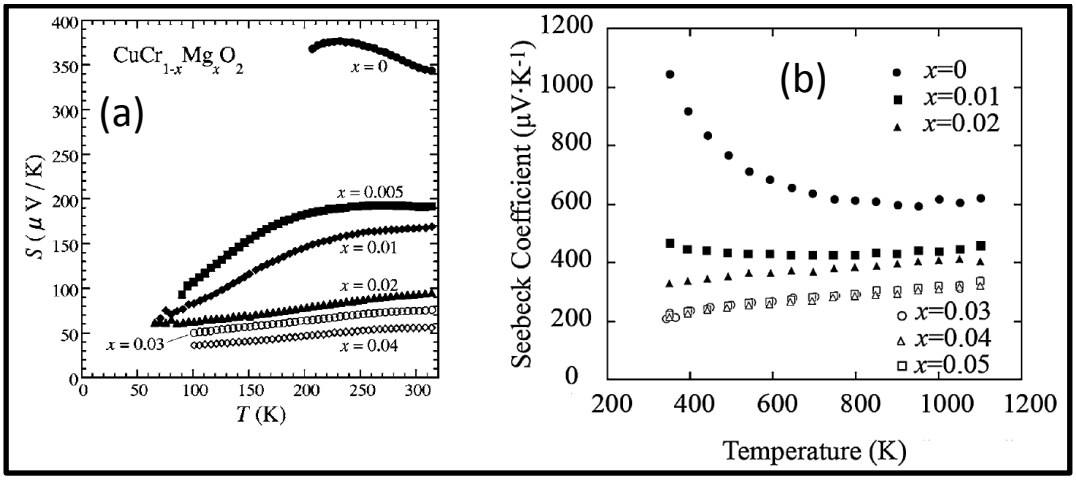

Figure 22 Seebeck coefficient of $CuCr_{1-x}Mg_x$ (x=0-0.05) at (a) 60-300K (b) 300-1100K

I.2.4.5 Band or small polaron conduction ?

In ionic compounds (like oxide materials), charge carriers may be regarded as polarons. A polaron consists in a quasi-charge due to the coupling between the charge carrier and the distortion of the ionic lattice induced by the carrier itself[138]. There is a distinction between large and small polarons[139], [140]. For large polarons, the distortion of the lattice induced around a charge carrier, extends over distances larger than the lattice constant. The carrier transport is still called “band conduction” like classical semiconductors, but the effective mass at the VBM or CBM is much higher due to the polaronic interaction between carriers and the

lattice[141]. For small polarons, the distortion of the lattice extends over distances smaller than the lattice constant. The carrier-lattice interaction is so strong that carriers become self-trapped by its own polarization generated in the ionic lattice[142]. In that case, polaron conduction is considered and being characterized by hopping properties.

The nature of the transport conduction is often determined by the limit of Bosman-Van Daal, i.e small polaron transport is considered to occur when $\mu << 0.1$ $cm^2/V.s$[143]. The measurement of such mobility by Hall effect requires high magnetic field setup that still makes the experimental determination of carrier mobility with Hall effect methods in polar oxides a challenge. As an alternative method, the scientific community also uses thermoelectric measurements and electrical conductivity[144], [145]. This allows to extract carrier concentration and mobility values, which are, however, still under debate. As example, it was pointed out for $ZnRhO_2$ (p-type TOS) that, if the effective density of states is assumed constant, $ZnRhO_2$ exhibits polaron conduction, while if it is assumed that the effective density of states is temperature dependent, $ZnRhO_2$ exhibits band conduction properties[146].

In delafossite $CuCrO_2$, and according to our knowledge, no group used this refined model to determine the mobility from Seebeck and electrical conductivity measurements. The lowest mobility reported was 0.04 $cm^2/V.s$ ($p \approx 10^{-21}$-10^{22} cm^{-3})[135] with Hall effect at 14T, which is not so low compared to Bosman-Van Dall limit. Therefore, small polaron or band conduction mechanisms in delafossite $CuCrO_2$ under high doping still need to be rigorously evidenced.

I.2.5 Optical properties

I.2.5.1 Transmission

Delafossite $CuCrO_2$ thin-films has a typical transmission in the visible spectrum between 40-65% for a thickness between 100-200nm (Table 14 in Annexe). This is typically lower than other delafossite thin films (Table 15 in annexe).

I.2.5.2 Absorption coefficient and optical gap

In the absorption process, a photon of a known energy excites an electron from a lower to a higher energy state. There are different possible transitions: band to band, excitons, between sub-bands, between impurities… Absorption is defined by its coefficient α.

In delafossite $CuCrO_2$, optical absorption appears near 3eV due to the band to band transition between the VBM and the CBM (Figure 23). The optical transition is attributed to Cu 3d + O 2p → Cr 3d + O 2p according to calculations (Figure 8).

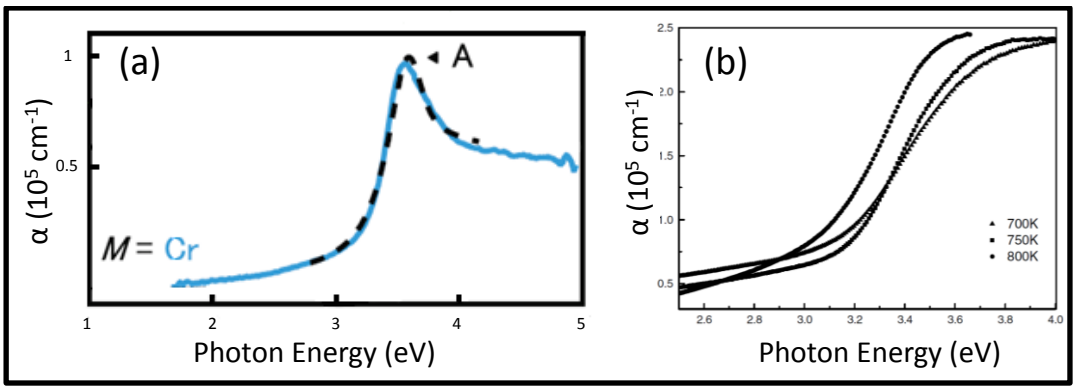

Figure 23 Absorption coefficient of undoped $CuCrO_2$ with PLD synthesis (a) at 10K [147] and (b) at room temperature [147]

From the absorption coefficient, optical direct gap can be calculated with the following relation[148]:

$$(\alpha h\nu)^2 = C(h\nu - E_g) \quad (8)$$

where hν is the photon energy, C is a constant and E_g is the optical band gap. According to the table in annexe, the optical gap of $CuCrO_2$ was reported in literature between 3.0-3.3eV.

Another transition can be also reported around 2.0 eV (Figure 24 (a))[149], [150]. This is attributed to the Cr 3d (t_{2g}) → Cr 3d(e_g) transition due to the octahedral environment of chromium atoms (crystal field splitting) (Figure 24 (b)). X-ray absorption studies on chromium in $CuCrO_2$ [118], confirmed an energy loss at 2.1 eV.

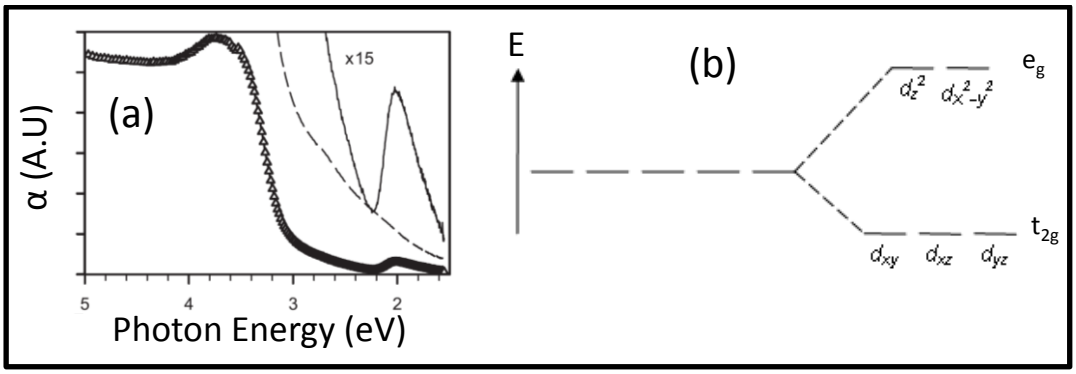

Figure 24 (a) Absorption coefficient of undoped $CuCrO_2$ [149] and (b) crystal field splitting effect on 3d levels in an octahedral environment

I.2.6 P-N junctions

Delafossite $CuCrO_2$ was studied for p-n junction applications. The synthesis methods were only physical vapour deposition (PVD) approach: PLD[42] and MS[151] synthesis. The respective devices are shown in Figure 25 (a) and (b). In all cases, devices were achieved with at least three layers of semiconductors. Electrical conductivity of $CuCrO_2$ for the PLD synthesis was 0.2 $S.cm^{-1}$ and 10 $S.cm^{-1}$ for undoped and Mg-doped respectively[42], while for MS synthesis it was between 0.06-0.3 $S.cm^{-1}$ for Mg doped (with carrier concentrations ranging from 10^{17}-10^{19} cm^{-3} respectively)[151]. The visible transparency was around 70% for both synthesis.

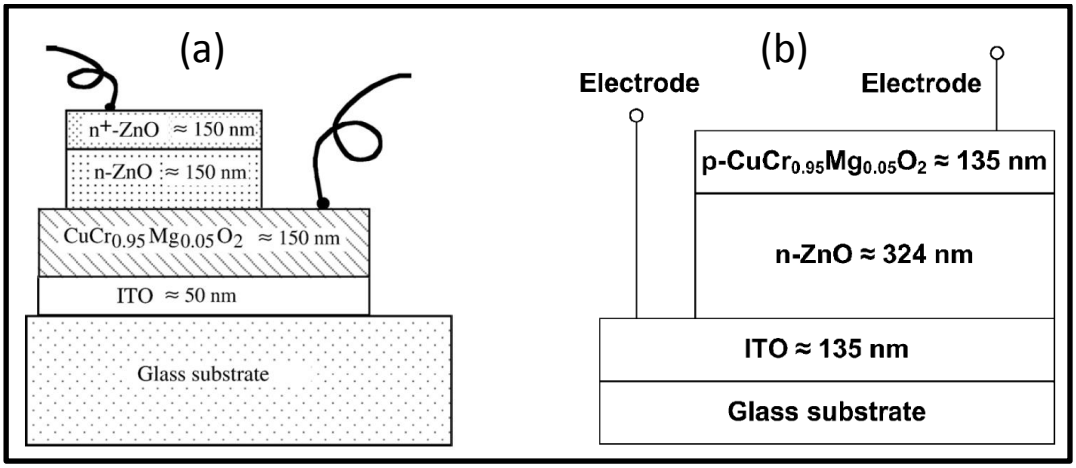

Figure 25 Transparent pn junction devices with $CuCrO_2$ as p-type material synthesized by (a) PLD[42] and (b) MS[151]

I-V characteristics of devices synthesized by PLD are shown in Figure 26 (a). The authors highlighted the necessity to dope delafossite $CuCrO_2$ and add a conductive layer of ZnO at the top of the junction, in order to increase the forward bias voltage. The transport mechanism was found to be limited by series resistance up to 2.5V, while between 1 and 2.5V it was space charge limited current (SCLC) mechanism[42]. The I-V characteristics of the junction fabricated by MS, Figure 26 (b), show a diode characteristic only for a $CuCrO_2$ grown at 450°C. but showing a rather poor crystallinity[151]

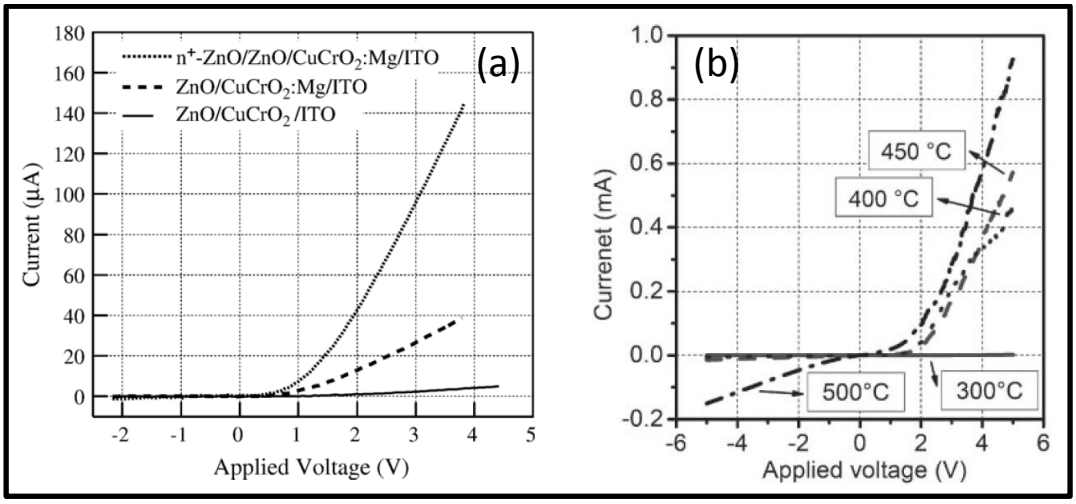

Figure 26 I-V curves of pn junctions with $CuCrO_2$ as p-type material synthesized by (a) PLD[42] and (b) MS[151]

Conclusions on delafossite $CuCrO_2$

Delafossite $CuCrO_2$ is very stable under air annealing. Among the delafossite compounds, $CuCrO_2$ also shows the best electrical conductivity, this features is attributed to the Cu-O-Cr covalent bonds and the good dopability of the materials. Moreover optical gap is suitable for applications requiring transparent properties within the visible wavelength range. These concomitant criteria are the rationales of the privileged selection of delafossite $CuCrO_2$ as p-type material for the fabrication of transparent p-n junction. However, the low temperature synthesis of crystalline $CuCrO_2$ over large area is still actually a challenge. Therefore, we decide in this work to investigate and to develop specifically the use of MOCVD process to grow high-quality $CuCrO_2$. In addition, the nature of the charge carrier transport in heavily doped $CuCrO_2$ is still a fundamental question to be addressed.

We select ZnO as n-type materials for the preparation of transparent p-n junction. A lot of published studies were dedicated to investigate electrical and transparency properties of ZnO, we present hereafter a very short resume of them.

I.3 N-type ZnO

Zinc oxide is a II_b–VI compound semiconductor particularly attractive because of the large abundances of Zn and O in the earth crust, 132 ppm and 49.4%, respectively, but also for its stability[152]. The research and development on ZnO is mainly motivated for it use as

transparent electrodes in thin film solar cells or flat panel displays to replace indium tin oxide (ITO), the dominant transparent electrode material today that suffers from the In scarcity (In abundance in the earth crust is only 0.1 ppm). ZnO has recently found other applications as transparent thin-film transistors, or spintronics [153], [154], photocatalytics [155], etc…

I.3.1 Crystalline structure

Zinc oxide crystallizes in the hexagonal wurtzite structure ($P6_3mc$). In the hexagonal unit cell of ZnO, Zn atoms are surrounded tetrahedrally by oxygen atoms and vice versa (Figure 27). This tetrahedral coordination is typical of sp^3 covalent bonding, but these materials also have a substantial ionic character. Lattice parameters of ZnO are 3.25 Å for a-axis and 5.21 Å for c-axis[156]–[158]

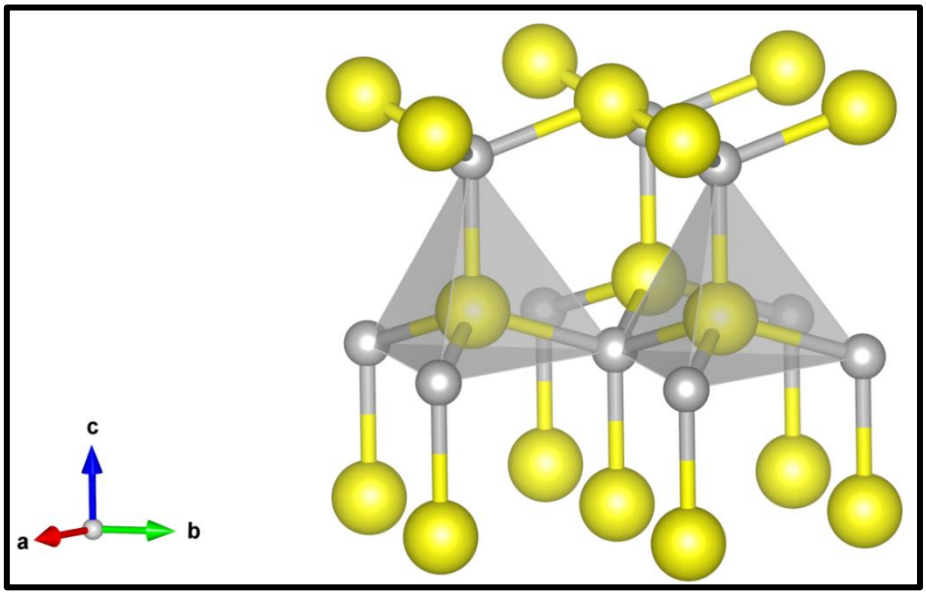

Figure 27 Crystal structure of ZnO (done with VESTA software)

I.3.2 Band structure

Zinc oxide is a direct semiconductor with a band gap energy of 3.4 eV[12]. DFT calculations [159][160][161] confirm that the valence band maximum and the conduction band minimum both occur at the Γ point k =0. The low lying valence bands ($E–E_V \approx 8.5$ eV) belong to Zn 3d states, while the upper valence bands (-5 to 0 eV) are composed of O 2p bonding levels. A schematic band structure of ZnO is displayed in Figure 28. The lowest conduction bands are strongly localized at Zn 3s levels. This is comparable to the band structure of indium

oxide, where the conduction band is also composed of s-like states of cation, i.e., indium atoms[162][163][164]

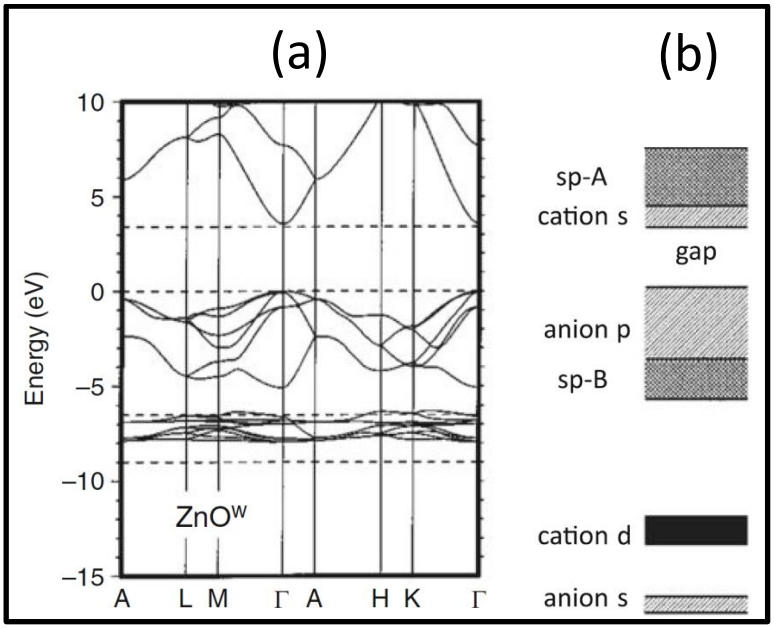

Figure 28 (a) ZnO band structure calculation and (b) the corresponding bonding and atomic orbitals bands[159]

I.3.3 Electrical properties

We present in this paragraph, electrical properties of ZnO with intrinsic or extrinsic doping

I.3.3.1 Intrinsic doping

The high n-type conductivity of ZnO at room temperature, can be induced by crystalline single point defects in the lattice (for instance oxygen vacancies or zinc interstitials). These defects introduce shallow donor levels in the electronic band gap of ZnO. Their concentrations are strongly impacted by the synthesis process. For ZnO thin-films, oxygen partial pressure and deposition rate are known to tailor the properties (concentration, chemical structure, structural position) of these defects[165]–[167].

Although electrical properties of intrinsic zinc oxide were investigated since more than five decades, the underlying origins of the doping mechanisms in intrinsic ZnO are still unclear. For a long time, it was believed that the oxygen vacancy was the dominant donor[168], [169]. This hypothesis was supported by experiments showing that an annealing of single crystals or

thin films under reducing conditions increased the carrier concentration, while an oxidizing treatment decreased the carrier concentration [165][170][171]

Recently, it was performed an electrical transport study on pure, intrinsic ZnO single crystals in which crystallographic defects were generated by high energy (MeV) electron irradiation[172]. Since the defect production was higher when the crystals were irradiated in (001) direction (Zn-face up) compared to electron bombardment along the (00-1) direction (O-face up), it was concluded that zinc interstitials are the intrinsic shallow donors. This conclusion was further supported by several calculations showing that oxygen vacancy induces a deep donor level in the band gap [161][173][174].

I.3.3.2 Extrinsic Doping

For n-type doping, one would choose to substitute Zn with atoms that have one electron more in the outer shell. Consequently the group III elements Al, Ga, and In are shallow and efficient donors on Zn cation sites according to

$$D^0 \leftrightarrow D^+ + e^-$$

where D^0 and D^+ are the neutral and ionized donors, respectively. Electron concentrations beyond 10^{20} cm^{-3} are obtained in ZnO:Al or ZnO:Ga[175][176], which result at room temperature in a degenerate electron gas in the conduction band.

It was also demonstrated that the hydrogen defect level is situated in or close to the conduction band, i.e., it constitutes a donor in ZnO [177][178]. Hydrogen is present during almost all growth processes, introducing a background concentration of Hydrogen in single crystals and films. More recently (2005) the intentional introduction of hydrogen as a donor during reactive magnetron sputtering of ZnO:Al was investigated[179]. Though a decrease of the resistivity from about 7 to 5 $x10^{-4}$ Ω.cm was observed, it was not clear whether the hydrogen-doping is stable under illumination and at higher operating temperatures.

I.3.4 Optical properties

Zinc oxide has an intrinsic band gap at room temperature of 3.24-3.37 eV [180]–[184] which is somewhat lower than that of the other n-type TOS materials like ITO (E_g = 3.75 eV) [185], [186] or SnO_2 (E_g =3.6 eV) [187][188].

I.3.5 ZnO growth

A lot of processes are studied for the growth of ZnO thin films. Here, we describe only rf magnetron sputtering and MOCVD, because magnetron sputtering is the most reported techniques and MOCVD is the synthesis technique that we have used in this work.

I.3.5.1 rf magnetron sputtering

One of the most popular growth techniques for early ZnO investigations was sputtering (dc sputtering, rf magnetron sputtering, and reactive sputtering). As compared to chemical-vapor deposition [189] [190] [191] the magnetron sputtering was a preferred method because of its low cost, simplicity, and low operating temperature. ZnO films typically grow at substrate temperatures between room temperature and 300°C [192], when sputtering from a high-purity ZnO target is sputtered using a rf magnetron sputter system. The growth is usually carried out with $O_2/Ar+O_2$ ratio ranging from 0 to 1 at pressures of $10^{-3} – 10^{-2}$ Torr. O_2 serves as the reactive gas and Ar acts as the sputtering enhancing gas. ZnO can also be grown by dc sputtering from a Zn target in an $Ar+O_2$ gas mixture. The rf power applied to the plasma is tuned to regulate the sputtering yield rate from the ZnO target. Although most of the earlier sputtered materials were polycrystalline or even amorphous, some important accomplishments were recently reported. Upon increasing the $O_2/Ar+O_2$ ratio in the growth atmospere, the visible emission in the room temperature photoluminescence spectra was drastically suppressed without degrading the band-edge emission intensity in the ultraviolet region. This is attributed to the reduction of the oxygen vacancies and zinc interstitials concentrations in the film, indicating that the visible emission in ZnO originates possibly from oxygen vacancy or zinc-interstitial-related defects[193].

I.3.5.2 Metal organic chemical vapour deposition (MOCVD)

For the ZnO growth, MOCVD technique typically involves the use of metal alkyls, usually dimethyl zinc [$(CH3)_2Zn$] (DMZ) or diethyl zinc [$(C_2H_5)_2Zn$] (DEZ) in combination with a separate source of oxygen and argon or nitrogen as a carrier gas. In earlier investigations, O_2 or H_2O were used as oxygen precursors[194][195]. However, DEZn and DMZn are highly reactive with oxygen and water vapour so that severe premature reaction in the gas phase often occurs in the cold zone of reactors, resulting in the formation of white powder, that degrades

the film quality and the reactor cleanliness. Nevertheless, great progress has been recently made in the ZnO growth by MOCVD. The improvement of the material quality is related to improved reactor designs[196] and/or the use of less-reactive precursors, allowing one to minimize parasitic pre-reactions in the gas phase. Stable metal-organic source of zinc acetylacetonate in combination with oxygen was successfully used for the growth of high-quality ZnO films on [197][198] sapphire substrates by atmospheric pressure MOCVD. For the group-VI precursor, a variety of oxygen compounds were employed: isopropanol (*i*-PrOH,[199]–[201], tertiary-butanol (*t*-BuOH)[202][203] ,N_2O[204][205] and NO_2[198].

The improvement of MOCVD technology also gave rise to great progress in the quality of ZnO layers grown with the use of DEZn and O_2. The pressure used for the growth was in the range of 5–250 Torr[196][206]. Lower-pressure effect was investigated and the results showed that the crystal quality was better for films grown at 6 Torr than those grown at 0.05 Torr[207].

As it was presented, zinc oxide is a n-type TOS with high electrical conductivity and optical transparency which are compatible for the integration of ZnO in technology as transparent p-n junctions.

I.4 Electrical transport in semiconductor

In this paragraph, we shortly describe models for the scattering mechanisms in semiconductors and small polaron transport.

The electrical transport of charge carriers in semiconductors is governed by several scattering mechanism[3]:

- intrinsic scattering due to the band structure of the semiconductor, which is governed only by intrinsic material parameters (sometimes called lattice scattering)

- extrinsic scattering caused by impurities, ionized or dopants. The intrinsic scattering process dominates for low carrier concentrations $n < 10^{16}$ cm^{-3} while the ionized impurity scattering governs the carrier transport for $n > 10^{18}$ cm^{-3} at room temperature.

- grain boundary scattering in polycrystalline films.

I.4.1 Lattice scattering

In polar oxide, lattice scattering process can be distinguished into two categories: scattering by acoustic and by optical phonons.

I.4.1.1 Acoustical mode scattering

Acoustical mode scattering is a lattice deformation scattering process due to a local energetic shift of the band edges originating from acoustical phonons. According to Bardeen and Shockley[208] the acoustical lattice mode Hall mobility is:

$$\mu_{Hac} = r_{Hac}\frac{\sqrt{8\pi}\hbar^4 c_l e}{3E_1^2\sqrt{m^{*5}(k_B T)^3}} \quad (9)$$

where c_l is the averaged longitudinal elastic constant, E_1 is the deformation potential (energy shift of the conduction band per unit dilation), $r_{Hac}= 3\pi/8 =1.178$ is the Hall coefficient for acoustic phonon scattering.

I.4.1.2 Optical mode scattering

Optical mode scattering is due to the interaction of electrons with the electric field, induced by the lattice vibration polarization occurring in polar semiconductors with partial ionic bonding. According to Devlin [209], the optical Hall mobility can be calculated by:

$$\mu = r_{Hopt}\Phi\frac{e}{2\alpha\omega_0 m^*}\left[e^{\left(\frac{\hbar\omega_0}{k_B T}\right)} - 1\right] \quad (10)$$

where the polaron coupling α constant is given by:

$$\left(\frac{1}{\varepsilon_\infty} - \frac{1}{\varepsilon_s}\right)\sqrt{\frac{m^* E_H}{m_e \hbar\omega_0}} \quad (11)$$

where ε_∞ and ε_s are the high frequency and the static dielectric constants, E_H is the first ionization energy of the hydrogen atom (13.595 eV), m* and m_e are the effective and the vacuum electron masses, while $\hbar\omega_0$ is the energy of the longitudinal optical phonon, r_{Hopt} is the Hall coefficient factor for optical mode scattering and Φ is a slowly varying function of the temperature. Usually it is assumed that $r_{Hopt}\Phi$ is equal to 1 [210].

Optical mode scattering can be also a lattice deformation scattering process due to a local energetic shift of the band edges as the acoustical mode scattering. The temperature dependence of the mobility is the same that acoustical mode scattering: $\mu \propto (k_B T)^{-3/2}$ [208]

I.4.2 Ionized impurity scattering

This scattering process is caused by ionized dopant atoms and dominates for carrier concentrations above about 10^{18} cm^{-3}. An analytical expression for the mobility μ_{ii} of degenerately doped semiconductors, taking into account the non-parabolicity of the conduction band, was given by Zawadzki [211] and refined by Pisarkiewicz et al. [212]:

$$\mu_{ii}^{ZP} = \frac{3(\varepsilon_r\varepsilon_0)^2 h^3}{Z^2 m^{*2} e^3} \frac{n}{N_i} \frac{1}{F_{ii}^{np}(\xi_d)} \quad (12)$$

With:

$$\xi_d = (3\pi^2)^{1/3} \frac{\varepsilon_r\varepsilon_0 h^2 n^{1/3}}{m^* e^2} \quad (13)$$

where the screening function F_{ii}^{np} is given by:

$$F_{ii}^{np} = \left[1 + \frac{4\xi_{np}}{\xi_d}\left(1 - \frac{\xi_{np}}{8}\right)\right] * ln(1+\xi_d) - \frac{\xi_d}{1+\xi_d} - 2\xi_{np}\left(1 - \frac{5\xi_{np}}{16}\right) \quad (14)$$

with the parameter $\xi_{np} = 1 - m_0^*/m^*$, which describes the non-parabolicity of the conduction band (m^*, m_0^* are effective masses in the conduction band and at the conduction band edge, respectively). The non-parabolicity is usually described by the dependence:

$$\frac{m^*}{m_0^*} = 1 + 2\beta(E - E_C) \quad (15)$$

where β is the non-parabolicity parameter, E and E_C are the energies of carriers in the conduction band and at its edge. The prefactor in Equation (12) shows, that the ionized-impurity limited mobility depends as $\mu_{ii} \approx (\varepsilon_r/m^*)^2$ on the material constants of the semiconductor and as $\mu_{ii} \approx Z^{-2}$ on the charge of the dopants (Z=1 for group III donors; Z=2 for oxygen vacancies).

The theoretical model given above is based on the assumption of a statistically homogeneous distribution of scattering centers, i.e., dopants. However, this is no longer valid for extremely high dopant concentrations (up to 3.10^{20} cm^{-3}) where the dopants form clusters [213], [214] which lead, due to their higher charge, to lower mobilities ($\mu_{ii} \approx Z^{-2}$).

I.4.3 Neutral impurity scattering

Since the shallow donors in TCO materials (for instance the group III elements in ZnO) exhibit ionization energies around about 50 meV[215], the concentration of neutral donors at

room temperature is very low, taking into account the further reduction of the ionization energy for degenerately doped semiconductors. The mobility due to neutral impurity scattering is:

$$\mu_n = \frac{m^* e^3}{A(T) 4\pi\varepsilon\varepsilon_0 \hbar^3 N_n} \quad (16)$$

Here, A(T) is the generally temperature-dependent scattering cross-section factor and N_n is the density of neutral scattering centers. The concentration of neutral impurities is given by $N_n = N_D - N_A - n(T)$, where N_D and N_A are the donor and acceptor concentrations, respectively.

I.4.4 Grain boundaries scattering

Polycrystalline films exhibit a vast amount of grain boundaries, which constitute crystallographically disturbed regions, leading to electronic defects in the band gap of semiconductors. These defects are charged by carriers from the interior of the grains. Depending on the type of the carriers (electrons or holes) and the type of defects (electron trap or hole trap), the charge balance causes depletion or accumulation zones around the barrier[216]. In TCO films which are typically n-type, a depletion zone is generated on both sides of a grain barrier accompanied by an energetic barrier of height Φ_b for the electrons[216]. This is due to the electron trap character of defects. The mobility μ_{GB} dominated by the thermionic emission across the grain barriers with an energetic height Φ_b becomes [216]:

$$\mu_{GB} = \mu_0 e^{-\Phi_b / k_B T} \quad (17)$$

where Φ_b is the energetic barrier height at the grain boundary, T the sample temperature, and k_B is the Boltzmann constant, respectively. The prefactor μ_0 in Equation (17)is:

$$\mu_0 = \frac{eL}{\sqrt{2\pi m^* k_B T}} \quad (18)$$

where L is the crystallite size

Depending on the doping concentration in the grains, two expressions for the barrier height can be derived:

* for $LN > N_t$:

$$\Phi_b = \frac{e^2 N_t^2}{8\varepsilon\varepsilon_0 N} \quad (19)$$

* for $LN < N_t$:

$$\Phi_b = \frac{e^2 L^2 N}{8\varepsilon\varepsilon_0} \quad (20)$$

where e is the elementary charge, N_t is the charge carrier trap density at the boundary, $\varepsilon\varepsilon_0$ is the static dielectric constant, N is the carrier density in the bulk of the grain and L the grain size. For $LN < N_t$ the traps are only partially filled and hence the crystallites are completely depleted, while for $LN > N_t$ only part of the grain is depleted and the traps are filled completely. The maximum barrier height Φ_{bmax} occurs for a doping concentration of $N(\Phi_{bmax}) = N_t/L$, accompanied by a minimum of the mobility according to Equation (17).

For degenerate semiconductors, the mobility due to grain boundaries is different from Equation (17). It is expressed as[217]:

$$\mu = \frac{4\pi e L m^* k_B T}{p_a h^3} \ln\left(1 + e^{-\left(\frac{\Phi_b}{k_B T} - \eta\right)}\right) \quad (21)$$

where L is the crystallite size, p_a is the average free carrier concentration in the crystallite, Φ_B is the potential barrier height and η is defined for a n-type semiconductor as:

$$\eta = \frac{E_F - E_C}{k_B T} \quad (22)$$

where E_c is the energy of the bottom of conduction band and E_F is the Fermi energy

For p-type semiconductors, the mobility depending on scattering mechanisms is also described by above equations, but for p-type material with degenerate valence band, the hole effective mass m_h^* is defined when the valence band is splitted as [218]:

$$m_h^* = \left((m_{lh}^*)^{3/2} + (m_{hh}^*)^{3/2}\right)^{2/3} \quad (23)$$

where m_{lh}^* is the light hole effective masse and m_{hh}^* is the high hole effective mass.

I.4.5 Small polaron transport

In small polaron model, for adiabatic case[e], the mobility is expressed as [219]–[221]:

$$\mu = \frac{\mu_0}{T} e^{-\frac{E_H}{k_B T}} \quad (24)$$

where E_H is activation for hopping and μ_0 defined as:

$$\mu_0 = \frac{g(1-c)ea^2\nu}{k_B} \quad (25)$$

[e] In adiabatic approximation, electrons or holes localized on an atom follow instantly the motion of this atom

where g is a geometric factor (≈1), e the elementary charge, a the distance of hopping and ν is the appropriate (optical mode) phonon frequency. The fraction of occupied site, c, is defined as c=n/N, where n is the carriers density and N is the density of available sites.

As the electrical conductivity is $\sigma = ne\mu$ and the mobility is defined by Equation (**24**) in small polaron transport, the electrical conductivity is expressed as:

$$\boldsymbol{\sigma = \frac{\sigma_0}{T} e^{-\frac{E_H}{k_B T}}} \qquad (26)$$

where $\sigma_0 = eNc\mu_0$

Conclusions

We exposed in this first chapter the state of the art of p-type delafossite $CuCrO_2$ and n-type ZnO materials. In comparison with others p-type TCM, delafossite $CuCrO_2$ materials exhibit one of the highest trade-off electrical conductivity-visible transparency with standard method synthesis. Both $CuCrO_2$ and ZnO are very stable under air and have similar band gap. High trade-off conductivity-transparency, air stability and wide band gap are suitable parameters for transparent p-n junction synthesis. Therefore, we decided to synthesize p-n junctions with p-type delafossite $CuCrO_2$ and n-type ZnO. However, for an up-scale of such architecture to the industry, transparent junctions should be synthesized at temperature as low as possible. The MOCVD synthesis was specifically developed in this study to grow $CuCrO_2$ thin-films. Charge carrier transport mechanisms in doped $CuCrO_2$ are still under debate in the scientific community. Specific thermoelectric and electrical conductivity measurements are also conducted to bring additional insights to this topic.

II. EXPERIMENTAL METHODS

In this chapter, we present the experimental techniques we have used during this work. The first part is dedicated to the MOCVD synthesis method and the second part reminds the characterization methods that have been preferably utilized to investigate the physical and chemical properties of the synthesized thin films.

II.1 MOCVD synthesis

Chemical Vapour Deposition (CVD) is defined as a chemical reaction on the substrate surface of gaseous reactants activated by its surrounding environment (heat, light or plasma). The chemical product is a stable solid structure (film, particles, wires etc.) on the substrate. A lot of various CVD modes like atmospheric pressure CVD, low pressure CVD, plasma enhanced CVD, rapid thermal CVD, atomic layer deposition (ALD) is reported… We give a short resume of CVD fundamentals in order to understand the concept of the Metal Organic CVD and the pulsed injection method.

II.1.1 Basic principles of CVD deposition

The CVD deposition can be divided into sequential steps (Figure 29):

(1) Production of the reactant species in a gas phase (sublimation of powder, liquid evaporation or gas introduction)

(2) Transport of species towards the reaction chamber.

(3) Gaseous reactants undergo gas phase reactions forming intermediate species:

(a) at high temperatures above the decomposition temperatures of precursors, intermediate species are generated inside the reactor via the precursor thermolysis. Parasitic homogeneous gas phase reaction may occur when the intermediate species undergo subsequent decomposition and/or chemical reaction, forming powders and volatile by-products in the gas phase. The parasitic powders pollute the reactor and the substrate surface. The collected powders on the substrate surface may act as crystallization seeds in some particular cases[48]. The gaseous by-products are transported away from the deposition chamber.

(b) at temperatures below the thermal dissociation of gaseous precursors, the diffusion/convection of the species across the boundary layer (a) (thin layer close to the substrate surface) occurs. These species subsequently undergo steps (4)–(7) described hereafter.

(4) Absorption of gaseous reactants onto the heated substrate. The heterogeneous reaction occurs at the gas–solid interface (i.e. heated substrate) which produces adatoms or solid clusters and gaseous-product species.

(5) Adatoms diffuse along the heated substrate surface forming the crystallisation seed for the growth of the film.

(6) Gaseous by-products are removed from the boundary layer through diffusion or convection.

(7) The unreacted gaseous precursors and by-products are transported away from the deposition chamber.

For the deposition of dense films and coatings, the process conditions are tailored to favour the heterogeneous reaction. Often a combination of heterogeneous and homogenous gas phase reaction is preferred for the deposition of porous coatings. In our case, we tune process parameters like growth temperature flow precursor, height of heated substrate etc… (see below) in order to get crystallised and dense films.

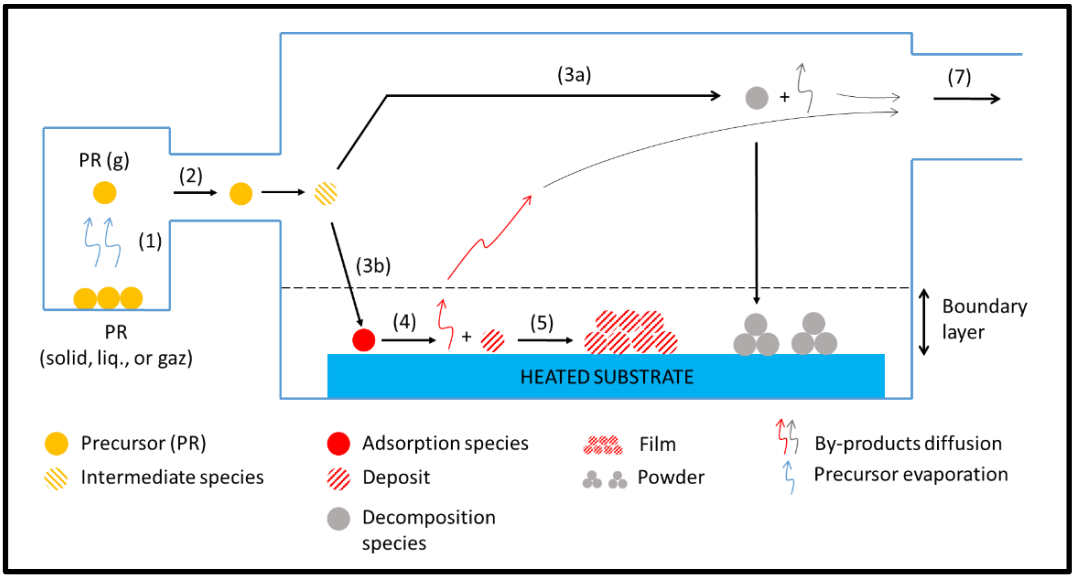

Figure 29 Steps of CVD during deposition

II.1.2 Kinetic reaction and growth rate

The growth rate of deposited coatings, depends on temperature, precursors, gas-phase transport of precursors and the chemical reaction on surface (Figure 30).

As depicted in Figure 30 (a), for temperature kT < Ea (Ea is the activation energy of thin film growth), the growth rate is limited by the chemical reaction kinetic on the surface (chemisorption and/or chemical reaction, surface migration, lattice incorporation). The growth rate gr in that case strongly depends on the substrate temperature and is defined as[48]:

$$gr = Ae^{\frac{-E_a}{kT}}$$

where A is a constant, E_a is the activation energy, k the Boltzmann constant and T the temperature

For temperature kT>Ea, Figure 30 (b) the growth rate is limited by the diffusion of gaseous species through the boundary layer to the substrate surface. In that case, the growth rate depends weakly of the temperature.

For high temperature (Figure 30 (c)), the growth rate decreases due to the precursor depletion and/or the increase of the desorption of reactants away from the surface. As previously described, homogeneous gas phase reactions may occur, producing parasitic powder and consuming precursors impairing the homogeneous growth of thin-film coating

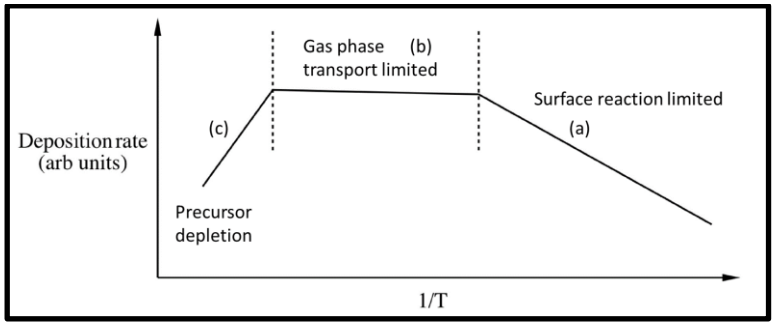

Figure 30 Growth rate of kinetic regimes in CVD synthesis, depending on the inverse of temperature

II.1.3 Growth mechanisms

During deposition, adatoms interact with the substrate surface and/or with others adatoms. The strength of interactions defines the growth mechanism of the films[222]

II.1.3.1 Van Der Merwe (two dimentional)

Two dimensional growth occurs when adatoms attach preferentially to the surface sites (Figure 31 (a)) resulting to the growth of thin-films via layer by layer mechanism (a homogeneous film is formed prior to the growth of any subsequent layer).

II.1.3.2 Wolmer-Weber (three dimentional)

Three dimensional growth occurs when adatoms interact preferentially with each other than with the surface. This results in the formation of adatom clusters or islands (Figure 31 (b)) leading to the growth of rough films over the substrate surface.

II.1.3.3 Stransky-Krastanov

A last growth mode involves both Wolmer-Weber and Van der Merwe mechanisms (Figure 31 (c)). A two dimensional growth occurs until a critical layer thickness (depending on the surface energy, the lattice parameters of both substrate and film…) is reached. Then, the three dimensional growth takes place.

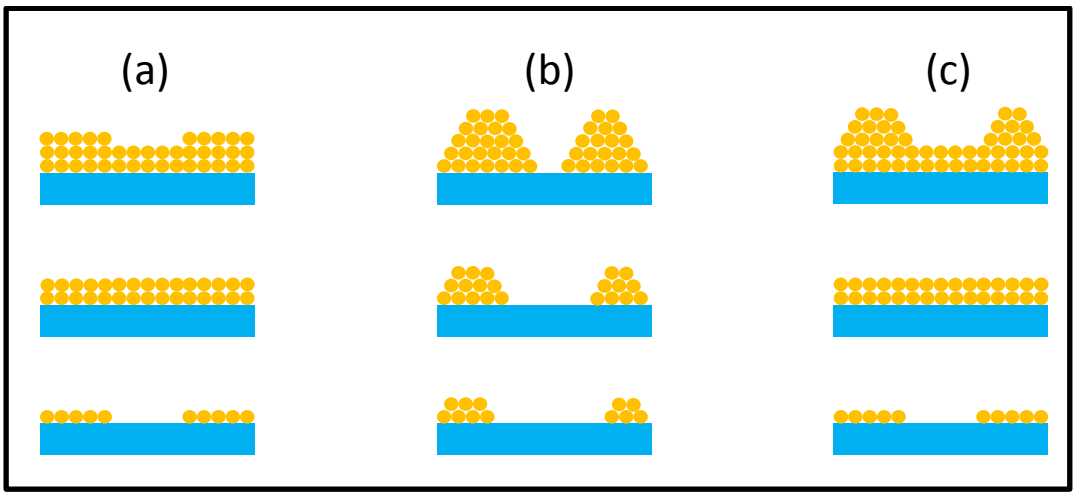

Figure 31 Growth mechanisms in CVD process: (a) Van Der Merwe (b) Wolmer-Weber and (c) Stransky-Krastanov

We focus now on the features of the MOCVD mode and the description of the apparatus we intensively used during this thesis.

II.1.4 MOCVD and pulsed injection

MOCVD is a CVD process with metalorganic precursors. Precursors containing metal atoms bonded to organic radicals are called “metalorganics” while precursors having direct metal-carbon bound are called “organometallic”. In this latter case, the process is called “organometallic chemical vapour deposition” (OMCVD). MOCVD offers a large choice of precursors compared to the classical CVD mode. A wide range of material chemistries (we

provide brief examples Table 4) can be grown in the form of amorphous, epitaxial and polycrystalline films or nanostructures. Metalorganics precusors have also a lower temperature decomposition than gaseous precursors used in conventional CVD, and as a consequence, the temperature deposition can be often decreased. This feature is particularly suitable in our case when the maximum temperature is limited by the glass substrate, i.e T<600°C.

Table 4 Examples of metalorganic and organometallic precursors for materials synthesis with MOCVD approach, extracted from [48] (Note: DE: diethyl; DIP: diisopropyl; DM: dimethyl; DTB: ditertiarybutyl; MA: methylallyl; TE: triethyl; TM: trimethyl.)

Materials	Precursors	Applications	Ref.
AlGaAs / GaAs	TMAl, TMGa, TEGa, AsH_3	LED, injection laser	[223]
InGaAs, InP, InGaAsP	TMIn, TMGa, TEGa, AsH_3, PH_3	Fibre optics, Communications, bipolar transistor	[224]–[226]
InAlGaN	TMIn, TMAl, TMGa, NH_3	Blue LEDs	[227]
ZnCdSe	DMZn, DMCd, H_2Se	Blu-green LEDs	[228]
ZnCdSSe, ZnMgSSe	DEZn, DMCd, DES, DMSe, DTBSe, $H_2S(MeCd)_2Mg$	LEDs	[229]
HgCdTe, HgCdZnTe	DMHg, DETe, MATe, DIPTe, DMCd, DMZn	Infrared detectors	[229], [230]
PbSnTe	TEPb, TESn, H_2Te	Infrared detectors	[231]
Cu, Al	$(CF_3COCHCOCF_3)_2Cu$, TMAl	Interconnects for Si integrated circuit	[232]

In 1995 Senateur *et al.*[233] have developed a new method of precursor's introduction called "pulsed injection CVD" where liquid precursors or precursor solutions are directly injected into the reactor in a pulsed way through a microelectrovalve. The main advantage of this pulsed injection method over others CVD precursor delivery approaches (e.g bubbler or sublimator) is the less stringent criteria for the use of given precursor in terms of volatility and stability, owing to the precursor partial pressure being dependent solely on the delivery conditions. There is also a better control of the thickness, the growth rate, the stoichiometry and the reproducibility of coatings [234][235].

II.1.5 MOCVD apparatus and chemistry

Thin films were deposited using pulsed injection MOCVD (MC200, produced by Annealsys). A schematic description of the setup is given Figure 32 with Cu and Cr chemistries

as an example. The precursor, in liquid phase, is maintained under a nitrogen pressure of 5 bars at room temperature ①, before its injection into the reactor under a pressure between 5-30 mbar ②. The liquid precursor enters in reactor due to the pressure difference ΔP. The precursor flow is controlled by an injector having successive opening and closing of the valve ③. Precursor evaporation occurs when entering in the reactor because of the sudden decrease of pressure leading to the flash evaporation of liquid droplets. Precursors and reactant gases (oxygen in our case) are introduced together ④ and are transported towards the substrate holder ⑤ by pumping down to reactor ⑥. The substrate ⑦ is heating by the substrate holder and then, chemical reactions occur near the substrate surface ⑧. We can tailor various process parameters for tuning the synthesis regime:

- Temperature of substrate holder ($RT \leq T < 750°C$)
- Pressure inside the reactor ($1\ mbar < P \leq ATM$)
- Precursor flow ($0.2g/min < prec._{flow} \leq 3g/min$)
- Gas flow of O_2, N_2, H_2O or NH_3 ($50sccm < gas_{flow} < 5000sccm$)
- Gas carrier flow (N_2) of precursor ($100sccm < gas\ carrier_{flow} < 1000scmm$)
- Injector frequency ($1Hz \leq f \leq 10Hz$)
- Height of substrate holder ($0 \leq h \leq 16cm$)
- Rotation of substrate holder ($0 \leq r \leq 30rpm$)

In our case, the precursors used are M(thd)x with M=Cu, Cr or Zn and x=2 or 3. M(thd)x precursors (which are metalorganic precursor) belong to the metal β-diketonates class who has attracted much attention due to their advantageous tuneable chemical and physical properties[236], [237]. The structure of the β-diketonate ligands can be altered, giving different volatility, temperature decomposition, etc… The (thd) ligand compounds present high thermal stability in air, adequate volatility, good coefficient diffusion (in nitrogen), and low thermal decomposition[238]–[240]. These peculiar properties make [$M(thd)_x$] precursors promising for the growth of TOS via a CVD process. Prior to the deposition process, the glass substrates were ultrasonically cleaned in ethanol, and acetone, dried with a nitrogen jet and then exposed during 15 minutes to oxygen plasma generated *in situ* the chamber.

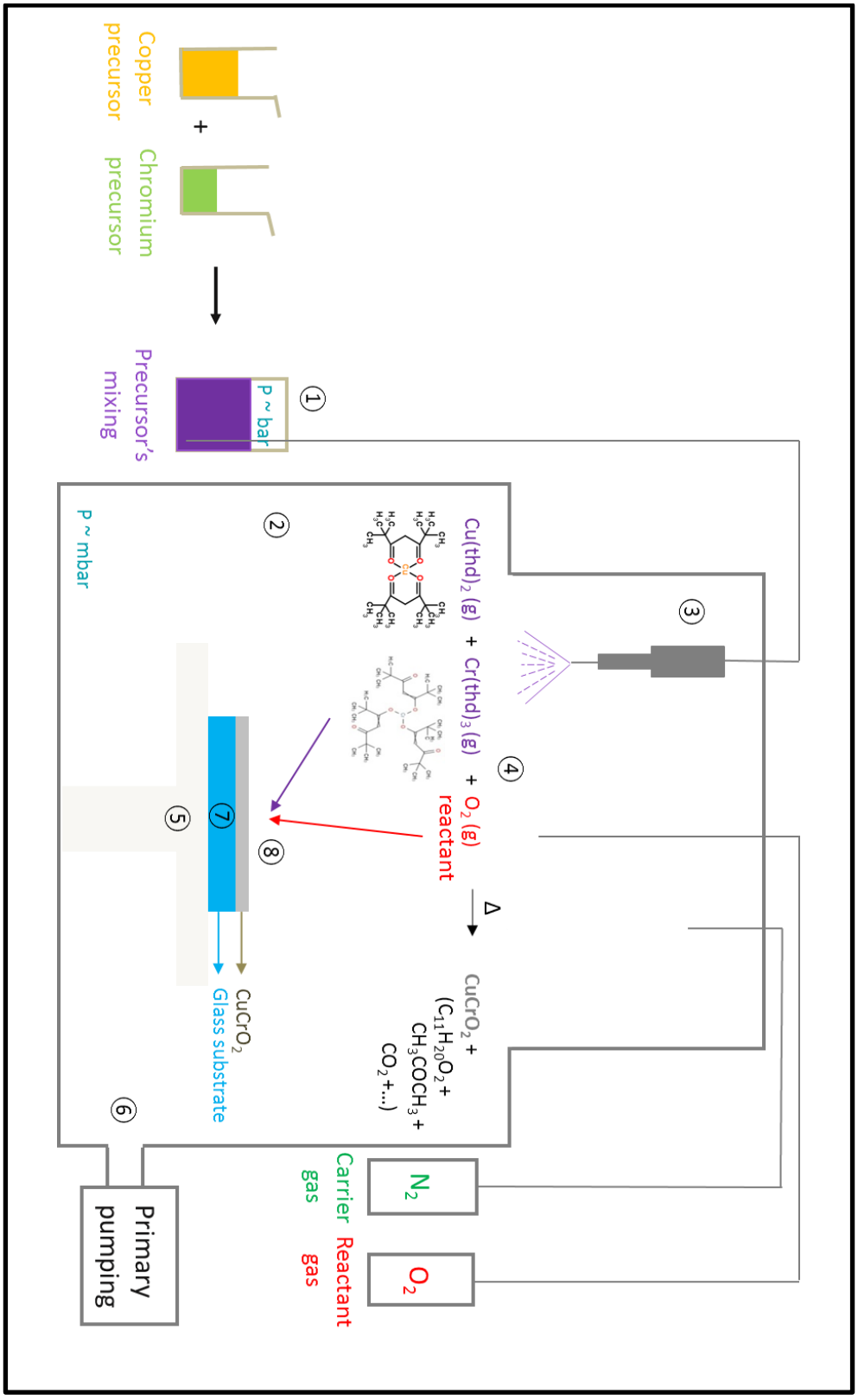

Figure 32 Schematic representation of the MOCVD set-up and chemical reaction of precursors

II.1.6 Atomic Layer Deposition (ALD)

Zinc oxide thin films were deposited by pulsed injection MOCVD and also by ALD (TFS 200, produced by Beneq) process. In that case, precursors and reactants are injected sequentially one after another, separated by N_2 purge.Technical details can be found in [REF]. The advantages of ALD are the conformality of the films and the low temperature deposition compared to classical CVD processes.

II.2 Characterization Methods

In this part, we briefly describe the characterization methods used to investigate structural, morphological, electrical and optical properties of our thin films synthesized by MOCVD.

II.2.1 Scanning Electron microscopy (SEM)

SEM is a microscope based on electron interaction with atoms from the sample, giving information about surface topography, morphology, chemical composition when coupled with EDX analysis etc..., depending on the nature of the electron scattering analysed (Secondary electrons, Backscattered electrons, Auger electrons…).

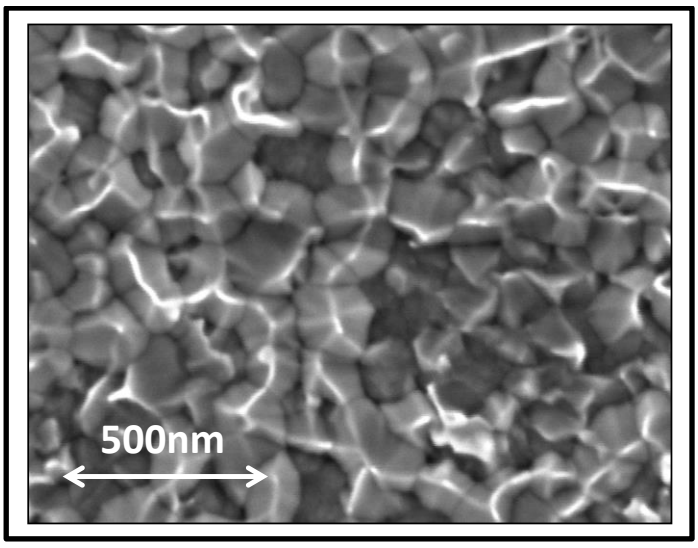

Figure 33 Top view SEM image of our ZnO thin film synthesized by MOCVD, SEM main parameters are electron voltage and current of 3kV and 25pA

The equipment used was SEM-FIB (FIB: Focused Ion Beam) HeliosNanolab 650 produced by FEI having an ultimate spatial resolution down to 10 nm. The analyses are performed under vaccum (≈10^{-6}mbar) and all images are obtained by secondary electron detection. Depending on the charge surface effect, the electron source voltage and current are tuned, from 2 to 5kV and from 25 to 100 pA, respectively. We give in Figure 33 an example of SEM picture.

II.2.2 X-Ray Diffraction (XRD)

XRD is based on the X-Ray light X-Ray diffraction by the crystalline sample. The wavelength of the X-Ray source is the same order of magnitude that the crystal lattice and interatomic distances (few Å) producing constructive or destructive interferences. The crystallographic parameters of the lattice are extracted using the Bragg's law (Figure 34):

$$\mathbf{2d_{hkl}\sin\theta = n\lambda} \qquad (27)$$

Where d_{hkl} is the distance lattice plane (hkl), θ is the Bragg diffraction angle (°) and λ is the source wavelength.

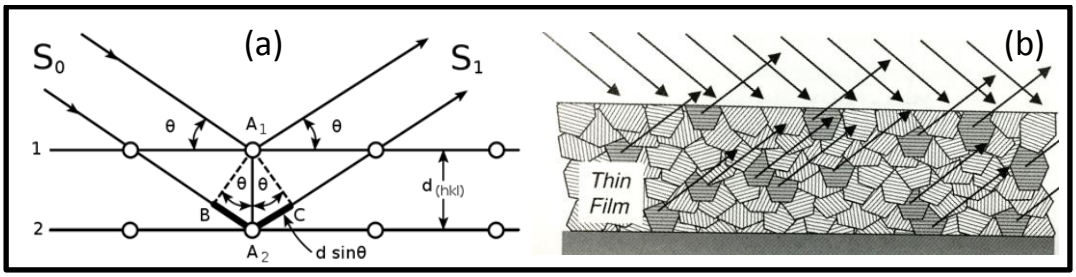

Figure 34 (a) Bragg diffraction on two atoms in two different lattice plans. Constructive interference occur when the path difference between two waves ($2d_{hkl}\sin\theta$) is equal to an integer multiple of the wavelength of the radiation (Equation (27)). (b) Crystallites diffraction planes in θ-2θ geometry [241]

The diffractometer used was a D8 Discover Brucker with a X-ray source of copper (λ=0.1542 nm). The angle scanning was typically performed between 20-80° with a step of 0.02°. The used geometry was θ-2θ or grazing angle depending on the targeted informations. In the θ-2θ geometry, only lattice planes (hkl) that are oriented to the surface plane can contribute to Bragg diffraction (Figure 34 (b)). However, for thin films, a large fraction of the diffractogram in θ-2θ geometry comes from the substrate due to the X-ray penetration depth. Therefore, grazing angle geometry is preferred to increase the thin-films diffraction and probe almost all diffractions planes of the polycrystalline thin films.

Crystallite size and microstrain[f] were evaluated by a single line profile analysis using a pseudo-Voigt fitting function of the measured diffractogram [241]. It was experimentally verified that the crystallite-size broadening can be approximated by a lorentzian function, whereas strain broadening is better described by a gaussian function [242]–[246]. The common used method, Williamson-Hall [241], [247], suppose only lorentzian function for both crystallite-size and strain broadening, impairing an accurate approximation of the shape of XRD peaks (Figure 35 (a)).

Pseudo Voigt function (PV) is a linear combination of lorentzian (L) and gaussian (G) functions with a coefficient η:

$$\boldsymbol{PV = \eta L + (1 - \eta) G} \qquad (28)$$

When η=0, the function is a pure gaussian and when η=1 the function is a pure lorentzian. In pseudo Voigt function, lorentzian contribution is attributed to the crystallite size broadening and the gaussian contribution is attributed to the broadening induced by the stain inside crystallites. (Figure 35 (b)).

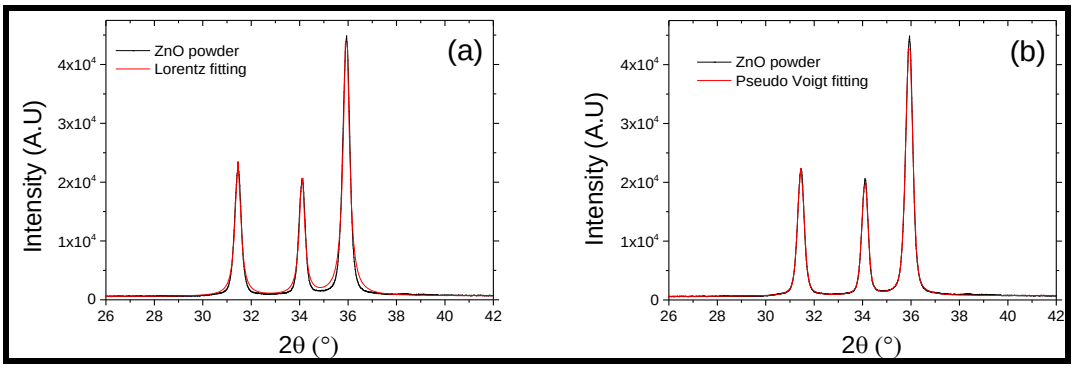

Figure 35 Diffractogram of ZnO powder synthesized at LIST with (a) Lorentz fitting and (b) Pseudo Voigt fitting

Integral breadth contribution[g] of lorentzian (β_L) and gaussian (β_G) to the integral breadth of the peak (β) is calculated by empirical formulaes[241]:

$$\boldsymbol{\beta_L = (0.017475 + 1.500484\eta - 0.534156\eta^2)\beta} \qquad (29)$$

$$\boldsymbol{\beta_G = \left(0.184446 + 0.812629\sqrt{1 - 0.998497\eta} - 0.659603\eta + 0.445542\eta^2\right)\beta} \qquad (30)$$

Thus, the crystallite size L, and the microstrain ε can be determined thanks to β_L and β_C. Indeed, the crystallite size L, is defined by (Debye-Scherrer equation)[241], [248]:

[f] Microstrain quantify the lattice distortion in the vicinity of a defect causing a slight variation of atomic bond lengths and interplanar spacings d.
[g] The integral breadth, β, is defined as the ratio of the peak area/peak maximum

$$\langle L \rangle_V = \frac{K\lambda}{\beta_L \cos\theta} \quad (31)$$

where $\langle L \rangle_V$ is the volume-weighted average crystallite size, K is a constant (≈0.9), λ is the X-ray wavelength, β_L is the lorentzian integral breadth and θ is the Bragg angle diffraction peak. And the microstrain ε[h] is defined as[241], [246]:

$$\varepsilon = \frac{\beta_G}{4tan\theta} \quad (32)$$

where β_G is the gaussian integral breadth and θ is the Bragg angle diffraction peak.

We give in Table 5 an example of the crystallite size and the microstrain as extracted from the pseudo Voigt fitting on ZnO powder (which is an ideal case for getting highly resolved diffraction peaks) before and after ozone annealing. The contribution of the instrumental error to the diffraction peak broadening is taken into account.

Table 5 Crystallite size and microstrain of ZnO powder before and after ozone annealing

Ozone treatment	Bragg diffraction peak	2θ (°)	Crystallite size (nm)	Microstrain (%)
Before	(100)	31.470	32(1)	0.183(0.005)
	(002)	34.123	37(2)	0.148(0.005)
	(101)	35.954	30(1)	0.167(0.003)
After	(100)	31.451	32(1)	0.345(0.006)
	(002)	34.100	38(2)	0.317(0.005)
	(101)	35.927	30(1)	0.317(0.002)

II.2.3 X-Ray photoemission spectroscopy (XPS)

XPS is a surface analysis giving information on chemical and electronic states of elements at the vicinity of the material surface. The surface is irradiated by X-Ray beam (hν) which extracts core electrons from the material with a kinetic energy (KE) depending on their binding energy (BE) in the material. The binding energy is defined as:

$$BE = h\nu - KE - \phi \quad (33)$$

where ϕ is the work function of the detector. The depth penetration of the incident beam is a few nanometers. A quantitative chemical composition of the analysed material is determined by calculating the ratio of the surface area of each peak. Depth chemical profile in films was also done by the sequential use of argon sputtering and XPS measurements. In Figure 36 we

[h] Microstrain ε is defined as $\varepsilon = \Delta d/d_0$ where d_0 is the undistorded spacing plans and Δd is the variation of interplanar spacing

give examples of XPS analysis of our ZnO thin films synthesized by MOCVD. Zinc element show the typical splitting energies of 2p and 3p peaks into $2p_{1/2}$-$2p_{3/2}$ and $3p_{1/2}$-$3p_{3/2}$ respectively (Figure 36 (c) and (d)) and due to the electron spin-orbit interaction.

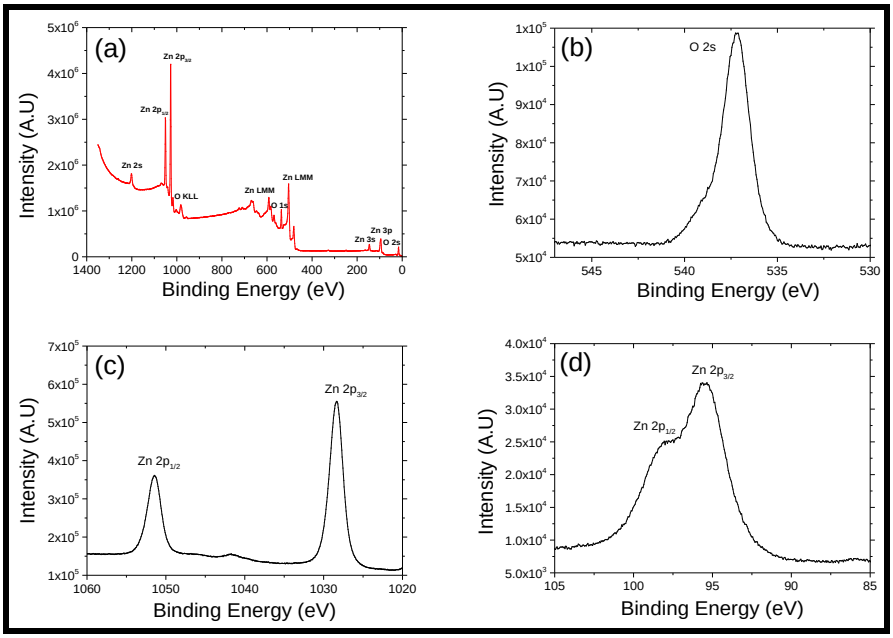

Figure 36 XPS survey spectra of ZnO thin films (a). High resolution of O 2s (b), Zn 2p (c) and Zn 3p (d) peaks

The XPS used was an Axis Ultra DLD producted by Kratos with a spherical deflection analyser. The X-Ray source was Al Kα (hν = 1486.6 eV) with a power of 150W. Surface analysis was 300 × 700 μm^2. Analysis was performed under high vacuum (P ≈ 10^{-8} mbar).

II.2.4 Electrical measurements

The electrical conductivity, carrier concentration and mobility were determined by a Hall effect Ecopia HMS 2000. The setup is able to measure conductivity with a Van Der Pauw configuration without magnetic field. The resistivity is defined as:

$$\boldsymbol{\rho = R_s * d} \qquad (34)$$

where d is the thickness and R_s the sheet resistance. The sheet resistance is determined by solving the equation:

$$\boldsymbol{e^{-\pi R_{vertical}/R_s} + e^{-\pi R_{horizontal}/R_s} = 1} \qquad (35)$$

where $R_{vertical}$ and $R_{horizontal}$ are defined as:

$$\boldsymbol{R_{vertical} = \frac{R_{12,34} + R_{34,12} + R_{21,43} + R_{43,21}}{4}} \quad (36)$$

and

$$\boldsymbol{R_{horizontal} = \frac{R_{23,41} + R_{41,23} + R_{32,14} + R_{14,32}}{4}} \quad (37)$$

where $R_{12,34}$, $R_{34,12}$ $R_{23,41}$ and $R_{41,23}$ are resistances measured with different configuration (Figure 37).

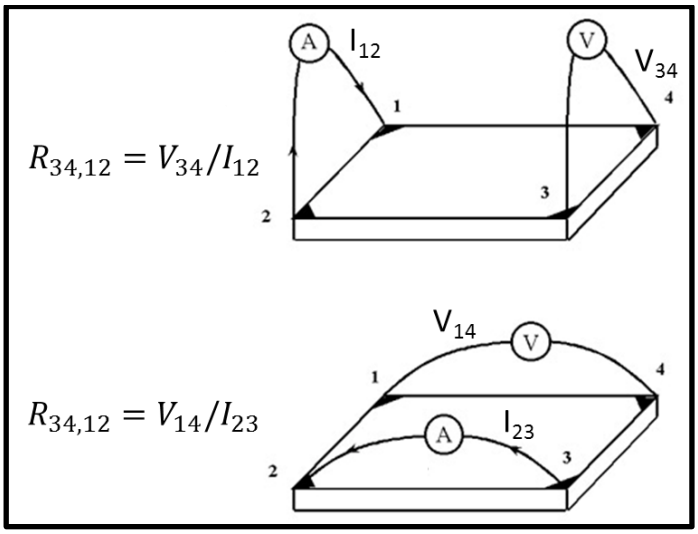

Figure 37 Geometrical configurations of resistances measurements in Van der Pauw geometry

Carrier concentrations were measured by Hall effect under a magnetic field at 0.5T. In addition, high magnetic field (9T) measurements were also performed using another Hall effect measurement set up based on a DRYICEVTI Cryogen Free Top Loading 9T System from ICEoxford Ltd. In both setup, applied current was 0.1 mA. The relation between carrier concentration and experimental measurement is:

$$\boldsymbol{n = \frac{IB}{teV_H}} \quad (38)$$

with I is the applied current, B the applied magnetic field, t the thickness of the film and V_H the Hall voltage. Mobility is deduced by the following relation:

$$\boldsymbol{\sigma = ne\mu \leftrightarrow \mu = \frac{\sigma}{ne}} \quad (39)$$

where μ is the mobility, n the carrier concentration and σ the electrical conductivity measured without magnetic field. At high magnetic field, Hall resistance (R_H) was measured by varying

the magnetic field (from -9T to 9T): $R_H = \frac{V_H}{I} = \frac{B}{nte}$. The carrier concentration was extracted from the slope $\frac{1}{nte}$ of the curve.

Thermoelectric measurements were done by « homemade » Seebek effect measurements setup. A gradient of temperature is applied through square samples (≈ 5mm*5mm) by heating (T_1) and cooling (T_2) opposite faces of the samples ($\Delta T=T_1-T_2$). Electrical potential (ΔV) is measured on each opposite face and Seebeck coefficient is extracted by calculating the slope of the plot ΔV versus ΔT (Equation (4)).

II.2.5 Optical measurements

Transmittance and reflectance were done with a Perkin Elmer Elmer Lambda 950 UV-Visible-NearIR spectrometer. The wide wavelength spectrum is covered by a Deuterium (UV)/ Tungsten (Vis) lamp and a photomultipIier (UV-Vis)/InGaAs (NIR) detector. The set-up uses an integratting sphere in order to collect the diffuse light transmittance and reflectance from the sample. In Figure 38, we give an example of transmittance and reflectance measurements with this spectrometer.

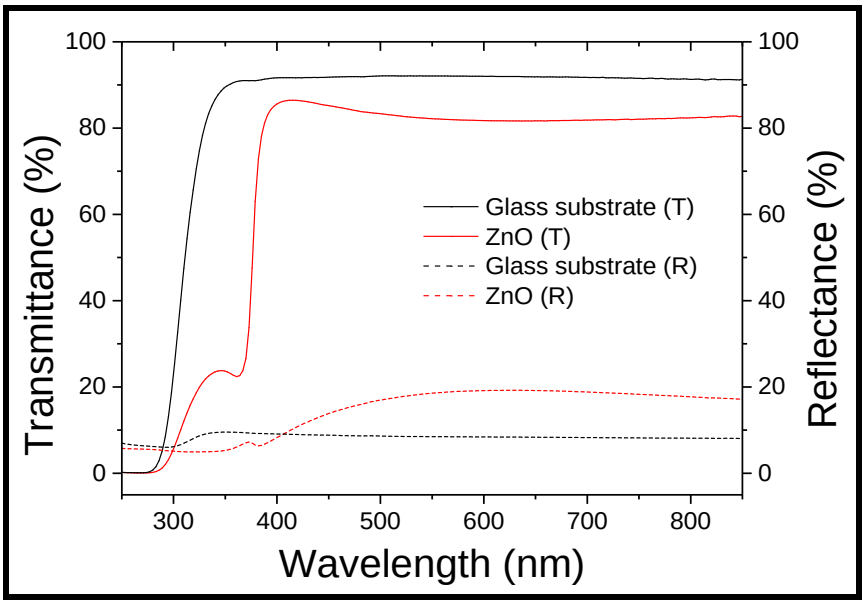

Figure 38 Transmittance and reflectance of glass substrate and ZnO thin film synthesized by MOCVD

III. OPTICAL MODEL DEVELOPMENT

In this chapter, we describe a new method that we have developed during this thesis, for calculating the absorption coefficient with an analytical approach (instead of standard numerical calculations) in a multiple reflections model. Although Vargas et al. developed a similar method with analytical approach[249], we proposed another way to obtain the exact formula of absorption coefficient.

Absorption coefficient was calculated assuming non-coherent film (with a thickness d) with multiple reflections inside the thin-film and a non-absorbing substrate (Figure 39). Then transmittance T, and reflectance R, are expressed as:

$$\boldsymbol{T = \frac{I_t}{I_0} = \frac{I_0(1-r)^2 e^{-\alpha d} + I_0(1-r)^2 r^2 e^{-3\alpha d} + \cdots}{I_0} = \frac{(1-r)^2 e^{-\alpha d}}{1 - r^2 e^{-2\alpha d}}} \quad (40)$$

$$\boldsymbol{R = \frac{I_r}{I_0} = \frac{rI_0 + I_0 r(1-r)^2 e^{-2\alpha d} + I_0 r^3 (1-r)^2 e^{-4\alpha d} + \cdots}{I_0}} = \boldsymbol{r + \frac{(1-r)^2 r e^{-2\alpha d}}{1 - r^2 e^{-2\alpha d}}} \quad (41)$$

where r is the reflectance of a simple air/film interface and α is the absorption coefficient of the film.

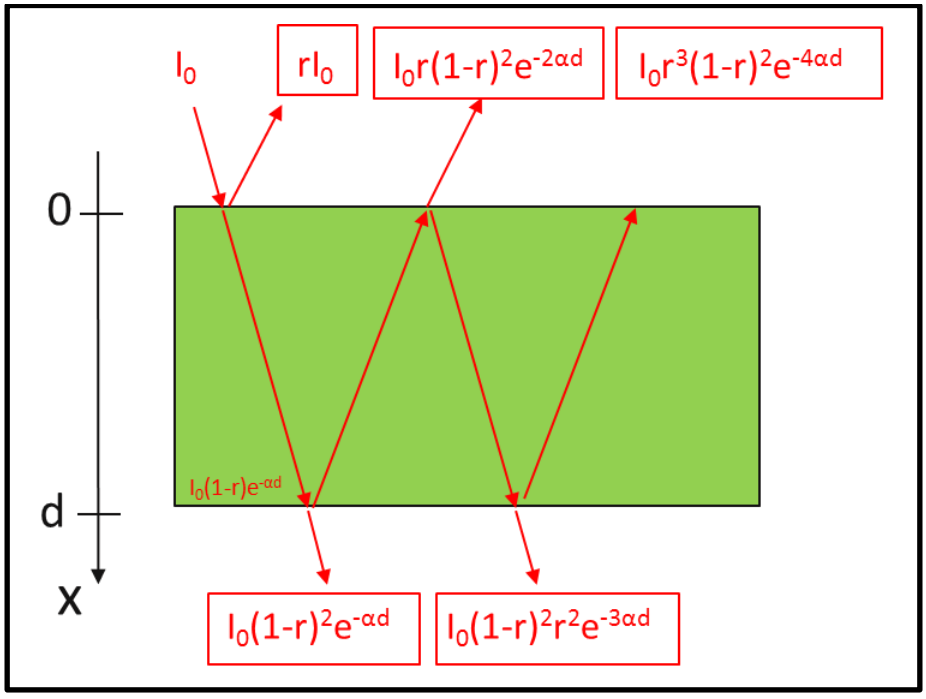

Figure 39 Schematic representation of multiple reflexions inside a film without any substrate

With Equation (40) and Equation (41), absorption coefficient α is usually calculated using standard numerical approach. During this thesis, we develop an analytic approach and propose an exact equation to determine analytically the absorption coefficient.

Indeed Equation (40) and Equation (41) are two equations with two unknown parameters (r and α), so the system can be resolved mathematically. Equation (41) can be expressed as:

$$\boldsymbol{R = r + rTe^{-\alpha d} = r\left(1 + Te^{-\alpha d}\right)} \quad (42)$$

Thus, the unknown parameter r is defined as:

$$\boldsymbol{r = \frac{R}{1 + Te^{-\alpha d}}} \quad (43)$$

When r is substituted by Equation (43) in Equation (40), the following equation appear:

$$\boldsymbol{T^2e^{-3\alpha d} + (2T - 2RT - T^3 + TR^2)e^{-2\alpha d} + ((1 - R)^2 - 2T^2)e^{-\alpha d} - T = 0} \quad (44)$$

If we write: $X = e^{-\alpha d}$, Equation (44) becomes:

$$\boldsymbol{X^3T^2 + X^2(2T - 2RT - T^3 + TR^2) + ((1 - R)^2 - 2T^2)X - T = 0} \quad (45)$$

Therefore, Equation (45) is a cubic equation with $X = e^{-\alpha d}$ as unknown. Equation (45) can be resolved analytically by Cardan's method[250] . The exact solution is:

$$\boldsymbol{X = 2\sqrt{\frac{-p}{3}}\cos\left(\frac{1}{3}\arccos\left(\frac{-q}{2}\sqrt{\frac{27}{-p^3}}\right)\right) - \frac{b}{3a}} \quad (46)$$

where :

$$\boldsymbol{p = -\frac{b^2}{3a^2} + \frac{c}{a}} \quad (47)$$

and :

$$\boldsymbol{q = \frac{b}{27a}\left(\frac{2b^2}{a^2} - \frac{9c}{a}\right) + \frac{d}{a}} \quad (48)$$

with:

$$\boldsymbol{a = T^2} \quad (49)$$

$$\boldsymbol{b = (2T - 2RT - T^3 + TR^2)} \quad (50)$$

$$\boldsymbol{c = (1 - R)^2 - 2T^2} \quad (51)$$

$$\boldsymbol{d = -T} \quad (52)$$

Finally, absorption coefficient α is defined as:

$$\alpha = \frac{1}{d}\ln\left(\frac{1}{2\sqrt{\frac{-p}{3}}\cos\left(\frac{1}{3}\arccos\left(\frac{-q}{2}\sqrt{\frac{27}{-p^3}}\right)\right) - \frac{b}{3a}}\right) \quad (53)$$

Absorption coefficient α calculated with Equation (53), is compared to a numerical resolution of the system (performed by Germain Rey) of Equation (40) and Equation (41) on a $CuCrO_2$ thin film (Figure 40 (a)). It appears that our analytical resolution is in a very good agreement with the usual numerical approach (Figure 40 (b)).

Moreover, when multiple reflexions are not taking into account, absorption coefficient is negative (which does not have physical sense) at low photon energy (Figure 40 (a)). The use of multiple reflexions model is fundamental to determine accurate values of α with enough precision on a large wavelength spectrum.

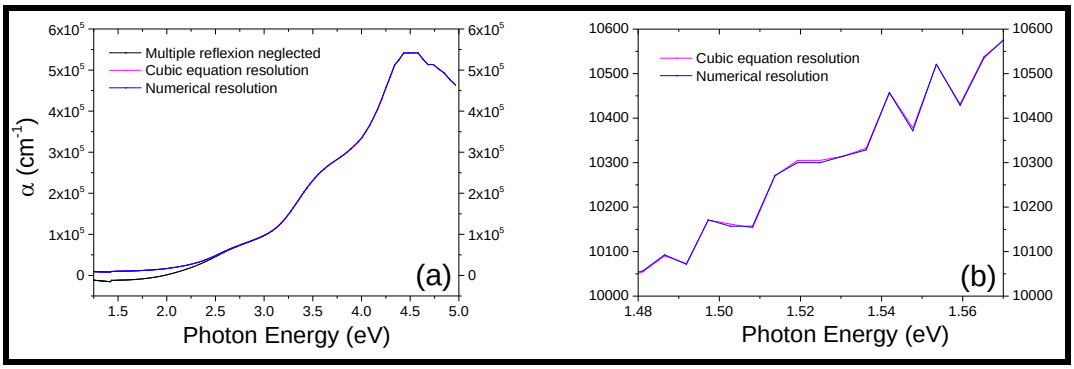

Figure 40 (a) and (b) Absorption coefficient calculated by analytical and numerical method

IV. CVD SYNTHESIS AND STRUCTURAL PROPERTIES

In this chapter, we present our characterization results of delafossite $CuCrO_2$ thin films grown by pulsed injection MOCVD. The effect of the growth temperature, the precursor volume ratio and the oxygen partial pressure on structural properties of films are depicted. Electrical and optical properties of films are presented in the next chapter.

IV.1 Growth temperature

During this thesis, we work in a first phase on optimizing process (precursors concentration, N_2 flow through injectors, the height and the rotation of the substrate holder) to get homogeneous deposition on substrates without the formation of powders. Afterwards, these parameters were kept constant for studying the effect of the growth temperature (and also the effect of the precursor volume ratio and the oxygen partial pressure).

IV.1.1 Crystalline structure

The effect of the growth temperature on the crystallographic phases of films, deposited on glass substrate, was investigated keeping constant all other parameters (Table 6).We defined '$T_{surface}$' as the surface temperature of the glass substrate before deposition (measured with a thermocouple)

Table 6 Parameters used for studied the effect of growth temperature

$T_{surface}$ (°C)	P_{total} (mbar)	P_{O2} (mbar)	χ	$C_{prec.}$ (10^{-3} mol.L^{-1})	$Flow_{prec.}$ (g.min^{-1})	N_2 carrier (sccm)	Height (cm)	Rotation (rpm)
310	6	2.1	0.33	5	1	350	16	15
350	6	2.1	0.33	5	1	350	16	15
370	6	2.1	0.33	5	1	350	16	15
410	6	2.1	0.33	5	1	350	16	15

The obtained diffractograms are displayed in Figure 41. According to the International Center for Diffraction Data (ICDD) (pdf n°04-010-3330), films obtained at $T_{surface}$=310°C and $T_{surface}$=370°C present a pure rhombohedral delafossite structure belonging to the $R\bar{3}m$ space group. The evaluation of the relative intensity of the diffracted peaks shows the most intense peak is (012) (2θ=36.4°), in the grazing incidence x-ray diffraction (GIXRD) configuration, with an increasing (006) peak intensity (2θ=31.5°) for deposition temperatures above 370°C. Films deposited at $T_{surface}$=410°C are characterized by the presence of Cu_2O and CuO phases (arrows in Figure 41). It is worth noticing that pure delafossite structure is grown at low

temperature, $T_{surface}$=310°C, and without any additional annealing step. This is a particularly attractive feature of the deposition process studied during this thesis.

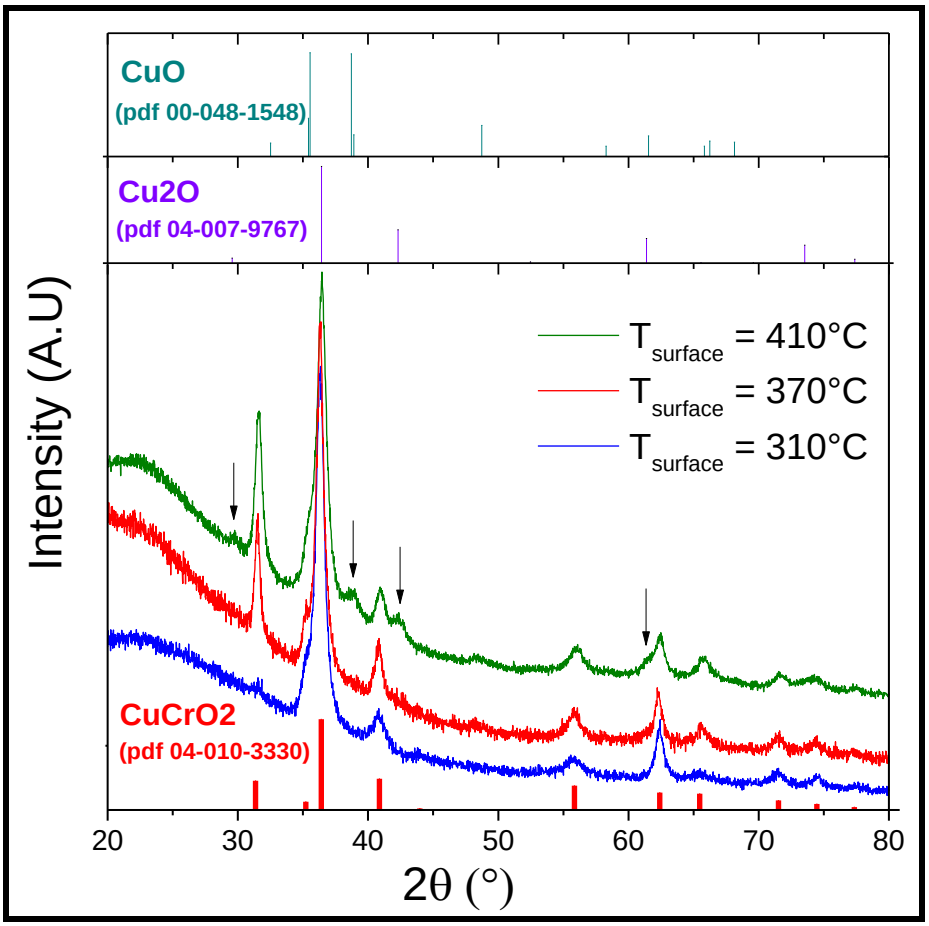

Figure 41 GIXRD diffractograms of films deposited at growth temperature of $T_{surface}$= 310, 370 and 410 °C and using a precursor volume ratio χ = 0.33. Bottom and top diagrams represent the expected peaks for the corresponding phases, according to the ICDD cards given on the figure.

IV.1.2 Morphology

The morphology of films is granular as shown by the SEM top-of-view pictures in Figure 42 (a), (b) and (c), for $T_{surface}$=310°C, 370°C and 410°C respectively. This morphology points also out the polycrystalline nature of films as observed by XRD. A granular aspect is also observed in films with SEM cross-section images (Figure 43). The films at $T_{surface}$=350°C (Figure 43 (a)) seems more dense than 370°C (Figure 43 (b)), while films at $T_{surface}$=410°C (Figure 43 (c)) have a more elongated and compacted grains morphology, may be due to the presence of copper oxide phases in the film.

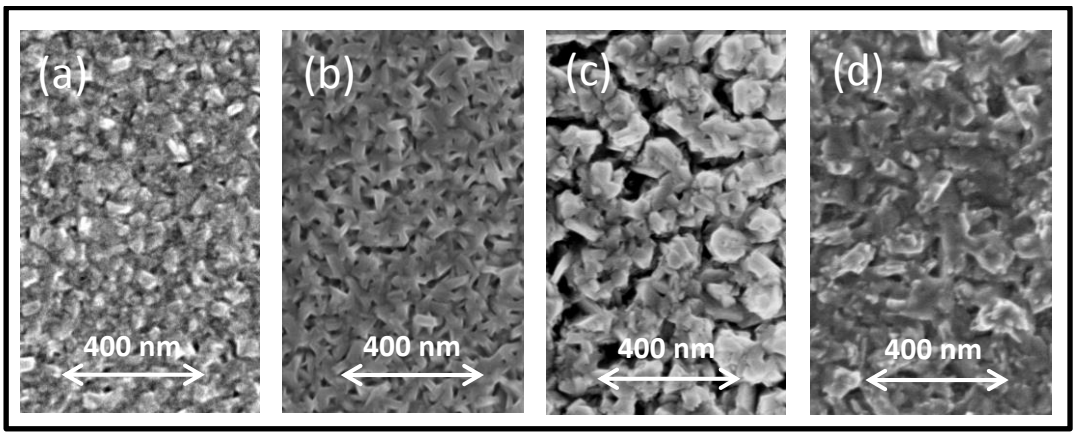

Figure 42 SEM top view images of (a) $T_{surface}$=310°C, (b) $T_{surface}$=350°C, (c) $T_{surface}$=370°C and (d) $T_{surface}$=410°C

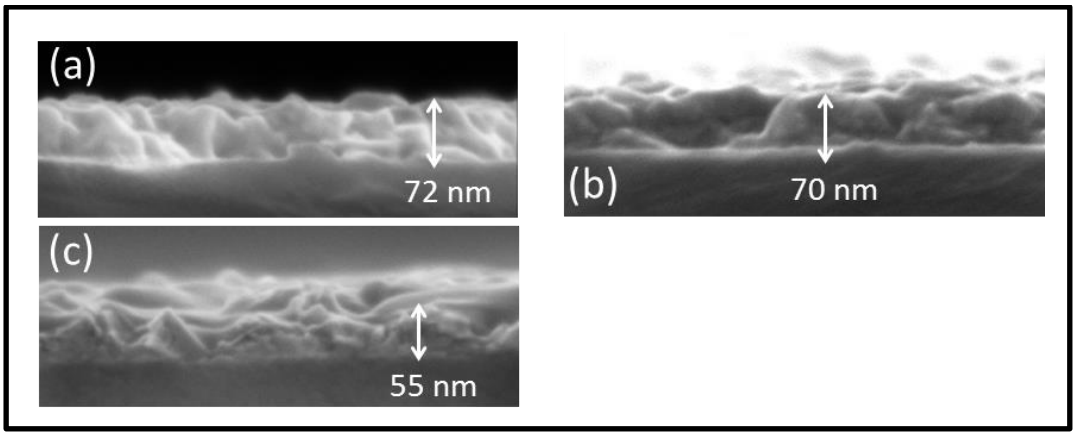

Figure 43 SEM cross-section images of (a) $T_{surface}$=350°C, (b) $T_{surface}$=370°C and (c) $T_{surface}$=410°C

IV.1.3 Chemical composition

Chemical quantification was done by XPS for $T_{surface}$=350°C, 370°C and 410°C (Figure 44). It was observed that thin films with delafossite structure ($T_{surface}$=350°C and 370°C), have an excess of chromium with a ratio Cu/Cr of 0.5-0.6 and a stoichiometric composition of oxygen (O=50%). When copper oxide phases appear in the films ($T_{surface}$=410°C), the ratio Cu/Cr is 1.1, meaning an increasing copper concentration in the film due to the contribution of copper from copper oxide phases. The oxygen composition also decreases (46%), due to Cu_2O phase in $CuCrO_2$ films (Figure 41). While in $CuCrO_2$, two oxygen atoms contribute to the chemical composition (50% in stoichiometric $CuCrO_2$), only one oxygen atom in Cu_2O contribute to the chemical composition. Then, the presence of Cu_2O in $CuCrO_2$ thin films tends to decrease oxygen composition determined with XPS

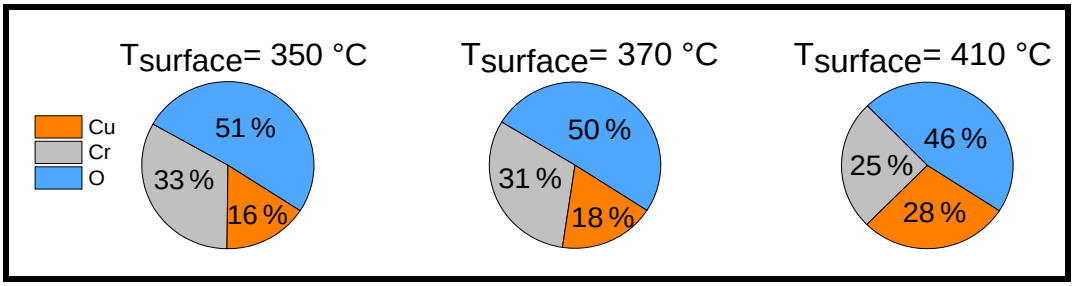

Figure 44 Chemical composition of $T_{surface}$=350, 370 and 410°C

We precise the observed phase for $T_{surface}$=350°C and 370°C is not the spinel phase $CuCr_2O_4$, as it was questioned in recent works on $CuCrO_2$ thin films synthesized by CVD[131], [132]. All diffractions peaks are attributed of $CuCrO_2$ phase and the chemical composition Cu:Cr:O is not 1:2:4.

IV.2 Precursor volume ratio

IV.2.1 Crystalline structure

The impact of the precursor volume ratio ($\chi=V_{Cu(thd)2}/(V_{Cr(thd)3}+V_{Cu(thd)2})$) was investigated at the growth temperature of $T_{surface}$=370°C (Table 7), temperature that promotes the growth of compact and continuous thin films of a pure $CuCrO_2$ delafossite phase (Figure 41)

Table 7 Parameters used for studied the effect of precursor volume ratio χ

$T_{surface}$ (°C)	P_{total} (mbar)	P_{O2} (mbar)	χ	$C_{prec.}$ (10^{-3} mol.L^{-1})	$Flow_{prec.}$ (g.min^{-1})	N_2 carrier (sccm)	Height (cm)	Rotation (rpm)
370	6	2.1	**0**	5	1	350	16	15
370	6	2.1	**0.2**	5	1	350	16	15
370	6	2.1	**0.33**	5	1	350	16	15
370	6	2.1	**0.5**	5	1	350	16	15
370	6	2.1	**0.6**	5	1	350	16	15
370	6	2.1	**0.66**	5	1	350	16	15
370	6	2.1	**0.8**	5	1	350	16	15
370	6	2.1	**1**	5	1	350	16	15

The XRD diffractograms of films deposited at various values of χ are depicted in Figure 45. Pure delafossite thin films are grown for $0.2 \leq \chi \leq 0.6$, while CuO and Cu_2O phases are

evidenced for $\chi \geq 0.66$ (highlighted by the arrows Figure 45). The Cu_2O phase is detected when the deposition was carried out with a precursor solution featuring χ=1, with a small signature of Cu metal at 2θ=43.5°. The amorphous background between 20-30° disappear with a precursor ratio of χ=1, because the film is more crystalline and thicker than the others films. It is worth noting that no film is grown at $\chi = 0$ (i.e. when only $Cr(thd)_3$ is used for deposition) and that excess of chromium precursor in the precursor solution does not lead to chromium oxide phases. Thus, deposition temperatures below $T_{surface}$=410°C and with copper fraction $\chi <$ 0.66 are necessary to avoid the formation of parasitic crystalline phases such as CuO and Cu_2O.

For pure delafossite thin films, the extracted lattice parameter "c" along the (006) direction, from the XRD results, is between 17.05 and 17.06 Å (±0.02 Å). It is slightly below the reported values at 17.10 Å for the rhombohedral delafossite structure of $CuCrO_2$[108], [251]. The extracted parameter "a", along the (012) peak (parameter "c" is known from to (006) direction) is 2.98 ±0.02 Å and is in good agreement with the values reported for crystalline $CuCrO_2$ delafossite (2.97 Å) [24], [108], [251]. According to the crystalline parameters "a" and "c", our materials lattice seems slightly compressed along the "c" axis by 0.3%. Pure polycrystalline delafossite $CuCrO_2$ phase is grown with large process windows of precursor volume ratio and growth temperature. This further reinforces the suitability of our pulsed-injection-CVD process for growing $CuCrO_2$ coatings over large area in an industrial perspective.

IV.2.2 Morphology

IV.2.2.1 SEM analysis

The surface SEM inspection (Figure 46) indicates that the morphology of the pure delafossite phase is strongly influenced by the relative precursor volume ratio χ. For χ=0.2, the as deposited films present a "spines" morphology, while for the χ=0.33 and χ=0.6, a grainy structure is observed. Films are more compact and the grain size, as observed on SEM pictures, decreases when the ratio χ increases. As measured from the SEM pictures, the average grain size is (160 ± 60) nm for χ=0.33, while (56 ± 27) nm is determined for χ=0.6. The thin-films thicknesses measured from cross-section SEM observations are 120, 140 and 160nm for χ=0.2, 0.33 and 0.6, respectively. A continuous closely packed thin film is obtained for a Cu-rich precursor solution (χ=0.6).

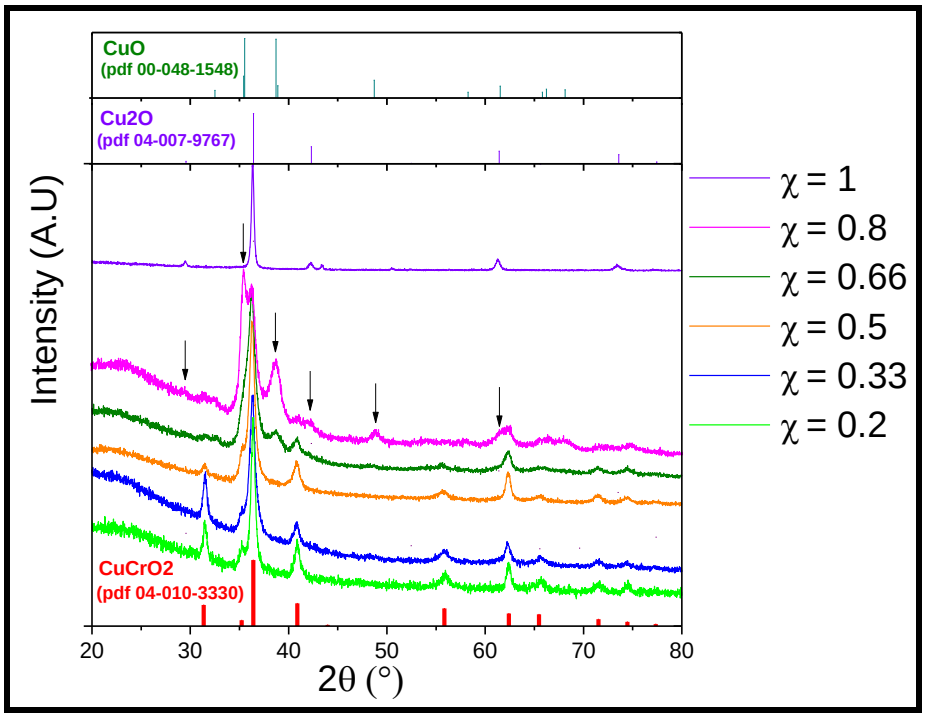

Figure 45 Influence of the precursor volume ratio χ on the crystallographic structure of the obtained films at $T_{surface}$=370°C. Bottom and top diagrams represent the expected peaks for the corresponding phases, according to the ICDD cards given on the figure

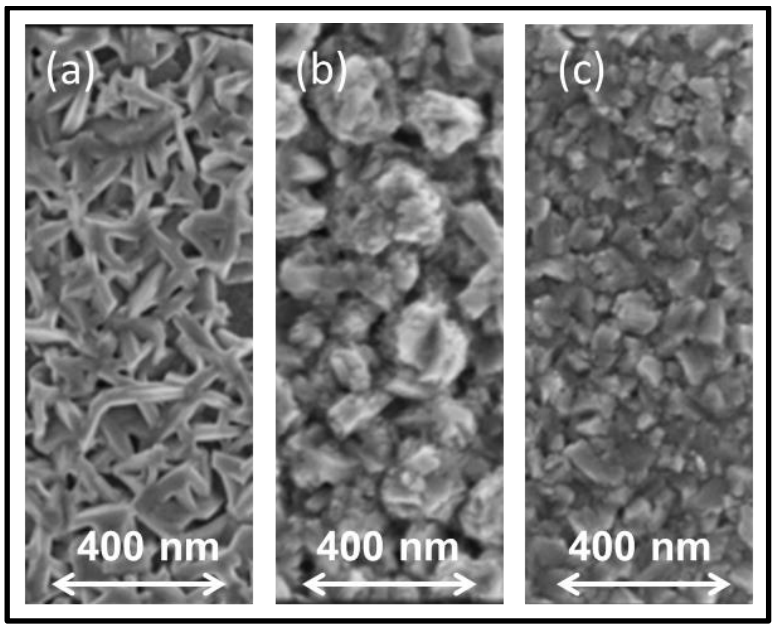

Figure 46 SEM micrographs for films deposited at $T_{surface}$=370°C and (a) χ=0.2, (b) χ=0.33 and (c) χ=0.6

The crystallites size extracted from the Equation (31) for (012) and (110) diffraction peaks (Figure 47 (a) and Figure 47 (b)) are larger for χ=0.2, 14 nm and 23 nm respectively. For higher ratio, the size is almost constant and the values are 9.5 nm and 15 nm respectively. The

difference of crystallite sizes between χ=0.2 and $0.33 \leq \chi \leq 0.6$ is aligned with the morphological observations (Figure 46) which shows bigger grains for "spines" than granular thin films. However, the microstrain extracted from the Equation (32) for (012) and (110) diffraction peaks (Figure 47 (a)-(b)), is also higher for χ=0.2, approximately 0.25%, while being 0.13% for $0.33 \leq \chi \leq 0.6$. Spines morphology has more lattice distortion than granular morphology, while the influence of the peculiar chemical composition in films cannot be excluded.

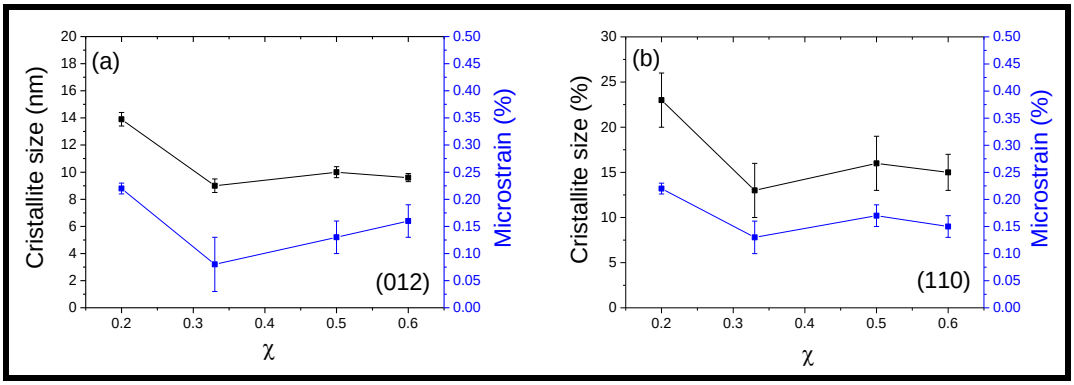

Figure 47 Crystallite size and microstrain of $0.2 \leq \chi \leq 0.6$ extracted from (a) (110) and (b) (110) diffraction peaks

IV.2.2.2 Transmission electron microscopy (TEM) analysis

The thin film grown with a ratio of precursors χ=0.33 was observed by TEM. In Figure 48, we show the chemical mapping of $CuCrO_2$ with high angle annular dark field (HAADF) analysis, which is a TEM scanning method. The contrast in Figure 48 (a) is due to the weight of atoms: the darker is the image, the lighter are the atoms. We observed in Figure 48 (b), (c) and (d) a relative homogeneous spatial chemical composition inside grains, especially for the chromium in our $CuCrO_2$ films.

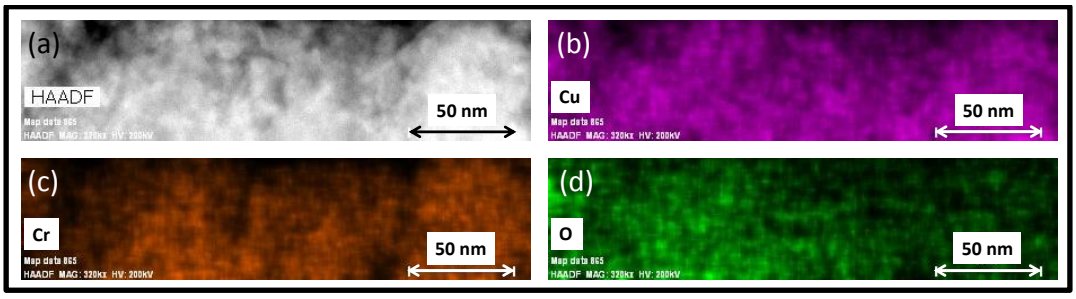

Figure 48 (a) HAADF analysis in a region of $CuCrO_2$ thin film (χ=0.33) (weight atoms contrast) (b) copper (c) chromium and (d) oxygen composition in film, with HAADF images superposed on energy dispersive x-ray spectroscopy (EDX) mapping

Selected area electron diffraction (SAED) analysis of another $CuCrO_2$ region of the same thin-film is presented Figure 49 (a). We identify diffracting planes (006), (104) and (202) of crystallites (according to pdf 04-010-330 of ICCD). We observed a lack of rings for diffracting planes, which would appear for poly-crystallites oriented randomly. The spots in SAED analysis indicate a textured structure, still meaning some preferred crystallographic orientations rather than a fully randomized orientation of diffracting crystallites. Finally, we show in Figure 49 (b) a HRTEM picture of a $CuCrO_2$ region (χ=0.33). The distance measured between lattice fringes are 2.8 and 1.4-1.6 Å which are attributed to (006) and (110) diffraction plans (oriented parallel to the picture). The crystallite size measured for the (110) diffraction (on the image in Figure 49 (b)) is 11 nm which is in line with the average crystallite size as extracted from the XRD measurement (Figure 47 (b)). We also notice in Figure 49 (b) that the two (006) crystallites are similarly oriented with regard the picture plan and (110) crystallites also feature this textured orientation.

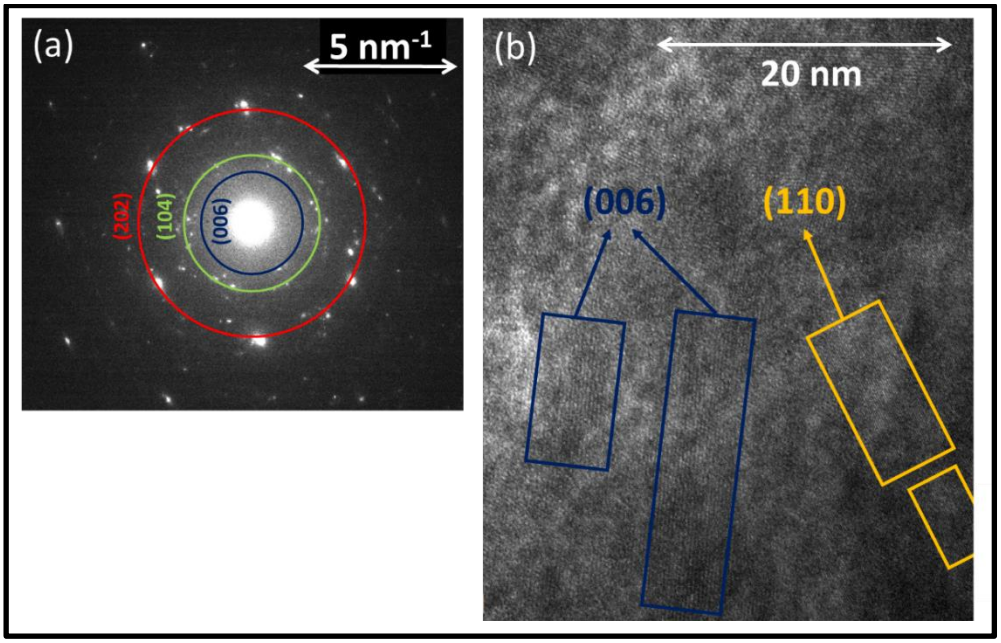

Figure 49 (a) SAED of a region of $CuCrO_2$ thin film (χ=0.33) and (b) HRTEM picture of another region

IV.2.3 Chemical composition

IV.2.3.1 XPS

Chemical composition of the grown films on glass substrates was studied by *ex-situ* XPS analysis and is given in Figure 50. For pure delafossite films ($0.2 \leq \chi \leq 0.6$), an over-

stoichiometric concentration of chromium is measured in the films even for $\chi > 0.5$ corresponding to a Cu-rich solution of precursors. It is reminded that no specific crystalline phase of chromium compound (except $CuCrO_2$) is detected by XRD in these cases. For $\chi > 0.66$, an excess of copper concentration is evident and is well in line with the concomitant detection of copper oxides phases. The graph inset in Figure 50, shows the percentage of copper and chromium in films with pure phase delafossite for the different precursor ratios investigated in our study. It appears that the relative deficiency of copper in the films is mainly counter balanced by an excess of chromium in $CuCrO_2$ thin-films. The oxygen concentration close to the stoichiometric value of 50% is also a specific feature of our thin-films when compared to the optimized thin-films reported by Farrell et al[131] . In their case, an excess of oxygen was observed (63%) for the optimum stoichiometry of $Cu_{0,4}CrO_{2,5}$. It is also noticed the trend of Cu/(Cu+Cr) for pure delafossite $CuCrO_2$ phase (green dash line in Figure (51)) is similar to the opposite trend of microstrain as a function of precursor ratio χ (Figure 47 (a) and (b)). It is perhaps due to the impact of chromium excess on the $CuCrO_2$ lattice: more chromium excess is introduce in the lattice, more distortions of lattice are observed.

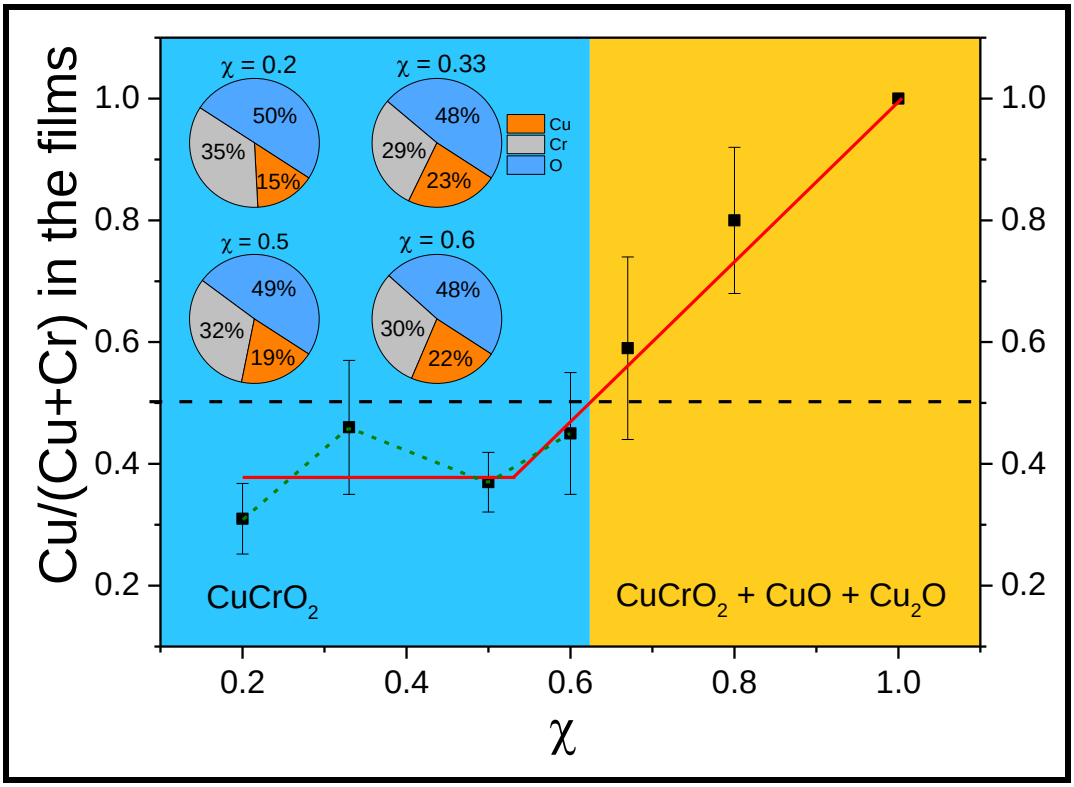

Figure 50 Chemical composition of films growth at $T_{surface}$=370 °C with precursor ratio featuring $0.2 \leq \chi \leq 0.8$ as measured with XPS

Considering the growth rate (Figure 51) of our films versus the ratio of precursors, thin-films are grown only when the Cu precursor is present. As previously stated, a precursor solution of pure $Cr(thd)_3$ does not lead to any film growth in the process conditions that have been investigated in our study. Interestingly, the growth rate increases almost linearly from 0 to 1 nm/min when the Cu concentration is incrementally increased from $\chi=0$ to $\chi=1$. Moreover, in the range where only $CuCrO_2$ polycrystalline phase is evidenced by XRD, the chemical concentration of Cr is almost stable while the growth rate is definitely increasing. We assume that Cu precursor or Cu-byproducts catalyse the thermal decomposition of $Cr(thd)_3$ and the growth reaction of Cr with Cu and oxygen to grow $CuCrO_2$.

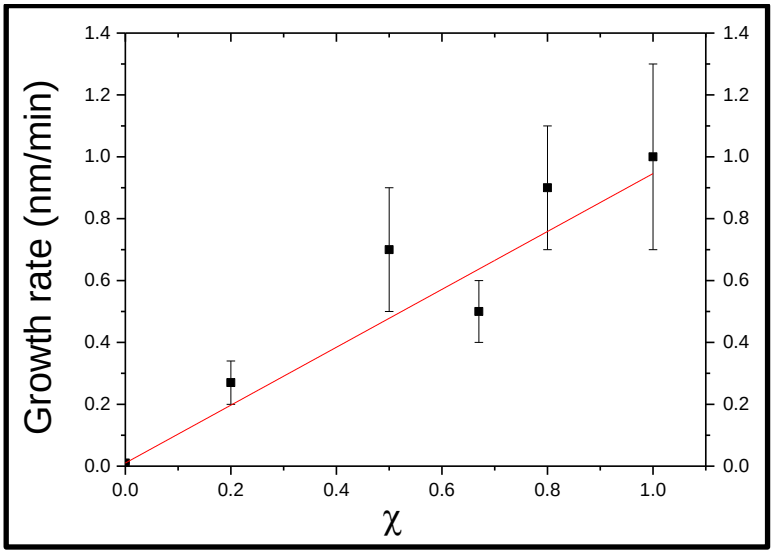

Figure 51 Growth rate at $T_{surface}$=370 °C with precursor volume ratio featuring $0 \leq \chi \leq 1$

We investigate the chemical environment of Cu and Cr in our pure $CuCrO_2$ delafossite thin films by detailed analysis of the XPS spectra. The XPS spectra of the deposited film with $\chi=0.5$ are shown in Figure 52 before (top surface analysis) and after surface cleaning with the use of *in situ* argon ion beam (inside the analysis chamber). While C1s peak is observed for the top-surface analysis of our thin-films, no carbon is detected anymore after the surface cleaning. Top-surface carbon contaminations are attributed to the exposure of our samples to the ambient air and correspond to organic residues on the sample surface. Carbon concentration in our thin-films is below 1at.%, (detection limit of the XPS analysis) highlighting the efficient surface reaction of our metal organic precursors and the fast removal of the carbonated by-products.

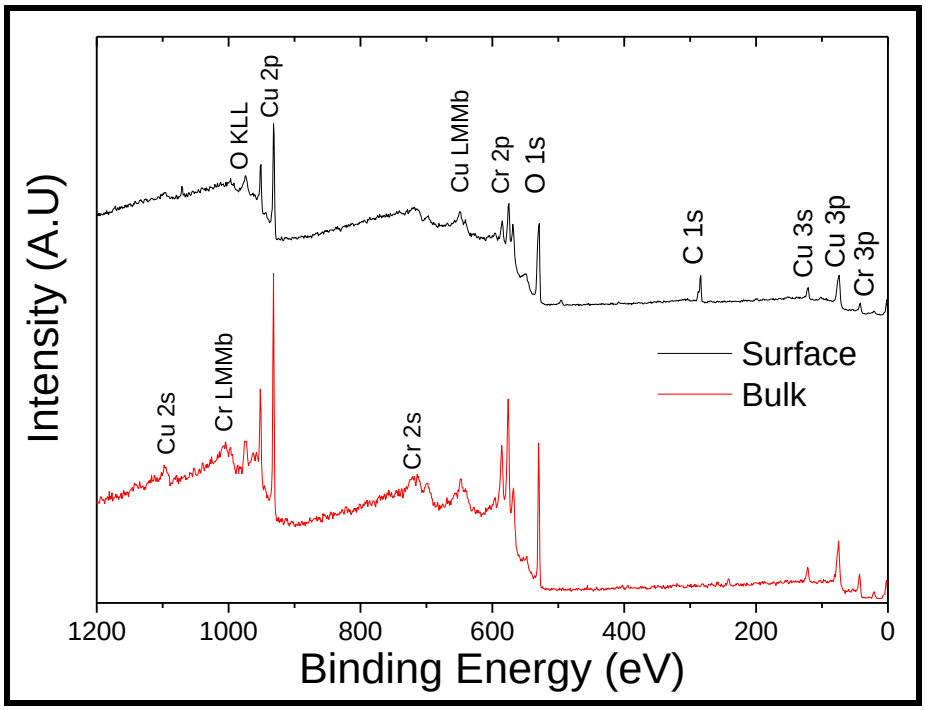

Figure 52 XPS spectrum, before and after surface cleaning, of the chromium copper oxide films grown with χ=0.5

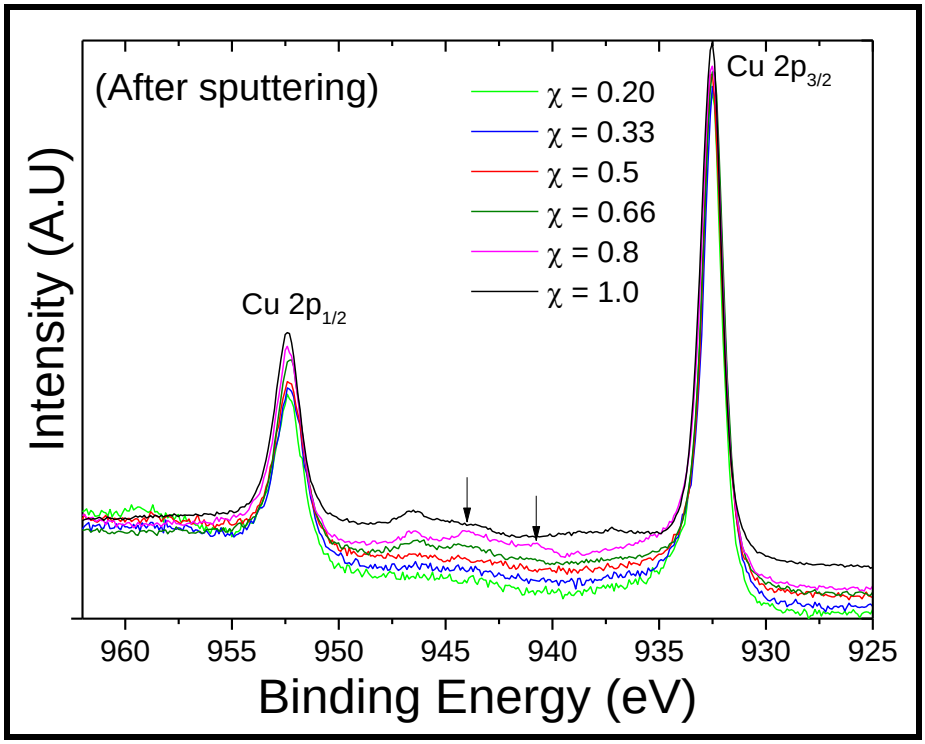

Figure 53 High resolution Cu 2p XPS scans for films grown at $T_{surface}$=370°C with $0.2 \leq \chi \leq 0.6$

Cu 2p spectra after sputtering for films deposited with various ratios ($0.20 \leq \chi \leq 1.0$) are depicted in Figure 53. All spectra are normalized to the Cu $2p_{3/2}$ peak intensity. The XPS spectrum shows Cu $2p_{1/2}$ at (952.4±0.1) eV and Cu $2p_{3/2}$ at (932.5±0.1) eV, providing a spin orbit splitting energy in good agreement with the reported data in the literature for $CuCrO_2$ phases, i.e. $\Delta_{Cu\ 2p}$=19.9±0.2 eV[252] for all ratios χ. One may remember that the determination of the oxidation state of Cu based on the fine analysis of Cu 2p, is almost impossible when considering Cu^0 and Cu^{+I} oxidation state, because both peaks are too closer to be distinguished by XPS instrument. We also observed, for χ =0.8, features at 944.0 eV and 940.8 eV (arrow in Figure 53), and a Cu $2p_{3/2}$ peak broader in the high energy range. These features indicate the presence of Cu^{+II} [253] for χ =0.8, as confirmed by XRD analysis highlighting the CuO phase.

Cr 2p XPS spectra after sputtering of $0.2 \leq \chi \leq 0.6$, are depicted Figure 54 (a). All films exhibit Cr $2p_{1/2}$ and Cr $2p_{3/2}$ peaks at the same binding energies, i.e. 582.2 eV ± 0.1 eV and 576.6 ± 0.1 eV respectively, which correspond to the (+III) oxidation state of Cr[252]. Interestingly, in the same range of energies, Cu Auger peak (Cu LMM) is detected. Cu LMM peak is centered at 569.9±0.2 eV when delafossite phase is contaminated by the presence of copper oxide phases ($0.66 \leq \chi \leq 1$), while the Cu LMM peak is 568.8±0.1 eV, for the pure delafossite phase (χ <0.66). The reference spectra of CuO (Cu^{+II}), Cu_2O (Cu^{+I}) and Cu (Cu^0) were also measured on the same instrument and using the same protocol[i]. The reference peaks of Cu are used for comparison of the Cu LMM peak obtained in the case of pure delafossite phase (as shown by the XRD measurements) i.e. χ=0.5. As depicted in Figure 54 (b), the Cu LMM peak is mainly due to the contribution of two oxidation states of copper, namely Cu^0 and Cu^{+I} Interestingly, Arnold et al [118] analyzed the Cu LMM peak (with Cr 2p peaks) of stoichiometric $CuCrO_2$, and they observed only a Cu^I contribution. Knowing that our delafossite $CuCrO_2$ thin-films are Cr-rich (Cu:20% and Cr:30%), we may attribute our specific Cu LMM signature to the influence of the excess of Cr (≈ +5%) which impacts the chemical environment of Cu atoms. It is worth reminding that the electronegativity of Cu being meaningfully higher than Cr (1.90 and 1.66 for Cu and Cr respectively[254]) , a close-proximity of excess Cr in interstitial site of O-Cu-O dumbbells would significantly impact the electronic configuration of Cu, in line with the observation of Cu^0 by XPS measurements.

[i] The shift of XPS and Auger peaks due to charging effect was not observed, because all samples were electrical conductor.

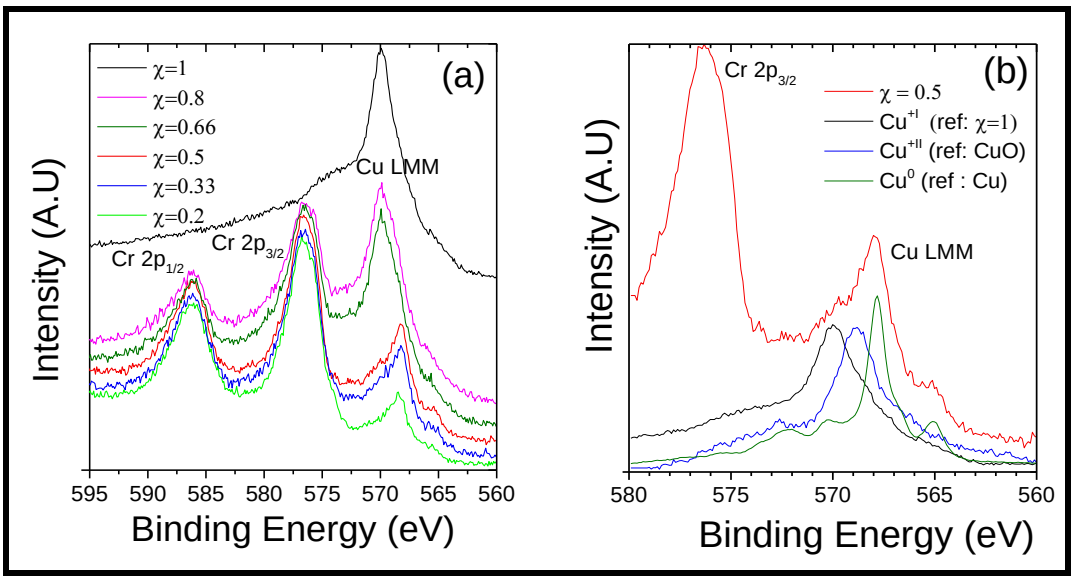

Figure 54 (a) High resolution Cr 2p and Cu LMM XPS scans for films grown at $T_{surface}$=370°C with $0.2 \leq \chi \leq 0.8$ (b) Cu LMM peak for χ=0.5 and Cu LMM peaks of copper oxidation sate Cu^0, Cu^I and Cu^{II}.

The quantifications of Cu oxidation states (0, +I and +II) were done by taking into account the weighting of reference peak in Figure 54 (b). The results are given in Table 8. It appears that Auger quantification on Cu LMM is not consistent with XPS analysis on Cu 2p. Indeed, Auger quantification gives Cu^{+II} as major contribution for $0.2 \leq \chi \leq 0.5$ while Cu^{+II} was not observed for this ratio (Figure 53). This inconsistency comes from the nature of the valence electron in Auger Cu LMM peak. The Auger notation is $L_3M_{45}M_{45}$, involving transitions of Auger electron from the Cu 3d valence level (Figure 55). Therefore, Cu LMM peak is highly sensitive to chemical environment of the bounding of Cu with neighboring atoms. Cu 2p peaks, involve core level and allow consistent chemical quantification.

Table 8 Chemical quantification of copper oxidation states on Cu LMM peak with $0.2 \leq \chi \leq 0.5$

χ	Cu^0 (%)	Cu^{+I} (%)	Cu^{+II} (%)
0.2	16	17	67
0.33	21	28	51
0.5	25	24	50

IV.2.4 Valence band

We investigated the energy profile of the valence band of pure delafossite thin films ($0.2 \leq \chi \leq 0.5$) with the Al Kα source beam of the XPS instrument. In first, the energy profile of the

valence band of copper metal and Cu_2O thin films (χ=1) were measured in order to validate our measurements protocols by comparing our results for Cu metal and Cu_2O with literature data.

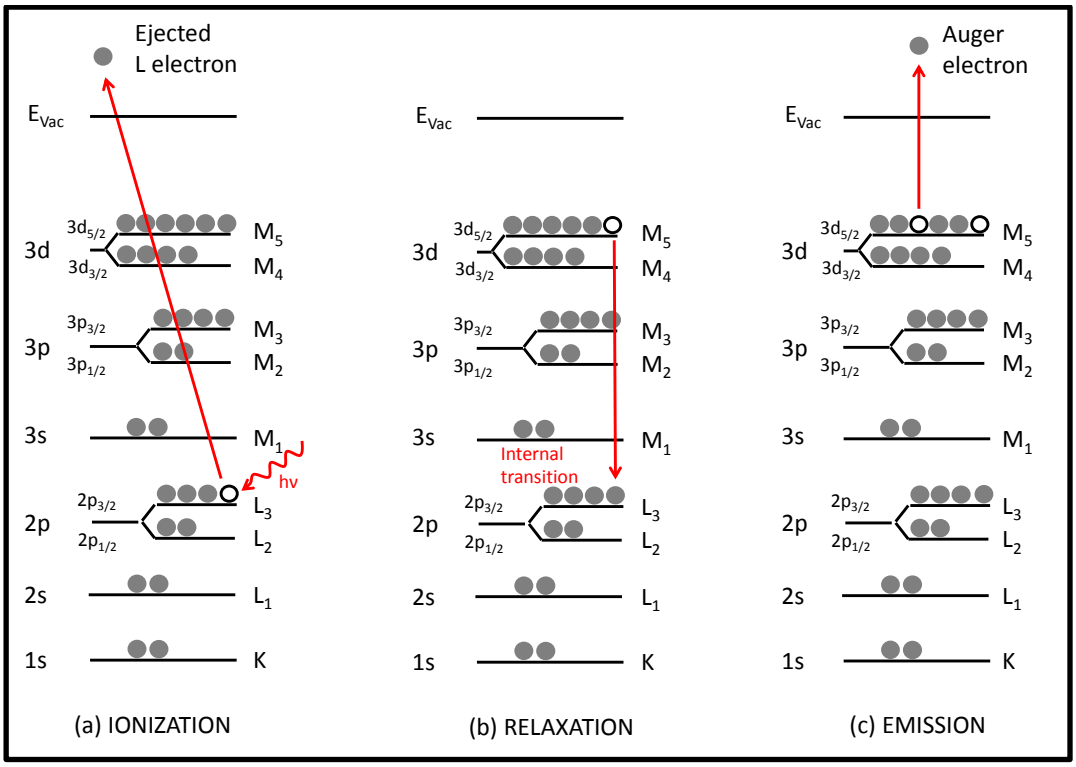

Figure 55 Auger electron transitions involving in Cu LMM for delafossite $CuCrO_2$ sample

Valence band of copper metal is presented Figure 56 (a); the intensity is the contribution of valence states in copper metal i.e. Cu 3d. The shape of valence band and the position of the most intense peak (2.6 eV) are in very good agreement with that reported in literature (Figure 56 (b)[255]).

Valence band of synthesized Cu_2O thin films (χ=1) is presented Figure 56 (c). We point-out that chemical quantification found by XPS showed a stoichiometric composition (Cu: 67% and O: 33%). For the Cu_2O sample, the measured binding energy profile of the valence band is the same as the ones reported into the literature. The energy profiles of Cu_2O and $CuCrO_2$ valence are similar when measured by XPS with source Al Kα (Figure 9(a)). Indeed, the cross section of electron ionization of Cu3d is 20x larger than the one of O2p and 10x larger than the one of Cr3d (when Al Kα excitation is used [81]). Furthermore, the chemical environment of Cu is almost identical (O-Cu-O) in Cu_2O and $CuCrO_2$ leading to bonding and anti-bonding energy states in the valence band of both materials. Therefore, XPS measurements with Al Kα source mainly show Cu3d states when the valence bands of Cu_2O and $CuCrO_2$ are probed.

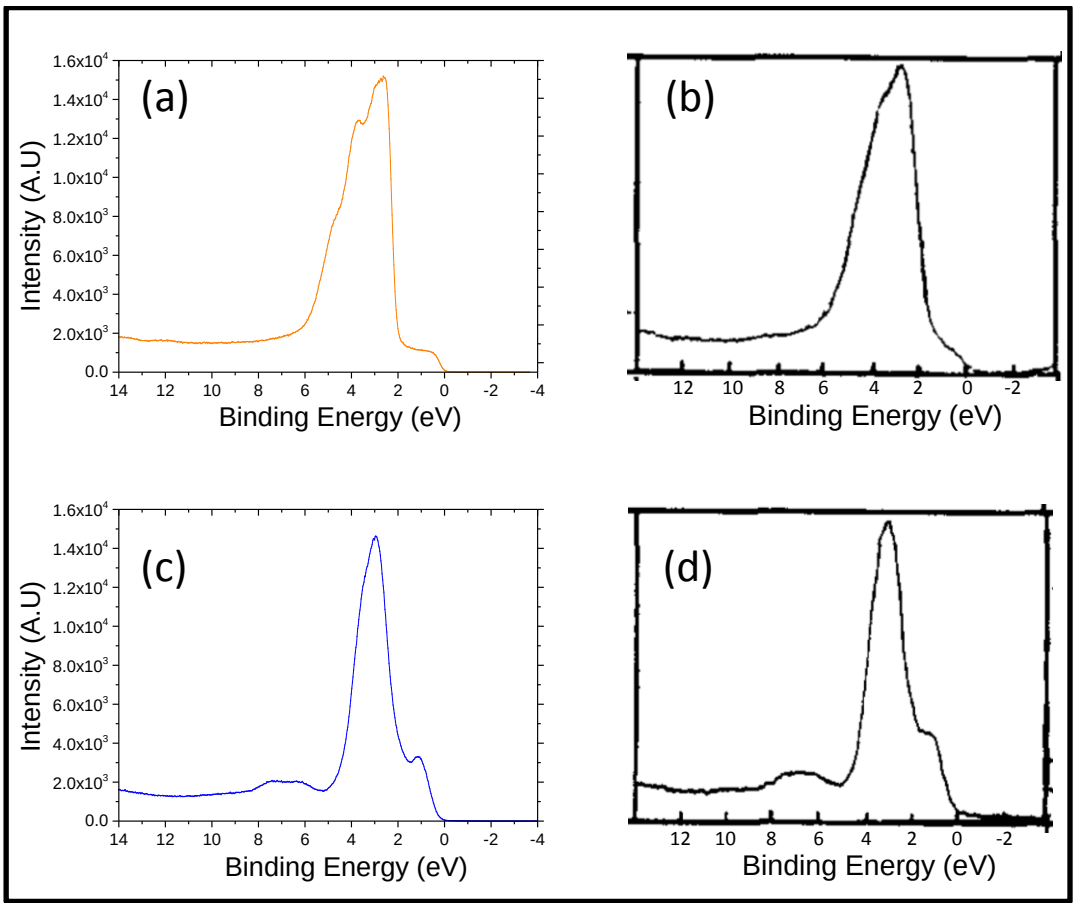

Figure 56 Measured valence bands under Al Kα excitation of (a) copper metal, (b) copper metal [255], (c) Cu_2O and (d) Cu_2O [255]

Energy profile of the valence band of our delafossite $CuCrO_2$ thin films ($0.2 \leq \chi \leq 0.5$) is shows Figure 57. The valence band profiles are very similar whatever the precursor ratio used to grow the $CuCrO_2$ thin films. The most intense peak is reported at 3.0-3.1eV which is in good agreement with the literature[18]. However, the valence band shapes are very different from the literature[18]. Indeed, the shoulder at 1.5 eV, corresponding to anti-bounding states between copper and oxygen (Figure 9), was not observed. Thus, we expect for our $CuCrO_2$ thin films, a lower contribution of the hybridized bounding states between oxygen and copper to the density-of-states of the valence band. This is in good agreement with the zero oxidation state of copper detected via XPS analysis in Figure 54. In stoichiometric delafossite $CuCrO_2$, Cu oxidation state is +I, then the valence states of copper is $(3d)^{10}$ which hybridized to $(3d)^9$ $(4s)^1$ when linear bounded to oxygen. In the case of $(Cu)^0$ oxidation state (which is evidenced in our case), the valence states of copper is $(3d)^{10}(4s)^1$ which is not favourable for a Cu 3d-4s hybridization with oxygen (because all orbitals of Cu 3d are fill by pair electrons and Cu 4s orbital is fill by one electron). The typical shoulder at 1.5 eV is absent maybe due to the lack of anti-bounding states between Cu^{+I} and O^{-II}. Another feature of the energy profile of the valence band of our samples

is the broader peak at 3-3.1 eV. In spite of the over-stoichiometry in Cr in our thin-films, the contribution of Cr atoms is not detected with our XPS setup. Due to the lack of Cu3d-O2p anti-bounding states, we may expect a disperse VBM and higher effective mass than the one of stoichiometric $CuCrO_2$ (Figure 2 (a) and Figure 9). Interestingly, X-Ray absorption spectroscopy and X-ray resonance photoemission could be extremely useful for determining the density of states at the VBM.

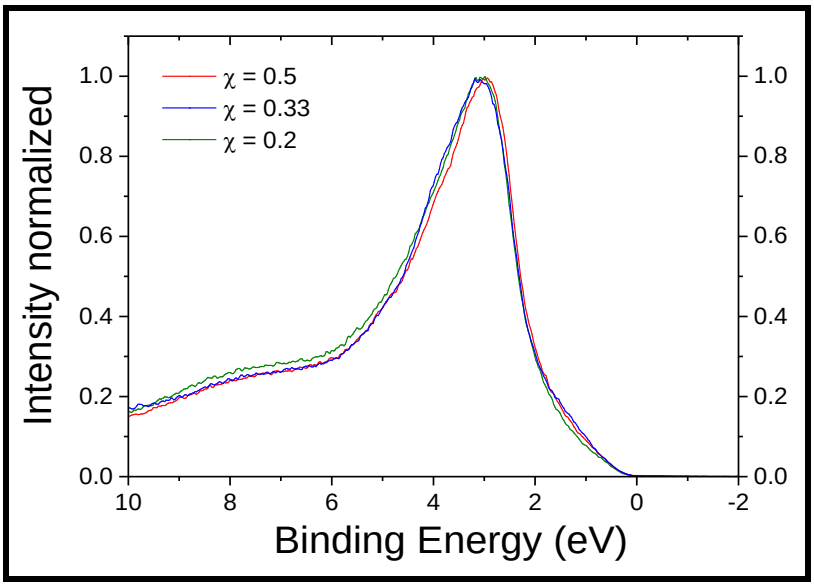

Figure 57 Measured valence bands of $CuCrO_2$ thin films with $0.2 \leq \chi \leq 0.5$

IV.3 Oxygen partial pressure

IV.3.1 Crystalline structure

The influence of oxygen partial pressure was also studied between P_{O2}=1.2-2.3 mbar at a fixed temperature of $T_{surface}$=370°C and a fixed ratio χ=0.5 (Table 9).

Table 9 Parameters used for studied the effect of oxygen partial pressure

$T_{surface}$ (°C)	P_{total} (mbar)	**P_{O2} (mbar)**	χ	$C_{prec.}$ (10^{-3} mol.L^{-1})	$Flow_{prec.}$ (g.min^{-1})	N_2 carrier (sccm)	Height (cm)	Rotation (rpm)
370	6	**1.2**	0.5	5	1	350	16	15
370	6	**1.4**	0.5	5	1	350	16	15
370	6	**1.6**	0.5	5	1	350	16	15
370	6	**1.8**	0.5	5	1	350	16	15
370	6	**1.9**	0.5	5	1	350	16	15
370	6	**2.1**	0.5	5	1	350	16	15
370	6	**2.3**	0.5	5	1	350	16	15

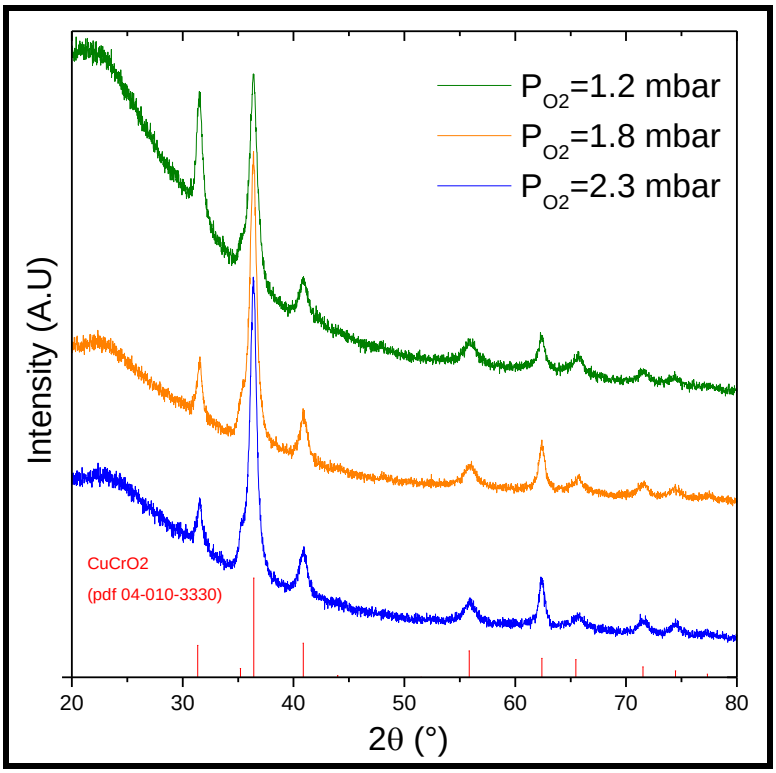

Figure 58 XRD diffractograms of films deposited at oxygen partial pressure P_{O2}=2.3, 1.8 and 1.2 mbar using a precursor ratio $\chi = 0.5$ Bottom diagrams represent the expected peaks for the $CuCrO_2$ phases according to the ICDD cards given on the figure.

It was observed in the range of P_{O2}=1.2-2.3 mbar, that oxygen partial pressure does not impact the crystallographic structure (Figure 58) of the grown thin films. Indeed, for all oxygen partial pressure, pure delafossite $CuCrO_2$ polycrystalline thin films were synthesized.

IV.3.2 Morphology

The influence of oxygen partial pressure on morphology is presented Figure 59. The films are less porous when P_{O2} increase but the grain size is mainly the same: 145±40nm, 146±48nm and 151±60nm for P_{O2}=1.4, 1.8 and 2.3 mbar respectively. According to the SEM cross-section (Figure 60), the films are more compact when the oxygen partial pressure increases. At 1.2 mbar, the growth mechanism seems to be Stranski-Krastanov (see Figure 31 (c)), while for 2.3 mbar it's rather than Van Der Merwe mechanism seems to occur (see Figure 31 (a)).

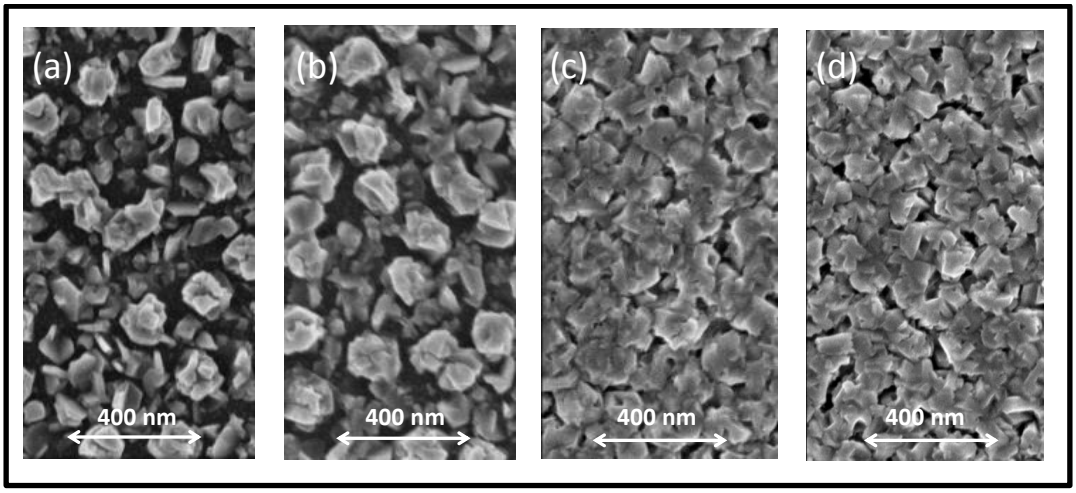

Figure 59 SEM top view images of (a) P_{O2}=1.2 mbar (b) P_{O2}=1.4 mbar (c) P_{O2}=1.8 mbar and (d) P_{O2}=2.3 mbar

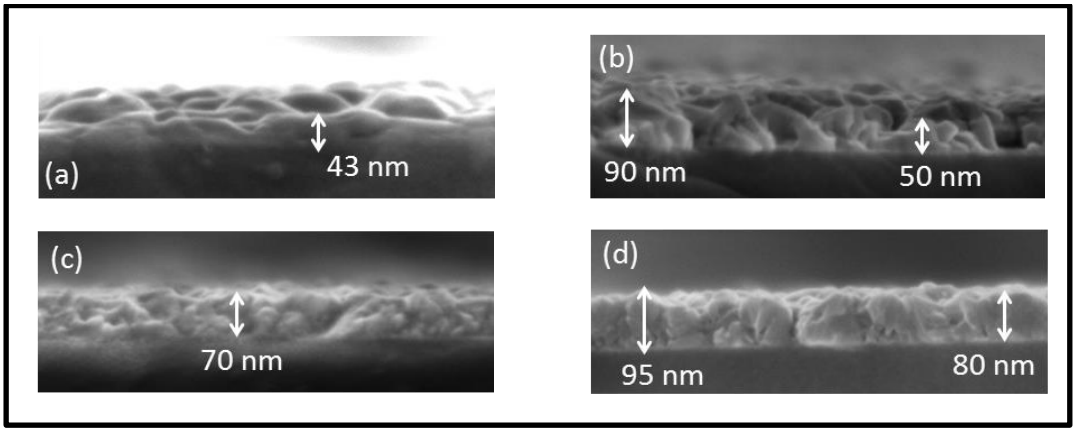

Figure 60 SEM cross section of (a) P_{O2}=1.2 mbar (b) P_{O2}=1.6 mbar (c) P_{O2}=1.8 mbar and (d) P_{O2}=2.3 mbar

The crystallites size (as extracted from the (012) diffraction peak) in Figure 61 increases slightly from 7.6 to 9.3nm when the oxygen partial pressure increases. It may be correlated to the decrease of the thin-films porosity and the increase of their thicknesses. The microstrain, as extracted from XRD measurements, shrinks from 0.27% to 0.18% when P_{O2} is increased up to 2.3mbar. This is attributed to the rise of the crystallites which allows to relax the strain inside crystallites.

In Figure 62, we show the growth rate as a function of the oxygen partial pressure. At $T_{surface}$=370°C, oxygen partial pressure higher than 1 mbar is required to initiate the growth reaction of $CuCrO_2$. The growth rate increases linearly with P_{O2} until reaching a 0.7 nm/min plateau. This value is lower than the typical growth rate obtained with other synthesis methods (2-5 nm/min) but in these cases we remind that high temperature synthesis and/or post-

annealing are needed to obtain a pure phase of delafossite $CuCrO_2$ (see § I.2.3). The growth rate increases linearly up to about 1.7 mbar of P_{O2} and is typically limited by the diffusion of oxygen gas through the boundary layer above the substrate surface. For higher partial pressure of oxygen, the growth rate is constant and is certainly limited by the chemical reaction kinetic on the surface (chemisorption and/or chemical reaction, surface migration, lattice incorporation).

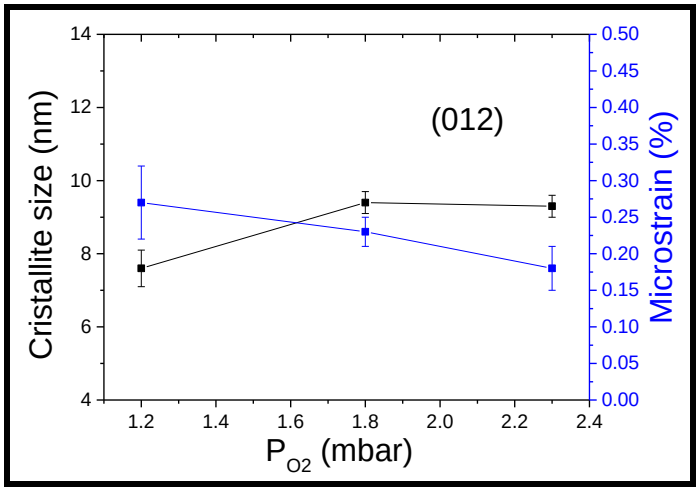

Figure 61 Cristallite size and microstrain of $1.2 \leq P_{O2} \leq 2.3$ mbar extracted from (012) diffraction peaks

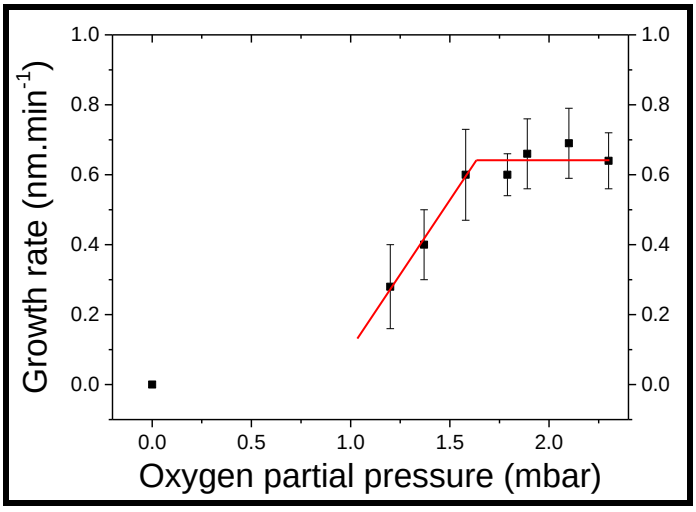

Figure 62 Growth rate of thin films synthesized as a function of oxygen partial pressure

IV.3.3 Chemical composition

Chemical composition does not significantly vary for P_{O2}=1.2-2.3 mbar (Figure 63). The ratio Cu/(Cu+Cr) is constant at 0.36 for P_{O2}=1.6-2.3 mbar while it tends slightly increase to 0.43 for P_{O2}=1.2 mbar.

The high resolution XPS spectra on Cu 2p (Figure 64 (a)), Cr 2p and CuLMM (Figure 64 (b)), do not show any difference when oxygen partial pressure is varied. The signature of Cu^0 in the Cu LMM peak is always observed at 568.8±0.1 eV.

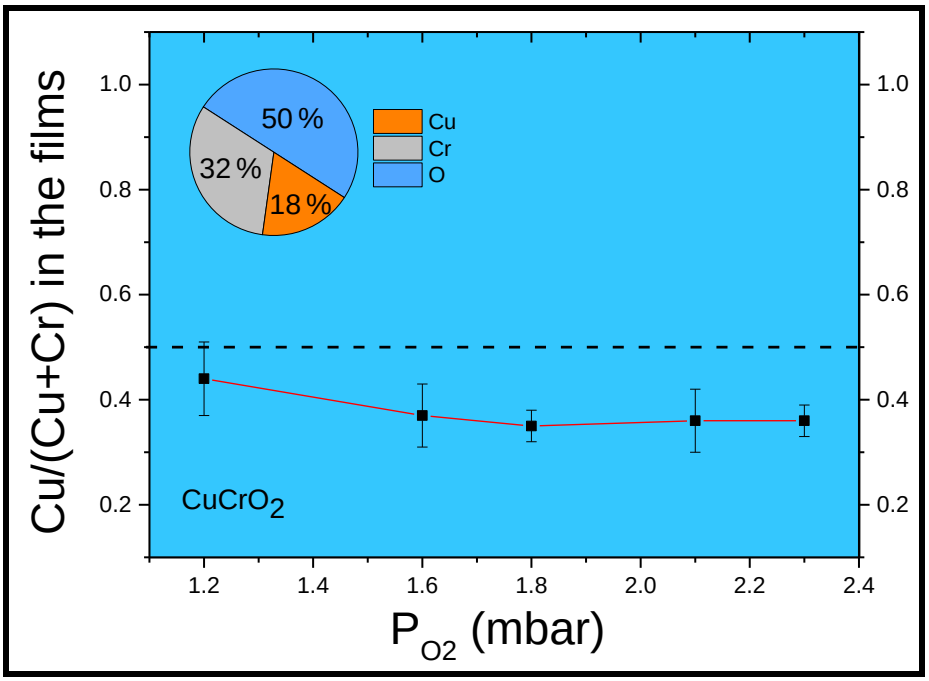

Figure 63 Chemical composition for films grown at χ=0.5 with oxygen partial pressure varied between $1.2 \leq P_{O2} \leq 2.3$ mbar

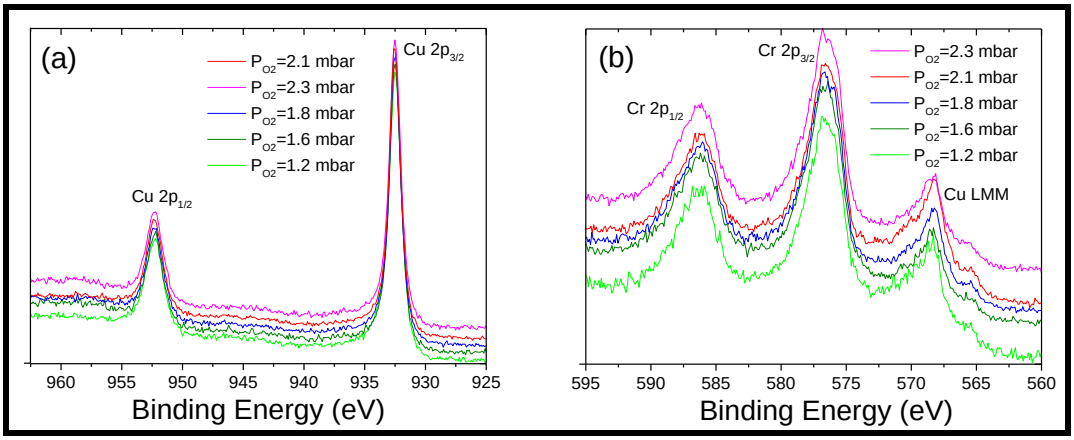

Figure 64 High resolution XPS scans for films grown at χ=0.5 with $1.2 \leq P_{O2} \leq 2.3$ mbar for (a) Cu 2p and (b) Cr 2p

V. ELECTRICAL AND OPTICAL CHARACTERIZATION

In this chapter, we first present our results on electrical and thermoelectrical measurements of $CuCrO_2$ thin films, following by a discussion on transport conduction of holes. We finish this chapter by optical measurements.

V.1 Electrical conductivity

V.1.1 Effect of the growth temperature

Electrical conductivity at room temperature (as measured in the Van Der Pauw configuration) is plotted as a function of the growth temperature (Figure 65) for the same precursor volume ratio χ=0.33. The conductivity is mainly constant for thin films with pure delafossite phase (310°C ≤ $T_{surface}$ ≤ 370°C), the value is near 10±3 $S.cm^{-1}$ which is unusually high for non-doped delafossite $CuCrO_2$ (see Table 14 in Annexes for comparison). At $T_{surface}$ ≥ 410°C, the conductivity decreases down to 5±2 $S.cm^{-1}$, this decrease is attributed to the mixing of $CuCrO_2$ and copper oxide phases (Figure 41).

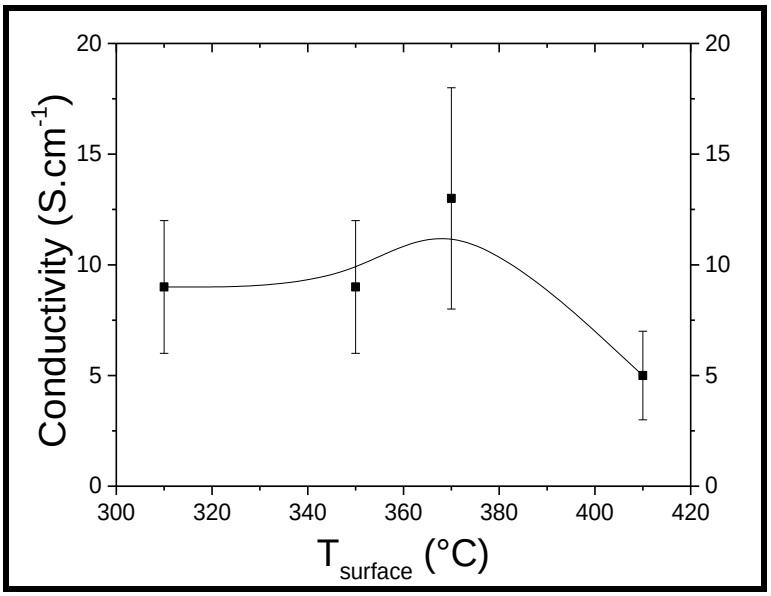

Figure 65 Electrical conductivity of thin films synthesized with χ=0.33 and a growth temperature between 310 ≤ $T_{surface}$ ≤ 410°C

V.1.2 Effect of precursor volume ratio

Electrical conductivity at room temperature is plotted as a function of χ (Figure 66) for a growth temperature of $T_{surface}$=370°C. For all samples, the thickness ranges from 120-160 nm.

The highest conductivity, 17±5 $S.cm^{-1}$, was obtained for $\chi = 0.5$, this conductivity is higher than any published data for undoped $CuCrO_2$ thin-films (Table 14 in Annexe). The observed morphology (Figure 46) provides critical insights to the decrease of the conductivity in the range of $\chi \leq 0.5$. Increasing the fraction of copper into the precursor solution improves the morphology of the thin-film, considering the in-plane electrical conduction path. In the range $\chi > 0.6$, the degraded conductivity is attributed to the incremental increase of Cu_2O and CuO phases in thin-films (Figure 45).

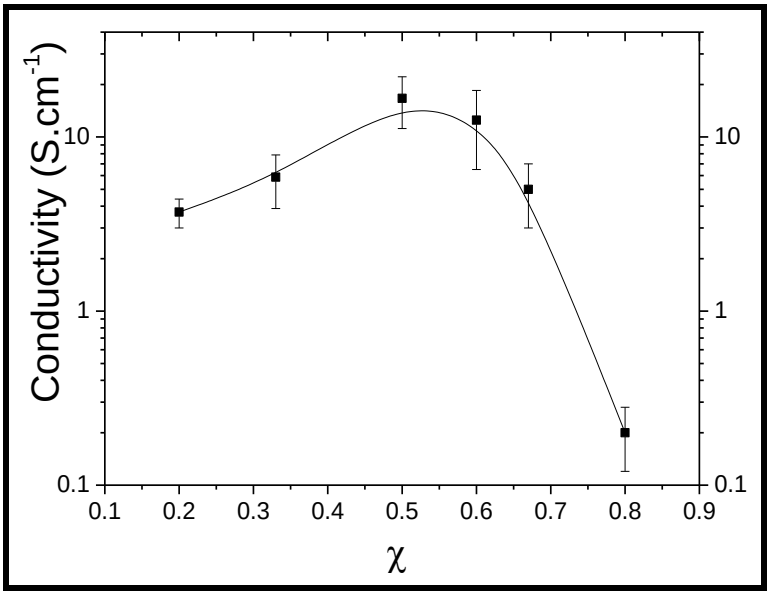

Figure 66 Electrical conductivity as a function of the ratio χ for films grown at $T_{surface}$=370 °C

For the thin-film grown at 370°C with χ=0.5, Hall resistance measurements were performed by varying the magnetic field between -9 and 9T at constant current of 0.25 mA. The slope (see §II.2.4) led to a hole concentration of $(9 \pm 3)\times10^{21}$ cm^{-3} and a hole mobility μ_h of $(1.1\pm0.4)\times10^{-2}$ $cm^2/V.s$. Such measurement at high magnetic field is mandatory to investigate the mobility of oxide semiconductors with low mobility [135]. It is worth highlighting that such a successful measurement is here obtained for the first time for $CuCrO_2$ polycrystalline thin-films.

V.1.3 Oxygen partial pressure

Electrical conductivity at room temperature is plotted in Figure 67 as a function of the oxygen partial pressure. The conductivity shows an exponential decay with the oxygen partial pressure and the maximum (17±6 $S.cm^{-1}$) is reached for a large plateau of sufficiently high

oxygen partial pressure. This highlights the very large window of the $CuCrO_2$ process developed here. Reminding that the chemical composition in films is almost independent of the oxygen partial pressure (Figure 63), the decrease of conductivity is mostly related to the thin-film morphology as presented in Figure 59 and Figure 60. The morphology is almost identical for oxygen partial pressure higher than 1.8 mbar. Beyond this threshold value, the thin-film exhibits closely-packed grains enhancing the in-plane electrical transport. Grains size and overall crystalline structures are not significantly modified when $P_{O2} > 1.8$ mbar.

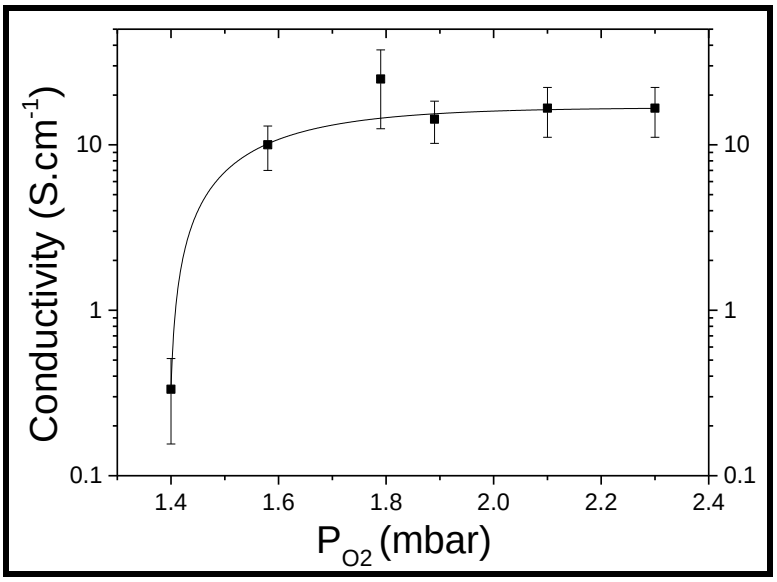

Figure 67 Electrical conductivity as a function of oxygen partial pressure for thin films grown at χ=0.5

V.1.4 Electrical conductivity vs temperature

The electrical conductivity continuously increases with the temperature increasing from 30 to 300K (Figure 68 (a)), confirming the semiconducting behaviour of our thin-films. The electrical conductivity versus temperature between 150-300K may be fitted by a classical thermally activated law (Figure 68 (b)) (when the band conduction model of classical semiconductors is used). The conductivity is expressed as Equation (2) (see §I.2.4.2) and the extracted transport activation energy E_a is 63 meV. This value is very well in line with the data reported in Barnabe *et al.* works[129], where they found a degenerate semiconductor behaviour of their $CuCrO_2$ thin films[129]. However, considering the low mobility value as given by the Hall Effect measurement and the relatively "high" effective mass of holes, m^*, in $CuCrO_2$ (ranging from 4.5 to 6 units of free electron mass)[20], the mean free path λ of holes (in classical

semiconductors) can be obtained by $\lambda = \nu_{th}\tau$ with ν_{th} being the thermal velocity of carriers at room temperature and τ the mean free time of carriers (holes) between collisions. ν_{th} is defined by Equation (54), assuming free hole with only kinetic energy [137]:

$$\mathbf{v_{th}} = \sqrt{\frac{\mathbf{3k_BT}}{\boldsymbol{m}^*}} \qquad (54)$$

and τ is given by:

$$\boldsymbol{\tau} = \frac{\boldsymbol{m}^* \boldsymbol{\mu_h}}{\mathbf{q}} \qquad (55)$$

where q being the elementary charge.

λ ranges from 1.6-1.8.10^{-3} nm, indicating that the free holes model from the Drude approach[137] is not appropriate. It was consistently proposed that delafossite compounds $CuAlO_2$, $CuScO_2$ and $CuYO_2$ exhibit electrical transport limited by small polaron hopping[256], [257]. In this model, the carrier is strongly localized within the lattice potential. The coupling of carrier with the lattice phonon forms polarons that are self-trapped. From a mechanistic point of view, Bosman and Van Daal set the condition occurrence of self-trapping (small polaron model) as[143]:

$$\boldsymbol{\tau} \gg \boldsymbol{\tau_0} \qquad (56)$$

where τ is the time for the hole transition from ion to ion, and τ_0 is the time of a lattice vibration. The time τ can be calculated with[143]:

$$\boldsymbol{\tau} = \frac{\mathbf{ea^2}}{\mathbf{2\mu k_BT}} \qquad (57)$$

where a is the lattice constant (a=2.98 Å in our case, assuming the hole transport is supported by Cu-planes[22]). The time τ_0 is defined by the approximation:

$$\mathbf{k_BT} \cong \frac{\mathbf{h}}{\mathbf{2\pi}}\boldsymbol{\omega_0} \qquad (58)$$

where $\omega_0 = \frac{2\pi}{\tau_0}$.

We obtained, at room temperature, 1.5x10^{-12} s for τ and 1.6.10^{-13}s for τ_0, in our specific case. The condition (56) seems to be well respected, although the experimental confirmation of small polaron conductivity is often troubled by the effects of impurities, grain boundaries and temperature-dependent changes of the transport mechanism [143], [146]. In our particular case, applying the small polaron model in Figure 68 (c) (see §I.4.5) leads to an activation of hopping E_H of 81 meV, higher than 65meV reported by Farrell *et al* [132] using also a small polaron model. In our case, Hall mobility measurement and the corresponding calculation of the time

for the hole transition from ion to ion suggests small polaron hopping conductivity. We investigated complementary transport characterization (§V.2 and §V.3) with thermoelectric measurements. For the very low temperature range of 30-90 K, none of the classical semiconductor or small polaron models fits the experimental data. A variable range hopping model (see Equation (3) in §I.2.4.2) is applied (Figure 68 (d)) as[258], [259]. In our case, the best fit is obtained for n=2 and T_0=79K, suggesting the hopping mechanisms of holes is confined to the two dimensions on the Cu-basal planes.

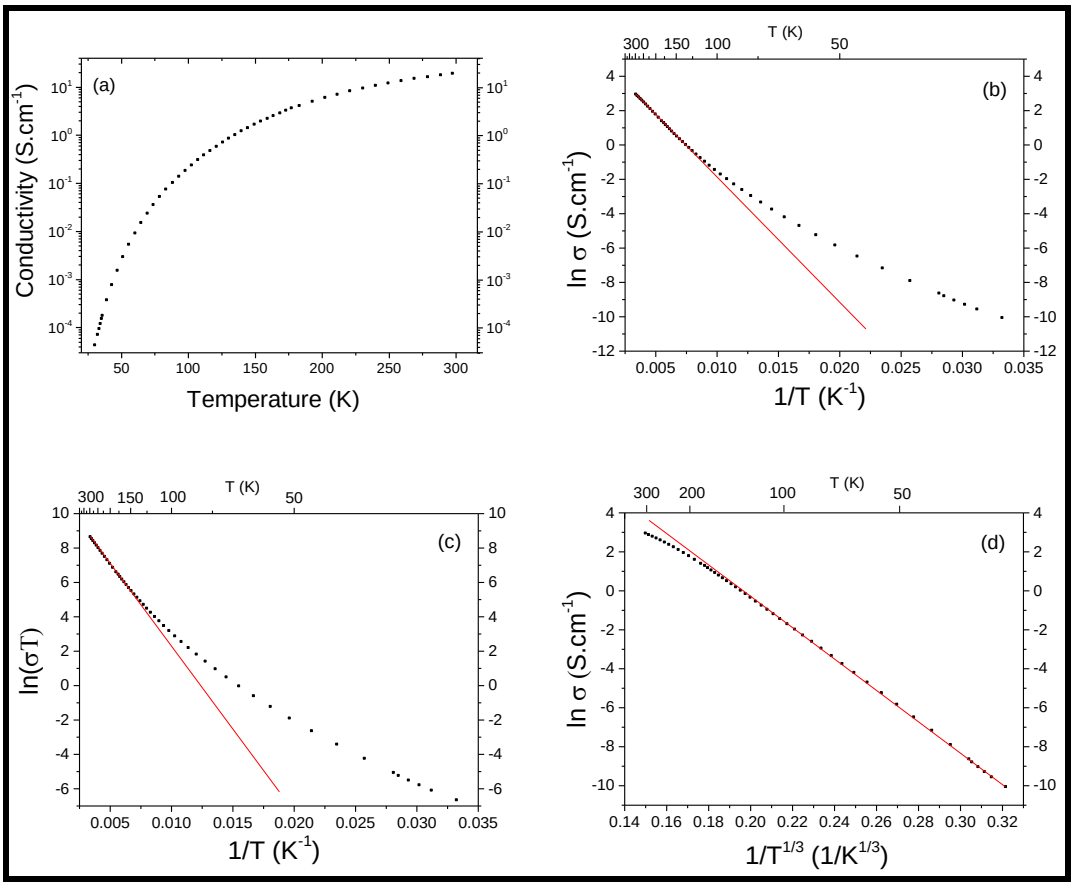

Figure 68 (a) Conductivity of χ=0.5 as a function of the temperature, (b) band conduction model, (c) small-polaron model and (d) VRH model with n=2

The electrical conductivity is mainly due to the high concentration of holes induced by crystalline point-defects. Considering the work reported by Ingram *et al.* [256] for $CuAlO_2$, a similar copper deficiency and an excess of +III cations (aluminium in their case) were noticed. P-type conductivity was attributed to a complex defect of Al on a Cu-site stabilized by two bound oxygen interstitials. In our particular case, an excess of oxygen is not significantly detected and impairs to draw similar conclusion that would imply the complexation of Cr with oxygen interstitials [23]. As an alternative hypothesis, we suggest that the excess of Cr vs Cu

is a specific feature for the growth of $CuCrO_2$ degenerated semiconductors thin-films. Recent defect calculations on $CuCrO_2$ show that copper vacancy is a shallow acceptor (0.37 eV) with the lowest intrinsic defect energy [22]. Additional defects energy calculations with excess of Cr would provide critical insights to definitly conclude on the results.

V.2 Seebeck effect

In this paragraph, we investigate thermoelectric properties of delafossite $CuCrO_2$ thin films with Seebeck coefficient measurements, at room temperature and with varying temperature from 130 to 400K.

V.2.1 Room temperature

V.2.1.1 Seebeck coefficient as a function of the growth temperature

Thermoelectric measurements at room temperature for various growth temperatures of thin-films are presented Figure 69. For pure delafossite phase ($330°C \leq T_{surface} \leq 370°C$), Seebeck coefficient is almost constant at $+ 124\pm4\ \mu V.K^{-1}$, while for a mix of copper oxides and $CuCrO_2$ phases (typically obtained at $T_{surface}=410°C$), Seebeck coefficient decreases to $+ 117\pm1\ \mu V.K^{-1}$. Positive sign of Seebeck coefficient confirms the p-type character of the grown $CuCrO_2$ thin-films.

V.2.1.2 Seebeck coefficient as a function of the ratio χ

We present in Figure 70 thermoelectric measurements as a function of ratio χ. Seebeck coefficient is almost identical for pure delafossite phases when χ varies from 0.33 to 0.6 ($+ 109\pm3\ \mu V.K^{-1}$). However, thin film grown with $\chi=0.2$, which is also a pure delafossite $CuCrO_2$ film, shows higher Seebeck coefficient ($+ 131\pm3\ \mu V.K^{-1}$). This effect may be due to the specific "spines" morphology of this thin-film (Figure 46 (a)), that would lower the averaged thermal conductivity of the sample. When thin films have a mixing phase between copper oxide and delafossite $CuCrO_2$ ($\chi > 0.6$), Seebeck coefficient still increases to reach almost a similar value than the one obtained for $\chi=0.2$.

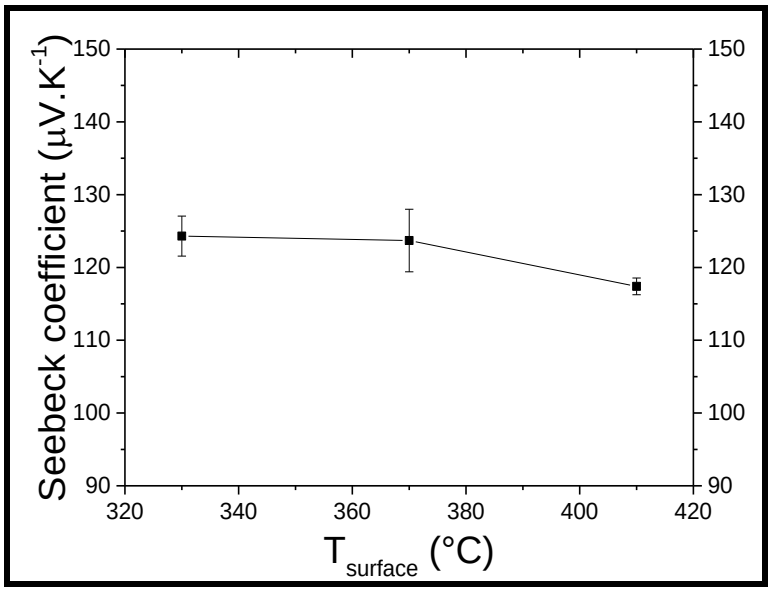

Figure 69 Seebeck coefficient as a function of temperature synthesis for films grown at χ=0.33

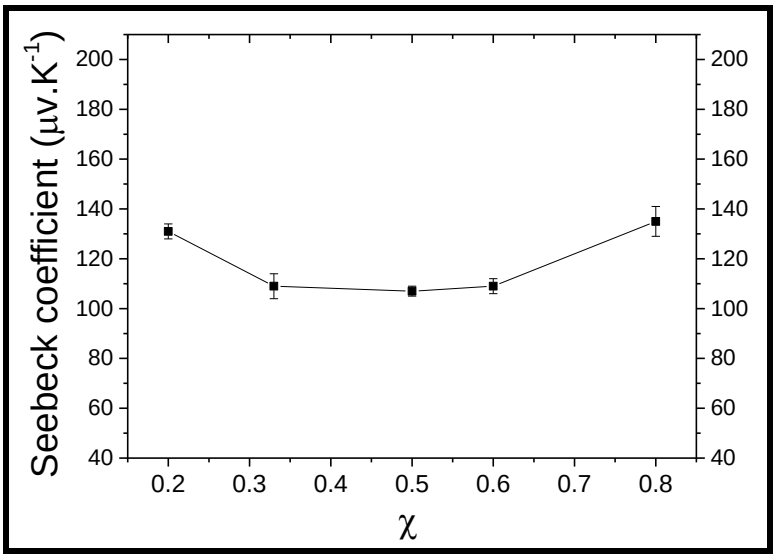

Figure 70 Seebeck coefficient measured at room temperature of films for $T_{surface}$=370°C and $0.2 \leq \chi \leq 0.6$

We compile in Figure 71 our Seebeck coefficient and electrical conductivity data for $0.2 \leq \chi \leq 0.6$ and compare them with data from literature when both Seebeck coefficient and electrical conductivity are rigorously measured on the same sample. In our case, the order of magnitude is in the same range of Mg-doped $CuCrO_2$ reported in the literature[24], [25], [129], which further confirms (i) the large carrier concentration in our films, (ii) that the crystalline point-defects of our samples do not significantly modify the carrier mobility and the lattice properties of $CuCrO_2$ when compared to Mg-doped $CuCrO_2$ grown by SS and MS synthesis.

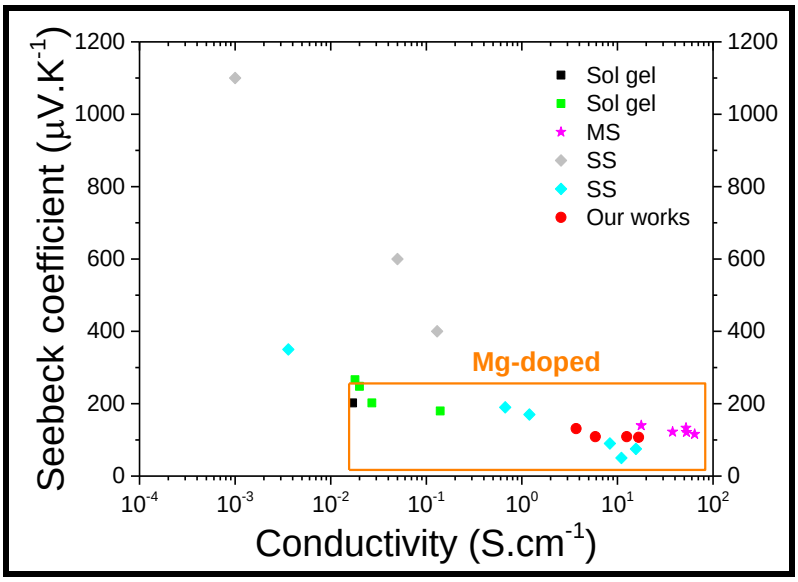

Figure 71 Comparison of Seebeck coefficients at room temperature of undoped and doped $CuCrO_2$ reported in literature (Table 14 in Annexes) and our works (red dots)

V.2.2 Temperature dependence of Seebeck coefficient

V.2.2.1 Seebeck coefficient vs temperature for different growth temperature

We presented in Figure 72 the temperature dependence of Seebeck coefficient for different growth temperature at a ratio of precursor χ=0.33. For pure delafossite $CuCrO_2$ phase ($T_{surface}$=330°C and $T_{surface}$=370°C), the values are very similar, as it was observed at room temperature (Figure 69). For these samples, at low temperature (140-250 K), Seebeck coefficient is mostly constant (110-115 $\mu V.K^{-1}$), while at temperature above 250 K, Seebeck coefficient is linearly dependent on temperature. This trend was also observed for Mg-doping $CuCrO_2$ [25][24] and is discussed in §V.3.

When delafossite $CuCrO_2$ is mixed with copper oxides phase ($T_{surface}$=410°C), at temperature above 300K, Seebeck coefficient is mainly the same compared to the other growth temperature. However, below 300 K, Seebeck coefficient is lower than pure delafossite $CuCrO_2$ phase ($T_{surface}$=330°C and $T_{surface}$=370°C) until reaching a constant value near 105 $\mu V.K^{-1}$ below 200K.

V.2.2.2 Precursor volume ratio

The effect of ratio of precursor volume χ on the Seebeck coefficient of thin films was also studied and is presented in Figure 73 for $0.2 \leq \chi \leq 0.8$. For χ =0.33, 0.5 and 0.6 (which

correspond to pure $CuCrO_2$ thin films), Seebeck coefficient values and trends are very similar in the temperature range measured (140-400K). However, pure $CuCrO_2$ thin film with χ=0.2 is different from χ=0.33, 0.5 and 0.6. Indeed, Seebeck coefficient of χ=0.2 is clearly higher than χ=0.33, 0.5 and 0.6 and seems to be mostly constant (130-135 $\mu V.K^{-1}$) between 140-400K. When thin film of delafossite $CuCrO_2$ is mixed with copper oxides (χ=0.8), Seebeck coefficient is also higher compared to χ=0.33, 0.5 and 0.6. This effect can be attributed to CuO phases in the film, Seebeck coefficient of CuO films being reported always up to 200 $\mu V.K^{-1}$ below room temperature even if it is doped [260][261].

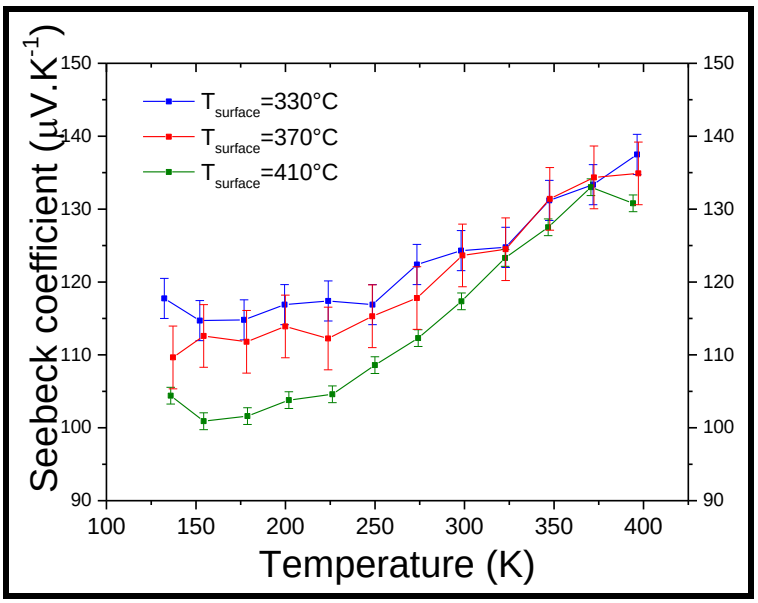

Figure 72 Seebeck coefficient as a function of temperature grown at $T_{surface}$=330°C, 370°C and 410°C and with χ=0.33

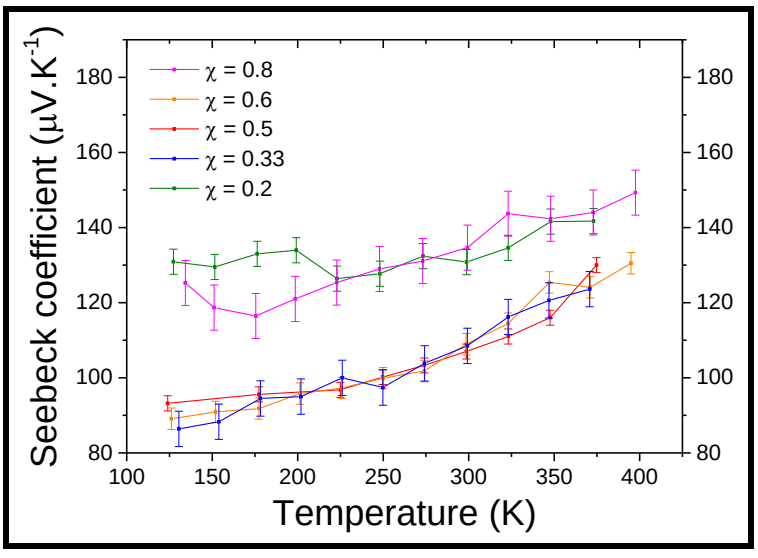

Figure 73 Seebeck coefficient as a function of temperature for ratio χ of 0.2, 0.33, 0.5, 0.6 and 0.8.

V.3 Hole transport: Discussion

We have studied the carrier transport with thermoelectrical and electrical conductivity measurements as a function of temperature. For the sake of clarity, we focus here only measurements for a ratio of χ=0.6, other delafossite thin films having similar thermoelectrical properties (Figure 72 and Figure 73). We show in Figure 74 (a) Seebeck coefficient as function of temperature and Figure 74 (b) electrical conductivity as a function temperature measured by four probes (Van Der Pauw configuration) in the same thermoelectric measurement set-up. We clearly observed two regimes in Figure 74 (a) for the Seebeck coefficient. Similar trends were observed for degenerate semiconductor, semimetallic or metallic materials in the range of 50-400 K [262]–[265]. In these cases, Seebeck coefficient is expressed as [262], [266], [267]:

$$\boldsymbol{S = AT + \frac{B}{T}} \qquad (59)$$

where A and B are parameters depending on materials. The linear contribution with the temperature is due to the "diffusion" of carrier and the dependence on the inverse of temperature is related to the phonon contribution via electron-phonon coupling [267].

In order to further extract carrier concentration and mobility as a function of temperature, three transport models could be considered when using Seebeck coefficient and electrical conductivity values: small polaron[139], [143], [219], non-degenerate[139], [146], [268] and degenerate[262], [269], [270] semiconductor models. In our case, our investigations clearly show that a high-level of carrier concentration (> 10^{20} cm^{-3}) is a specific feature of our samples. Therefore, we only consider either small polaron or degenerate semiconductor models to extract mobility and activation energy values from our measurements. Such results are then critically discussed.

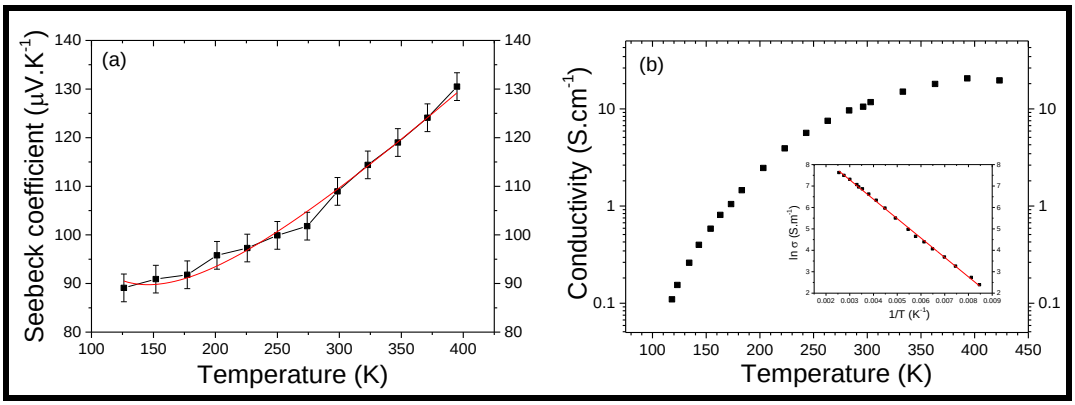

Figure 74 (a) Seebeck coefficient and (b) electrical conductivity as a function of temperature for χ=0.6

V.3.1 Model of small polarons

Seebeck coefficient in small polaron model is defined as [219], [271]:

$$S = \frac{k_B}{e} ln\left(\frac{2(1-c)}{c}\right) \quad (60)$$

where c is the fraction of occupied site by polarons. As detailed in the first chapter, VBM of $CuCrO_2$ is composed in majority by Cu 3d states, and then copper atoms are host sites of polarons. Therefore, the fraction c can be written as:

$$c = \frac{[Cu^{2+}]}{[Cu^{+}]} \quad (61)$$

where $[Cu^{2+}]$ is the number of occupied site by polarons, i.e. the hole carrier concentration p, and $[Cu^{+}]$ is the concentration of copper atoms in a $CuCrO_2$ crystal (i.e. $3.05x10^{22}$ cm^{-3}). Therefore, carrier concentration is determined by:

$$p = [Cu^{+}] * \frac{1}{\frac{e^{\frac{Se}{k_B}}}{2} + 1} \quad (62)$$

From our Seebeck and conductivity measurements, we report in Figure 75 the extracted carrier concentration and the mobility ($\mu=\sigma/pe$) as a function of temperature. We observe a slight decrease of carrier concentration with the temperature, from $1.3x10^{22}$ to $9.5x10^{21}$ cm^{-3}, while the mobility clearly increases with the temperature from $7.8.10^{-5}$ to 10^{-2} $cm^2/V.s$.

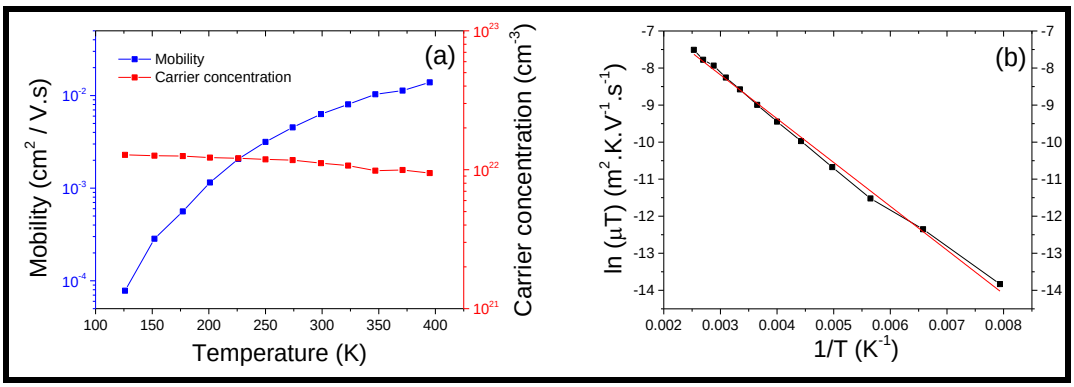

Figure 75 (a) Carrier concentration and mobility as a function of temperature calculated with small polaron model (b) fitting of ln(μT) vs 1/T to determine E_H and μ_0

Figure 75 shows ln(μT) as a function of 1/T in order to determine E_H and μ_0 from Equation (24) (see § I.4.5). The extracted values are compared with other materials in Table 10. We find 103 meV for E_H and 97 $Kcm^2/V.s$ for μ_0. Both values are smaller than any data

reported in literature (Table 10) but remain in the same range than the published data for similar materials.

Table 10 Reported fitting parameters E_H and μ_0 in the literature

Materials	E_H (meV)	μ_0 (K.cm^2/V.s)	Ref.
$CuAlO_2$	140	500	[256]
$CuScO_2$	220	650	[257]
$CuYO_2$	230	610	[257]
$ZnRh_2O_4$	250	1320	[144]
$CuCrO_2$ (our work)	103	97	

V.3.2 Degenerate semiconductor

For a metal or a degenerate semiconductor material, Seebeck coefficient is defined by Equation (59), where the parameter A is expressed as [272]:

$$A = \frac{8\pi^2 k_B^2 m^*}{3eh^2}\left(\frac{\pi}{3p}\right)^{2/3} \quad (63)$$

where h is Planck constant and p carrier concentration. The parameter B is proportional to lattice specific heat of the material. In Figure 74 (a), we fitted Seebeck coefficient with Equation (59). We find (2.85±0.03)x10^{-7} V.K^{-2} for A and (7.1±0.2)x10^{-4} V for B. From A, we extract the carrier concentration p from Equation (63):

$$p = \frac{\pi}{3\left(\frac{3Aeh^2}{8\pi^2 k_B^2 m^*}\right)^{3/2}} \quad (64)$$

with an effective mass of m^*/m_e =6, 10 and 20, we find 1.8x10^{21}, 3.8x10^{21} and 1.1x10^{22} cm^{-3} respectively. Even with the lowest effective mass, the carrier concentration is higher than 10^{21} cm^{-3}, being in agreement with Hall measurement ((9±3)×10^{21} cm^{-3}) and with a degenerate semiconductor model. We show in Figure 76 the mobility as a function of temperature for the respective carrier concentrations. As carrier concentration is constant with temperature in degenerate semiconductor, the mobility relies on the activation energy of the electrical conductivity ($\mu=\sigma/pe$). According to electrical transport models in semiconductor (see Chapter I.4), only grains boundaries model fits with an activated mobility.

Indeed, for degenerate semiconductors, the mobility is defined as Equation (21) (see §I.4.4). In Figure 76 (b), we apply the fit of mobility (for p=1.1x10^{22}cm^{-3}) using the equation:

$$\mu = ATln\left(1 + e^{-\frac{B}{T}}\right) \quad (65)$$

We put in Table 11 "A" values obtained by fitting three carrier concentrations. Assuming p_a is equivalent to p which is a good approximation for a strong degeneracy, we deduce L, the crystallite size (Table 11). It appears that the calculated crystallite size is smaller than the one extracted from the XRD measurement (0.1-0.3 nm and 10-15nm respectively) (Figure 47). This calls further analysis and discussion.

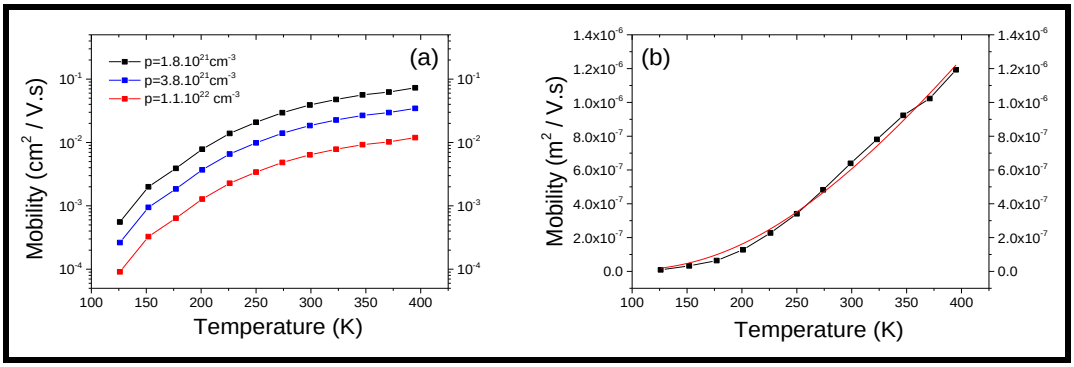

Figure 76 Mobility as a function of temperature calculated with degenerate semiconductor model for (a) p=1.8.10^{21}, 3.8.10^{21} and 1.1.10^{22} cm^{-3} and (b) fitting of mobility with a model of grain boundaries for degenerate semiconductor

Table 11 Fitting parameter "A" and the extracted cristallite size "L"as a function of carrier concentrations

p (cm^{-3})	A (m^2/(V.s.K))	L (Å)
1.8.10^{21} (m^*/m_e=6)	9.03.10^{-8}	3.0
3.8.10^{21} (m^*/m_e=10)	4.28.10^{-8}	1.8
1.1.10^{22} (m^*/m_e=20)	1.48.10^{-8}	0.9

V.3.3 Contradictory discussion

Extracted parameters when using the small polaron model are in relatively good agreement with those reported in literature for delafossite compounds and other p-type TOS. Degenerate semiconductor model may also well explain the results of the experimental Seebeck coefficient vs. temperature but the extracted crystallite size is not consistent with the average crystallite size found by XRD analysis. A critical discussion is further required to balance (a) the validity of the small polaron model in our case and (b) the results obtained by using the degenerate semiconductor model.

(a) Validity of small polaron model

We raise some concerns regarding the usual small polaron model:

(i) It was demonstrated by Nagaraja *et al.*[146], that even if extracted parameters μ_0 and E_H could be in the range of values reported for materials showing proven small polaron conductivity, this may not necessarily mean that the small polaron mechanism triggers the electronic transport inside the material. Indeed, with a model of small polaron applied on Rh_2ZnO_4, Nagaraja *et al.*found, from thermoelectric measurements, μ_0 and E_H, having values of 1320 K.cm^2/V.s and 320 meV respectively, which are indeed in the range of small polaron materials. The mobility extracted at room temperature was $3x10^{-4}$ cm^2/V.s which tends to establish the conductivity of Rh_2ZnO_4 being governed by small polaron transport. However, Nagaraja *et al.* performed also direct measurement of the mobility with Hall effect at high magnetic field (14T). They found a value of 0.18 cm^2/V.s (at room temperature) which is two orders of magnitude higher than the extracted value when applying the small polaron conductivity model to thermoelectric measurements. According to the Bosman-Van Daal limit, Hall effect measurement proved a band conduction transport in Rh_2ZnO_4 ($\mu > 0.1$ cm^2/V.s), which is contradictory to small polaron transport from thermoelectric measurement ($\mu = 3x10^{-4}$ cm^2/V.s). Nagaraja *et al.* explained this difference of mobility come from the assumption of the temperature independence of the effective density of state, near the VBM, in Equation (60) which is not true if the material is a band conduction transport. Then, the mobility extracted from thermoelectric measurement could be a mobility of small polaron transport but this value could be wrong. Nagaraja *et al.* showed by taking into account the temperature dependence of the effective density of state into the thermoelectric models of Rh_2ZnO_4, theorical calculations lead to a mobility of 0.12 cm^2/V.s for the same measurements, which becomes in a very good agreement with experimental Hall-effect measurements. Then, the authors preferred to consider a band conduction transport for this material.

In our case, the impact of a similar approximation of the small polaron model cannot be excluded. However our mobility measured by Hall effect (10^{-2} cm^2/V.s) for a specific sample is still well under the Bosman-Van Daal limit. Nevertheless, the application of this Bosman-Van Daal limit for polar oxides needs to be debated.

(ii) The limit of Bosmann-Van Daal ($\mu << 0.1$ cm^2/V.s)[143], under which one the material conductivity is considered to be governed by the small polaron transport in polar oxide, cannot prove unambiguously the transport mechanism in our delafossite $CuCrO_2$ thin films even if this condition is clearly matched. Indeed, as Bosmann-Van Daal [143]mentioned in their paper, high doping level ($>10^{20}$ cm^{-3}) or grain boundaries may partly modifiy the properties of pure material by significantly decreasing the mobility. In their work, Bosmann-

Van Daal have proved small polaron transport in p-type MnO[143], when doped with lithium (0.1%), by reducing the effect of grain boundaries in their material when tailoring the materials synthesis. They found holes carrier concentration of $7x10^{17}cm^2/V.s$ and a mobility of $3.10^{-5}cm^2/Vs$ which is far lower than the Bosmann-Van Daal limit. Interestingly, for undoped and lowly doped delafossite $CuCrO_2$, the mobility reported for a carrier concentration around 10^{18} $cm^2/V.s$ (Figure 19), is between 0.2-10 $cm^2/V.s$ which is significantly higher than the Bosmann-Van Daal limit. According to these experimental results, crystal of delafossite $CuCrO_2$ does not seem to feature small polaron transport.

(iii) Experimental measurements of the valence band of our delafossite $CuCrO_2$ thin films by XPS further puzzle the conclusions that we may draw regarding the carrier transport. Indeed, for our delafossite $CuCrO_2$ thin films, we observe a valence band profile (Figure 57) being significantly different from the one reported in literature (Figure 9) because anti-bonding states of O-Cu-O bond are seriously diminished in our case. Theorically, it was demonstrated by S. Lany[273]–[275] and A. Zunger[274] that low bonding or anti-bonding density of states at the band edge (VBM or CBM) is more favourable to conduction band than small polaron transport. Further cyclotron experiments, would be very helpful as it was done for Cu_2O[276], where an unambiguously band conduction transport was found.

(b) Results of degenerate semiconductor model:discussion

We found that degenerate semiconductor model can explain the non-linear trend of Seecbeck coefficient below 300K but this model is called into question because of the unrealistic values of the extracted crystallite size. This latter result requires specific discussion in our case.

We remind that the chemical composition in the films grown with χ=0.6 is (Figure 50): 22% of copper, 30% of chromium and 48% of oxygen. The excess of chromium was always observed in our pure delafossite $CuCrO_2$ thin films. As observed by TEM in Figure 48, the excess of Cr is not localized in grain boundaries, but seems to be diluted into the lattice. Knowing that the larger interstitial site is between two copper atoms, in the copper atoms plane (Figure 4), then the Cr excess may preferably occupy this interstitial site[j]. As the chemical concentration of oxygen is almost stoichiometric (≈50%), 30% of chromium means that there is one additional atom of chromium in the lattice, for five copper atoms in the stoichiometric lattice. In that simple case, the distance between chromium atoms supposedly being in

[j] Copper substitution with chromium (Cr_{Cu}) should not appear in our case, because this defect is a donor ($Cr^{3+}+2e^- \leftrightarrow Cr^+$), while we obtained a p-type material. Moreover, this defect has a high formation energy [125]

interstitial sites, when considering an homogeneous distribution of the excess of chromium, is 2-3x the distance between copper-copper atoms i.e 6-9 Å. It is believed [22] that the holes transport in copper based delafossite is mostly localized in the copper atoms plan, meaning a quasi-2D conduction of holes within the Cu plane. Therefore, we may suppose that each 6-9 Å, a hole may statistically undergo a scattering event on interstitial Cr. Interestingly, this distance is the same order of magnitude than the "apparent" crystallite size as extracted from thermoelectric measurements when the band conduction model of degenerate semiconductor is applied. However, such impurity scattering mechanism would not agree with the measured exponential increase of the carrier mobility with the temperature (ranging from 130K to 400K). Such trend is usually attributed to grain boundaries barriers (see chapter I.4).

Chemical concentration of copper (22%) underlines a lack of copper atoms in thin films, which may be attributed to copper vacancies necessary to accommodate the excess of Cr in the Cu in-plane interstitial sites. The concentration of copper vacancies (3% for χ=0.6), which correspond to a concentration of unoccupied site of $4x10^{21}$ cm^{-3}, is in good agreement with the order of magnitude of the holes concentration was determined by Hall Effect measurement ($(9\pm3)x10^{21}$ cm^{-3}). It is worth reminding that XPS measurements reveal a copper oxidation state of zero, Cu^0 (Figure 54 and Figure 64), which may be attributed to the higher electronegativity of copper atoms vs. Cr atoms. Cu (+I) in close proximity with the chromium atoms in interstitial sites (additional chromium) may gain one electron from a bonding with Cr, resulting in Cu^0. At this stage, it is premature to assess the impact of Cu^0 on the electrical transport, in particular if Cu^0 may contribute to the conduction by generating a Cu^0/Cu^{+I} doping level in the bandgap or if Cu^0 may behave as a hole trap.

Several ambiguities of small polaron and band conduction models prevent any conclusion on the nature of the transport conduction in our $CuCrO_2$ thin films. Further analysis on cyclotron and X-ray spectroscopies should be useful in order to determine the transport conduction.

V.4 Optical measurement

V.4.1 Transmittance/Reflectance

Optical transmittance (T) and reflectance (R) were measured for thin-films grown at three growth temperature: $T_{surface}$=350°C, 370°C and 410°C (Figure 77). The transmittance of

the glass substrate is also reported as a reference spectrum. In the visible range (between 400-800 nm), the average transmittance of the reference glass substrate is 90% while for thin-films, the average transmittance is near 50%. We observe in the range of 550nm-850nm that thin-film grown at $T_{surface}$=410°C have better transmittance than other films and its reflectance is almost the same as the film grown at $T_{surface}$=370°C. This highest transmittance is attributed to the lower thickness (55 nm) of the thin-film grown at $T_{surface}$=410°C while in the range of 375-500nm wavelength, the transmittance is degraded when compared to thin-films grown at lower temperature. This is attributed to the absorption induced by the copper oxide phases mixed with $CuCrO_2$ in this sample (Figure 41). Indeed, Cu_2O and CuO have lower bandgap (2.2eV[277], [278] and 1.6eV[279], [280] respectively) than $CuCrO_2$.

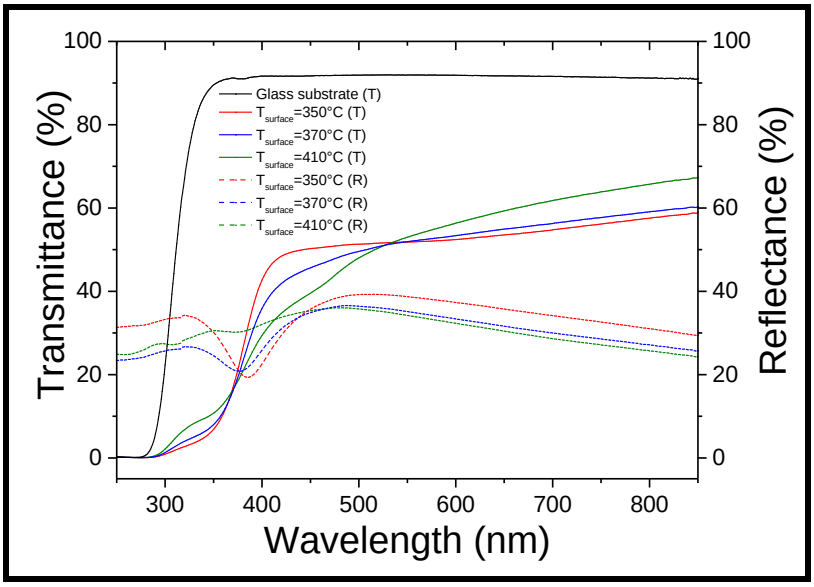

Figure 77 Transmittance (T) and reflectance (R) spectra of glass substrate and $CuCrO_2$ thin films synthesized at growth temperature of $T_{surface}$=350°C, 370°C and 410°C

The optical transmittance was also measured in the range of 250-850 nm for films grown with $0.2 \leq \chi \leq 0.8$ at $T_{surface}$=370°C, the corresponding spectra are shown in Figure 78. The range of thicknesses for all films is between 120-160 nm. The average transmittance in the 400-800 nm range decreases from 40%-50%, for $0.2 \leq \chi \leq 0.6$, down to 30% for higher χ. For this latter case, the transmittance decrease is attributed to the concomitant existence of Cu_2O and CuO phases, having a much lower bandgap than $CuCrO_2$. The pure delafossite phase features a higher averaged transmittance relative to the contaminated films with a maximum transparency for χ=0.2. For this specific film, the transmittance improvement is mainly attributed to the morphology of the thin-film which is not continuous as evidenced by the SEM picture of Figure 46 (a).

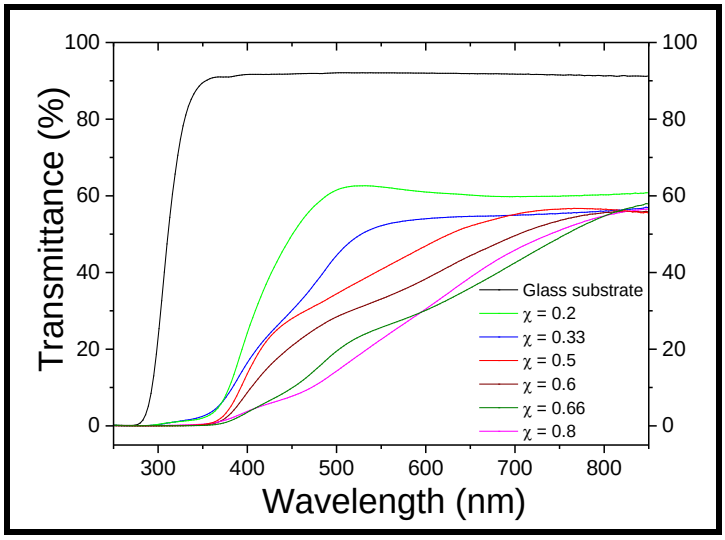

Figure 78 Transmittance spectra of glass substrate and $0.2 \leq \chi \leq 0.8$

V.4.2 Absorption coefficient

Absorption coefficients of thin films (calculated with Equation (53)) with $T_{surface}$=350°C, 370°C and 410°C are presented in Figure 79 (a). For pure delafossite phase, $T_{surface}$=350°C and 370°C, α increase from 3.0 eV, with a constant slope between 3.2-3.5eV, which is due to the $CuCrO_2$ absorption. However, for mixed copper oxide and $CuCrO_2$ phases, thin-films grown at $T_{surface}$=410°C, α increase from 2.5eV and two slope of α can be clearly distinguished: one between 2.5-3.0 eV, due to the absorption of copper oxide phases and the other one between 3.2-3.5 eV attributed to the additional absorption of the $CuCrO_2$ phase.

Direct optical gap of $T_{surface}$=350°C, 370°C and 410°C, are evaluated using a linear fit of the Tauc's plot (Figure 79 (b)) with the Equation (8) (see §I.2.5.2): the extracted direct band gap E_g is found to be between 3.2-3.3 eV which is in very good agreement with previous experimental and theoretical works [17], [33], [34], [37], [39], [41], [44], [47], [49] regarding $CuCrO_2$ materials.

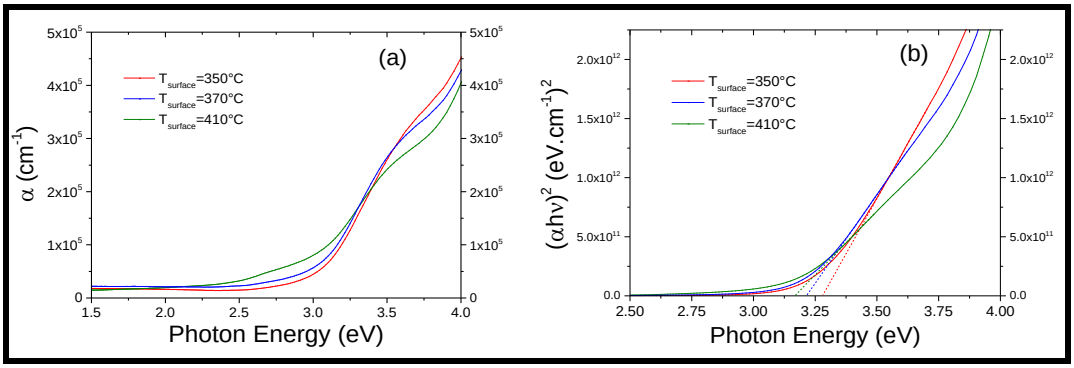

Figure 79 (a) absorption coefficient α and (b) Tauc's plot of $T_{surface}$=350°C, 370°C and 410°C

The absorption coefficient for $0.2 \leq \chi \leq 1$ (calculated with Equation (53)) and the corresponding normalized derivative are plotted in Figure 80. All films containing the delafossite phase show a steep increase of the absorption coefficient at 3.1-3.2 eV with a corresponding maximum for the derivative curve. However, another steep increase of the absorption is noticed at 2.5 eV for $x \geq 0.66$. This absorption edge at 2.5 eV is particularly steep for the Cu_2O reference coating ($\chi = 1$). This feature further confirms the growth of parasitic Cu_2O for $\chi \geq 0.66$.

Direct optical gap of $0.2 \leq \chi \leq 0.5$, are evaluated using a linear fit of the Tauc's plot with the Equation (8). The extracted direct band gap E_g is also found to be between 3.1-3.3 eV, which is in very good agreement with previous experimental and theoretical works [17], [33], [34], [37], [39], [41], [44], [47], [49] regarding $CuCrO_2$ materials.

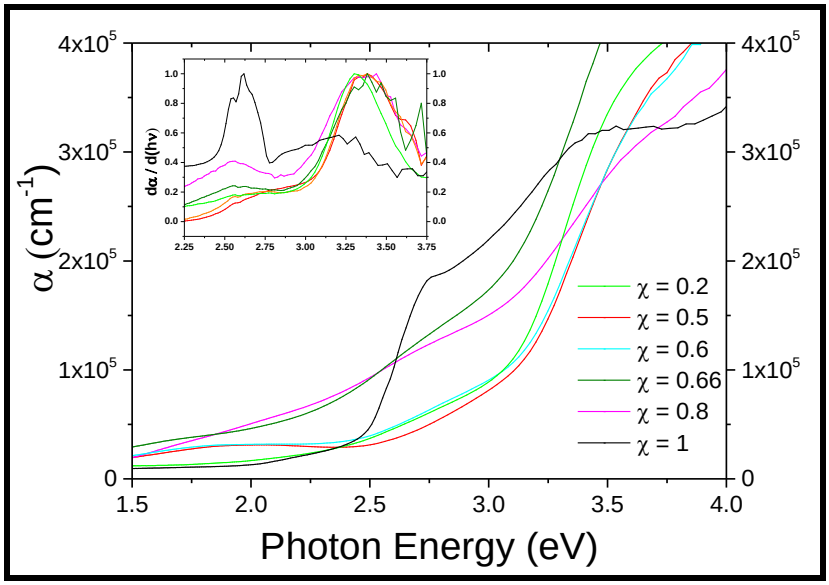

Figure 80 Absorption coefficient of $0.2 \leq \chi \leq 1$ as a function of photon energy. The inset graph is the derivative of absorption coefficient

Discussions

We close this chapter by comparing our undoped delafossite $CuCrO_2$ thin film properties and those reported in literature (see Table 14 in Annexes). In Table 12, we summarize growth parameters, electrical conductivities and visible transparency for different $CuCrO_2$ synthesis processes. According to the data reported in Table 12, it appears that we synthesized $CuCrO_2$ at the lowest temperature (vs the published data) and without any additional annealing. Interestingly, the electrical conductivity is enhanced when the material is grown with our pulsed injection synthesis while visible transparency is still moderate. Figure 81 show a plot of

electrical conductivity and visible transparency for our pulsed injection synthesis (best value) and various synthesis methods for undoped $CuCrO_2$. The inset graph in Figure 81 show our delafossite $CuCrO_2$ thin film, deposited on a large surface area (10x10 cm) of glass.

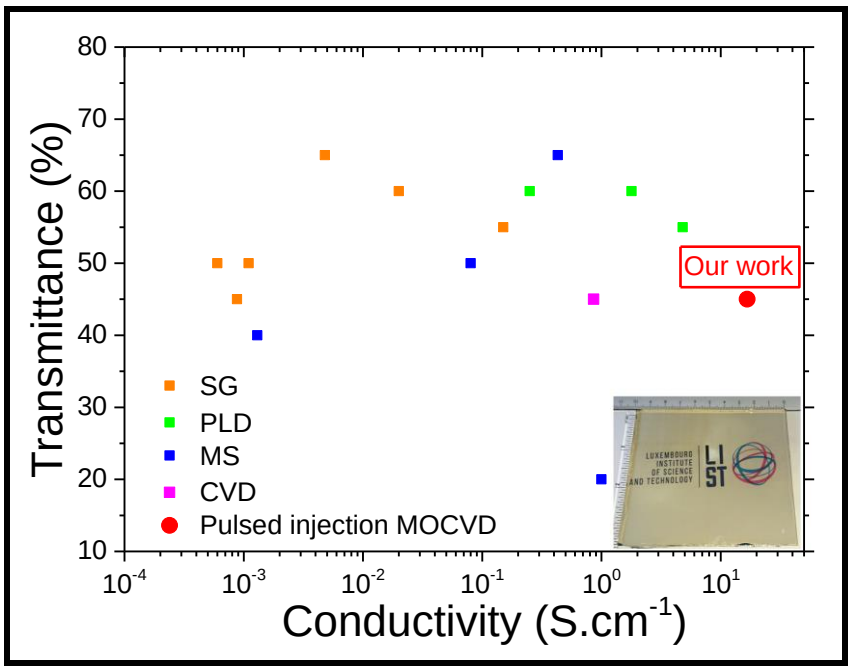

Figure 81 Plot of electrical conductivity and transmittance for various synthesis methods and comparison with our work (best value)

Table 12 Properties of delafossite $CuCrO_2$ synthesized with various synthesis methods

Synthesis	Growth		Annealing		σ (S.cm^{-1})	Transmission (%)	Thickness (nm)
	temperature (°C)	time (h)	temperature (°C)	time (h)			
SS	850-1200	12-48	900-1200	10-100	10^{-4} - 10^{-3}	Not reported	Not reported
SG	300-500	0.1-1	700-800	0.5-2	6.10^{-4}-10^{-2}	45-60	100-200
PLD	550-750	0.5-2	None	None	1-5	55-65	60-130
MS	RT	1	600-900	2-4	10^{-3}- 1	40-60	100-300
	750	1.5	None	None			
CVD	240-550	0.5	700-950	Not reported	1-2	40	400
Pulsed injection (our work)	310-370	2	None	None	17	40-50	140

VI. PN JUNCTIONS

In this chapter, we present in the first part the synthesis process for the fabrication of p-n junctions and their structural properties. The second part deals with their electrical and optical properties.

VI.1 Synthesis and structural properties

Two approaches were studied for the synthesis of p-n junctions. The first relies on the deposition of $CuCrO_2$ thin film on ZnO layers both synthesized by MOCVD on glass substrates. The second approach uses the ALD of conformal ZnO layers on $CuCrO_2$ thin films previously grown on glass by MOCVD.

VI.1.1 MOCVD process flow

In this approach, p-n junctions were synthesized with only MOCVD process. The first layer was ZnO (undoped or aluminium doped) deposited on glass, and the second layer was $CuCrO_2$ (Figure 82). After $CuCrO_2$ deposition, the electrical conductivity of ZnO was strongly diminished, perhaps due to the difference of the growth temperature ($T_{surface}(ZnO)$ =600°C and $T_{surface}(CuCrO_2)$=370°C) and the oxygen partial pressure ($P_{O2}(ZnO)$=1.2 mbar and $P_{O2}(CuCrO_2)$=2.1 mbar) between the two processes. Growth temperature and oxygen partial pressure are known to impact significantly the stoichiometry and the chemical stability of defects (oxygen vacancies, etc…) of ZnO thin films [3], [12]. Moreover, the porosity of $CuCrO_2$ synthesized on ZnO thin films, induced electrical short circuit in the junction (i.e punchthrough) of the p-type layer by the probes. Therefore, we did not consider this approach and proposed the deposition of ZnO by ALD on $CuCrO_2$ in order to take benefit of the low growth temperature of ZnO (T=150°C) that should not modify the electrical properties of $CuCrO_2$. The conformal deposition by ALD is also seen as critical benefit to avoid empty interface regions between $CuCrO_2$ and ZnO.

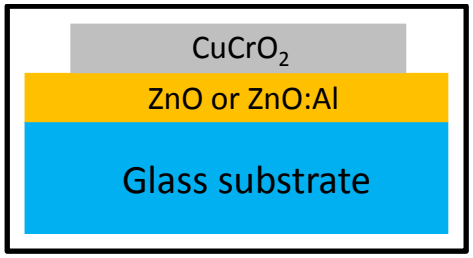

Figure 82 Schematic representation of pn junction synthesized with MOCVD approach.

VI.1.2 MOCVD/ALD process flow

The first layer was $CuCrO_2$ synthesized by MOCVD, and the second layer was ZnO synthesized by ALD. The process parameters for the growth of $CuCrO_2$ thin films are resumed in Table 13. Zinc oxide was synthesized by ALD with diethylzinc (DEZ) as precursor and water as oxydant at 150°C and 5mbar. The pulse sequence was: 150ms DEZ pulse/10s N_2 purge/200ms water pulse/10s N_2 purge.

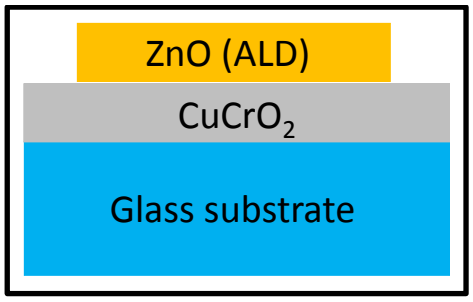

Figure 83 Schematic representation of p-n junction synthesized with MOCVD/ALD approach.

Table 13 Parameters used for synthesis of $CuCrO_2$/ZnO junctions with only MOCVD/ALD technics.

Material	$T_{surface}$ (°C)	P_{total} (mbar)	P_{O2} (mbar)	χ	$C_{prec.}$ (10^{-3} mol.L^{-1})	$Flow_{prec.}$ (g.min^{-1})	$N_{2\ carrier}$ (sccm)	Height (cm)	Rotation (rpm)
$CuCrO_2$	370	6	2.1	0.2-0.5	5	0.8	350	16	30

VI.1.2.1 Crystalline structure

An example of XRD diffractogram of MOCVD/ALD pn junctions is given Figure 84 for $CuCrO_2$ thin films synthesized by χ=0.5. The peaks reported at 2θ=31.5°, 36.3° and 62.3° cannot be distinctively attributed to ZnO or $CuCrO_2$, they can be either of the materials due to their closed reported peak diffraction data. However, the peaks at 2θ=40.9° and 68.0° make no doubt about the presence of $CuCrO_2$ and ZnO crystallographic phases respectively (arrows in Figure 84).

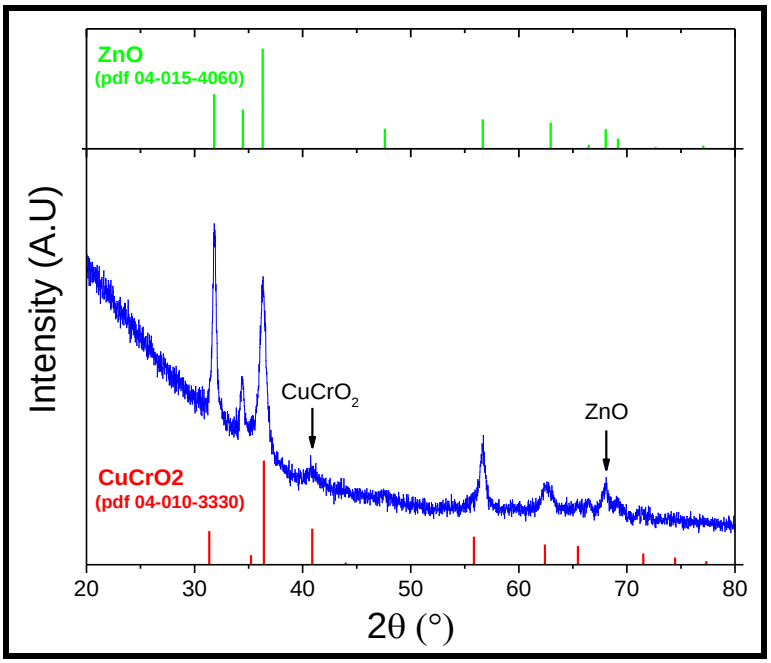

Figure 84 XRD diffractograms of MOCVD/ALD junction for $CuCrO_2$ thin films synthesized by χ=0.5

VI.1.2.2 Morphology

VI.1.2.2.1 SEM

The morphologies observed from SEM top view pictures of the MOCVD/ALD p-n junctions, after ALD synthesis, are presented in Figure 85. We show in Figure 85 (a) and (b) $CuCrO_2$ (χ=0.2)/ZnO (ALD) junction : (a) is $CuCrO_2$ (χ=0.2) and (b) is ZnO (ALD). Delafossite $CuCrO_2$ thin film keeps its morphology of "spines" (see Figure 46 (a)) and ZnO adopt a compact elongated grains structure. Similar observations are performed for delafossite $CuCrO_2$ (χ=0.33 and χ=0.5) and ZnO deposited by ALD, in Figure 85 (c), (d), (e) and (f): $CuCrO_2$ keep its post deposition morphology (Figure 46) and ZnO have a compact elongated grains structure It is noticed for the junction with $CuCrO_2$ synthesized with χ=0.5, elongated grains structure of ZnO (Figure 85 (f)) are smaller than others ZnO thin films (Figure 85 (b) and (d)). It is may be due to the morphology effect of smaller $CuCrO_2$ grains (which influence the growth of ZnO films) compared to $CuCrO_2$ grains in Figure 85 (a) and (c)

VI.1.2.2.2 TEM

A TEM observation of the junction grown with χ=0.33 for the $CuCrO_2$ thin films was done. The interface of the junction was observed with HAADF (Figure 86 (a)), and EDX

combined with HAADF (Figure 86 (b)). It appears that the interface is well defined, and a quantity of chlorine was introduced between $CuCrO_2$ and ZnO. Chlorine is attributed to the HCl chemical etching (1-5 $mol.l^{-1}$) of ZnO at a corner of the sample, in order to contact $CuCrO_2$ layers.

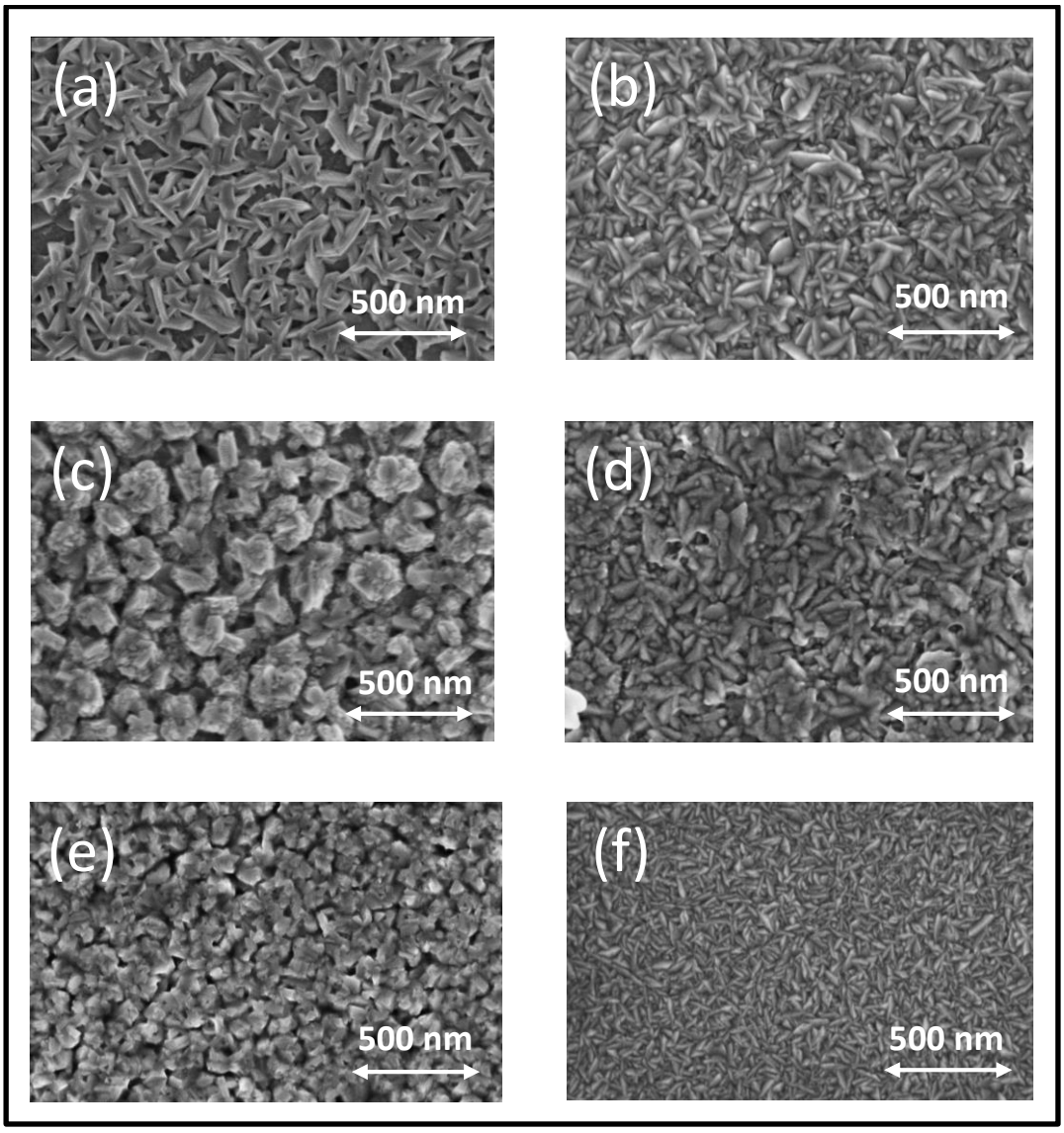

Figure 85 SEM top view images of MOCVD/ALD junctions after ZnO deposition on $CuCrO_2$ with (a) χ=0.2, (c) χ=0.33 and (d) χ=0.5. Images of respective ZnO deposition are (b), (d) and (e)

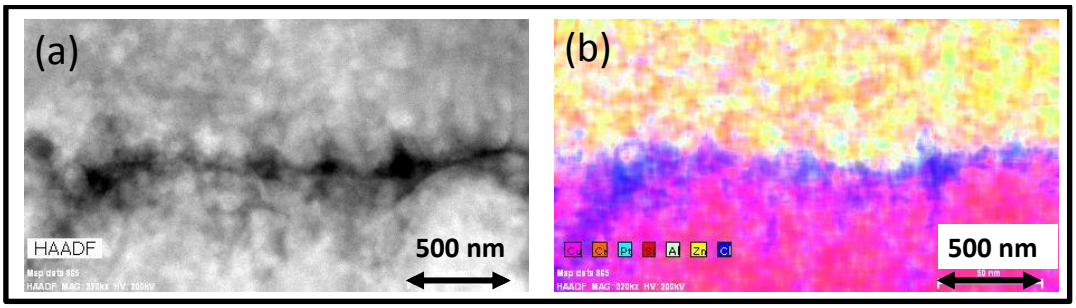

Figure 86 (a) HAADF observation of the pn junction interface with χ=0.33 for $CuCrO_2$ (b) EDX combined with HAADF mapping on the same region in (a)

In Figure 87 (a),(b),(c),(d) and (e), we show individual chemical mapping of Cu, Cr, O, Cl and Zn respectively when EDX is combined with HAADF. It was observed that chromium and zinc elements (Figure 87 (b) and (e)) don't diffuse in ZnO and $CuCrO_2$ films respectively. The chromium and zinc elements are homogeneous in $CuCrO_2$ and ZnO films respectively, as the oxygen element in both films (Figure 87 (c)). Copper seems to diffuse in ZnO films (Figure 87 (a)), but the redeposition of copper on ZnO film due to the sample preparation with FIB, cannot be exluded[k]. Finally, we observe the presence of chlorine in both $CuCrO_2$ and ZnO films, with an increased concentration at the interface.

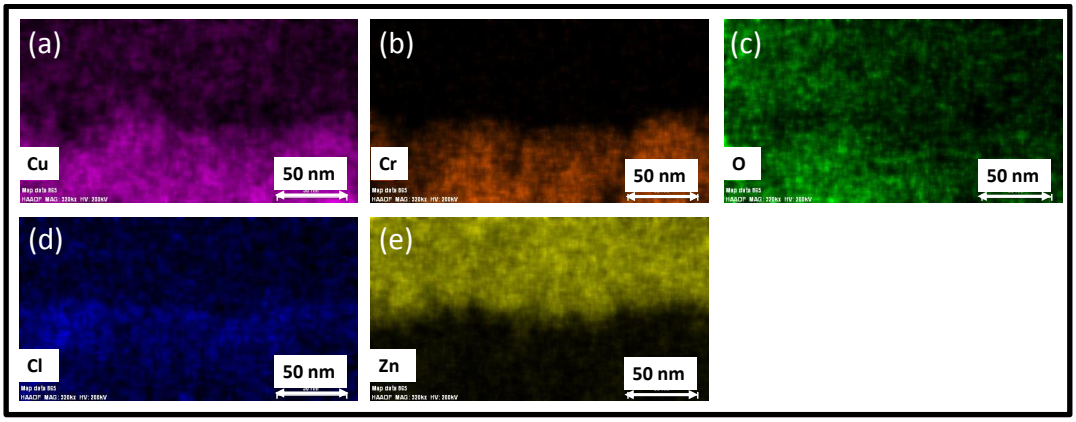

Figure 87 Individual chemical mapping done by EDX combined with HAADF of: (a) copper, (b) chromium, (c) oxygen, (d) chlorine and (e) zinc elements

VI.1.2.3 Chemical composition analysis

We investigate the chlorine concentration profile at the interface of p-n junctions with secondary ions mass spectrometry (SIMS) analysis for the MOCVD/ALD junctions. In Figure

[k] FIB technic used a gallium sputtering of the sample for TEM preparation. The sample is fixed on a support which is a piece of copper metal.

88 (a), (b) and (c), we show SIMS results of junction fabricated with χ=0.2, 0.33 and 0.5 respectively used for the growth of $CuCrO_2$ films. In all junctions, chlorine at the ZnO/$CuCrO_2$ interface was detected. For the junction with χ=0.2, 0.33, the chlorine peak at the interface is broader and less intense than in the case of the junction grown with χ=0.5. This is attributed to a more porous morphology of $CuCrO_2$ thin film with χ=0.2, 0.33 than χ=0.5 (Figure 85 (a), (c) and (e)) that may facilitate the diffusion of Cl into $CuCrO_2$ thin films

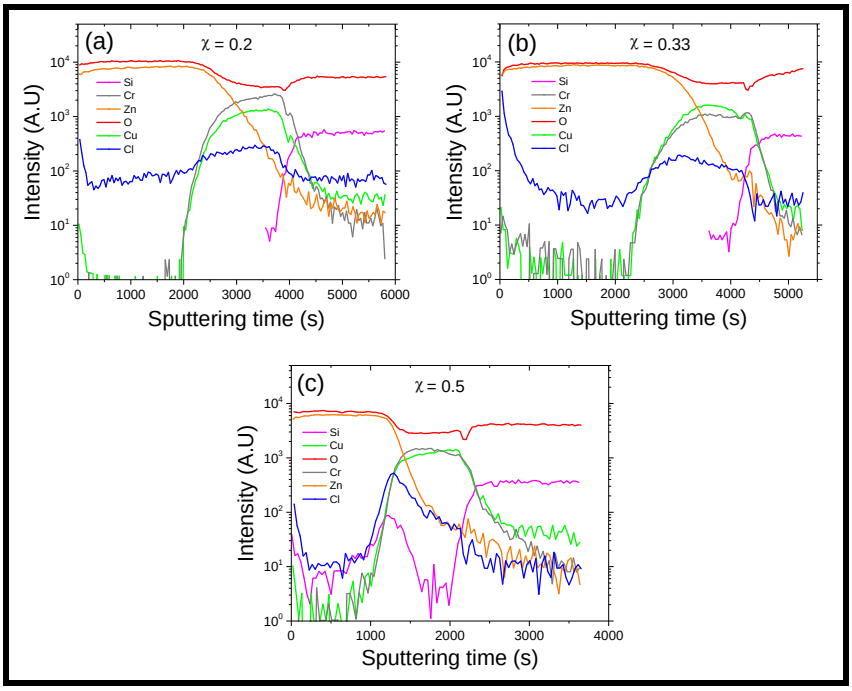

Figure 88 SIMS analysis of MOCVD/ALD p-n junction for $CuCrO_2$ thin films synthesized with (a) χ=0.2, (b) χ=0.33 and (c) χ=0.5

VI.2 Electrical and optical characterization

We present in this section, electrical and optical measurements of the MOCVD/ALD junctions

VI.2.1 Electrical properties

VI.2.1.1 MOCVD-ALD junction

The electrical measurements were done by applying two tungsten probes on material(s). I-V measurements of MOCVD/ALD junction is shown Figure 89 for delafossite $CuCrO_2$

synthesized with χ=0.33. An ohmic contact on $CuCrO_2$[1] thin film is obtained (Figure 89 (a)), while very low current (< $5x10^{-8}$A), close to the apparatus limits, was measured for ZnO thin films (Figure 89 (b)). Interestingly, I-V characteristic of a diode is observed for this junction (red line in Figure 89 (a)). However, it was observed an ohmic characteristic for the others junctions (synthesized with χ=0.2 and 0.5 for $CuCrO_2$ thin films), when "junction contact" is measured.

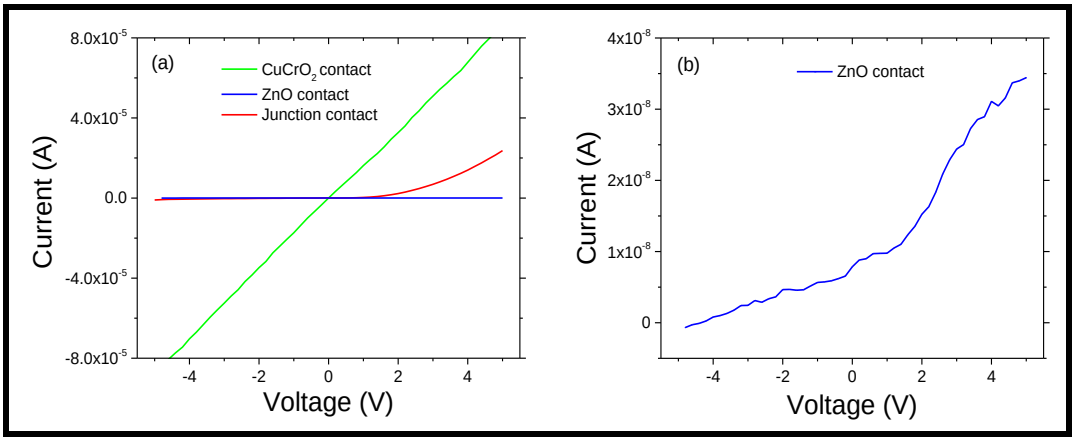

Figure 89 I-V curves of (a) $CuCrO_2$, ZnO and junction for the junction with delafossite $CuCrO_2$ synthesized with χ=0.33 (b) Zoom on I-V curve of ZnO

VI.2.1.2 Transport models

In this section, we report transport models to characterize our junction exhibited a diode characteristic (rectifying behaviour). I-V measurements were done at room temperature and at 130°C, in dark environment.

At room temperature (Figure 90), the reverse current (from -5V to 0V) is still very low as shown by the plot of current logarithm versus voltage (inset graph in Figure 90). This leakage current may be attributed to surface or generation-recombination of carrier effect[218].

The forward current exhibit at high voltage (2-5 V) a straight line (red line dot in Figure 90). This linear dependence of the current is due to the series resistance of the junction[218]. Between 0-1V, the forward current has an exponential dependence, as shown by the linear trend of the current logarithmic in this voltage range (inset graph in Figure 90). This trend can be in a first approximation modelled by the standard junction current model[218]:

[1] The contact on $CuCrO_2$ was measured by applying two tungsten probes on $CuCrO_2$ thin films. The same protocol was done for contact on ZnO. The I-V characteristic of diodes was measured with a probe on $CuCrO_2$ and another on ZnO.

$$\boldsymbol{I = I_0\left(e^{\frac{qV}{\eta k_B T}} - 1\right)} \qquad (66)$$

where I_0 is the reverse current, V the applied voltage and η the ideality factor.

The ideality factor equals 1 if the diffusion current dominates, or 2 if the recombination current dominates[218]. If the quantity $e^{\frac{qV}{\eta k_B T}}$ is higher than 1, then the current logarithm as a function of the voltage should be a straight line with a slope of $\frac{q}{\eta k_B T}$.

The threshold voltage is estimated when $I/I_o=100$ approximatively (Equation (66)). We found a threshold voltage at 1V which is in good agreement with the reported values for $CuCrO_2$/ZnO junctions (between 1 and 2V)[42][151].

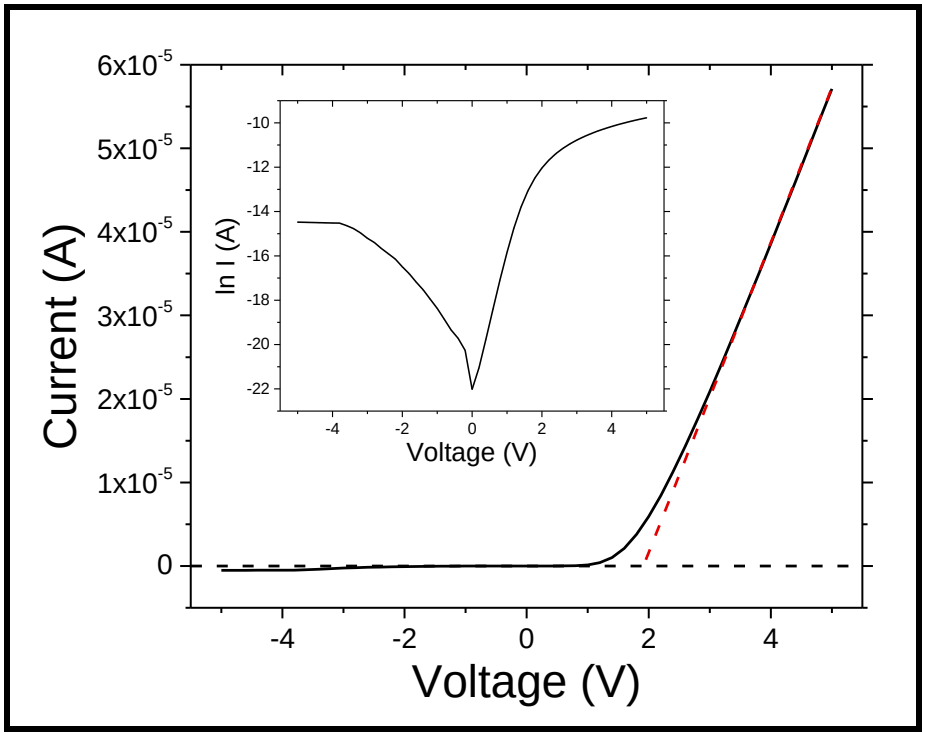

Figure 90 I-V curve of the MOCVD/ALD junction for $CuCrO_2$ synthesized with χ=0.33 at room temperature and in dark environment. The plot of the logarithm of the current is show in the inset graph.

The ideality factor of the junction is determined by the following relation[218]:

$$\boldsymbol{\eta = \frac{q}{k_B T}\left(\frac{dV}{d\ln I}\right)} \qquad (67)$$

which is valid for $e^{\frac{qV}{\eta k_B T}} \gg 1$, i.e for $V/\eta \geq 0.12$. It is observed in Figure 91, that our ideality factor is only constant in the range of 0.25-1V, and increases above an applied voltage of 1V. The ideality factor is not considered above 2V because the series resistance effect dominates

(Figure 90). According to the condition of $V/\eta \geq 0.12$, the ideality factor can take the values $6 \leq \eta \leq 15$ (Figure 91), which are in all cases, higher than 1 or 2 as for a classical diode. Such high ideality factor in p-n junctions were also observed for material with wide band gap like GaN[281], ZnO[282][283]… The mechanism involved in these cases is usually a tunnelling current between parasitic electronic states in the bandgap.

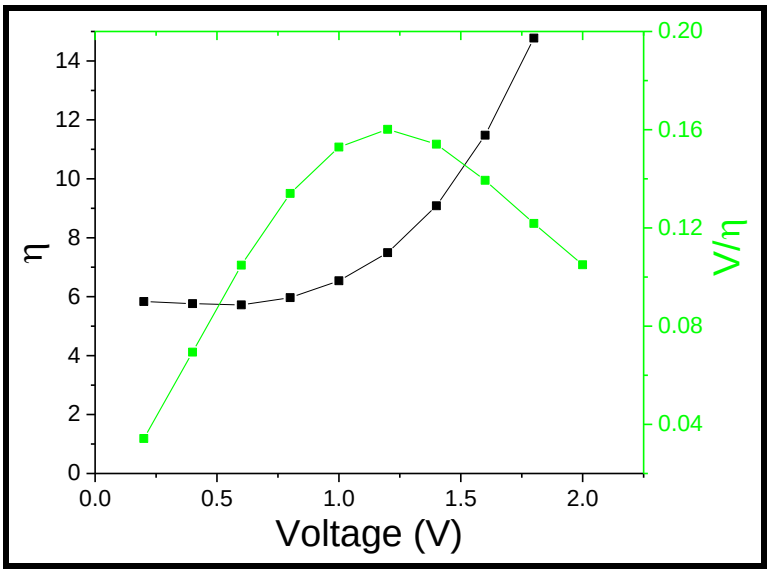

Figure 91 Ideality factor η and the quantity V/η as a function of applied voltage.

The intermediate regime between 1V to 2V, before series resistance effect (> 2V), is neither linear nor exponential dependent (Figure 90). It was reported in the literature, SCLC mechanism between 1-2.5V for a ZnO/$CuCrO_2$:Mg p-n junction (see §I.2.6) and for others p-n junctions [281], [284]. The SCLC mechanism is dependent on V^2 [218], [284], [285]. However, the quadratic fitting between 1V to 2V doesn't matched our I-V characteristic (not show). As the series resistance effect dominate on a large scale (>2V), we tried to fit our diode characteristic between -5V to 5V, with an electrical model based on p-n junction in series with high resistance. If series resistance effect is taking account in Equation (67), in that case the Equation (66) becomes [218]:

$$\boldsymbol{I = I_0\left(e^{(V-IR_s)/\eta V_T} - 1\right)} \qquad (68)$$

where R_s is the series resistance and $V_T=k_BT/q$. The current equation as a function of the applied voltage is not easily defined in Equation (68) due to the current term in the exponential factor in this equation. Numerical methods are often used to solve Equation (68), but an exact analytical solution has been preferably used in our case [286], [287] and is defined as:

$$I = \frac{\eta V_T}{R_s} lambertW\left(\frac{I_0 R_s}{\eta V_T} e^{\frac{V+I_0 R_s}{\eta V_T}}\right) - I_0 \qquad (69)$$

The "*lambertW*(x)" is a function like sin(x), ln(x), e^x etc… . This function is defined for real numbers between $]-\frac{1}{e};+\infty[$, is derivable and *lambertW*(xe^x)=x (like ln(e^x)=x)[288].

We show in Figure 92 a fitting of the I-V response of our diode (Figure 90) between -5V and +5V with the Equation (69). The fit perfectly match the measured I-V curve from -2V to 5V. The extracted parameter Rs (49.4kΩ) is also close to 54kΩ, the measured resistance between 4-5V (the inverse slope of the I-V curve). The extracted ideality factor was 7.9, which is in good agreement with wide band gap diodes [281]–[283]

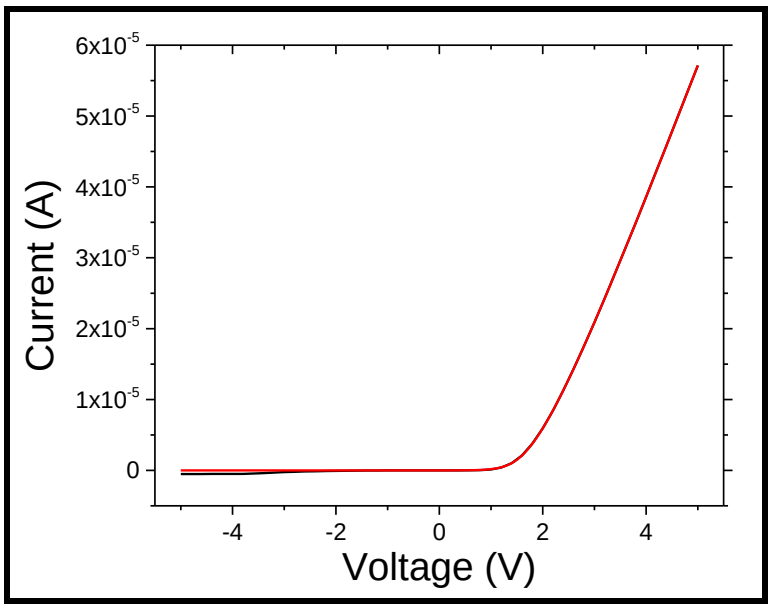

Figure 92 I-V curve at 30°C fitted with series resistance model

We also consider the p-n junction under heating at a temperature of 130°C. I-V curve at room temperature and at 130°C are compared in Figure 93 (a). The series resistance effect is also observed at 130°C but only above 4V and the threshold voltage is estimated at 1.8V. At 130°C, the trend below 4V is more similar to an exponential function than at room temperature, if we compare the exponential fit of the I-V curve (with Equation (66)) in Figure 93 (b). Again, the fitting with series resistance model at 130°C (Figure 93 (c)) is very close to the measured I-V curve, the extracted parameters R_s and η are 19.6kΩ and 11.9 respectively.

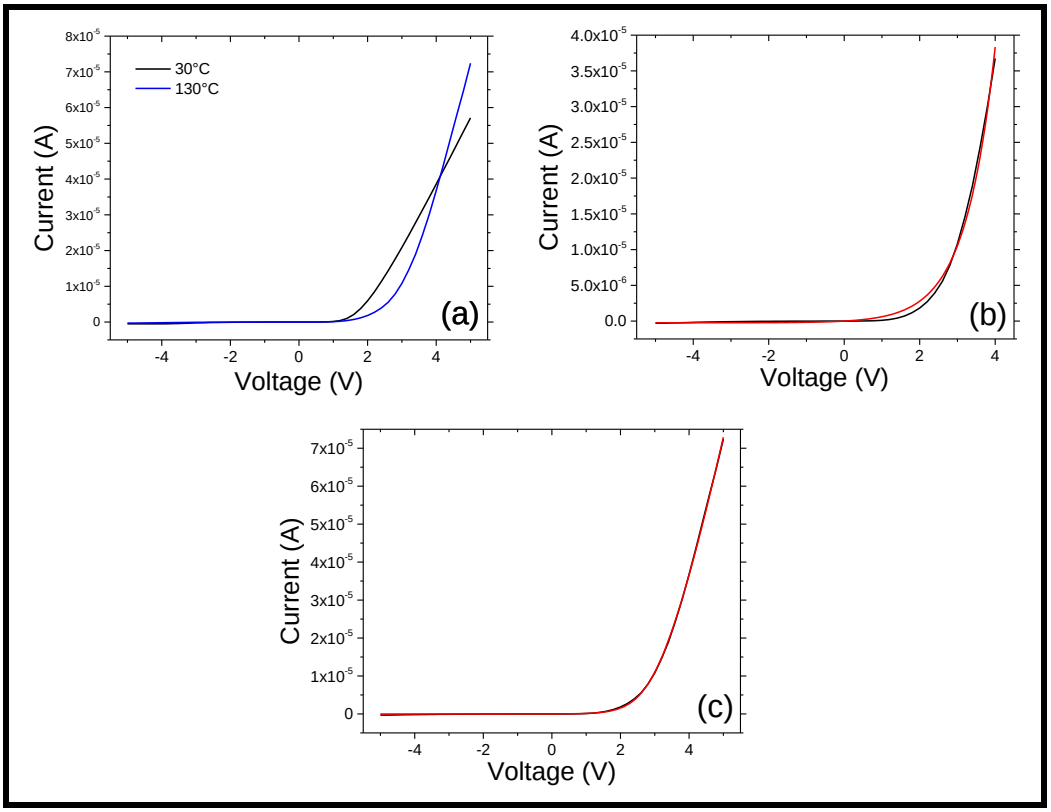

Figure 93 (a) I-V curves of the diode at 30°C and 130°C (b) I-V curve at 130°C (black line) fitted with Equation (66) (red line) and (c) I-V curve at 130°C (black line) fitted with Equation (69) (red line)

VI.2.1.3 UV illumination

I-V measurements of the junction under the UV illumination (λ_{UV} = 250 nm, 5.0 eV) was conducted. The flux of UV on the junction was varied by increasing the height between the junction and the UV lamp. I-V curves are presented in Figure 94 and the forward current increases significantly when the UV flux increases (the height of lamp decrease). This trend is attributed to an effect on series resistance. The threshold voltage decreases from 1 to 0.5V when the height of the lamp decreases from 80 to 10cm. Under the highest flux of UV (height of 10 cm), the reverse current is not negligible anymore ($-2x10^{-6}$ A). Our junction is efficiently acting as an UV detector.

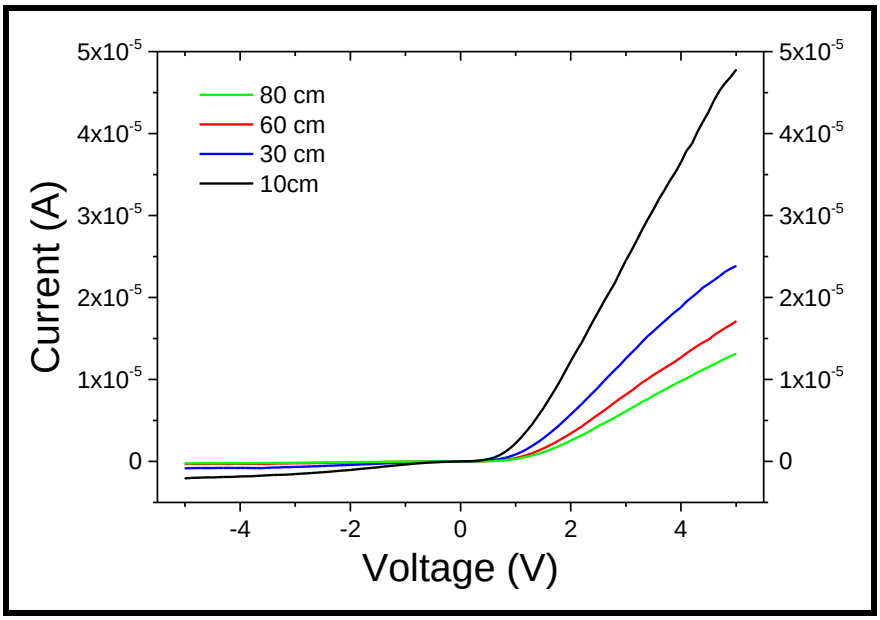

Figure 94 I-V curves under UV illuminations of the MOCVD/ALD junction synthesized with χ=0.33 for $CuCrO_2$

VI.2.2 Optical properties

The transmittance of the MOCVD/ALD junction with χ=0.33 for $CuCrO_2$ thin film is presented in Figure 95. It appears that the average transmittance of the p-n junction in the visible range (400-800 nm) is around 45-50% which is less than the reported $CuCrO_2$/ZnO p-n junctions, around 70% (see § I.2.6).

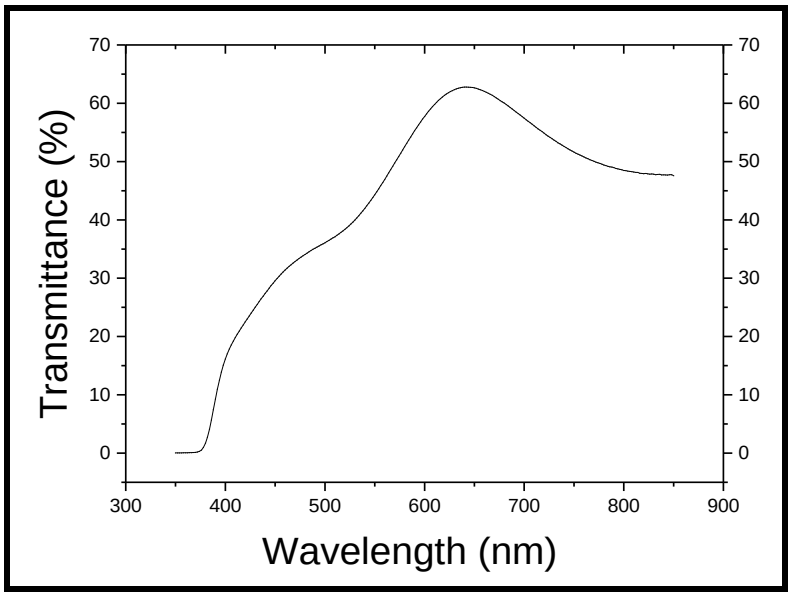

Figure 95 Transmittance of the p-n junction of the MOCVD/ALD junction synthesized with χ=0.33 for $CuCrO_2$

CONCLUSIONS AND OUTLOOK

Even if transparent electronic still need an archetypal of low cost transparent p-n junction, we show in this thesis a possible opportunity to achieve this objective with the synthesis of p-type $CuCrO_2$ by CVD approach.

Thin films of delafossite $CuCrO_2$ were synthesized by the pulsed injection MOCVD method and exhibited pure and polycrystalline phases under suitable growth parameters. The carbon contamination from chemical precursors during the synthesis was below 1%, which is far lower than classical CVD semiconductors synthesis. $CuCrO_2$ phase was synthesized by one step, without annealing, and with a growth temperature as low as 310°C. Direct $CuCrO_2$ synthesis at such low temperature was never previously reported. Interestingly, it was found that delafossite $CuCrO_2$ phases obtained by pulsed injection MOCVD features a significant excess of chromium in this films while maintaining the crystalline quality of the material. Such feature was very recently observed in works of Farrell et al.[131]. This excess of chromium influenced the chemical environment of copper, as it was observed a Cu^0 oxidation state and a lack of Cu 3d anti-bonding states near the VBM.

Our undoped delafossite $CuCrO_2$ thin films showed similar electrical properties than those reported for doped $CuCrO_2$ films. The measured electrical conductivity at room temperature was the highest reported of undoped films, due to the large carrier concentration meaning an important intrinsic doping that are correlated to the over stoichiometry of chromium and copper. The mobility measured was very low and activated with the temperature. Several ambiguities of small polaron and band conduction models prevent any conclusion on the nature of the transport conduction in our $CuCrO_2$ thin films. Optical band gap and transmittance of $CuCrO_2$ thin films are in the same range than $CuCrO_2$ thin films synthesized by others method. We obtained the best trade-off electrical conductivity-visible transparency of undoped $CuCrO_2$ films reported in literature.

PN junctions were synthesized with $CuCrO_2$ by pulsed injection MOCVD and ZnO by ALD. A functional junction was achieved with a mushroom morphology of $CuCrO_2$ thin films. This functional junction was obtained with only two layers while reported junctions of $CuCrO_2$ and ZnO used at least three layers. The visible transparency of our junction was between 45-50%. A high series resistance effect in the forward current of the diode is measured but is reduced when the temperature increase. The I-V response of the diode under UV illumination showed that our device can be used as an UV detector.

A first perspective of this work, could be a deeper study of electrical characterizations of the functional junction, like C-V measurement, in order to understand and model the transport of carriers in such junction architecture. The second perspective is the tailoring of the

carrier concentration of $CuCrO_2$ thin films in order to build functional transparent electronic p-type transistors. This objective may be achieved by annealing under nitrogen atmosphere or by the synthesis of stoichiometric $CuCrO_2$ films. An other perspective is the synthesis of our p-n junction on flexible substrates which handle at 300°C. The last perspective is the fundamental/experimental determination of the charge carrier transport (small polaron vs band conduction) in our $CuCrO_2$ thin films by X-ray spectroscopies and cyclotron

ANNEXES

Table 14 Compilation of delafossite $CuCrO_2$ properties reported in literature

Synthesis	Cristallinity	Dopant	Concentration	Conductivity ($S.cm^{-1}$) at RT	Activation energy (eV)	Carrier concentration (cm^{-3}) at RT	Mobility ($cm^2/V.s$)	Seebeck ($\mu V.K^{-1}$)	Transparency (in visible range)	Band gap direct (eV)	Band gap indirect (eV)	Thickness (nm)	REF
SG	polycristalline	Xxxxx	xxxxx	0.00088		1.42 E15	3.89		45	3.14	2.79	320	[34]
SG	polycristalline	Xxxxx	xxxxx	0.02		1.3 E17	0.96		55-65	3		150-180	[35]
SG	polycristalline	Xxxxx	xxxxx	0.038		1.7 E17	1.4						[35]
SG	polycristalline	xxxxx	xxxxx	0.023		1.9 E17	0.76						[35]
SG	polycrystalline	xxxxx	xxxxx	0.0048					60-70	3.15	2.66	90	[37]
SG	polycristalline	xxxxx	xxxxx	0.017				202	40			280	[289]
SG	polycristalline	xxxxx	xxxxx	0.15		1.7 E18	0.56	20	50-55	3		190	[290]
SG	polycristalline	Zn	0.01	0.26		2.15 E18	0.76	40	50	3.05		220	[290]
SG	polycristalline	Zn	0.03	0.47		3.2 E18	0.92	113	50	3.05		205	[290]
SG	polycristalline	xxxxx	xxxxx	0.0006	0.321	2.9 E14	14.3		50	3.09	2.72	250	[33]
SG	polycristalline	Ga	0.2	0.0017	0.284	2.19 E15	5.05		50	3.13	2.78	240	[33]
SG	polycristalline	Ga	0.4	0.0024	0.252	7.29 E15	2.18		50	3.18	2.83	250	[33]
SG	polycristalline	xxxxx	xxxxx	0.0011	0.285	2.8 E14	25		45-55	2.95		190	[38]
SG	polycristalline	Cr deficient	0.05	0.0032		3.8 E15	5.3		45-55			190	[38]
SG	polycristalline	xxxxx	0.1	0.0044	0.275	5.9 E15	4.7		60	3		190	[38]
SG	polycristalline	xxxxx	0.2	0.16	0.180	1.8 E16	56		60	3.1		210	[38]
SG	single crystal	xxxxx	xxxxx	0.018		3.14 E15	6.75	266	65-70	3.15	2.8	103	[117]
SG	single crystal	Mg	0.03	0.027		2.53 E16	3.47	202	60	3.12	2.77	107	[117]
SG	single crystal	Mg	0.05	0.14		3.14 E18	2.13	180	60	3.11	2.76	113	[117]
SG	single crystal	Mg	0.07	0.02		6.23 E15	6.12	248	60	3.1	2.75	115	[117]
PLD	single crystal	xxxxxx	xxxxx	0.25			0.1<		55-60	3.2		130	[39]
PLD	single crystal	xxxxxx	xxxxx	4.8	0.169	3.13 E19	0.97		55	3.13			[133]
PLD	single crystal	Mn	0.05	0.017		1.63 E17	0.64						[133]
PLD	single crystal	Mn	0.1	0.008		6.59 E16	0.76						[133]
PLD	single crystal	Mn	0.15	0.08		1.26 E17	4.12						[133]

Table 14 Compilation of delafossite $CuCrO_2$ properties reported in literature (next)

Synthesis	Cristallinity	Dopant	Concentration	Conductivity ($S.cm^{-1}$) at RT	Activation energy (eV)	Carrier concentration (cm^{-3}) at RT	Mobility ($cm^2/V.s$)	Seebeck ($\mu V.K^{-1}$)	Transparency (in visible range)	Band gap direct (eV)	Band gap indirect (eV)	Thickness (nm)	REF
PLD	single crystal	xxxxxx	xxxxx	1.79	0.110	1.4 E18	7.7		65	3.17		25	[41]
PLD	single crystal	Fe	0.05	2.53	0.067	2.52 E18	6.27		55	3.1		36	[41]
PLD	single crystal	Fe	0.1	5.55	0.064	6.51 E18	5.32		55	3.1		38	[41]
PLD	single crystal	Fe	0.15	27.8	0.04	4.09 E19	4.2		55	3.1		52	[41]
PLD	polycristalline	xxxxxx	xxxxx	0.015					55	3.2		57	[43]
PLD	polycristalline	xxxxxx	xxxxx	0.33					60	3.2		127	[43]
PLD	polycristalline	xxxxxx	xxxxx	0.011					60	3.2		134	[43]
PLD		xxxxxx	xxxxx	0.015					60	3.2		57	[128]
PLD		Mg	0.02	2.5					60	3.2		57	[128]
PLD	polycristalline	Mg	0.1	66.67		1 E22	0.042					135	[135]
PLD	single crystal	xxxxxx	xxxxx	8.3					60-65			50	[291]
PLD	single crystal	Mg	0.2	16.35					60-65			50	[291]
PLD	single crystal	Mg\VCr	0.2	29.63					60-65			50	[291]
MS	polycristalline	xxxxxx	xxxxx	1								200-300	[17]
MS	polycristalline	Mg	5%	220									[17]
MS	polycristalline	Mg	0.03	17.76				140	40	3.3		100	[129]
MS	polycristalline	Mg	0.03	64.27	0.055			116	45	3.3		100	[129]
MS	polycristalline	Mg	0.03	52.82	0.055			121	50	3.3		100	[129]
MS	polycristalline	Mg	0.03	37.78	0.055			122	55	3.3		100	[129]
MS	polycristalline	Mg	0.03	52.16	0.055			133	60	3.3		100	[129]
MS	polycristalline	xxxxx	xxxxx	0.43		1.4 E19	0.19		60-65	3.14		100	[44]
MS	polycristalline	xxxxx	xxxxx	0.38		1.2 E19	0.18						[44]
MS	polycristalline	xxxxxx	xxxxx	0.08		4.5 E18	0.11		50	3.05		280-300	[47]
MS	polycristalline	N	0.1	0.018		8.7 E18	0.14		50	3.11		280-301	[47]
MS	polycristalline	N	0.2	0.11		3.0 E19	0.25		50	3.15		280-302	[47]

Table 14 Compilation of delafossite $CuCrO_2$ properties reported in literature (next)

Synthesis	Cristallinity	Dopant	Concentration	Conductivity ($S.cm^{-1}$) at RT	Activation energy (eV)	Carrier concentration (cm^{-3}) at RT	Mobility ($cm^2/V.s$)	Seebeck ($\mu V.K^{-1}$)	Transparency (in visible range)	Band gap direct (eV)	Band gap indirect (eV)	Thickness (nm)	REF
MS	polycristalline	N	0.3	1.7	0.035	1.4 E20	0.81		50			280-303	[47]
MS	polycristalline	Mg	0.05	0.057		10 E17	0.2			3.2		135	[151]
MS	polycristalline	Mg	0.05	0.17		2.5 E18	0.25			3.2		135	[151]
MS	polycristalline	Mg	0.05	0.4		6 E18	0.4			3.2		135	[151]
CSD	polycristalline	Mg		0.28		8 E18	0.2		50	3.1		197	[292]
CSD	polycristalline	Mg		3.13		5 E19	0.7		70	3.1		195	[292]
CSD	polycristalline	Mg		0.14		1 E18	0.7		70	3.1		195	[292]
CVD	polycristalline	xxxxxx	xxxxx	0.86	0.108	4.8 E17*	11*		40-50	3.08		390	[49]
SS	polycristalline	xxxxxx	xxxxx	0.001	0.280			1100					[30]
SS	polycristalline	Mg	0.005	0.05	0.17			600					[30]
SS	polycristalline	Mg	0.01	0.13	0.17			400					[30]
SS	polycristalline	xxxxx	xxxxx	0.0036	0.278			350					[25]
SS	polycristalline	Mg	0.005	0.67	0.119			190					[25]
SS	polycristalline	Mg	0.01	1.2	0.095			170					[25]
SS	polycristalline	Mg	0.02	8.33	0.036			90					[25]
SS	polycristalline	Mg	0.03	15.6	0.026			75					[25]
SS	polycristalline	Mg	0.04	11		8.7 E20	0.078	50					[25]
SS	polycristalline	xxxxxx		0.000949	0.29								[134]
SS	polycristalline	Ni	2%	0.01	0.24								[134]
SS	polycristalline	Ni	4%	0.03	0.23								[134]
SS	polycristalline	Ni	6%	0.047	0.23								[134]

Table 15 Compilation of delafossite compounds properties reported in literature

Material	Synthesis	Cristallinity	Dopant	Concentration	Conductivity ($S.cm^{-1}$) at RT	Activation energy (eV)	Carrier concentration (cm^{-3}) at RT	Mobility ($cm^2/V.s$)	Seebeck ($\mu V/K^{-1}$)	Transparency in visible range (%)	Band gap direct (eV)	Band gap indirect (eV)	Thickness (nm)	REF
CuAlO2	MS	polycrystalline	xxxxx	xxxxx	0.01								400-800	[293]
CuAlO2	MS	polycrystalline	xxxxx	xxxxx	0.08	0.26	3.7 E17	1.4	128	70	3.66	2.1	700	[294]
CuAlO2	MS	polycrystalline	Excess oxygen	0.05	0.4	196	1.2 E18	1.4	213				500	[295]
CuAlO2	MS	polycrystalline	Excess oxygen	0.02	0.08	245	4.2 E17	1.19					500	[295]
CuAlO2	MS	polycrystalline	Excess oxygen	0.005	0.15	270	2,8 E17	3.35					500	[295]
CuAlO2	MS	polycrystalline	xxxxx	xxxxx	0.22	0.25	4.4 E17	3.1	115	80	3.75	1.85	?	[296]
CuAlO2	MS		xxxxx	xxxxx	0.0021					50			310	[297]
CuAlO2	MS	polycrystalline	xxxxx	xxxxx	0.01		3.7 E16	1.8		65	3.4		300	[298]
CuAlO2	MS	polycrystalline	xxxxx	xxxxx	8,2 E-6		8,88 E13	0.6						[299]
CuAlO2	MS	polycrystalline	xxxxx	xxxxx	0.00019		1,45 E15	0.82						[299]
CuAlO2	MS	polycrystalline	xxxxx	xxxxx	0.0013		8.2 E16	0.1						[299]
CuAlO2	MS	polycrystalline	xxxxx	xxxxx	0.2	0.23	1.0 E18	1.3	130					[300]
CuAlO2	MS	polycrystalline	xxxxx	xxxxx	0.0021		3,09 E16	0.42		70			90	[301]
CuAlO2	MS	polycrystalline	xxxxx	xxxxx	0.0104		4,11 E16	1.58		50			165	[301]
CuAlO2	MS	polycrystalline	xxxxx	xxxxx	0.0143		4,72 E16	1.87		50			305	[301]
CuAlO2	MS	polycrystalline	xxxxx	xxxxx	0.0155		4,70 E16	2.02		45			460	[301]
CuAlO2	MS	polycrystalline	xxxxx	xxxxx	0.0166		4.84 E16	2.11		40	3.25	1.7	580	[301]
CuAlO2	MS	polycrystalline	xxxxx	xxxxx	0.0041		2,0 E16	1.25			3.3		460	[302]
CuAlO2	MS	polycrystalline	xxxxx	xxxxx	0.0043		1,7 E16	1.37			3.3		460	[302]
CuAlO2	MS	polycrystalline	xxxxx	xxxxx	0.038		4.8 E16	4.08			3.1		530	[303]
CuAlO2	MS	polycrystalline	xxxxx	xxxxx	0.032		4.0 E16	3.6			3		530	[303]
CuAlO2	MS	polycrystalline	xxxxx	xxxxx	0.066		8.9 E17	0.5					120-130	[304]
CuAlO2	MS	polycrystalline	xxxxx	xxxxx	0.125		7 E17	1					120-130	[304]
CuAlO2	MS	polycrystalline	xxxxx	xxxxx	0.25		3 E17	7.5					120-130	[304]
CuAlO2	MS	polycrystalline	xxxxx	xxxxx	0.3		1.5 E17	13		55	3.5		120-130	[304]

Table 15 Compilation of delafossite compounds properties reported in literature (next)

Material	Synthesis	Cristallinity	Dopant	Concentration	Conductivity ($S.cm^{-1}$) at RT	Activation energy (eV)	Carrier concentration (cm^{-3}) at RT	Mobility ($cm^2/V.s$)	Seebeck ($\mu V/K^{-1}$)	Transparency in visible range (%)	Band gap direct (eV)	Band gap indirect (eV)	Thickness (nm)	REF
CuAlO2	MS	polycrystalline	xxxxx	xxxxx	0.17		3 E17	5					120-130	[304]
CuAlO2	MS	polycrystalline	xxxxx	xxxxx	0.031		1.1 E17	1.6						[305]
CuAlO2	MS	polycrystalline	xxxxx	xxxxx	0.056		1.2 E17	3						[305]
CuAlO2	MS	polycrystalline	xxxxx	xxxxx	0.11		1.5 E17	4						[305]
CuAlO2	MS	polycrystalline	xxxxx	xxxxx	0.33		2.3 E17	7						[305]
CuAlO2	MS	polycrystalline	xxxxx	xxxxx	0.51		3.3 E17	9.4						[305]
CuAlO2	MS	polycrystalline	xxxxx	xxxxx	0.027		3.4 E16	4		55	3.0-3.8			[306]
CuAlO2	PLD	single crystal	xxxxx	xxxxx	0.3	0.2	2.7 E19	0.13	214	70	3.5	1.8	500	[307]
CuAlO2	PLD	polycrystalline	xxxxx	xxxxx	1	0.2	1.3 E17	10.4	183	40	3.5		500	[14]
CuAlO2	PLD		xxxxx	xxxxx	0.01						3.4		270	[308]
CuAlO2	SS		xxxxx	xxxxx	0.0017		1.1 E19	0.001	670			1.65		[309]
CuAlO2	SS	polycrystalline	xxxxx	xxxxx	0.0077		5.8 E16	1.1	300					[310]
CuAlO2	SS	polycrystalline	xxxxx	xxxxx	0.013		3.8 E17	0.22						[311]
CuAlO2	SS	polycrystalline	Na	0.07	0.013		5.7 E17	0.14						[311]
CuAlO2	SG	polycrystalline	xxxxx	xxxxx	0.067					45	3.8		400	[312]
CuAlO2	SG		xxxxx	xxxxx	0.0015				440	65			530	[289]
CuAlO2	SG	polycrystalline	xxxxx	xxxxx	0.04		4.99 E16	5					200-450	[313]
CuAlO02	SG	polycrystalline	xxxxx	xxxxx	0.05		4.16 E16	7.5					200-450	[313]
CuAlO2	SG	polycrystalline	xxxxx	xxxxx	0.1		5.94 E16	10.5					200-450	[313]
CuAlO2	SG	polycrystalline	xxxxx	xxxxx	0.5		2.08 E17	15					200-450	[313]
CuAlO2	CSD	polycrystalline	xxxxx	xxxxx	0.0066	0.133	6.7 E16	0.6		70	3.48		250	[314]
CuAlO2	CSD		xxxxx	xxxxx	0.0028	0.108				70	3.0-3.2		270	[315]
CuAlO2	uwave		xxxxx	xxxxx	0.02				700		3.9	2.9	200-300	[316]
CuAlO2	Flux method		xxxxx	xxxxx	0.017	0.6					3.4	2.22	1000	[317]
CuAlO2	Epit.		xxxxx	xxxxx	10E-3 - 10E-4					70	3.6		100	[318]

Table 15 Compilation of delafossite compounds properties reported in literature (next)

Material	Synthesis	Cristallinity	Dopant	Concen-tration	Conductivity ($S.cm^{-1}$) at RT	Activation energy (eV)	Carrier concentration (cm^{-3}) at RT	Mobility ($cm^2/V.s$)	Seebeck ($\mu V/K^{-1}$)	Transparency in visible range (%)	Band gap direct (eV)	Band gap indirect (eV)	Thickness (nm)	REF
CuAlO2	Hydro.	polycrystalline	xxxxx	xxxxx	2.4	0.14	5.4 E18	3.6	1050	55	3.75		420	[319]
CuYO2	SS		xxxxx	xxxxx	< 0.000001						3.5			[106]
CuYO2			xxxxx	xxxxx	< 0.018		0.026 E20<	< 0.04						[257]
CuScO2			xxxxx	xxxxx	< 0.37		0.45 E20<	< 0.05						[257]
CuScO2			xxxxx	xxxxx	0.00012					70	3.7			[320]
CuScO2			xxxxx	xxxxx	1.00E-06					75	3.7			[321]
CuScO2			xxxxx	xxxxx	15									[322]
CuScO2			xxxxx	xxxxx	0.001		4.5 E16	0.14	968					[323]
CuFeO2			xxxxx	xxxxx	0.097									[324]
CuFeO2			xxxxx	xxxxx	1.9 E-5		1.2 E20	1.00E-05						[325]
CuFeO2			xxxxx	xxxxx	0.67									[326]
CuFeO2			xxxxx	xxxxx	0.1-0.6									[327]
CuFeO2			xxxxx	xxxxx	0.65									[328]2
CuGaO2			xxxxx	xxxxx	0.063		1.7 E18	0.23	560	80				[329]
CuGaO2			xxxxx	xxxxx	0.0056		2.4 E18	0.015	790					[330]
CuGaO2			xxxxx	xxxxx	0.02				360	70-85			500	[7]
CuGaO2			xxxxx	xxxxx	0.017		5 E17	0.2						[331]
CuInO2			xxxxx	xxxxx	2.00E-10									[332]
CuInO2			xxxxx	xxxxx	0.056		1.6 E19	0.2		70				[333]

Table 16 Compilation of p-type non delafossite TOS properties reported in literature

P-TCO	Synthesis	Doping	Conductivity ($S.cm^{-1}$) at RT	Activation energy (eV)	Carrier concentration (cm^{-3}) at RT	Mobility ($cm^2/V.s$)	Seebeck coefficient ($\mu V.K^{-1}$)	Transparency in visible range (%)	Band gap direct (eV)	Band gap indirect (eV)	Thickness (nm)	Ref.
$SrCu_2O_2$	PLD		0.007				+46.61	60	3.3		220	[81]
$SrCu_2O_2$	PLD		0.0039	0.2			260	70	3.3		150	[80]
$SrCu_2O_2$	PLD	K	0.048	0.1	6.1 E17	0.46	260	75	3.3		120	[80]
$SrCu_2O_2$	e-beam		0.053		1.5 E17	2.2		60	3.12		70-100	[79]
$SrCu_2O_2$	Sol gel		0.002					55			500	[82]
$SrCu_2O_2$	Sol gel	K	0.012		3 E17	0.27	280	50			500	[82]
$NiCo_2O_4$	MS		333					15			100	[91]
$NiCo_2O_4$	Solid state		30				370					[89]
$NiCo_2O_4$	Solid state	Ca	60				370					[89]
$NiCo_2O_4$	Sol gel		17					60			20	[92]
$NiCo_2O_4$	Hydrothermal								2.1/3.6			[88]
$ZnCo_2O_4$	PLD		0.39/0.61	0.042			131	26	2.26		100-300	[96]
$ZnCo_2O_4$	MS		9.0	0.041	2.8 E20	0.2		15	2.63		400	[94]
$ZnRh_2O_4$	Solid State		0.84/4.0		1.4 E20	0.18						[146]
$ZnRh_2O_4$	PLD		2.75/2.83	0.022			+63.4	55	2.74		100-300	[96]
$ZnRh_2O_4$	RF sputtering		0.7	0.037			140		2.1			[97]
$ZnIr_2O_4$	PLD		3.39/2.09	0.047			+53.9	61	2.97		100-300	[96]
LaCuOS	R-SPE		0.66		1 E19	0.5	250				150	[98]
LaCuOSe	R-SPE		24		2 E19	8	250				150	[98]
LaCuOSe	R-SPE	Mg	910		1.7 E21	4			2.8		50	[99]

BIBLIOGRAPHY

[1] J. F. Wager, D. A. Keszler, and R. E. Presley, *Transparent Electronics*, Springer. New York, 2008.
[2] G. Helwig, "Elektrische Leitfähigkeit und Struktur aufgestäubter Kadmiumoxydschichten," *Zeitschrift für Phys.*, vol. 132, pp. 621–642, 1952.
[3] D. S. Ginley, H. Hosono, and D. C. Paine, *Handbook of transparent conductors*, no. November. New York: Springer, 2010.
[4] D. S. Ginley and C. Bright, "Transparent conducting oxides," *MRS Bull.*, vol. 25, no. 08, pp. 15–18, 2000.
[5] F. Yang and S. R. Forrest, "Organic Solar Cells Using Transparent SnO2-F Anodes," *Adv. Mater.*, vol. 18, no. 15, pp. 2018–2022, 2006.
[6] Y. Z. Zheng, X. Tao, L. X. Wang, H. Xu, Q. Hou, W. L. Zhou, and J. F. Chen, "Novel ZnO-based film with double light-scattering layers as photoelectrodes for enhanced efficiency in dye-sensitized solar cells," *Chem. Mater.*, vol. 22, no. 3, pp. 928–934, 2010.
[7] J. Tate, M. K. Jayaraj, A. D. Draeseke, T. Ulbrich, A. W. Sleight, K. A. Vanaja, R. Nagarajan, J. F. Wager, and R. L. Hoffman, "p-Type oxides for use in transparent diodes," *Thin Solid Films*, vol. 411, no. 1, pp. 119–124, 2002.
[8] M. Gratzel, "Photoelectrochemical Cells," *Nature*, vol. 414, no. 6861, pp. 338–344, 1995.
[9] H. Hosono, "Built-in Nanostructures in Transparent Oxides for Novel Photonic and Electronic Functions Materials," *Int. J. Appl. Ceram. Technol.*, vol. 1, pp. 106–118, 2004.
[10] C. G. Granqvist and A. Hultåker, "Transparent and conducting ITO films: new developments and applications," *Thin Solid Films*, vol. 411, no. 1, pp. 1–5, 2002.
[11] M. Batzill and U. Diebold, "The surface and materials science of tin oxide," *Prog. Surf. Sci.*, vol. 79, no. 2–4, pp. 47–154, 2005.
[12] Ü. Özgür, Y. I. Alivov, C. Liu, A. Teke, M. A. Reshchikov, S. Do, and V. Avrutin, "A comprehensive review of ZnO materials and devices," *J. Appl. Phys.*, vol. 98, p. 041301, 2005.
[13] H. Ohta, K. Kawamura, M. Orita, M. Hirano, N. Sarukura, and H. Hosono, "Current injection emission from a transparent p-n junction composed of p-SrCu2O2/n-ZnO," *Appl. Phys. Lett.*, vol. 77, no. 4, pp. 475–477, 2000.
[14] H. Kawazoe, M. Yasukawa, H. Hyodo, M. Kurita, H. Yanagi, and H. Hosono, "P-type electrical conduction in transparent thin films of CuAlO2," *Nature*, vol. 389, no. 6654, pp. 939–942, 1997.
[15] H. Kawazoe, H. Yanagi, K. Ueda, and H. Hosono, "Transparent p-Type Conducting Oxides: Design and Fabrication of p-n Heterojunctions," *MRS Bull.*, vol. 25, pp. 28–36, 2000.
[16] M. A. Marquardt, N. A. Ashmore, and D. P. Cann, "Crystal chemistry and electrical properties of the delafossite structure," *Thin Solid Films*, vol. 496, no. 1, pp. 146–156, 2006.
[17] R. Nagarajan, A. D. Draeseke, A. W. Sleight, and J. Tate, "p-type conductivity in CuCr1-xMgxO2 films and powders," *J. Appl. Phys.*, vol. 89, no. 12, pp. 8022–8025, 2001.
[18] T. Arnold, D. J. Payne, A. Bourlange, J. P. Hu, R. G. Egdell, L. F. J. Piper, L. Colakerol, A. Masi, P. A. Glans, T. Learmonth, K. E. Smith, J. Guo, D. O. Scanlon, A. Walsh, B. J. Morgan, and G. W. Watson, "X-ray spectroscopic study of the electronic structure of CuCrO," *Phys. Rev. B*, vol. 79, p. 075102, 2009.
[19] D. O. Scanlon, A. Walsh, B. J. Morgan, G. W. Watson, D. J. Payne, and R. G. Egdell, "Effect of Cr substitution on the electronic structure of CuAl1-xCrxO2," *Phys. Rev. B*,

vol. 79, no. 3, p. 035101, 2009.
[20] D. O. Scanlon, K. G. Godinho, B. J. Morgan, and G. W. Watson, "Understanding conductivity anomalies in CuI -based delafossite transparent conducting oxides: Theoretical insights," *J. Chem. Phys.*, vol. 132, no. 2, 2010.
[21] T. Yokobori, M. Okawa, K. Konishi, R. Takei, K. Katayama, S. Oozono, T. Shinmura, T. Okuda, H. Wadati, E. Sakai, K. Ono, H. Kumigashira, M. Oshima, T. Sugiyama, E. Ikenaga, N. Hamada, and T. Saitoh, "Electronic structure of the hole-doped delafossite oxides CuCr 1-xMgxO2," *Phys. Rev. B*, vol. 87, no. 19, p. 195124, 2013.
[22] D. O. Scanlon and G. W. Watson, "Understanding the p-type defect chemistry of CuCrO2," *J. Mater. Chem.*, vol. 21, no. 11, p. 3655, 2011.
[23] D. O. Scanlon and G. W. Watson, "Conductivity Limits in CuAlO2 from Screened-Hybrid Density Functional Theory," *J. Phys. Chem. Lett.*, vol. 1, no. 21, pp. 3195–3199, 2010.
[24] Y. Ono, K. I. Satoh, T. Nozaki, and T. Kajitani, "Structural, magnetic and thermoelectric properties of delafossite-type oxide, CuCr1-xMgxO2 (0<x<0.05)," *Jpn. J. Appl. Phys.*, vol. 46, pp. 1071–1075, 2007.
[25] T. Okuda, N. Jufuku, S. Hidaka, and N. Terada, "Magnetic, transport, and thermoelectric properties of the delafossite oxides CuCr1-xMgxO2 (0<x<0.04)," *Phys. Rev. B*, vol. 72, no. 14, p. 144403, 2005.
[26] Y. Ma, X. Zhou, Q. Ma, A. Litke, P. Liu, Y. Zhang, C. Li, and E. J. M. Hensen, "Photoelectrochemical Properties of CuCrO2: Characterization of Light Absorption and Photocatalytic H2 Production Performance," *Catal. Letters*, vol. 144, pp. 1487–1493, 2014.
[27] S. Kato, R. Kawashima, and M. Ogasawara, "Oxygen storage–release behavior of delafossite-type CuCr1−xMxO2 (M = Fe, Ga)," *J. Mater. Sci.*, vol. 50, no. 7, pp. 2876–2883, 2015.
[28] M. Amami, C. V. Colin, P. Strobel, and A. Ben Salah, "Al-doping effect on the structural and physical properties of delafossite-type oxide CuCrO2," *Phys. B*, vol. 406, no. 11, pp. 2182–2185, 2011.
[29] M. Poienar, F. Damay, C. Martin, V. Hardy, A. Maignan, and G. André, "Structural and magnetic properties of CuCr1−xMgxO2 by neutron powder diffraction," *Phys. Rev. B*, vol. 79, no. 1, p. 014412, 2009.
[30] A. Maignan, C. Martin, R. Frésard, V. Eyert, E. Guilmeau, S. Hébert, M. Poienar, and D. Pelloquin, "On the strong impact of doping in the triangular antiferromagnet CuCrO2," *Solid State Commun.*, vol. 149, no. 23–24, pp. 962–967, 2009.
[31] A. P. Amrute, Z. Łodziana, C. Mondelli, F. Krumeich, and J. Pérez-Ramírez, "Solid-state chemistry of cuprous delafossites: Synthesis and stability aspects," *Chem. Mater.*, vol. 25, no. 21, pp. 4423–4435, 2013.
[32] R. Bywalez, S. Götzendörfer, and P. Löbmann, "Structural and physical effects of Mg-doping on p-type CuCrO2 and CuAl0.5Cr0.5O2 thin films," *J. Mater. Chem.*, vol. 20, no. 31, pp. 6562–6570, 2010.
[33] M. Han, K. Jiang, J. Zhang, W. Yu, Y. Li, Z. Hu, and J. Chu, "Structural, electronic band transition and optoelectronic properties of delafossite CuGa1−xCrxO2 ($0 \leq x \leq 1$) solid solution films grown by the sol–gel method," *J. Mater. Chem.*, vol. 22, no. 35, pp. 18463–18470, 2012.
[34] M. J. Han, Z. H. Duan, J. Z. Zhang, S. Zhang, Y. W. Li, Z. G. Hu, and J. H. Chu, "Electronic transition and electrical transport properties of delafossite CuCr1-xMgxO2 (0<x<12%) films prepared by the sol-gel method: A composition dependence study," *J. Appl. Phys.*, vol. 114, no. 16, p. 163526, 2013.
[35] H.-Y. Chen and K.-P. Chang, "Influence of Post-Annealing Conditions on the

Formation of Delafossite-CuCrO2 Films," *ECS J. Solid State Sci. Technol.*, vol. 2, no. 3, pp. P76–P80, 2013.
[36] M. Asemi and M. Ghanaatshoar, "Preparation of CuCrO2 nanoparticles with narrow size distribution by sol-gel method," *J. Sol-Gel Sci. Technol.*, vol. 70, no. 3, pp. 416–421, 2014.
[37] J. Wang, P. Zheng, D. Li, Z. Deng, W. Dong, R. Tao, and X. Fang, "Preparation of delafossite-type CuCrO2 films by sol–gel method," *J. Alloys Compd.*, vol. 509, no. 18, pp. 5715–5719, 2011.
[38] H.-Y. Chen, K.-P. Chang, and C.-C. Yang, "Characterization of transparent conductive delafossite CuCr1−xO2 films," *Appl. Surf. Sci.*, vol. 273, pp. 324–329, 2013.
[39] D. Li, X. Fang, Z. Deng, S. Zhou, R. Tao, W. Dong, T. Wang, Y. Zhao, G. Meng, and X. Zhu, "Electrical, optical and structural properties of CuCrO2 films prepared by pulsed laser deposition," *J. Phys. D. Appl. Phys.*, vol. 40, no. 16, pp. 4910–4915, 2007.
[40] P. W. Sadik, M. Ivill, V. Craciun, and D. P. Norton, "Electrical transport and structural study of CuCr1−xMgxO2 delafossite thin films grown by pulsed laser deposition," *Thin Solid Films*, vol. 517, no. 11, pp. 3211–3215, 2009.
[41] F. Lin, C. Gao, X. Zhou, W. Shi, and A. Liu, "Magnetic, electrical and optical properties of p-type Fe-doped CuCrO2 semiconductor thin films," *J. Alloys Compd.*, vol. 581, pp. 502–507, 2013.
[42] K. Tonooka and N. Kikuchi, "Preparation of transparent CuCrO2:Mg/ZnO p-n junctions by pulsed laser deposition," *Thin Solid Films*, vol. 515, no. 4, pp. 2415–2418, 2006.
[43] D. Li, X. Fang, A. Zhao, Z. Deng, W. Dong, and R. Tao, "Physical properties of CuCrO2 films prepared by pulsed laser deposition," *Vacuum*, vol. 84, no. 6, pp. 851–856, 2010.
[44] R.-S. Yu and C.-P. Tasi, "Structure, composition and properties of p-type CuCrO2 thin films," *Ceram. Int.*, vol. 40, no. 6, pp. 8211–8217, 2014.
[45] H. Sun, M. Arab Pour Yazdi, P. Briois, J.-F. Pierson, F. Sanchette, and A. Billard, "Towards delafossite structure of Cu–Cr–O thin films deposited by reactive magnetron sputtering: Influence of substrate temperature on optoelectronics properties," *Vacuum*, vol. 114, pp. 101–107, 2015.
[46] T.-W. Chiu, Y.-C. Yang, A.-C. Yeh, Y.-P. Wang, and Y.-W. Feng, "Antibacterial property of CuCrO2 thin films prepared by RF magnetron sputtering deposition," *Vacuum*, vol. 87, pp. 174–177, 2013.
[47] G. Dong, M. Zhang, X. Zhao, H. Yan, C. Tian, and Y. Ren, "Improving the electrical conductivity of CuCrO2 thin film by N doping," *Appl. Surf. Sci.*, vol. 256, no. 13, pp. 4121–4124, 2010.
[48] K. L. Choy, "Chemical vapour deposition of coatings," *Prog. Mater. Sci.*, vol. 48, no. 2, pp. 57–170, 2003.
[49] S. Mahapatra and S. A. Shivashankar, "Low-pressure metal-organic CVD of transparent and p-type conducting CuCrO2 thin films with high conductivity," *Chem. Vap. Depos.*, vol. 9, no. 5, pp. 238–240, 2003.
[50] A. Ohki, N. Shibata, K. Ando, and A. Katsui, "Nitrogen-doped p-type ZnSe films grown by MOVPE," *J. Cryst. Growth*, vol. 93, pp. 692–696, 1988.
[51] M. Grün, A. Haury, J. Cibert, and A. Wasiela, "The nitrogen acceptor energy in ZnTe measured by Hall effect and optical spectroscopy," *J. Appl. Phys.*, vol. 79, p. 7386, 1996.
[52] G. H. Tariq, N. A. Niaz, and M. Anis-Ur-Rehman, "Effects of dopant's profile on physical properties of ZnTe thin films," *Chalcogenide Lett.*, vol. 11, pp. 461–470, 2014.

[53] H. Shi, B. Saparov, D. J. Singh, A. S. Sefat, and M.-H. Du, “Ternary chalcogenides Cs2Zn3Se4 and Cs2Zn3Te4: potential p-type transparent conducting materials,” *Phys. Rev. B*, vol. 90, no. 18, p. 184104, 2014.
[54] L. Duclaux, F. Donsanti, J. Vidal, M. Bouttemy, N. Schneider, and N. Naghavi, “Simulation and growing study of Cu-Al-S thin films deposited by atomic layer deposition,” *Thin Solid Films*, vol. 594, pp. 232–237, 2015.
[55] F.-Q. Huang, M.-L. Liu, and C. Yang, “Highly enhanced p-type electrical conduction in wide band gap Cu1+xAl1−xS2 polycrystals,” *Sol. Energy Mater. Sol. Cells*, vol. 95, no. 10, pp. 2924–2927, 2011.
[56] M. L. Liu, F. Q. Huang, and L. D. Chen, “P-Type electrical conduction and wide optical band gap in Mg-doped CuAlS2,” *Scr. Mater.*, vol. 58, pp. 1002–1005, 2008.
[57] M. L. Liu, F. Q. Huang, L. D. Chen, Y. M. Wang, Y. H. Wang, G. F. Li, and Q. Zhang, “P-type transparent conductor: Zn-doped CuAlS2,” *Appl. Phys. Lett.*, vol. 90, pp. 7–10, 2007.
[58] M. Yang, Y. Wang, G. Li, Z. Shi, and Q. Zhang, “Zn-doped CuAlS2 transparent p-type conductive thin films deposited by pulsed plasma deposition,” *J. Vac. Sci. Technol. A Vacuum, Surfaces, Film.*, vol. 27, pp. 1316–1319, 2009.
[59] J. López-García and C. Guillén, “Formation of semitransparent CuAlSe2 thin films grown on transparent conducting oxide substrates by selenization,” *J. Mater. Sci.*, vol. 46, no. 23, pp. 7603–7610, 2011.
[60] J. Lopez-Garca, J. Montero, C. Maffiotte, C. Guillèn, and J. Herrero, “Crystallization of wide-bandgap CuAlSe2 thin films deposited on antimony doped tin oxide substrates,” *J. Alloys Compd.*, vol. 648, pp. 104–110, 2015.
[61] G. Hautier, A. Miglio, G. Ceder, G.-M. Rignanese, and X. Gonze, “Identification and design principles of low hole effective mass p-type transparent conducting oxides,” *Nat. Commun.*, vol. 4, p. 2292, 2013.
[62] J. E. Sansonetti and W. C. Martin, “Handbook of basic atomic spectroscopic data,” *J. Phys. Chem. Ref. Data*, vol. 34, no. 4, pp. 1559–2259, 2005.
[63] H. Sato and T. Minami, “Transparent conducting p-type NiO thin films prepared by magnetron sputtering,” vol. 236, pp. 27–31, 1993.
[64] B. A. Reguig, A. Khelil, L. Cattin, M. Morsli, and J. C. Bernède, “Properties of NiO thin films deposited by intermittent spray pyrolysis process,” *Appl. Surf. Sci.*, vol. 253, pp. 4330–4334, 2007.
[65] U. S. Joshi, Y. Matsumoto, K. Itaka, M. Sumiya, and H. Koinuma, “Combinatorial synthesis of Li-doped NiO thin films and their transparent conducting properties,” *Appl. Surf. Sci.*, vol. 252, no. 7, pp. 2524–2528, 2006.
[66] P. Zhai, Q. Yi, J. Jian, H. Wang, P. Song, C. Dong, X. Lu, Y. Sun, J. Zhao, X. Dai, Y. Lou, H. Yang, and G. Zou, “Transparent p-type epitaxial thin films of nickel oxide.,” *Chem. Commun.*, vol. 50, pp. 1854–1856, 2014.
[67] X. Chen, L. Zhao, and Q. Niu, “Electrical and optical properties of p-type Li,Cu-codoped NiO thin films,” *J. Electron. Mater.*, vol. 41, no. 12, pp. 3382–3386, 2012.
[68] F. H. Hsu, N. F. Wang, Y. Z. Tsai, Y. S. Cheng, and M. P. Houng, “A new p-Ni1−xO:Li / n-Si heterojunction solar cell fabricated by RF magnetron sputtering,” *J. Phys. D. Appl. Phys.*, vol. 46, p. 275104, 2013.
[69] M. Yang, H. Pu, Q. Zhou, and Q. Zhang, “Transparent p-type conducting K-doped NiO films deposited by pulsed plasma deposition,” *Thin Solid Films*, vol. 520, pp. 5884–5888, 2012.
[70] O. F. Schirmer, “ Bound Small Polarons in Oxide Materials,” *J. Phys. Condens. Matter*, vol. 18, no. 43, pp. R667–R704, 2006.
[71] I. G. Austin, B. D. Clay, and C. E. Turner, “Optical absorption of small polarons in

semiconducting NiO and CoO in the near and far infra-red," *J. Phys. C Solid State Phys.*, vol. 1, pp. 1418–1434, 1968.
[72] J. Mistry, B. V. Mistry, U. N. Trivedi, R. Pinto, U. S. Joshi, A. B. Garg, R. Mittal, and R. Mukhopadhyay, "Fabrication and Electrical Properties of Transparent n-ZnO:Al / p-NiO:Li Junction," *AIP Conf. Proc.*, vol. 725, no. 2011, pp. 725–726, 2011.
[73] K. Wang, Y. Vygranenko, and A. Nathan, "Fabrication and characterization of NiO/ZnO/ITO p-i-n heterostructure," *Thin Solid Films*, vol. 516, no. 7, pp. 1640–1643, 2008.
[74] H. Ohta, M. Kamiya, T. Kamiya, M. Hirano, and H. Hosono, "UV-detector based on pn-heterojunction diode composed of transparent oxide semiconductors, p-NiO/n-ZnO," *Thin Solid Films*, vol. 445, no. 2, pp. 317–321, 2003.
[75] R. Karsthof, H. Von Wenckstern, and M. Grundmann, "Transparent JFETs Based on p-NiO / n-ZnO Heterojunctions," vol. 62, pp. 3999–4003, 2015.
[76] R. Karsthof, P. Räcke, H. von Wenckstern, and M. Grundmann, "Semi-transparent NiO/ZnO UV photovoltaic cells," *Phys. Status Solidi Appl. Mater. Sci.*, vol. 37, no. 1, pp. 30–37, 2015.
[77] M. Warasawa, Y. Watanabe, J. Ishida, and Y. Murata, "Fabrication of Visible-Light-Transparent Solar Cells Using p-Type NiO Films by Low Oxygen Fraction Reactive RF Sputtering Deposition," *Jpn. J. Appl. Phys.*, vol. 52, p. 021102, 2013.
[78] Z. Huang, G. Natu, Z. Ji, P. Hasin, and Y. Wu, "p-Type Dye-Sensitized NiO Solar Cells: A Study by Electrochemical Impedance Spectroscopy," *J. Phys. Chem. C*, vol. 115, pp. 25109–25114, 2011.
[79] E. Bobeico, F. Varsano, C. Minarini, and F. Roca, "P-type strontium–copper mixed oxide deposited by e-beam evaporation," *Thin Solid Films*, vol. 444, pp. 70–74, 2003.
[80] A. Kudo, H. Yanagi, H. Hosono, and H. Kawazoe, "SrCu2O2: A p-type conductive oxide with wide band gap," *Appl. Phys. Lett.*, vol. 73, pp. 220–222, 1998.
[81] E. L. Papadopoulou, M. Varda, A. Pennos, M. Kaloudis, M. Kayambaki, M. Androulidaki, K. Tsagaraki, Z. Viskadourakis, O. Durand, G. Huyberechts, and E. Aperathitis, "The effect of PLD deposition parameters on the properties of p-SrCu2O2 / n-Si diodes," *Thin Solid Films*, vol. 516, pp. 8154–8158, 2008.
[82] B. Roy, J. D. Perkins, T. Kaydanova, D. L. Young, M. Taylor, A. Miedaner, C. Curtis, H. J. Kleebe, D. W. Readey, and D. S. Ginley, "Preparation and characterization of sol– gel derived copper– strontium–oxide thin films," *Thin Solid Films*, vol. 516, pp. 4093–4101, 2008.
[83] A. Khan, C. Jiménez, O. Chaix-Pluchery, H. Roussel, and J.-L. Deschanvres, "Effect of thermal annealing on electrical and optical properties of Ba-doped SrCu2O2 thin films on glass substrates," *Phys. Status Solidi*, vol. 210, pp. 2569–2574, 2013.
[84] K. G. Godinho, J. J. Carey, B. J. Morgan, D. O. Scanlon, and G. W. Watson, "Understanding conductivity in SrCu2O2: stability , geometry and electronic structure of intrinsic defects from first principles," *J. Mater. Chem.*, vol. 20, pp. 1086–1096, 2010.
[85] T. R. Paudel, A. Zakutayev, S. Lany, M. D'Avezac, and A. Zunger, "Doping rules and doping prototypes in A2BO4 spinel oxides," *Adv. Funct. Mater.*, vol. 21, no. 23, pp. 4493–4501, 2011.
[86] A. Zakutayev, T. R. Paudel, P. F. Ndione, J. D. Perkins, S. Lany, A. Zunger, and D. S. Ginley, "Cation off-stoichiometry leads to high p-type conductivity and enhanced transparency in Co2ZnO4 and Co2NiO4 thin films," *Phys. Rev. B - Condens. Matter Mater. Phys.*, vol. 85, p. 085204, 2012.
[87] L. Hu, L. Wu, M. Liao, X. Hu, and X. Fang, "Electrical Transport Properties of Large, Individual NiCo2O4 Nanoplates," *Adv. Funct. Mater.*, vol. 22, no. 5, pp. 998–1004,

2012.
[88] B. Cui, H. Lin, Y.-Z. Liu, J.-B. Li, P. Sun, X.-C. Zhao, and C.-J. Liu, “Photophysical and photocatalytic properties of core-ring structured NiCo2O4 nanoplatelets,” *J. Phys. Chem. C*, vol. 113, pp. 14083–14087, 2009.
[89] Y. Fujishiro, K. Hamamoto, O. Shiono, S. Katayama, and M. Awano, “Synthesis and thermoelectric characterization of polycrystalline Ni1-xCaxCo2O4 (x = 0-0.05) spinel materials,” *J. Mater. Sci. Mater. Electron.*, vol. 15, no. 12, pp. 769–773, 2004.
[90] K. Dileep, B. Loukya, P. Silwal, A. Gupta, and R. Datta, “Probing optical band gaps at nanoscale from tetrahedral cation vacancy defects and variation of cation ordering in NiCo2O2 epitaxial thin films,” *J. Phys. D. Appl. Phys.*, vol. 47, p. 405001, 2014.
[91] F. Windisch, C, G. J. Exarhos, K. F. Ferris, M. H. Engelhard, and D. C. Stewart, “Infrared transparent spinel films with p-type conductivity,” *Thin Solid Films*, vol. 398–399, pp. 45–52, 2001.
[92] C. F. Windisch, K. F. Ferris, and G. J. Exarhos, “Synthesis and characterization of transparent conducting oxide cobalt–nickel spinel films,” *J. Vac. Sci. Technol. A*, vol. 19, p. 1647, 2001.
[93] M. N. Amini, H. Dixit, R. Saniz, D. Lamoen, and B. Partoens, “The origin of p-type conductivity in ZnM2O4 (M = Co, Rh, Ir) spinels.,” *Phys. Chem. Chem. Phys.*, vol. 16, pp. 2588–2596, 2014.
[94] H. J. Kim, I. C. Song, J. H. Sim, H. Kim, D. Kim, Y. E. Ihm, and W. K. Choo, “Electrical and magnetic properties of spinel-type magnetic semiconductor ZnCo2O4 grown by reactive magnetron sputtering,” *J. Appl. Phys.*, vol. 95, pp. 7387–7389, 2004.
[95] D. O. Scanlon and G. W. Watson, “Band gap anomalies of the ZnM2(III)O4 (M(III)=Co, Rh, Ir) spinels.,” *Phys. Chem. Chem. Phys.*, vol. 13, no. 20, pp. 9667–9675, 2011.
[96] M. Dekkers, G. Rijnders, and D. H. a Blank, “ZnIr2O4, a p-type transparent oxide semiconductor in the class of spinel zinc-d6-transition metal oxide,” *Appl. Phys. Lett.*, vol. 90, no. 2, p. 021903, 2007.
[97] H. Mizoguchi, M. Hirano, S. Fujitsu, T. Takeuchi, K. Ueda, and H. Hosono, “ZnRh2O4: A p-type semiconducting oxide with a valence band composed of a low spin state of Rh3+ in a 4d6 configuration,” *Appl. Phys. Lett.*, vol. 80, no. 7, pp. 1207–1209, 2002.
[98] H. Hiramatsu, K. Ueda, H. Ohta, M. Hirano, T. Kamiya, and H. Hosono, “Degenerate p-type conductivity in wide-gap LaCuOS1-xSex (x = 0-1) epitaxial films,” *Appl. Phys. Lett.*, vol. 82, no. 7, pp. 1048–1050, 2003.
[99] H. Hiramatsu, K. Ueda, H. Ohta, M. Hirano, M. Kikuchi, H. Yanagi, T. Kamiya, and H. Hosono, “Heavy hole doping of epitaxial thin films of a wide gap p -type semiconductor, LaCuOSe, and analysis of the effective mass,” *Appl. Phys. Lett.*, vol. 91, no. 1, pp. 17–20, 2007.
[100] C. T. Prewitt, R. D. Shannon, and D. B. Rogers, “Chemistry of noble metal oxides. II. Crystal structures of PtCoO2, PdCoO2, CuFeO2 and AgFeO2,” *Inorg. Chem.*, vol. 10, no. 4, p. 719, 1971.
[101] D. Xiong, H. Wang, W. Zhang, X. Zeng, H. Chang, X. Zhao, W. Chen, and Y.-B. Cheng, “Preparation of p-type AgCrO2 nanocrystals through low-temperature hydrothermal method and the potential application in p-type dye-sensitized solar cell,” *J Allo Compo*, vol. 642, pp. 104–110, 2015.
[102] R. S. Ajimsha, K. A. Vanaja, M. K. Jayaraj, P. Misra, V. K. Dixit, and L. M. Kukreja, “Transparent p-AgCoO2/n-ZnO diode heterojunction fabricated by pulsed laser deposition,” *Thin Solid Films*, vol. 515, pp. 7352–7356, 2007.
[103] W. C. Sheets, E. S. Stampler, M. I. Bertoni, M. Sasaki, T. J. Marks, T. O. Mason, and

K. R. Poeppelmeier, “Silver delafossite oxides,” *Inorg. Chem.*, vol. 47, no. 7, pp. 2696–2705, 2008.
[104] M. N. Huda, Y. Yan, A. Walsh, S. Wei, and M. M. Al-jassim, “Group-IIIA versus IIIB delafossites : Electronic structure study,” *Phys. Rev. B*, vol. 80, p. 035205, 2009.
[105] T. I. Draskovic, M. Yu, and Y. Wu, “2H-CuScO $_2$ Prepared by Low-Temperature Hydrothermal Methods and Post-Annealing Effects on Optical and Photoelectrochemical Properties,” *Inorg. Chem.*, vol. 54, no. 11, pp. 5519–5526, 2015.
[106] M. Trari, a. Bouguelia, and Y. Bessekhouad, “P-Type CuYO2 as hydrogen photocathode,” *Sol. Energy Mater. Sol. Cells*, vol. 90, pp. 190–202, 2006.
[107] J. Li, A. W. Sleight, C. Y. Jones, and B. H. Toby, “Trends in negative thermal expansion behavior for AMO2 (A=Cu or Ag ; M=Al , Sc , In , or La) compounds with the delafossite structure,” *J. Solid State Chem.*, vol. 178, pp. 285–294, 2005.
[108] O. Crottaz and F. Kubel, “Crystal structure of copper(I) chromium(III) oxide 3R-CuCrO2,” *Zeitschrift für Krist.*, vol. 211, p. 482, 1996.
[109] C. Delorme, “Sur quelques composés du type M_2O_3–Cu_2O,” *Acta Crystallogr.*, vol. 9, no. 2, pp. 200–200, 1956.
[110] F. Lin, W. Shi, and A. Liu, “Optical bandgap modulation and magnetic characterization of Fe-doped CuCrO2 nanopowders,” *J. Alloys Compd.*, vol. 529, pp. 21–24, 2012.
[111] O. Crottaz and F. Kubel, “Crystal structure of copper (I) chromium (III) oxide, 2H-CuCrO2,” *Zeitschrift für Krist.*, vol. 211, p. 481, 1996.
[112] O. Crottaz, “Preparation of Trigonal and Hexagonal Cuprous Chromite and Phase Transition Study Based on Single Crystal Structure Data,” *J. Solid State Chem.*, vol. 122, pp. 247–250, 1996.
[113] M. Lalanne, A. Barnabé, F. Mathieu, and P. Tailhades, “Synthesis and thermostructural studies of a CuFe(1-x)Cr(x)O(2) delafossite solid solution with 0<x<1,” *Inorg. Chem.*, vol. 48, pp. 6065–6071, 2009.
[114] Y. Kumekawa, M. Hirai, Y. Kobayashi, S. Endoh, E. Oikawa, and T. Hashimoto, “Evaluation of thermodynamic and kinetic stability of CuAlO2,” *J. Therm. Anal. Calorim.*, vol. 99, pp. 57–63, 2010.
[115] F. Fujishiro, S. Takaichi, K. Hirakawa, and T. Hashimoto, “Analysis of oxidation decomposition reaction scheme and its kinetics of delafossite-type oxide CuLaO2 by thermogravimetry and high-temperature X-ray diffraction,” *J. Therm. Anal. Calorim.*, vol. 123, pp. 1833–1839, 2015.
[116] R. Gillen and J. Robertson, “Band structure calculations of CuAlO2, CuGaO2, CuInO2, and CuCrO2 by screened exchange,” *Phys. Rev. B*, vol. 84, p. 035125, 2011.
[117] Y. Wang, Y. Gu, T. Wang, and W. Shi, “Structural, optical and electrical properties of Mg-doped CuCrO2 thin films by sol-gel processing,” *J. Alloys Compd.*, vol. 509, no. 19, pp. 5897–5902, 2011.
[118] T. Arnold, D. J. Payne, A. Bourlange, J. P. Hu, R. G. Egdell, L. F. J. Piper, L. Colakerol, A. Masi, P. A. Glans, T. Learmonth, K. E. Smith, J. Guo, D. O. Scanlon, A. Walsh, B. J. Morgan, and G. W. Watson, “X-ray spectroscopic study of the electronic structure of CuCrO2,” *Phys. Rev. B*, vol. 79, p. 075102, 2009.
[119] J. J. Yeh and I. Lindau, “Atomic subshell photoionization cross section and asymmetry parameters: 1<Z<103,” *At. data Nucl. data tables*, vol. 32, pp. 1–155, 1985.
[120] S. Lany, J. Osorio-Guillén, and A. Zunger, “Origins of the doping asymmetry in oxides: Hole doping in NiO versus electron doping in ZnO,” *Phys. Rev. B*, vol. 75, p. 241203, 2007.
[121] A. Zunger, “Practical doping principles,” *Appl. Phys. Lett.*, vol. 83, no. 1, pp. 57–59, 2003.
[122] S. B. Zhang, S.-H. Wei, A. Zunger, and H. Katayama-Yoshida, “Defect physics of the

CuInSe2 chalcopyrite semiconductor," *Phys. Rev. B*, vol. 57, pp. 9642–9656, 1998.
[123] S. Zhang, S.-H. Wei, and A. Zunger, "Microscopic Origin of the Phenomenological Equilibrium 'Doping Limit Rule' in n-Type III-V Semiconductors," *Phys. Rev. Lett.*, vol. 84, no. 6, pp. 1232–1235, 2000.
[124] H. Katayama-Yoshida, T. Nishimatsu, T. Yamamoto, and N. Orita, "Codoping method for the fabrication of low-resistivity wide band-gap semiconductors in p-type GaN, p-type AlN and n-type diamond: prediction versus experiment," *J. Phys. Condens. Matter*, vol. 13, no. 40, pp. 8901–8914, 2001.
[125] Z.-J. Fang, J.-Z. Zhu, J. Zhou, and M. Mo, "Defect properties of CuCrO2: a density functional theory calculation," *Chinese Phys. B*, vol. 21, no. 8, p. 087105, 2012.
[126] S. Kumar, S. Marinel, M. Miclau, and C. Martin, "Fast synthesis of CuCrO2 delafossite by monomode microwave heating," *Mater. Lett.*, vol. 70, pp. 40–43, 2012.
[127] H.-Y. Chen, W.-J. Yang, and K.-P. Chang, "Characterization of delafossite-CuCrO2 thin films prepared by post-annealing using an atmospheric pressure plasma torch," *Appl. Surf. Sci.*, vol. 258, no. 22, pp. 8775–8779, 2012.
[128] D. Li, X. Fang, Z. Deng, W. Dong, R. Tao, and S. Zhou, "Characteristics of CuCr1−xMgxO2 films prepared by pulsed laser deposition," *J. Alloys Compd.*, vol. 486, pp. 462–467, 2009.
[129] A. Barnabé, Y. Thimont, M. Lalanne, L. Presmanes, and P. Tailhades, "p-Type conducting transparent characteristics of delafossite Mg-doped CuCrO2 thin films prepared by RF-sputtering," *J. Mater. Chem. C*, vol. 3, pp. 6012–6024, 2015.
[130] S. H. Lim, S. Desu, and A. C. Rastogi, "Chemical spray pyrolysis deposition and characterization of p-type CuCr1-xMgxO2 transparent oxide semiconductor thin films," *J. Phys. Chem. Solids*, vol. 69, no. 8, pp. 2047–2056, 2008.
[131] L. Farrell, E. Norton, C. M. Smith, D. Caffrey, I. Shvets, and K. Fleischer, "Synthesis of nanocrystalline Cu deficient CuCrO2 – a high figure of merit p-type transparent semiconductor," *J. Mater. Chem. C*, vol. 4, pp. 126–134, 2015.
[132] L. Farrell, E. Norton, B. J. O. Dowd, D. Caffrey, I. V Shvets, and K. Fleischer, "Spray pyrolysis growth of a high figure of merit , nano-crystalline , p-type transparent conducting material at low temperature," *Appl. Phys. Lett.*, vol. 107, p. 031901, 2015.
[133] X. Zhou, F. Lin, W. Shi, and A. Liu, "Structural, electrical, optical and magnetic properties of p-type Cu(Cr1-xMnx)O2 thin films prepared by pulsed laser deposition," *J. Alloys Compd.*, vol. 614, pp. 221–225, 2014.
[134] S. Y. Zheng, G. S. Jiang, J. R. Su, and C. F. Zhu, "The structural and electrical property of CuCr1−xNixO2 delafossite compounds," *Mater. Lett.*, vol. 60, pp. 3871–3873, 2006.
[135] M. O'Sullivan, P. Stamenov, J. Alaria, M. Venkatesan, and J. M. D. Coey, "Magnetoresistance of CuCrO2-based delafossite films," *J. Phys. Conf. Ser.*, vol. 200, no. 5, p. 052021, 2010.
[136] A. F. Ioffe, *Physics of Semiconductors*. New York: Academic Press, 1960.
[137] N. W. Ashcroft and N. D. Mermin, *Solid State Physics*. New York: Holt, 1976.
[138] L. D. Landau, "Über die Bewegung der Elektronen in Kristalgitter," *Phys. Z. Sowjetunion*, vol. 3, pp. 644–645, 1933.
[139] I. G. Austin and N. F. Mott, "Polarons in crystalline and non-crystalline materials," *Adv. Phys.*, vol. 50, pp. 757–812, 2010.
[140] G. L. Trigg, E. S. Vera, and W. Greulich, *Encyclopedia of Applied Physics (vol. 14)*. New York: Wiley-VCH, 1996.
[141] Frolich, "Electrons in lattice fields," *Adv. Phys.*, vol. 3, pp. 325–361, 1953.
[142] J. Yamashita and T. Kurosawa, "On electronic current in NiO," *J. Phys. Chem. Solids*, vol. 5, pp. 34–43, 1958.

[143] A. J. Bosman and H. J. van Daal, “Small-polaron versus band conduction in some transition-metal oxides,” *Adv. Phys.*, vol. 19, no. 77, pp. 1–117, 1970.
[144] N. Mansourian-Hadavi, S. Wansom, N. H. Perry, A. R. Nagaraja, T. O. Mason, L. Ye, and A. J. Freeman, “Transport and band structure studies of crystalline ZnRh2O4,” *Phys. Rev. B*, vol. 81, p. 075112, 2010.
[145] B. J. Ingram, T. O. Mason, R. Asahi, K. T. Park, and A. J. Freeman, “Electronic structure and small polaron hole transport of copper aluminate,” *Phys. Rev.*, vol. 64, p. 155114, 2001.
[146] A. R. Nagaraja, N. H. Perry, T. O. Mason, Y. Tang, M. Grayson, T. R. Paudel, S. Lany, and A. Zunger, “Band or Polaron : The Hole Conduction Mechanism in the p-type spinel Rh2ZnO4,” *J. Am. Chem. Soc.*, vol. 95, pp. 269–274, 2012.
[147] H. Hiraga, T. Makino, T. Fukumura, H. Weng, and M. Kawasaki, “Electronic structure of the delafossite-type CuMO2 (M = Sc, Cr, Mn, Fe, and Co): Optical absorption measurements and first-principles calculations,” *Phys. Rev. B*, vol. 84, no. 4, p. 041411(R), 2011.
[148] P. Y. Yu and M. Cardona, *Fundamentals of Semiconductors*. Berlin: Springer, 2005.
[149] D. Shin, J. S. Foord, R. G. Egdell, and A. Walsh, “Electronic structure of CuCrO2 thin films grown on Al2O3(001) by oxygen plasma assisted molecular beam epitaxy,” *J. Appl. Phys.*, vol. 112, no. 11, p. 113718, 2012.
[150] X. Li, M. Han, X. Zhang, C. Shan, Z. Hu, Z. Zhu, and J. Chu, “Temperature-dependent band gap, interband transitions, and exciton formation in transparent p-type delafossite CuCr1-xMgxO2 films,” *Phys. Rev. B*, vol. 90, no. 3, p. 035308, 2014.
[151] L.-F. Chen, Y.-P. Wang, T.-W. Chiu, W.-C. Shih, and M.-S. Wu, “Fabrication of Transparent CuCrO2:Mg/ZnO p–n Junctions Prepared by Magnetron Sputtering on an Indium Tin Oxide Glass Substrate,” *Jpn. J. Appl. Phys.*, vol. 52, p. 05EC02, 2013.
[152] G. S. Parks, C. E. Hablutzel, and L. E. Webster, “The heat of formation of zinc oxide,” *J. Am. Chem. Soc.*, vol. 49, pp. 2792–2795, 1927.
[153] S. Gupta, W. E. Fenwick, A. Melton, T. Zaidi, H. Yu, V. Rengarajan, J. Nause, A. Ougazzaden, and I. T. Ferguson, “MOVPE growth of transition-metal-doped GaN and ZnO for spintronic applications,” *J. Cryst. Growth*, vol. 310, pp. 5032–5038, 2008.
[154] P. Sharma, A. Gupta, F. J. Owens, A. Inoue, and K. V. Rao, “Room temperature spintronic material - Mn-doped ZnO revisited,” *J. Magn. Magn. Mater.*, vol. 282, pp. 115–121, 2004.
[155] V. Rogé, N. Bahlawane, G. Lamblin, I. Fechete, F. Garin, a. Dinia, and D. Lenoble, “Improvement of the photocatalytic degradation property of atomic layer deposited ZnO thin films: the interplay between film properties and functional performances,” *J. Mater. Chem. A*, vol. 3, no. 21, pp. 11453–11461, 2015.
[156] H. Karzel, W. Potzel, M. Köfferlein, W. Schiessl, M. Steiner, U. Hiller, G. Kalvius, D. Mitchell, T. Das, P. Blaha, K. Schwarz, and M. Pasternak, “Lattice dynamics and hyperfine interactions in ZnO and ZnSe at high external pressures,” *Phys. Rev. B*, vol. 53, no. 17, pp. 11425–11438, 1996.
[157] S. Desgreniers, “High-density phases of ZnO: Structural and compressive parameters,” *Phys. Rev. B*, vol. 58, no. 21, pp. 14102–14105, 1998.
[158] L. Gerward and J. S. Olsen, “The high-pressure phase of zincite.,” *J. Synchrotron Radiat.*, vol. 2, pp. 233–235, 1995.
[159] D. Vogel, P. Kruger, and J. Pollmann, “Self-interaction and relaxation-corrected pseudopotentials for II-VI semiconductors,” *Phys. Rev. B*, vol. 54, no. 8, pp. 5495–5511, 1996.
[160] P. Schroer, P. Krüger, and J. Pollmann, “First-principles calculation,” *Phys. Rev. B*, vol. 47, pp. 6971–6980, 1993.

[161] P. Erhart, K. Albe, and A. Klein, “First-principles study of intrinsic point defects in ZnO: Role of band structure, volume relaxation, and finite-size effects,” *Phys. Rev. B*, vol. 73, p. 205203, 2006.
[162] O. Mryasov and A. Freeman, “Electronic band structure of indium tin oxide and criteria for transparent conducting behavior,” *Phys. Rev. B*, vol. 64, no. 23, pp. 2–4, 2001.
[163] K. Nomura, H. Ohta, A. Takagi, T. Kamiya, M. Hirano, and H. Hosono, “Room-temperature fabrication of transparent flexible thin-film transistors using amorphous oxide semiconductors.,” *Nature*, vol. 432, no. 7016, pp. 488–492, 2004.
[164] S. A. Knickerbocker, “Estimation and verification of the optical properties of indium tin oxide based on the energy band diagram,” *J. Vac. Sci. Technol. A*, vol. 14, no. 3, p. 757, 1996.
[165] D. C. Look, D. C. Reynolds, J. R. Sizelove, R. L. Jones, C. W. Litton, G. Cantwell, and W. C. Harsch, “Electrical properties of bulk ZnO,” *Solid State Commun.*, vol. 105, pp. 399–401, 1998.
[166] E. Ziegler, A. Heinrich, H. Oppermann, G. Stover, and G. Stöver, “Electrical properties and non-stoichiometry in ZnO single crystals,” *Phys. Status Solidi*, vol. 66, p. 635, 1981.
[167] R. A. Hutson, “Hall Effect Studies of Doped Zinc Oxide Single Crystals,” *Phys. Rev.*, vol. 108, pp. 222–230, 1957.
[168] A. Janotti and C. G. Van De Walle, “Fundamentals of zinc oxide as a semiconductor,” *Reports Prog. Phys.*, vol. 72, p. 126501, 2009.
[169] A. Janotti and C. G. Van De Walle, “Oxygen vacancies in ZnO,” *Appl. Phys. Lett.*, vol. 87, p. 122102, 2005.
[170] R. J. Lad, “Postdeposition annealing behavior of rf sputtered ZnO films,” *J. Vac. Sci. Technol.*, vol. 17, p. 808, 1980.
[171] Y. Kamada, M. Furuta, T. Hiramatsu, and T. Kawaharamura, “Study on oxygen source and its effect on film properties of ZnO deposited by radio frequency magnetron sputtering,” *Appl. Surf. Sci.*, vol. 258, pp. 695–699, 2011.
[172] D. Look, J. Hemsky, and J. Sizelove, “Residual Native Shallow Donor in ZnO,” *Phys. Rev. Lett.*, vol. 82, no. 12, pp. 2552–2555, 1999.
[173] P. Erhart and K. Albe, “First-principles study of migration mechanisms and diffusion of oxygen in zinc oxide,” *Phys. Rev. B*, vol. 73, no. 11, p. 115207, 2006.
[174] P. Erhart and K. Albe, “Diffusion of zinc vacancies and interstitials in zinc oxide,” *Appl. Phys. Lett.*, vol. 88, p. 201918, 2006.
[175] H. Kato, M. Sano, K. Miyamoto, and T. Yao, “Growth and characterization of Ga-doped ZnO layers on a -plane sapphire substrates grown by molecular beam epitaxy,” *J. Cryst. Growth*, vol. 237, no. 30, pp. 538–543, 2002.
[176] S. Y. Myong, S. J. Baik, C. H. Lee, W. Y. Cho, and K. S. Lim, “Extremely Transparent and Conductive ZnO:Al Thin Films Prepared by Photo-Assisted Metalorganic Chemical Vapor Deposition (photo-MOCVD) Using AlCl3(6H2O) as New Doping Material,” *Japanese Soc. Appl. Phys.*, vol. 36, p. L1078, 1997.
[177] C. G. Van De Walle, “Hydrogen as a Cause of Doping in Zinc Oxide,” *Phys. Rev. Lett.*, vol. 85, pp. 1012–1015, 2000.
[178] D. M. Hofmann, A. Hofstaetter, F. Leiter, H. Zhou, F. Henecker, B. K. Meyer, S. B. Orlinskii, J. Schmidt, and P. G. Baranov, “Hydrogen: a relevant shallow donor in zinc oxide.,” *Phys. Rev. Lett.*, vol. 88, no. 4, p. 045504, 2002.
[179] F. Ruske, V. Sittinger, W. Werner, B. Szyszka, K.-U. van Osten, K. Dietrich, and R. Rix, “Hydrogen doping of DC sputtered ZnO:Al films from novel target material,” *Surf. Coatings Technol.*, vol. 200, pp. 236–240, 2005.

[180] V. Srikant and D. R. Clarke, “Optical absorption edge of ZnO thin films: the effect of substrate,” *J. Appl. Phys.*, vol. 81, pp. 6357–6364, 1997.
[181] M. Rebien, W. Henrion, M. Bär, and C. H. Fischer, “Optical properties of ZnO thin films: Ion layer gas reaction compared to sputter deposition,” *Appl. Phys. Lett.*, vol. 80, pp. 3518–3520, 2002.
[182] A. Ohtomo, M. Kawasaki, T. Koida, K. Masubuchi, H. Koinuma, Y. Sakurai, Y. Yoshida, T. Yasuda, and Y. Segawa, “MgxZn1-xO as a II-VI widegap semiconductor alloy,” *Appl. Phys. Lett.*, vol. 72, pp. 2466–2468, 1998.
[183] M. . Tokumoto, A. Smith, C. . Santilli, S. . Pulcinelli, A. . Craievich, E. Elkaim, A. Traverse, and V. Briois, “Structural electrical and optical properties of undoped and indium doped ZnO thin films prepared by the pyrosol process at different temperatures,” *Thin Solid Films*, vol. 416, pp. 284–293, 2002.
[184] I. Takeuchi, W. Yang, K.-S. Chang, M. A. Aronova, T. Venkatesan, R. D. Vispute, and L. A. Bendersky, “Monolithic multichannel ultraviolet detector arrays and continuous phase evolution in MgxZn1−xO composition spreads,” *J. Appl. Phys.*, vol. 94, p. 7336, 2003.
[185] V. Christou, M. Etchells, O. Renault, P. J. Dobson, O. V. Salata, G. Beamson, and R. G. Egdell, “High resolution x-ray photoemission study of plasma oxidation of indium–tin–oxide thin film surfaces,” *J. Appl. Phys.*, vol. 88, p. 5180, 2000.
[186] A. Klein, “Electronic properties of In2O3 surfaces,” *Appl. Phys. Lett.*, vol. 77, p. 2009, 2000.
[187] B. Stjerna, E. Olsson, and C. G. Granqvist, “Optical and electrical properties of radio frequency sputtered tin oxide films doped with oxygen vacancies, F, Sb, or Mo,” *J. Appl. Phys.*, vol. 76, pp. 3797–3817, 1994.
[188] E. Shanthi, V. Dutta, A. Banerjee, and K. L. Chopra, “Electrical and optical properties of undoped and antimony-doped tin oxide films,” *J. Appl. Phys.*, vol. 51, pp. 6243–6251, 1980.
[189] M. Kasuga and M. Mochisuki, “Orientation Relationships of Zinc Oxide on Sapphire in Heteroepitaxial Chemical,” *J. Cryst. Growth*, vol. 54, pp. 185–194, 1981.
[190] S. K. Tiku, C. K. Lau, and K. M. Lakin, “Chemical vapor deposition of ZnO epitaxial films on sapphire,” *Appl. Phys. Lett.*, vol. 36, no. 4, p. 318, 1980.
[191] G. Galli, “Epitaxial ZnO on sapphire,” *Appl. Phys. Lett.*, vol. 16, p. 439, 1970.
[192] O. Kluth, G. Schöpe, J. Hüpkes, C. Agashe, J. Müller, and B. Rech, “Modified Thornton model for magnetron sputtered zinc oxide: film structure and etching behaviour,” *Thin Solid Films*, vol. 442, pp. 80–85, 2003.
[193] C. H. Ahn, Y. Y. Kim, D. C. Kim, S. K. Mohanta, and H. K. Cho, “A comparative analysis of deep level emission in ZnO layers deposited by various methods,” *J. Appl. Phys.*, vol. 105, p. 013502, 2009.
[194] W. Kern and R. Heim, “Chemical Vapor Deposition of Silicate Glasses for Use with Silicon Devices,” *J. Electrochem. Soc.*, vol. 117, p. 562, 1970.
[195] F. T. J. Smith, “Metalorganic chemical vapor deposition of oriented ZnO films over large areas,” *Appl. Phys. Lett.*, vol. 43, no. 12, pp. 1108–1110, 1983.
[196] C. R. Gorla, N. W. Emanetoglu, S. Liang, W. E. Mayo, Y. Lu, M. Wraback, and H. Shen, “Structural, optical, and surface acoustic wave properties of epitaxial ZnO films grown on (01$\bar{1}$2) sapphire by metalorganic chemical vapor deposition,” *J. Appl. Phys.*, vol. 85, no. 5, p. 2595, 1999.
[197] Y. Kashiwaba, K. Haga, H. Watanabe, P. B. Zhang, Y. Segawa, and K. Wakatsuki, “Structures and Photoluminescence Properties of ZnO Films Epitaxially Grown by Atmospheric Pressure MOCVD,” *Phys. Status Solidi*, vol. 229, pp. 921–924, 2002.
[198] T. Yasuda and Y. Segawa, “Zinc oxide thin films synthesized by metal organic

chemical reactions," *Phys. Status Solidi*, vol. 241, no. 3, pp. 676–679, 2004.
[199] T. Gruber, C. Kirchner, and A. Waag, "MOCVD growth of ZnO on different substrate materials," *Phys. Status Solidi*, vol. 229, pp. 841–844, 2002.
[200] T. Gruber, C. Kirchner, K. Thonke, R. Sauer, and A. Waag, "MOCVD growth of ZnO for Optoelectronic Applications," *Phys. Status Solidi*, vol. 192, pp. 166–170, 2002.
[201] N. Oleynik, A. Dadgar, J. Christen, J. Blasing, M. Adam, T. Riemann, A. Diez, A. Greiling, M. Seip, and A. Krost, "Growth of ZnO Layers by Metal Organic Chemical Vapor Phase Epitaxy," *Phys. Status Solidi*, vol. 192, pp. 189–194, 2002.
[202] B. Hahn, G. Heindel, and W. Gebhardt, "MOCVD layer growth of ZnO using DMZn and tertiary butanol," *Semicond. Sci. Technol.*, vol. 13, pp. 788–791, 1998.
[203] C. Kirchner, T. Gruber, F. Reuss, and K. Thonke, "MOVPE growth of ZnO using various oxygen precursors," *J. Cryst. Growth*, vol. 248, pp. 20–24, 2003.
[204] K. Ogata, K. Maejima, S. Fujita, and S. Fujita, "ZnO Growth Toward Optical Devices by MOVPE Using N2O," *J. Electron. Mater.*, vol. 30, pp. 659–661, 2001.
[205] A. Dadgar, N. Oleynik, D. Forster, S. Deiter, H. Witek, J. Bläsing, F. Bertram, A. Krtschil, A. Diez, J. Christen, and A. Krost, "A two-step metal organic vapor phase epitaxy growth method for high-quality ZnO on GaN/Al2O3 (0 0 0 1)," *J. Cryst. Growth*, vol. 267, pp. 140–144, 2004.
[206] W. I. Park, G.-C. Yi, and H. M. Jang, "Metalorganic vapor-phase epitaxial growth and photoluminescent properties of Zn1−xMgxO (0⩽x⩽0.49) thin films," *Appl. Phys. Lett.*, vol. 79, pp. 2022–2024, 2001.
[207] B. P. Zhang, L. H. Manh, K. Wakatsuki, T. Ohnishi, M. Lippmaa, N. Usami, M. Kawasaki, and Y. Segawa, "Epitaxial growth and polarity of ZnO films on sapphire (0001) substrates by low-pressure metal organic chemical vapor deposition," *Japanese J. Appl. Physics*, vol. 42, no. 4 B, pp. 2291–2295, 2003.
[208] J. Bardeen and W. Shockley, "Deformation potentials and mobilities in non-polar crystals," *Phys. Rev.*, vol. 80, no. 1, pp. 72–80, 1950.
[209] S. S. Devlin, *Physics and Chemistry of II-VI Compounds*. Amsterdam, 1967.
[210] K. I. Hagemark and L. C. Chacka, "Electrical transport properties of Zn doped ZnO," *J. Solid State Chem.*, vol. 15, no. 3, pp. 261–270, 1975.
[211] W. Zawadzki, *Handbook on Semiconductors*. Amsterdam, 1982.
[212] T. Pisarkiewicz, K. Zakrzewska, and E. Leja, "Conducting Thin Oxide Films With a Non-Parabolic Conduction Band," *Thin Solid Films*, vol. 174, pp. 217–223, 1989.
[213] D. B. M. Klaassen, "A unified mobility model for device simulation-II. Temperature dependence of carrier mobility and lifetime," *Solid. State. Electron.*, vol. 35, no. 7, pp. 961–967, 1992.
[214] P. Ebert, T. Zhang, F. Kluge, M. Simon, Z. Zhang, and K. Urban, "Importance of Many-Body Effects in the Clustering of Charged Zn Dopant Atoms in GaAs," *Phys. Rev. Lett.*, vol. 83, no. 4, pp. 757–760, 1999.
[215] B. K. Meyer, J. Sann, D. M. Hofmann, C. Neumann, and A. Zeuner, "Shallow donors and acceptors in ZnO," *Semicond. Sci. Technol.*, vol. 20, pp. S62–S66, 2005.
[216] J. Y. W. Seto, "The electrical properties of polycrystalline silicon films," *J. Appl. Phys.*, vol. 46, pp. 5247–5254, 1975.
[217] A. Bikowski and K. Ellmer, "Analytical model of electron transport in polycrystalline , degenerately doped ZnO films," *J. Appl. Crystallogr.*, vol. 116, p. 143704, 2014.
[218] S. M. Sze and K. K. NG., *Physics of Semiconductor Devices (Third Edition)*. USA: Wiley-Interscience, 2007.
[219] H. L. Tuller and A. S. Nowick, "Small polaron electron transport in reduced CeO2 single crystals," *J. Phys. Chem. Solids*, vol. 38, pp. 859–867, 1977.
[220] T. Holstein, "Studies of polaron motion Part II. The 'small' polaron," *Ann. Phys. (N.*

Y)., vol. 8, pp. 343–389, 1959.
[221] D. Emin and T. Holstein, "Studies of small-polaron motion IV. Adiabatic theory of the Hall effect," *Ann. Phys. (N. Y).*, vol. 53, pp. 439–520, 1969.
[222] K. Oura, V. G. Lifshits, A. A. Saranin, A. V. Zotov, and M. Katayama, "Surface Science: An Introduction." Springer, Berlin, 2003.
[223] N. Holonyak, R. M. Kolbas, R. D. Dupuis, and P. D. Dapkus, "Quantum-Well Heterostructure Lasers," *J. Quantum Electron.*, vol. 16, no. 2, pp. 170–186, 1980.
[224] J. P. Duchemin, M. Bonnet, F. Koelsch, and D. Huyghe, "A new method for the growth of GaAs epilayer at low H2 pressure," *J. Cryst. Growth*, vol. 45, pp. 181–186, 1978.
[225] K. Kurishima, H. Nakajima, S. Yamahata, T. Kobayashi, and Y. Matsuoka, "High-performance Zn-doped-base InP/InGaAs double-heterojunction bipolar transistors grown by metalorganic vapor phase epitaxy," *Appl. Phys. Lett.*, vol. 64, no. 9, p. 1111, 1994.
[226] M. Ohkubo, T. Ijichi, A. Iketani, and T. Kikuta, "980-nm Aluminum-Free InGaAs/InGaAsP/InGaP GRIN-SCH SL-QW Lasers," *J. Quantum Electron.*, vol. 30, no. 2, pp. 408–414, 1994.
[227] T. Egawa, H. Ishikawa, T. Jimbo, and M. Umeno, "Heteroepitaxial growth of III-V compound semiconductors for optoelectronic devices," *Bull. Mater. Sci.*, vol. 226, no. 3, pp. 363–367, 2006.
[228] J. Zhang, X. W. Fan, B. J. Yang, Z. P. Guan, Y. M. Lu, and D. Z. Shen, "Excitonic emission in ZnCdSe-ZnSe multiple quantum wells," *J. Cryst. Growth*, vol. 138, pp. 838–841, 1994.
[229] L. Sugiura, K. Shigenaka, F. Nakata, and K. Hirahara, "Misfit dislocation microstructure and kinetics of HgCdTe/CdZnTe under tensile and compressive stress," *J. Cryst. Growth*, vol. 145, pp. 547–551, 1994.
[230] P. L. Anderson, A. Erbil, C. R. Nelson, G. S. Tompa, and K. Moy, "A high-speed, rotating-disc metalorganic chemical vapor deposition system for the growth of (Hg,Cd)Te and related alloys," *J. Cryst. Growth*, vol. 135, pp. 383–400, 1994.
[231] H. M. Manasevit and W. I. Simpson, "The Use of Metal-Organics in the Preparation of Semiconductor Materials," *J. Electrochem. Soc.*, vol. 122, pp. 444–450, 1975.
[232] J. R. Creighton and J. E. Parmeter, "Critical Reviews in Solid State and Materials Sciences Metal CVD for microelectronic applications : An examination of surface chemistry and kinetics Metal CVD for," *Solid States Mater. Sci.*, vol. 18, pp. 175–238, 1993.
[233] J. P. Sénateur, F. Felten, S. Pignard, F. Weiss, A. Abrutis, V. Bigelyte, A. Teiserskis, Z. Saltyte, and B. Vengalis, "Synthesis and characterisation of YBCO thin films grown by injection-MOCVD," *J. Alloys Compd.*, vol. 251, pp. 288–291, 1997.
[234] J.-P. Sénateur, C. Dubourdieu, F. Weiss, M. Rosina, and A. Abrutis, "Pulsed injection MOCVD of functional electronic oxides," *Adv. Mater. Opt. Electron.*, vol. 10, pp. 155–161, 2000.
[235] P. A. Premkumar, N. Bahlawane, and K. Kohse-Höinghaus, "CVD of metals using alcohols and metal acetylacetonates, Part I: Optimization of process parameters and electrical characterization of synthesized films," *Chem. Vap. Depos.*, vol. 13, no. 5, pp. 219–226, 2007.
[236] B. D. Fahlman and A. R. Barron, "Substituent Effects on the Volatility of Metal β-diketonates," *Adv. Mater. Opt. Electron.*, vol. 10, pp. 223–232, 2000.
[237] A. C. Jones, H. C. Aspinall, and P. R. Chalker, "Molecular design of improved precursors for the MOCVD of electroceramic oxides," *Surf. Coatings Technol.*, vol. 12, pp. 2576–2590, 2002.
[238] E. I. Tsyganova and L. M. Dyagileva, "The reactivity of metal β-diketonates in the

thermal decomposition reaction," *Russ. Chem. Rev.*, vol. 65, pp. 315–328, 1996.
[239] M. A. Siddiqi, R. A. Siddiqui, and B. Atakan, "Thermal Stability , Sublimation Pressures , and Diffusion Coefficients of Anthracene , Pyrene , and Some Metal Diketonates," *J. Chemi. Eng. Data*, vol. 54, pp. 2795–2802, 2009.
[240] O. Nilsen, H. Fjellvåg, and A. Kjekshus, "Inexpensive set-up for determination of decomposition temperature for volatile compounds," *Thermochim. Acta*, vol. 404, pp. 187–192, 2003.
[241] M. Birkholz, *Thin film analysis by X-ray scattering*. Weinheim: Wiley, 2006.
[242] H. P. Klug and L. E. Alexander, *X-ray Diffraction Procedures*. New York: Wiley, 1974.
[243] T. H. de Keijser, J. I. Langford, E. J. Mittemeijer, and A. B. P. Vogels, "Use of the Voigt function in a single-line method for the analysis of X-ray diffraction line broadening," *J. Appl. Crystallogr.*, vol. 15, pp. 308–314, 1982.
[244] R. K. Nandi and S. P. S. Gupta, "The Analysis of X-ray Diffraction Profiles from Imperfect Solids by an Application of Convolution Relations," *J. Appl. Crystallogr.*, vol. 11, pp. 6–9, 1978.
[245] T. de Keijser, E. J. Mittemeijer, and H. C. F. Rozendaal, "The determination of crystallite-size and lattice-strain parameters in conjunction with the profile-refinement method for the determination of crystal structures," *J. Appl. Crystallogr.*, vol. 16, pp. 309–316, 1983.
[246] R. Delhez, T. H. de Keijser, and E. J. Mittemeijer, "Determination of crystallite size and lattice distortions through X-ray diffraction line profile analysis," *Fresenius Z. Anal. Chem.*, vol. 312, pp. 1–16, 1982.
[247] G. K. Williamson and W. H. Hall, "X-Ray line broadening from filed aluminium and wolfram," *Acta Metall.*, vol. 1, pp. 22–31, 1953.
[248] J. I. Langford and A. J. C. Wilson, "Scherrer after sixty years: A survey and some new results in the determination of crystallite size," *J. Appl. Crystallogr.*, vol. 11, pp. 102–113, 1978.
[249] W. E. Vargas, D. E. Azofeifa, and N. Clark, "Retrieved optical properties of thin films on absorbing substrates from transmittance measurements by application of a spectral projected gradient method," *Thin Solid Films*, vol. 425, pp. 1–8, 2003.
[250] N. Jacobson, *Basic Algebra I (Second Edition)*. San Francisco: Dover Publication, 2008.
[251] W. Dannhauser and P. A. Vaughan, "The Crystal Structure of Cuprous Chromite," *J. Am. Chem. Soc.*, vol. 77, no. 4, p. 896, 1955.
[252] C. D. Wagner, W. M. Riggis, L. E. Davis, J. F. Moulder, G. E. Mulenberg, and . , Perkin Elmer, Eden Prarie, MN, *Handbook of X-Ray Photoelectron Spectroscopy*. Minnesota: Perkin-Elmer, 1979.
[253] N. Pauly, S. Tougaard, and F. Yubero, "Determination of the Cu 2p primary excitation spectra for Cu, Cu 2O and CuO," *Surf. Sci.*, vol. 620, pp. 17–22, 2014.
[254] A. L. Allred, "Electronegativity values from thermochemical data," *J. Inorg. Nucl. Chem*, vol. 17, pp. 215–221, 1961.
[255] G. Deroubaix and P. Marcus, "X-ray Photoelectron Spectroscopy Analysis of Copper and Zinc Oxides and Sulphides," *Surf. Interface Anal.*, vol. 18, pp. 39–46, 1992.
[256] B. J. Ingram, G. B. Gonzalez, T. O. Mason, D. Y. Shahriari, A. Barnabe, D. Ko, and K. R. Poeppelmeier, "Transport and Defect Mechanisms in Cuprous Delafossites. 1. Comparison of Hydrothermal and Standard Solid-State Synthesis in CuAlO2," *Chem. Mater.*, vol. 16, pp. 5616–5622, 2004.
[257] B. J. Ingram, B. J. Harder, N. W. Hrabe, T. O. Mason, and K. R. Poeppelmeier, "Transport and Defect Mechanisms in Cuprous Delafossites . 2 . CuScO2 and

CuYO2," *Chem. Mater.*, vol. 16, pp. 5623–5629, 2004.
[258] N. F. Mott, "Conduction in glasses containing transition metal ions," *J. Non. Cryst. Solids*, vol. 1, pp. 1–17, 1968.
[259] N. F. Mott, "Conduction in non-crystalline materials," *Philos. Mag.*, vol. 19, no. 160, pp. 835–852, 1969.
[260] S. Suda, S. Fujitsu, K. Koumoto, and H. Yanagida, "The Effect of Atmosphere and Doping on Electrical Conductivity of CuO," *Jpn. J. Appl. Phys.*, vol. 31, pp. 2488–2491, 1992.
[261] D. Hartung, F. Gather, P. Hering, C. Kandzia, D. Reppin, a. Polity, B. K. Meyer, and P. J. Klar, "Assessing the thermoelectric properties of CuxO (x = 1 to 2) thin films as a function of composition," *Appl. Phys. Lett.*, vol. 106, no. 25, p. 253901, 2015.
[262] M. Cutler, J. F. Leavy, and R. L. Fitzpatrick, "Electronic transport in semimetallic cerium sulfide," *Phys. Rev.*, vol. 133, pp. A1143–A1152, 1964.
[263] T. H. Geballe and G. W. Hull, "Seebeck Effect in Silicon," *Phys. Rev.*, vol. 98, no. 4, pp. 940–947, 1955.
[264] T. H. Geballe and G. W. Hull, "Seebeck effect in Germanium," *Phys. Rev.*, vol. 94, p. 1134, 1954.
[265] K. D. Belashchenkov and D. V. Livanov, "Effect of impurities on thermoelectric power due to phonon drag in metals," *J. Exp. Theor. Phys.*, vol. 84, no. 6, pp. 1221–1224, 1997.
[266] D. K. C. MacDonald, *Thermoelectricity*, Wiley. New York, 1962.
[267] F. J. Blatt, "Thermoelectric power in metals at normal temperatures-reply to a query," *Proc. Physics. Soc*, vol. 83, pp. 1065–1068, 1964.
[268] M. S. Hossain, R. Islam, M. Shahjahan, and K. A. Khan, "Studies on the thermoelectric effect in semiconducting ZnTe thin films," *J. Mater. Sci. Mater. Electron.*, vol. 19, pp. 1114–1121, 2008.
[269] J. Cui, Y. Li, Z. Du, Q. Meng, and H. Zhou, "Promising defect thermoelectric semiconductors Cu1-xGaSbxTex (x=0-0.1) with the chalcopyrite structure," *J. Mater. Chem. A*, vol. 1, pp. 677–683, 2013.
[270] K. S. Urmila, T. N. Asokan, R. R. Philip, V. Ganesan, G. S. Okram, and B. Pradeep, "Structural, optical, electrical and low temperature thermoelectric properties of degenerate polycrystalline Cu7Se4 thin films," *Phys. Status Solidi*, vol. 251, no. 3, pp. 689–696, 2014.
[271] P. M. Chaikin and G. Beni, "Thermopower in the correlated hopping regime," *Phys. Rev. B*, vol. 13, p. 647, 1976.
[272] A. H. Wilson, *The Theory of Metals*. New York: Cambridge University Press, 1953.
[273] S. Lany, "Semiconducting transition metal oxides," *J. Phys. Condens. Matter*, vol. 27, p. 283203, 2015.
[274] S. Lany and A. Zunger, "Polaronic hole localization and multiple hole binding of acceptors in oxide wide-gap semiconductors," *Phys. Rev. B*, vol. 80, p. 085202, 2009.
[275] H. Peng and S. Lany, "Semiconducting transition-metal oxides based on d5 cations: theory for MnO and Fe2O3," *Phys. Rev. B*, vol. 85, no. 20, p. 201202, 2012.
[276] J. W. Hodby, T. E. Jenkins, C. Schwab, H. Tamura, and D. Trivich, "Cyclotron resonance of electrons and of holes in cuprous oxide Cu2O," *J. Phys. C Solid State Phys.*, vol. 9, pp. 1429–1439, 1976.
[277] B. K. Meyer, A. Polity, D. Reppin, M. Becker, P. Hering, P. J. Klar, T. Sander, C. Reindl, J. Benz, M. Eickhoff, C. Heiliger, M. Heinemann, J. Bläsing, A. Krost, S. Shokovets, C. Müller, and C. Ronning, "Binary copper oxide semiconductors: From materials towards devices," *Phys. Status Solidi B*, vol. 249, no. 8, pp. 1487–1509, 2012.

[278] C. Malerba, F. Biccari, C. Leonor Azanza Ricardo, M. D'Incau, P. Scardi, and A. Mittiga, "Absorption coefficient of bulk and thin film Cu2O," *Sol. Energy Mater. Sol. Cells*, vol. 95, no. 10, pp. 2848–2854, 2011.
[279] B. V. Karpenko, A. V. Kuznetsov, and V. V. Dyakin, "The theory of the magnon spectrum for CuO," *J. Phys. Condens. Matter*, vol. 8, pp. 1785–1795, 1996.
[280] F. G. Marabelli, B. Parravicini, and F. Salghetti-Drioli, "Optical gap of CuO," *Phys. Rev. B*, vol. 52, no. 3, pp. 1433–1436, 1995.
[281] X. a. Cao, E. B. Stokes, P. M. Sandvik, S. F. LeBoeuf, J. Kretchmer, and D. Walker, "Diffusion and tunneling currents in GaN/InGaN multiple quantum well light-emitting diodes," *IEEE Electron Device Lett.*, vol. 23, pp. 535–537, 2002.
[282] Y. W. Heo, Y. W. Kwon, Y. Li, S. J. Pearton, and D. P. Norton, "p-type behavior in phosphorus-doped (Zn,Mg)O device structures," *Appl. Phys. Lett.*, vol. 84, no. 18, pp. 3474–3476, 2004.
[283] Y. Cao, L. Miao, S. Tanemura, M. Tanemura, Y. Kuno, and Y. Hayashi, "Low resistivity p-ZnO films fabricated by sol-gel spin coating," *Appl. Phys. Lett.*, vol. 88, p. 251116, 2006.
[284] D. S. Shang, Q. Wang, L. D. Chen, R. Dong, X. M. Li, and W. Q. Zhang, "Effect of carrier trapping on the hysteretic current-voltage characteristics in Ag/La0.7Ca0.3MnO3/Pt heterostructures," *Phys. Rev. B*, vol. 73, no. 24, p. 245427, 2006.
[285] K. C. Kao and W. Hwang, *Electrical Transport in Solids*. Oxford: Pergamon, 1981.
[286] A. Ortiz-Conde, F. J. García Sánchez, and J. Muci, "Exact analytical solutions of the forward non-ideal diode equation with series and shunt parasitic resistances," *Solid. State. Electron.*, vol. 44, pp. 1861–1864, 2000.
[287] T. C. Banwell and A. Javakumar, "Exact analytical solution for current flow through diode with series resistance," *Electron. Lett.*, vol. 36, pp. 291–292, 2000.
[288] R. . M. Corless, G. H. Gonnet, D. E. G. Hare, D. J. Jeffrey, and D. E. Knuth, "On the Lambert W function," *Adv. Comput. Math.*, vol. 5, pp. 329–359, 1996.
[289] S. Götzendörfer, C. Polenzky, S. Ulrich, and P. Löbmann, "Preparation of CuAlO2 and CuCrO2 thin films by sol-gel processing," *Thin Solid Films*, vol. 518, no. 4, pp. 1153–1156, 2009.
[290] H. Y. Chen and C. C. Yang, "Transparent p-type Zn-doped CuCrO2 films by sol-gel processing," *Surf. Coatings Technol.*, vol. 231, pp. 277–280, 2013.
[291] L. Umar, S;Hee, Y.L;Jai-Yeoul, "Characteristics of the Mg-doped Cr deficient CuCr1-xMgxO2 thin films prepared by using pulsed laser deposition," *J. Nanosci. Nanotechnol.*, vol. 15, no. 7, pp. 5163–5166, 2015.
[292] T. W. Chiu, S. W. Tsai, Y. P. Wang, and K. H. Hsu, "Preparation of p-type conductive transparent CuCrO 2:Mg thin films by chemical solution deposition with two-step annealing," *Ceram. Int.*, vol. 38S, pp. S673–S676, 2012.
[293] N. Tsuboi, Y. Takahashi, S. Kobayashi, H. Shimizu, K. Kato, and F. Kaneko, "Delafossite CuAlO2 films prepared by reactive sputtering using Cu and Al targets," *J. Phys. Chem. Solids*, vol. 64, no. 9–10, pp. 1671–1674, 2003.
[294] A. N. Banerjee, S. Kundoo, and K. K. Chattopadhyay, "Synthesis and characterization of p-type transparent conducting CuAlO2 thin film by DC sputtering," *Thin Solid Films*, vol. 440, pp. 5–10, 2003.
[295] A. N. Banerjee, C. K. Ghosh, and K. K. Chattopadhyay, "Effect of excess oxygen on the electrical properties of transparent p-type conducting CuAlO2+x thin films," *Sol. Energy Mater. Sol. Cells*, vol. 89, no. 1, pp. 75–83, 2005.
[296] A. N. Banerjee, R. Maity, and K. K. Chattopadhyay, "Preparation of p-type transparent conducting CuAlO2 thin films by reactive DC sputtering," *Mater. Lett.*, vol. 58, no. 1–

2, pp. 10–13, 2004.
[297] J. Pan, W. Lan, H. Liu, Y. Sheng, B. Feng, X. Zhang, and E. Xie, “Preparation and properties of transparent conductive N-doped CuAlO2 films using N2O as the N source,” *J. Mater. Sci. Mater. Electron.*, vol. 25, no. 9, pp. 4004–4007, 2014.
[298] Y. Zhang, Z. Liu, D. Zang, and L. Feng, “Structural and opto-electrical properties of Cu-Al-O thin films prepared by magnetron sputtering method,” *Vacuum*, vol. 99, pp. 160–165, 2014.
[299] J. Luo, Y. J. Lin, H. C. Hung, C. J. Liu, and Y. W. Yang, “Tuning the formation of p-type defects by peroxidation of CuAlO2 films,” *J. Appl. Phys.*, vol. 114, p. 033712, 2013.
[300] A. N. Banerjee and S. W. Joo, “Poole–Frenkel effect in sputter-deposited CuAlO2+x nanocrystals,” *Nanotechnology*, vol. 24, p. 165705, 2013.
[301] G. Dong, M. Zhang, M. Wang, Y. Li, F. Gao, H. Yan, and X. Diao, “Influences of film thickness on the structural, electrical and optical properties of CuAlO2 thin films,” *Superlattices Microstruct.*, vol. 71, pp. 177–184, 2014.
[302] R.-S. Yu and H.-H. Yin, “Structural and optoelectronic properties of p-type semiconductor CuAlO2 thin films,” *Thin Solid Films*, vol. 526, pp. 103–108, 2012.
[303] R.-S. Yu, C.-J. Lu, D.-C. Tasi, S.-C. Liang, and F.-S. Shieu, “Phase Transformation and Optoelectronic Properties of p-Type CuAlO2 Thin Films,” *J. Electrochem. Soc.*, vol. 154, no. 9, pp. H838–H843, 2007.
[304] A. S. Reddy, P. S. Reddy, S. Uthanna, and G. M. Rao, “Characterization of CuAlO2 films prepared by dc reactive magnetron sputtering,” *J. Mater. Sci. Mater. Electron.*, vol. 17, no. 8, pp. 615–620, 2006.
[305] A. S. Reddy, H.-H. Park, G. M. Rao, S. Uthanna, and P. S. Reddy, “Effect of substrate temperature on the physical properties of dc magnetron sputtered CuAlO2 films,” *J. Alloys Compd.*, vol. 474, pp. 401–405, 2009.
[306] W. Lan, W. L. Cao, M. Zhang, X. Q. Liu, Y. Y. Wang, E. Q. Xie, and H. Yan, “Annealing effect on the structural, optical, and electrical properties of CuAlO2 films deposited by magnetron sputtering,” *J. Mater. Sci.*, vol. 44, no. 6, pp. 1594–1599, 2009.
[307] P. H. Hsieh, Y. M. Lu, W. S. Hwang, J. J. Yeh, and W. L. Jang, “Effect of Al content on electrical conductivity and transparency of P-type Cu-Al-O thin film,” *Surf. Coatings Technol.*, vol. 205, pp. S206–S209, 2010.
[308] Z. Deng, X. Fang, R. Tao, W. Dong, D. Li, and X. Zhu, “The influence of growth temperature and oxygen on the phase compositions of CuAlO2 thin films prepared by pulsed laser deposition,” *J. Alloys Compd.*, vol. 466, pp. 408–411, 2008.
[309] F. A. Benko and F. P. Koffyberg, “Opto-electronic properties of CuAlO2,” *J. Phys. Chem. Solids*, vol. 45, pp. 57–59, 1984.
[310] H. S. Kim, B. S. Lee, S. H. Ji, H. Kim, D. Kim, Y. E. Ihm, and W. K. Choo, “Transport and magnetic properties of delafossite CuAl1−xMnxO2 ceramics,” *Phys. Status Solidi*, vol. 241, pp. 1545–1548, 2004.
[311] R. Liu, Y. Li, B. Yao, Z. Ding, R. Deng, L. Zhang, H. Zhao, and L. Liu, “Experimental and first-principles study of photoluminescent and optical properties of Na-doped CuAlO2: the role of the NaAl - 2Nai complex,” *J. Phys. D. Appl. Phys.*, vol. 48, no. 33, p. 335102, 2015.
[312] Y. Ren, G. Zhao, C. Zhang, and Y. Chen, “Preparation of CuAlO2 thin films with high transparency and low resistivity using sol-gel method,” *J. Sol-Gel Sci. Technol.*, vol. 61, no. 3, pp. 565–569, 2012.
[313] K. R. Murali and M. Balasubramanian, “Properties of CuAlO2 thin films deposited by polyacrylamide gel route,” *Mater. Sci. Semicond. Process.*, vol. 16, no. 1, pp. 38–42,

2013.
[314] S. H. Chiu and J. C. A. Huang, “Characterization of p-type CuAlO2 thin films grown by chemical solution deposition,” *Surf. Coatings Technol.*, vol. 231, pp. 239–242, 2013.
[315] G. Li, X. Zhu, H. Lei, H. Jiang, W. Song, Z. Yang, J. Dai, Y. Sun, X. Pan, and S. Dai, “Preparation and characterization of CuAlO2 transparent thin films prepared by chemical solution deposition method,” *J. Sol-Gel Sci. Technol.*, vol. 53, no. 3, pp. 641–646, 2010.
[316] T. Suriwong, T. Thongtem, and S. Thongtem, “Thermoelectric and optical properties of CuAlO2 synthesized by direct microwave heating,” *Curr. Appl. Phys.*, vol. 14, no. 9, pp. 1257–1262, 2014.
[317] J. S. Yoon, Y. S. Nam, K. S. Baek, C. W. Park, H. L. Ju, and S. K. Chang, “Growth and properties of transparent conducting CuAlO2 single crystals by a flux self-removal method,” *J. Cryst. Growth*, vol. 366, pp. 31–34, 2013.
[318] H. Luo, M. Jain, T. M. McCleskey, E. Bauer, a. K. Burrell, and Q. Jia, “Optical and Structural Properties of Single Phase Epitaxial p-Type Transparent Oxide Thin Films,” *Adv. Mater.*, vol. 19, no. 21, pp. 3604–3607, 2007.
[319] S. Gao, Y. Zhao, P. Gou, N. Chen, and Y. Xie, “Preparation of CuAlO2 nanocrystalline transparent thin films with high conductivity,” *Nanotechnology*, vol. 14, no. 5, pp. 538–541, 2003.
[320] Y. Kakehi, S. Nakao, K. Satoh, and T. Yotsuya, “Properties of copper-scandium oxide thin films prepared by pulsed laser deposition,” *Thin Solid Films*, vol. 445, no. 2, pp. 294–298, 2003.
[321] Y. Kakehi, K. Satoh, T. Yotsuya, S. Nakao, T. Yoshimura, A. Ashida, and N. Fujimura, “Epitaxial growth of CuScO2 thin films on sapphire a-plane substrates by pulsed laser deposition,” *J. Appl. Phys.*, vol. 97, no. 8, p. 083535, 2005.
[322] N. Duan, A. W. Sleight, M. K. Jayaraj, and J. Tate, “Transparent p-type conducting CuScO2+x films,” *Appl. Phys. Lett.*, vol. 77, no. 9, p. 1325, 2000.
[323] Y. Kakehi, K. Satoh, T. Yotsuya, K. Masuko, T. Yoshimura, A. Ashida, and N. Fujimura, “Optical and electrical properties of CuScO2 epitaxial films prepared by combining two-step deposition and post-annealing techniques,” *J. Cryst. Growth*, vol. 311, no. 4, pp. 1117–1122, 2009.
[324] Z. Deng, X. Fang, S. Wu, Y. Zhao, W. Dong, J. Shao, and S. Wang, “Structure and optoelectronic properties of Mg-doped CuFeO2 thin films prepared by sol–gel method,” *J. Alloys Compd.*, vol. 577, pp. 658–662, 2013.
[325] P. Dordor, J. P. Chaminade, A. Wichainchai, E. Marquestaut, J. P. Doumerc, M. Pouchard, and P. Hagenmuller, “Crystal growth and electrical properties of CuFeO2 single crystals,” *J. Solid State Chem.*, vol. 75, pp. 105–112, 1988.
[326] H.-Y. Chen and J.-R. Fu, “Delafossite–CuFeO2 thin films prepared by atmospheric pressure plasma annealing,” *Mater. Lett.*, vol. 120, pp. 47–49, 2014.
[327] H. Y. Chen and G. W. Fu, “Influences of post-annealing conditions on the formation of delafossite-CuFeO2 thin films,” *Appl. Surf. Sci.*, vol. 288, pp. 258–264, 2014.
[328] F. A. Benko and F. P. Koffyberg, “Optoelectronic properties of p- and n-type delafossite CuFeO2,” *J. Phys. Chem. Solids*, vol. 48, no. 5, pp. 431–434, 1987.
[329] K. Ueda, T. Hase, H. Yanagi, H. Kawazoe, H. Hosono, H. Ohta, M. Orita, and M. Hirano, “Epitaxial growth of transparent p-type conducting CuGaO2 thin films on sapphire (001) substrates by pulsed laser deposition,” *J. Appl. Phys.*, vol. 89, no. 3, pp. 1790–1793, 2001.
[330] F. A. Benko and F. P. Koffyberg, “The optical interband transitions of the semiconductor CuGaO2,” *Phys. Status Solidi*, vol. 94, pp. 231–234, 1986.

[331] T. Mine, H. Yanagi, K. Nomura, T. Kamiya, M. Hirano, and H. Hosono, “Control of carrier concentration and surface flattening of CuGaO2 epitaxial films for a p-channel transparent transistor,” *Thin Solid Films*, vol. 516, no. 17, pp. 5790–5794, 2008.
[332] M. Singh, B. R. Mehta, D. Varandani, and V. N. Singh, “Electrical and optical properties of Sn doped CuInO2 thin films: Conducting atomic force microscopy and spectroscopic ellipsometry studies,” *J. Appl. Phys.*, vol. 106, no. 5, p. 053709, 2009.
[333] B. Yang, Y. He, A. Polity, and K. B. Meyer, “Structural, optical and electrical properties of transparent conducting CuInO2 thin films prepared by RF sputtering,” *Mater. Res. Soc. Symp. Proc.*, vol. 865, pp. 1–5, 2005.
[334] J. P. Perdew, K. Burke, and M. Ernzerhof, “Generalized Gradient Approximation Made Simple,” *Phys. Rev. Lett.*, vol. 77, pp. 3865–3868, 1996.
[335] J. Heyd, G. E. Scuseria, and M. Ernzerhof, “Hybrid functionals based on a screened Coulomb potential,” *J. Chem. Phys.*, vol. 118, p. 8207, 2003.

ABSTRACT

Transparent conducting oxides such as ITO, FTO or AZO, are currently used in a number of commercial applications, such as transparent electrodes for flat panel displays, light-emitting diodes and solar cells. These applications rely essentially on n-type conductive materials. The developments towards electronic devices based on transparent p-n junctions have triggered an intense research for the synthesis of p-type transparent conductors with sufficiently high quality. Copper-based delafossite materials are thought to hold one of the highest potential and among them $CuCrO_2$ has exhibited strong potential in terms of trade off electrical conductivity and optical transparency. In this work, we report for the first time on $CuCrO_2$ thin-films, grown using a pulsed injection MOCVD. We particularly highlight the influence of the growth temperature, the volume precursor ration and the oxygen partial pressure on chemical, morphological, structural, electrical and optical properties of the films. Delafossite $CuCrO_2$ thin films are synthesized as low as 310°C on glass substrate, which is the lowest growth temperature reported to our knowledge. The films exhibit a carbon contamination below 1%, an excess of chromium and a p-type conductivity. Electrical conductivity at room temperature is measured as high as $17 S.cm^{-1}$ with a moderate visible transparency at 50%. We report the highest trade off electrical conductivity and visible transparency of $CuCrO_2$ thin films. We investigate the transport conduction with simultaneous electrical and thermoelectrical measurements and band conduction and small polaron models are controversially discussed. A functional transparent p-n junction $CuCrO_2$/ZnO, based on only two-layers, is synthesized with a visible transparency of 45-50%. The junction shows a typical current-voltage characteristic of a diode, with high series resistance features. The device is efficiently acting as an UV detector.